Contributions to High Technology Readiness Level Experimental Turbine Aerothermal Research and Applications



Mathias Michaud

Department of Engineering

University of Oxford

A thesis submitted for the degree of

Doctor of Philosophy

University College

February 2022

Abstract

This thesis reports a series of contributions to high technology readiness level (TRL) experimental turbine aerothermal research (testing facilities, instrumentation and data processing techniques) and the application of high TRL research techniques to study turbine in-service deterioration. High TRL research is key in turbine development to derisk engine program by validating the aerothermal performance of novel turbine component designs earlier in the engine development programs, thus allowing for more innovative solutions to be considered. It therefore accelerates, derisks and reduces the cost of the development of new turbine components for more efficient engine operation. Data from high TRL experiments can also prove fruitful for fundamental research. While most of the turbine research is achieved by having a fundamental understanding of the flow physics with simplified studies isolating certain effects (*bottom-up* approach), high TRL experiments can be regarded as a *top-down* approach where all the boundary conditions are coupled, to accurately provide the final result of the complex system. High TRL experiments can then validate the accuracy of the superposition (in a model) of individual effects obtained in the bottom-up approach, therefore making the two approaches complimentary.

This thesis is presented as a collection of five academic publications related to high TRL experimental turbine research. The first publication is on the upgrade of a high TRL turbine testing facility to independently control the Mach number and Reynolds number. The second publication is on the development of instrumentation for high-accuracy in situ infrared calibration in environment with through-wall heat flux and surface temperature non-uniformity. The third publication is on the development of a new post-processing method to extract the heat transfer coefficients (internal and external) from transient overall cooling effectiveness measurements on internally cooled turbine components. The fourth and fifth publications are on the application of high-TRL research techniques to study the impact of in-service deterioration on the aerodynamic and thermal performance of real turbine components, respectively.

To Marie-Joëlle

Acknowledgements

I would like to firstly acknowledge Prof. Huu Duc Vo for believing in me and encouraging my desire to pursue graduate studies. His rigorous training and support made possible something that initially seemed impossible.

I am very grateful to my project supervisor Prof. Thomas Povey for giving me the opportunity to be part of his research group. I feel very privileged to have worked with him in such a prestigious research institution. His unmatched problem-solving capabilities and contagious enthusiasm made my time in the Osney lab an intellectually enriching and enjoyable experience.

I would like to thank Rolls-Royce and the CDT in Gas Turbine Aerodynamics for funding my research project. Special thanks to Frédéric Goenaga, David Newman and Dougal Jackson for their support.

I would also like to thank my colleagues from the blowdown area for their continuous support on the ECAT facility. To Nafiz for firing all of my 500 ECAT runs, to Dan for the support with the traverse system and to Dom for always finding solutions to all my rig-related problems.

Acknowledgements are also due to all my Oxford friends who made my life in and out of the lab enjoyable. To Tales and Isadora for all our dinners together to find the best restaurants in Oxford and London. To Gabrielle and Fabian for the fun day trips and great evenings chatting, singing and dancing until late. To Philippa for your patience, joy, and careful listening during the though bits of the writing-up period. To James for entertaining all those parties and convincing me that linear cascades can actually be cool. To Anna for your authenticity and making me laugh during all those early mornings and weekends in the lab. To Francesco for your sincere kindness, invaluable technical and moral support, and unparalleled devotion to pizza—it was a privilege to have had such a great mentor.

To all my family, in particular my parents, my brother and my in-laws for their love and continuous encouragements.

Finally, my sincerest gratitude goes to my best friend and wife Marie-Joëlle for following me into this great adventure. Thank you for your patience, joy and love. This degree would not have been possible without you as my lighthouse in this ocean of emotions that is life.

Contents

Acknowledgements iv

Nomenclature vii

1. Introduction 1

2. Literature Review 8

3. Annular Dump Diffuser and Deswirl System for Back-pressure Control in an Engine-scale Transonic Annular Cascade 29

4. Methodology for High-accuracy Infrared Calibration in Environments with Through-wall Heat Flux 52

5. Impact of In-service Deterioration on the Aerodynamic Performance of High-Pressure Nozzle Guide Vanes 63

6. Impact of In-service Deterioration on the Thermal Performance of High-Pressure Nozzle Guide Vanes 83

7. Methods to Extract Underlying Boundary Conditions from Transient Overall Cooling Effectiveness Measurements 103

8. Conclusions 123

9. References 126

Nomenclature

Abreviations

ABB	ASEA Brown Boveri
AFRL	Air Force Research Laboratory
ASC	Annular Sector Cascade
CF	Capacity Facility
DLR	German Aerospace Center
DMLS	direct metal laser sintering
EBPVD	electron-beam physical vapor deposition
ECAT	Engine Component AeroThermal (facility)
EXP	experiment
HCTF	Hot Component Testing Facilities
HP	high pressure
HSAC	High Speed Annular Cascade
HSTF	Hot Section Testing Facilities
HTC	heat transfer coefficient
IHI	Ishikawajima-Harima Heavy Industries Co.
IR	infrared
KTH	Royal Institute of Technology
LE	leading edge
MTO	max-take-off
NASA	National Aeronautics and Space Administration
NDTL	Notre-Dame Turbomachinery Laboratory
NGV	nozzle guide vane
OTRF	oxford turbine research facility
PETAL	Purdue Experimental Turbine Aerothermal Laboratory
PIV	particle image velocimetry
PR	pressure ratio
PS	pressure surface
SS	suction surface
TBC	thermal barrier coating
TCRF	Turbine Cooling Research Facility
TE	trailing edge
TET	turbine entry temperature
TLC	thermochromic liquid crystals
TR	temperature ratio
TRF	Turbine Research Facility
TRL	technology readiness level
TTF	Turbine Test Facility
TTTF	Transonic Turbine Test Facility
UV	ultraviolet
VKI	Van Karman Institute
YSZ	yttria-stabilized zirconia

Greek

Λ_s	roughness shape-density parameter
η_C	isentropic compressor efficiency
η_f	adiabatic film cooling effectiveness
$\bar{\eta}_f$	laterally-average adiabatic film cooling effectiveness
$\bar{\bar{\eta}}_f$	area-average adiabatic film cooling effectiveness
η_T	isentropic turbine efficiency
θ	overall cooling effectiveness
κ	thermal conductivity

Roman

A	planform (flat) surface area
A_s	windward frontal (projected) surface area of a roughness element
A_f	windward wetted surface area of a roughness element
B	blowing ratio
c	recovery ratio
C	tangential chord
h	heat transfer coefficient
$\bar{h}$	laterally-average heat transfer coefficient
$\bar{\bar{h}}$	area-average heat transfer coefficient
i	index in the x direction
I	momentum flux ratio
j	index in the y direction
k	roughness height
k_s	equivalent sandgrain roughness height
L	streamwise surface length
M	Mach number
N_x	total number of points in the x direction
N_y	total number of points in the y direction
R_a	centerline average roughness height for a 2D profile
R_z	maximum peak-to-valley height for a 2D profile
Re	Reynolds number
S_a	centerline average roughness height for a 3D profile
S_z	maximum peak-to-valley height for a 3D profile
St	Stanton number
T	temperature
Tu	turbulence intensity
x	streamwise direction on a vane
y	spanwise direction on a vane
z	wall-normal direction on a vane

General subcripts

0	total property
c	coolant property
cell	cell element of the measured surface profile
m	mainstream property
w	wall property

1. Introduction

Air transport plays a crucial role in our modern societies. It provides the broadest worldwide transport network and brings huge economic, social and technological benefits to people. Air transport is however a major emitter of greenhouse gases, contributing to approximately 2.5 % of global CO_2 emissions. In order to maintain global warming within 1.5 degrees Celsius of pre-industrial temperatures, the aviation industry is now under great pressure to decarbonise air travel by 2050. This requires drastic improvement of every component of a jet engine, but since the current timescale for the introduction of a new technology in an engine can be up to 10 years, there is a strong need to change the way we develop and scale gas turbine technologies to meet the CO_2 emission targets in time.

Figure 1.1a shows a simplified schematic of the main components of a gas turbine and Figure 1.1b shows a simplified entropy-enthalpy thermodynamic diagram of a gas turbine. Gas turbines for aircraft propulsion operate in an open basis. Air from the atmosphere (station 1 in Figure 1.1a) is continuously drawn into a compressor to increase its pressure. The compressed air (station 2) then enters the combustor to be mixed with fuel and ignited for combustion to occur. The combustion occurs at relatively constant pressure and creates combustion products at elevated temperature. The high temperature combustion products (station 3) then enter the turbine to extract work. A fraction of the extracted work by the turbine is to drive the compressor, the other fraction is typically used to drive a fan to propel the aircraft.

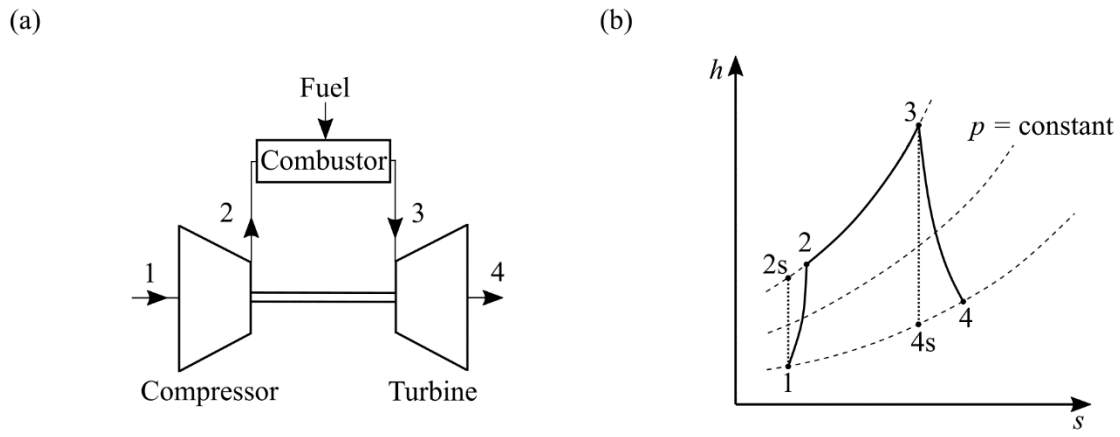


Figure 1.1: (a) schematic of the main components of a single-shaft gas turbine; (b) entropy-enthalpy thermodynamic diagram.

The efficiency of the gas turbine cycle—also known as the Brayton cycle—is function of the compressor pressure ratio (PR), the temperature ratio (TR) between the turbine entry temperature (TET) at station 3 and the compressor inlet temperature (atmospheric), and the isentropic efficiencies of the compressor (η_C) and turbine (η_T). Figure 1.2a shows the Brayton cycle efficiency versus non-dimensional power out as a function of PR and TR for non-isentropic compressor and turbine. We see that in the achievable compressor PR in the current gas turbines, it is of interest to increase the temperature ratio (i.e. increasing TET) to increase the cycle efficiency.

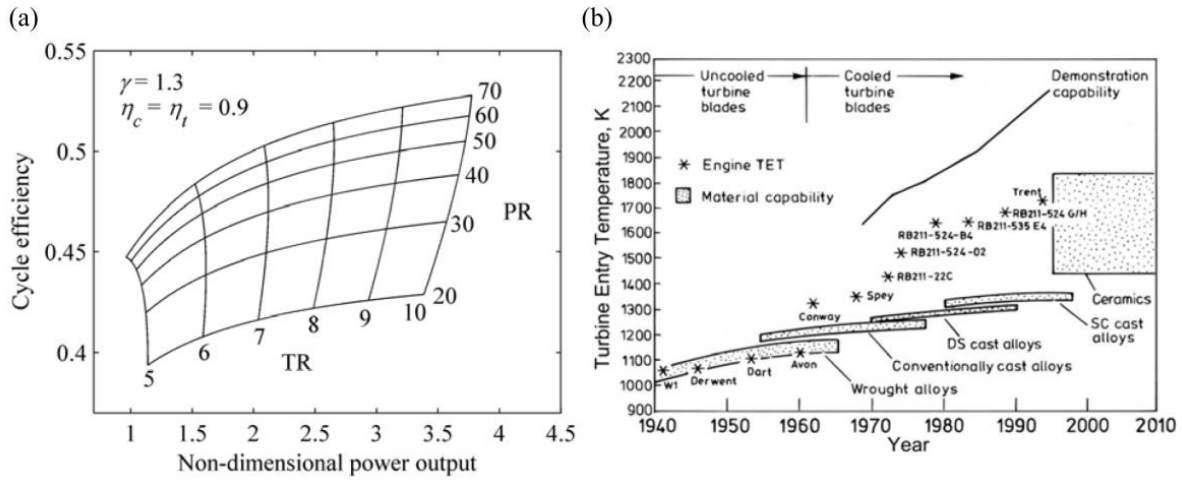


Figure 1.2: (a) Brayton cycle efficiency versus non-dimensional power out as a function of pressure ratio and temperature ratio for non-isentropic compressor and turbine [1]; (b) TET of Rolls-Royce engines since 1940 [1].

This is why over the last 80 years TET has significantly increased in gas turbines as shown in Figure 1.2b. The turbine entry temperature (TET) is limited by material, cooling technology and cost. Considerable efforts are thus put in the development of efficient high-pressure (HP) turbine components (vanes and blades) that can sustain such elevated temperatures, since it plays a significant role in setting the overall engine performance.

The heat transfer between the hot gases from the combustor and the turbine components occurs through convection. The convective heat flux q'' is proportional to the difference between the fluid temperature T_{01} and the surface temperature T_{w} (Equation 1.1). The convection heat transfer coefficient h between the fluid and the surface depends on the boundary layer condition, which is influenced by the geometry, the nature of the fluid motion, and an assortment of fluid thermodynamic properties.

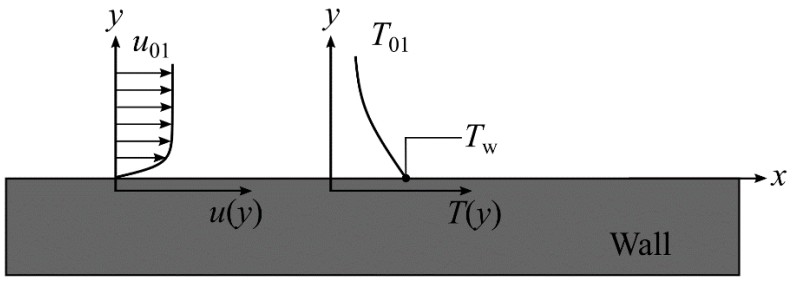


Figure 1.3: Diagram of a velocity boundary layer and a thermal boundary layer

$$q'' = h(T_{01} - T_{\mathrm{w}}) \tag{1.1}$$

Turbine designers put a lot of effort to maintain the external surface temperature of the turbine component T_{w} below the material fusion point by: reducing the heat flux to the wall by ejecting a thin film of coolant (air from the compressor that is colder than the combustion products) just above the wall of the component to reduce the driving temperature; and/or by internally cooling the component. Very elaborate cooling schemes as shown in Figure 1.4 are therefore common in HP turbines to allow for a high TET. Despite their complexity, the overall aerothermal performance (flow capacity, thermal performance and aerodynamic performance)

of fully-featured HP components (as installed in an engine) are typically never measured or only measured under engine conditions during engine tests.

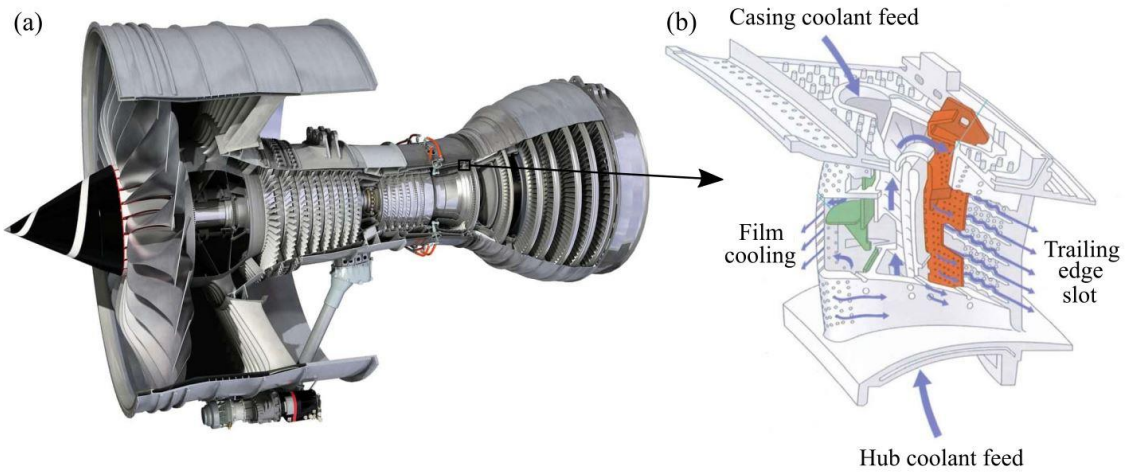


Figure 1.4: (a) Cross section of a Rolls-Royce Trent 900 engine; (b) example of a modern heavily cooled HP vane [1].

For instance, manufacturers will perform thermal paint tests during the certification tests of a new engine to measure the overall thermal performance of their HP components. However, engine tests are extremely expensive and because they are performed at the end of the engine development program, engine manufacturers are very conservative and avoid using new and riskier designs that could be promising. This significantly extends the cost and time to introduce new technologies in HP turbine components and reduces the design space.

The development of high technology readiness level (TRL) turbine aerothermal research facilities is therefore key to allow researchers and manufacturers to test the aerothermal performance of real-engine HP component geometries under engine-representative conditions earlier in the engine development program. Such facilities accelerate, derisk and reduce the cost of the development of new HP component designs for more efficient engine operation. High TRL turbine research facilities are even more powerful with the maturation of direct metal laser sintering (DMLS) technologies, which now allows the fast 3D printing of vanes with more complex cooling designs compared to the traditional casting process.

High TRL turbine aerothermal research facilities can also be used for fundamental research. The vast majority of gas turbine experimental research is achieved by having a fundamental understanding of the flow physics with simplified studies isolating certain effects. This philosophy can be regarded as a *bottom-up approach*, where the individual boundary conditions measured in isolation are superposed in a model to predict the final result of a complex coupled system (e.g. a turbine component). On the other hand, high TRL experiments which can be regarded as a *top-down approach* where all the boundary conditions are coupled, accurately provide the final result of the complex system. Data from high TRL experiments can be used to assess prediction errors in the bottom-up approach, therefore making the two approaches complimentary. Some decoupling on high TRL data can also be done to understand the individual boundary conditions of the system.

1.1. Research Outcomes

This thesis is mainly focused on the development of high TRL turbine aerothermal research facilities, instrumentation and post-processing methods. The results of a high TRL experimental research campaign to study the impact of in-service turbine deterioration is also presented. The research outcomes of this thesis are:

- A new annular dump diffuser and deswirl system was designed to control the back-pressure of a transonic fully annular turbine cascade. The purpose of this system is to provide independent control of Mach number and Reynolds number, while maintaining good optical and probe access (without interaction effects) and to reduce the risk of exit static pressure disturbances (due to particular duct design). The proposed system was commissioned in the Oxford Engine Component AeroThermal (ECAT) facility, a high TRL HP nozzle guide vane (NGV) cascade. With this new system installed, the ECAT facility can be used to validate engine HP NGV designs at different engine-representative operating conditions (cruise and max-take-off, MTO). The facility can now also be used to isolate

Mach number and/or Reynolds number effects during more fundamental research programs.

- New instrumentation was developed for accurate in situ infrared (IR) calibration in environments with significant through-wall heat flux and surface temperature non-uniformity (e.g. real engine components). The proposed sensor is particularly relevant for facilities performing overall cooling effectiveness measurements, but also for IR measurements on adiabatic surfaces with significant lateral temperature variations (e.g. adiabatic film cooling effectiveness measurements).
- A new post-processing method was developed to extract the heat transfer coefficients (internal and external) from transient overall cooling effectiveness measurements on internally cooled components (like most turbine components). While the proposed method is still at an early stage in its development, it provides a first step towards the decoupling of the underlying boundary conditions in highly coupled environment (e.g. high TRL experiments). A complete uncertainty analysis on the method is presented.
- An experimental study was performed to assess the impact of in-service deterioration on the aerothermal performance of HP NGVs. A total of 15 mid-life to end-of-life vanes were removed from operational engines and tested in the ECAT facility to measure their overall aerodynamic and thermal performances. The purpose of this high TRL study is to provide aerothermal performance reference points for whole-life engine performance assessment. This study is also a demonstration of the importance of high TRL research when studying highly-coupled systems (e.g. in-service deteriorated turbine components) where many deterioration effects interact with each other.

The content of this thesis covers a broad range of topics and it is hoped that—as a whole—it will contribute to the advancement of high TRL turbine aerothermal research to accelerate and

derisk the development of more efficient turbine components in an effort to decarbonise air transport.

1.2. Thesis Outline

This thesis is a collection of academic publications and is divided into the following chapters:

- Chapter 2 reviews the relevant published literature on high TRL turbine research facilities and measurement techniques, and in-service deterioration aerothermal effects. Further reference to the relevant literature is included in the other chapters.
- Chapter 3 describes the design and commissioning of a new dump diffuser and deswirl system in the Oxford ECAT facility.
- Chapter 4 describes the development of new instrumentation for accurate in situ IR calibration in environments with significant through-wall heat flux and surface temperature non-uniformity.
- Chapter 5 describes the results of an experimental study to characterise the overall aerodynamic performance of in-service deteriorated HP NGVs.
- Chapter 6 describes the results of an experimental study to characterise the overall thermal performance of in-service deteriorated HP NGVs.
- Chapter 7 describes a new method to extract the heat transfer coefficients (internal and external) from transient overall cooling effectiveness measurements on internally cooled turbine components.
- Chapter 8 summarises the key conclusions of this thesis and outlines areas of future investigation.

2. Literature Review

In this chapter, a review of the high TRL turbine aerothermal research facilities and measurement techniques is presented. A review of the published literature on in-service deterioration effects on HP NGVs is also presented. Further reference to the relevant literature is included in the appropriate chapter.

2.1. High Technology Readiness Level Turbine Research

A review of the high TRL turbine research facilities and measurement techniques is now considered.

2.1.1. Review of high TRL turbine research facilities

Most of turbine research is performed in cascade experiments as it allows to isolate a vane row, a blade row or a stage in a controlled environment for an in-depth investigation of the flow physics. Four types of cascades are mainly used in turbine research (in order of increasing complexity and cost): linear, annular sector, fully annular and rotating.

Linear cascades are linearised annular sectors of stationary vanes or blades that form a rectangular test section. Linear cascades are the cheapest due to their geometric simplicity and they offer a very easy adjustment of the flow properties such as the inlet flow angle, inlet/outlet Mach number and outlet Reynolds number. The two main disadvantages of linear cascades are that they can suffer from periodicity issues and that the radial pressure gradient encountered in real machines cannot be replicated. With some exceptions (e.g. [3]), linear cascades are often better suited for low TRL research.

Annular sector cascades—as the name suggests—consist of an annular sector of stationary vanes. Like all annular cascades (sector, full and rotating), annular sector cascades have the capability of testing real engine hardware and can replicate the radial pressure gradient for more engine-representative secondary flow features. Annular cascades are therefore better suited for high TRL research. Annular sector cascades are smaller and cheaper to build and

operate compared to fully annular cascades. The main disadvantage of annular sector facilities compared to fully annular facilities is their lack of inherent periodicity. Moreover, the swirling motion of the flow downstream of annular cascades (sector, full and rotating) makes it more challenging (as compared to linear cascades) to have independent control on the exit Mach number and exit Reynolds number. This will be discussed in more detail in Chapter 3.

Fully annular cascades consist of an entire stationary ring of vanes. This type of cascade is free from periodicity issues and can be particularly useful to study the flow capacity of a full ring of HP NGV, a relevant parameter that sets the operating point of the engine. Fully annular and annular sector cascades have the advantage (over rotating cascades) of having good optical and probe access downstream of the vanes because of the absence of a rotor.

Rotating cascades consist of an entire turbine stage—a full ring of stationary vanes followed by a full ring of blades mounted on a rotor. Rotating cascades allow to replicate representative tip clearance flows, centrifugal forces and Coriolis forces on the blade flow. They can also be used to study interactions between the vane row and the blade row, and measure stage efficiency. Rotating cascades are however the most complex and expensive cascades.

Most high TRL turbine cascades operate at engine-representative conditions in terms of Mach number, Reynolds number and inlet turbulence intensity, and some cascades even operate at engine-representative mainstream-to-coolant temperature ratio (~2). Table 2.1 lists the major high TRL annular turbine cascades and their measurement capabilities. Half of the listed facilities have the capability to test real engine hardware [4, 5, 6, 7, 10, 11, 16, 19]. In the other facilities not using engine components (i.e. not internally cooled), the tested vanes and/or blades will have at least engine-representative film cooling schemes.

Table 2.1: List of the major high TRL annular turbine cascades.

Facility	Cascade type	Institution	Measurement capabilities
Sector [4]	Annular sector	Oxford	Overall cooling effectiveness
TCRF [5]	Annular sector	NASA	Overall cooling effectiveness
HCTF [6]	Annular sector	ABB	Overall cooling effectiveness
IHI cascade [7]	Annular sector	IHI	Overall cooling effectiveness
ASC [8]	Annular sector	KTH	Aerodynamics
HSTF [9]	Fully annular	NASA	Aerodynamics Overall cooling effectiveness
CF [10]	Fully annular	Oxford	Capacity
ECAT [11]	Fully annular	Oxford	Aerodynamics Capacity Overall cooling effectiveness
OTRF [12]	Rotating	Oxford	Aerodynamics Stage efficiency External heat transfer
CT3 [13]	Rotating	VKI	Aerodynamics Stage efficiency External heat transfer
NG-Turb [14]	Rotating	DLR	Aerodynamics Stage efficiency External heat transfer
TTTF [15]	Rotating	TU Graz	Aerodynamics Stage efficiency PIV
PETAL [16]	Rotating	Purdue	Aerodynamics Stage efficiency Overall cooling effectiveness PIV
NDTL [17]	Rotating	Notre-Dame	Aerodynamics Stage efficiency
TRF [18]	Rotating	AFRL	Aerodynamics Stage efficiency External heat transfer
TTF [19]	Rotating	Ohio State	Aerodynamics Stage efficiency External heat transfer

2.1.2. Review of measurement techniques in turbine research facilities

The measurement techniques in high TRL turbine research facilities are now considered. Aerodynamic measurements in high TRL facilities are typically performed by traversing multi-hole pneumatic probes or hot wires upstream and downstream of the vane row and/or blade row to measure the static and total pressures, and flow angle distributions [20]. This allows researchers to assess the overall aerodynamic performance of the tested components by measuring the profile loss, endwall loss and tip leakage loss (in rotating cascades). Some facilities [15, 16] have the capability to perform particle image velocimetry (PIV) measurements. By seeding the flow with tracer particles illuminated with a stroboscope or a laser, the velocity and the direction of the tracer particles (hence the flow) through the cascade can be followed with a camera.

Most rotating turbine facilities have the capability to measure the efficiency of the turbine stage, defined as the ratio of actual work extracted from the turbine rotor to the ideal work possible from an isentropic expansion across the same pressure ratio. The actual work out of the turbine rotor is usually calculated by measuring the output torque and velocity of the rotor.

Turbine facilities that are fully annular and capable of accurately measuring mass flow rate [10, 11] can measure the flow capacity characteristic of HP vane rings [21], an essential parameter for engine performance evaluation.

External heat flux measurements can be performed on turbine components using heat flux gauges [22]. The change in the material resistance of the gauge is used to infer a change in temperature, which can then be converted into a heat flux from the mainstream gas to the external surface of the component. With further post-processing, the measured heat flux can be used to determine the external heat transfer coefficient, a parameter very useful for turbine designers. The main advantages of heat flux gauges are that they can be placed almost anywhere on the aerofoil (even on rotating blades) and can acquire data at very high frequencies

(up to 100 kHz), important in short duration facilities. Heat flux film gauges have been used extensively for many years in many major turbine research facilities [12, 13, 18, 19].



Figure 2.1: Heat flux gauges installed on turbine blades [23].

When the tested turbine components are internally cooled, the overall cooling effectiveness can be measured. Overall cooling effectiveness is usually defined by

$$\theta = \frac{cT_{0\mathrm{m}} - T_{\mathrm{w}}}{cT_{0\mathrm{m}} - T_{0\mathrm{c}}} \tag{2.2}$$

where T_{w} is the tested component external wall temperature, $T_{0\mathrm{m}}$ is the mainstream total temperature upstream of the cascade, $T_{0\mathrm{c}}$ is the coolant total temperature upstream of the cascade and c is the mainstream recovery ratio [4]. The external wall temperature T_{w} can be measured using thermocouples to measure the external surface temperature of the tested component. However, thermocouples are intrusive and only provide pointwise measurements. Moreover, it will be shown in Chapter 4 that surface thermocouple measurements are sensitive to their installation conditions. Full coverage and less intrusive temperature measurements methods like thermochromic paints, thermochromic liquid crystals and IR thermography are more suitable for overall cooling effectiveness measurements.

Thermochromic paints change colour at certain temperature due to activated chemicals reactions in the constituent of the pigments [24]. The paint is applied on components of interest prior to the test. After the test, the maximum temperature the paint was exposed to can be inferred from its colour. The advantage of thermochromic paints is that they do not require

optical access during the test, which makes them the ideal solution to assess the overall cooling effectiveness of turbine components during engine tests before production [25]. However, thermochromic paints are cumbersome to use due to their single usage and high toxicity, making them not so suitable in laboratory environments where many tests are repeated at various operating conditions.

Thermochromic liquid crystals reversibly change colour with temperature [26]. Using a calibration, the temperature of the surface can be inferred from the change in colour with a high degree of accuracy. Once applied over a test surface, liquid crystals form a coating that can be considered to be geometrically and thermally thin. Although they require optical access during the test, liquid crystals are a cheaper and more flexible way to measure surface temperature than thermochromic paints, hence better for laboratory environments. Liquid crystals have been use for overall cooling effectiveness measurements on engine HP NGVs in [27]. The disadvantages of liquid crystals are that they have a limited operating temperature range (−30°C to 150°C) [26] and have a maximum heat flux (~2×10^4 W m^{-2}) [26] and therefore cannot be used in every facilities. The calibration of liquid crystals is sensitive to age, ultraviolet (UV) radiations and other contaminants [26].

IR thermography is another full-coverage and non-intrusive technique to measure the external surface temperature of components. As spatial resolution and internal calibration stability of IR cameras has improved, they have become more popular as research instruments in the gas turbine community. An IR cameras converts the total radiance it receives from the surface of interest into an equivalent black-body temperature by means of a black-body calibration. With knowledge of the emissivity of the surface of interest and the transmissivity of the elements in the optical path (e.g. windows), the equivalent black-body temperature can be converted into the true external surface temperature of the component. The overall cooling effectiveness of the component can then be obtained as shown in Figure 2.2.

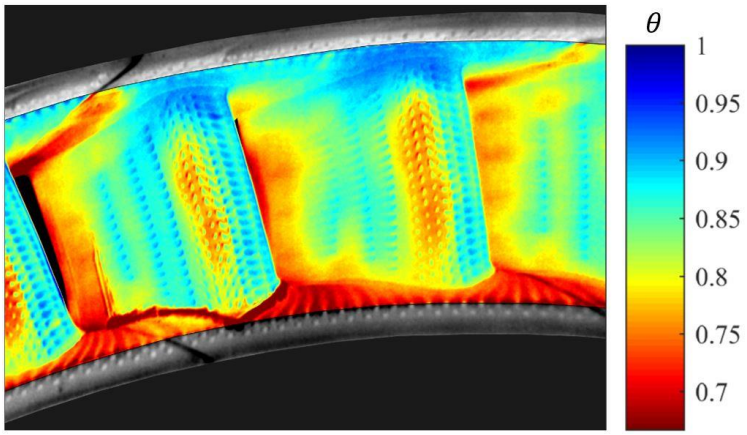


Figure 2.2: Example of overall cooling effectiveness measurement on the front face of HP NGVs using an IR camera in the ECAT facility [11].

IR thermography is now used for overall cooling effectiveness measurements in many turbine facilities [4, 5, 6, 7, 9, 11, 16]. While IR thermography has mostly been done on stationary components, considerable efforts are put in the development of IR measurements on rotating components as shown in Figure 2.3.

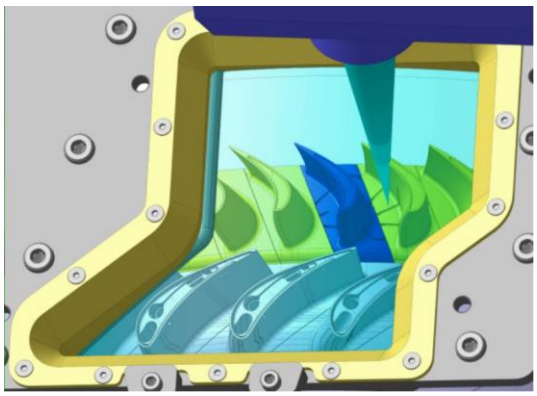


Figure 2.3: Optical access through the casing of a rotating turbine cascade [28].

IR measurements require to be calibrated in situ against a known temperature in the field of view of the camera to account for the surrounding radiance reflected on the surface of interest and also to account for the transmissivity of the elements in the optical path. It will be shown in Chapter 4 that performing an in situ calibration in environments with significant through-wall heat flux and surface temperature non-uniformity (e.g. overall cooling effectiveness experiments) can be challenging and a new calibration sensor is proposed. The main

disadvantage of IR thermography is the very high cost of IR cameras and IR-transparent windows. The emissivity of the surface of interest must also be accurately known.

Overall cooling effectiveness measurements are particularly useful for evaluating the thermal performance of cooled turbine components because of the complexity and degree of interaction of the underlying boundary conditions. An intrinsic limitation of overall cooling effectiveness measurement data is that the individual boundary conditions (the internal and external heat transfer coefficients, for example) cannot be directly obtained from the final measurement. In Chapter 7, a new processing method to extract the heat transfer coefficients from transient overall cooling effectiveness data on internally cooled components is presented.

2.2. In-service Deterioration of High-Pressure Nozzle Guide Vanes

The literature on in-service deterioration effects on HP NGVs is now considered. HP NGVs operate in very hostile environments. The vanes are continuously in contact with the extremely hot and corrosive combustion gases as well as the particles ingested by the engine, which make their deterioration over service time inevitable as shown in Figure 2.4.

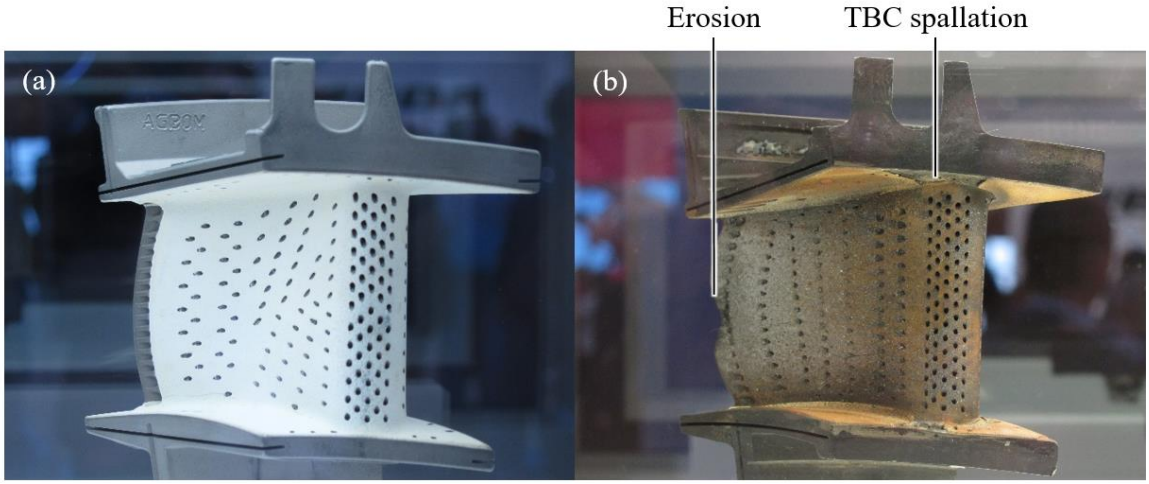


Figure 2.4: (a) New HP NGV; (b) deteriorated HP NGV [29].

Turbine vane deterioration occurs under five main mechanisms: erosion, deposition, corrosion, oxidation and damage [30]. Erosion is the abrasive removal of material on the vane aerofoil

and endwalls caused by the impingement of the solid particles ingested by the engine [31]. These foreign particles are usually dust or sand that are ingested by the engine while the aircraft is moving on the runway during the takeoff and landing phases of a flight. Removal of material through erosion will change the external surface roughness and external geometry of the vanes as shown in Figure 2.4b [31, 32]. Erosion can also cause the spallation of the critical thermal barrier coating (TBC) [33], thus exposing the underlying metal to very high gas temperatures. Deposition occurs when the ingested particles adhere to the vanes and the annulus surfaces [31]. Deposition of particles can modify the external geometry of the vanes and increases their external surface roughness. Figure 2.5 is a photograph of a cross-section of an HP NGV showing roughness caused by deposits of foreign materials on the external surface and in a film cooling hole.



Figure 2.5: Photograph of the cross-section of an HP NGV [34].

Corrosion is the loss of material caused by chemical reactions between the vane and contaminants, such as salts, mineral acids or reactive gases [30–37]. Corrosion alters the external surface of the vanes and thus its roughness. Oxidation is the chemical reaction that occurs between the surface of the vane and the oxygen in the gaseous environment [30–37]. Oxidation also alters the external surface of the vanes and thus its roughness. Damage to vanes can be caused by the impact of foreign objects on the vanes [30]. These objects are either ingested by the engine (birds, rocks, etc.) or are pieces of the engine that broke off inside the gas path. Damage can also occur due to the overheating of the vanes, which can melt some parts of the vanes (e.g. leading edge and/or trailing edge). Overheating of vanes can, for instance, occur in the presence of non-uniformities in the vanes inlet temperature profiles

(radially and circumferentially) or if some film cooling holes are partially or completely blocked by particles.

These in-service deterioration mechanisms have two main consequences on the vanes: (i) a change in the external surface roughness of the vanes; (ii) a change in the geometry of the vanes, including TBC spallation, cracks, shrunk or blocked film cooling holes, eroded or burnt trailing edge (TE). The following sections review the work that has been done (if any) to understand the effect of each of these deterioration features on the aerothermal performances of HP NGVs.

2.2.1. Surface Roughness Characterisation in Turbines

Surface roughness corresponds to variations in height of the surface relative to a reference plane. These variations in height are measured using a profilometer. Stylus profilometers measure 2D surface profiles like the ones shown in Figure 2.6, while optical profilometers measure 3D surface profiles as shown in

Figure 2.7. To quantify roughness from a measured profile, two metrics among others are commonly used in the literature: (i) centerline average roughness R_a; (ii) equivalent sandgrain roughness height k_s [38].

For a 2D profile (i.e. in the *x*-*z* plane), the centerline average roughness R_a is defined by the average absolute height of the peaks and valleys of the surface profile $z(x)$ with respect to the mean height of the profile $\bar{z}$. The mean height of the profile $\bar{z}$ and the centerline average roughness R_a are given by Equations 2.3 and 2.4, respectively. S_a is the 3D equivalent of R_a and involves integrating $z(x, y)$ in both x and y directions.

$$\bar{z} = \frac{1}{L}\int_0^L z(x)\,\mathrm{d}x \tag{2.3}$$

$$R_{\mathrm{a}} = \frac{1}{L}\int_0^L |z(x) - \bar{z}\,|\,\mathrm{d}x \tag{2.4}$$

Despite being convenient, height parameters like R_{a} and S_{a} do not provide a complete characterization of the surface profile. They are only a measure of the vertical height of the asperities on the surface and do not provide any information on the shape, length and slope of the asperities as well as the frequency of their occurrence, which is relevant from a fluid mechanics point of view [38]. For instance, all the profiles presented in Figure 2.6b all have the same value of R_{a} although they have totally different roughness profiles. Hence, R_{a} and S_{a} are not sufficient to quantify roughness in gas turbines and this was clearly demonstrated by Goodhand et al. [39].

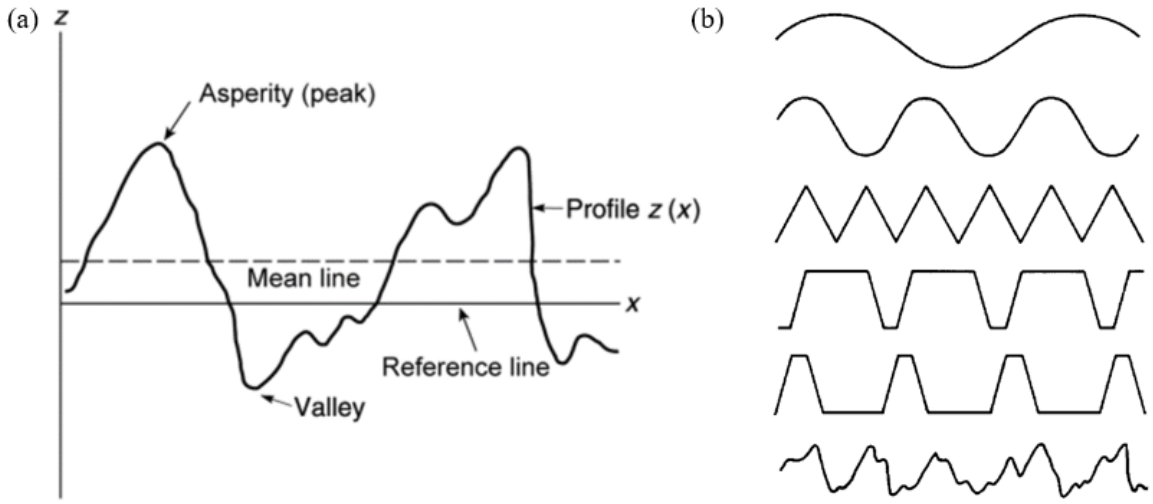


Figure 2.6: (a) 2D surface profile [38]; (b) various surface profiles having the same R_a [38].

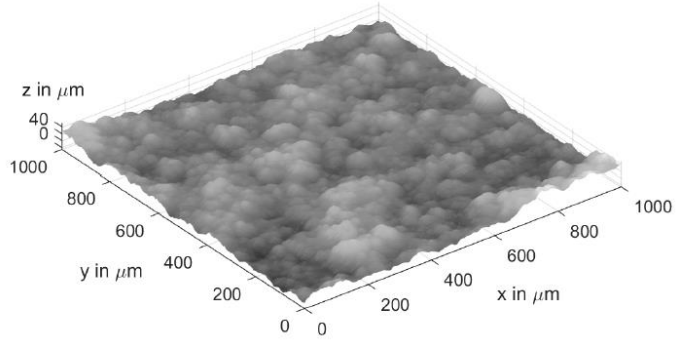


Figure 2.7: 3D surface measured by an optical profilometer [40].

To better characterize the surface roughness, the equivalent sandgrain roughness height k_s is more commonly used. Introduced by Schlichting [41], k_s is defined as the roughness height of a sandgrain surface (Figure 2.8) that would yield the same skin friction as the studied surface.

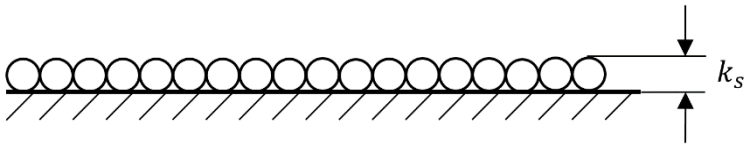


Figure 2.8: Equivalent sandgrain roughness height [41].

Numerous studies attempted to provide correlations between measurable surface roughness parameters (e.g. R_a and S_a) and equivalent sandgrain roughness height k_s. More than 20 of these studies are carefully listed in Bons [42]. However, the wide variety of surface profiles encountered in gas turbines prevents all those correlations to be universal. For that matter, parameters accounting on the shape and the density of roughness gained popularity. Sigal and Danberg [43] introduced a shape-density parameter Λ_s to calculate k_s on simulated roughness (hemisphere, truncated cones, etc.). Λ_s is given by Equation 2.5 and is the product of the total-surface-to-total-frontal area ratio and a shape factor which takes into account the average inclination of the windward surface of the roughness elements.

$$\Lambda_s = \frac{A}{A_f}\left(\frac{A_f}{A_s}\right)^{-1.6} \tag{2.5}$$

A is the planform area of a roughness element, A_f is the windward projected area of a roughness element and A_s is the windward wetted area of a roughness element. A large value of Λ_s represents a surface with sparse, gradually sloped roughness elements while a small value of Λ_s signifies densely packed, abrupt elements [44]. The equation of Λ_s was adapted by Bons [44] for real 3-dimensionally measured profile $z(x, y)$ (e.g.

Figure 2.7) and is given by Equation 2.6.

$$\Lambda_s = \left(\frac{\sum_{i=1}^{N_x}\sum_{j=1}^{N_y} A_{\text{cell},ij}}{\sum_{i=1}^{N_x}\sum_{j=1}^{N_y} A_{\text{f,cell},ij}}\right)\left(\frac{\frac{1}{N_x N_y}\sum_{i=1}^{N_x}\sum_{j=1}^{N_y} A_{\text{f,cell},ij}}{\frac{1}{N_x N_y}\sum_{i=1}^{N_x}\sum_{j=1}^{N_y} A_{\text{s,cell},ij}}\right)^{-1.6} \quad (2.6)$$

A cell is defined as the surface area bounded by four contiguous surface height points in the measured rectilinear grid [44].

The ratio k_s/k can then be calculated from Λ_s using correlations. k corresponds to the roughness height. A few studies have developed correlations between k_s/k and shape factors for both simulated and real roughness [43, 45, 46], but the most recent one for real roughness encountered in gas turbines was developed by Bons [44] and is given by Equation 2.7.

$$\log\left(\frac{k_s}{k}\right) = -0.43\log(\Lambda_s) + 0.82 \quad (2.7)$$

For simulated roughness (hemisphere, truncated cones, etc.), k simply corresponds to the height of the roughness elements. The definition of k is however not so clear for real roughness and varies from one study to another. Some studies have assigned the value of k to be the maximum peak-to-valley height (R_z or S_z) on the measured profile [47, 48, 49] while other studies determined the value of k using analytical methods [40, 45]. Bons [44] proposed to average the maximum peak-to-valley height difference over multiple regions (> 100) of the measured 3D surface profile. There is therefore no universal definition of k for real roughness and this requires careful consideration when comparing equivalent sandgrain roughness height k_s between studies.

Surface roughness data on new turbine components with various surface finish treatments are documented in [50] and surface roughness data on deteriorated turbine components are documented in [34, 40, 47, 51, 52, 53].

2.2.2. Surface Roughness Effects on Turbine Vane Aerodynamics

There have been several cascade experiments to assess the impact of surface roughness on turbine component aerodynamic performance. Most of these studies have used simple simulated roughness elements (sandgrain, hemisphere and truncated cones) [54, 55, 56] or different surface finish arising from manufacturing processes [50, 57, 58, 59, 60, 61], with only one study—to the author knowledge— attempting to simulate engine-representative roughened surfaces on an aerofoil [48]. A comprehensive review of all the literature (up to 2010) on effects due to roughness was provided by Bons [42]. The primary effects are earlier laminar-turbulent boundary layer transition, and an increased rate of thickening of the boundary layer (both laminar and turbulent), leading to higher aerodynamic loss. One exception is the case of low Reynolds number operation (low pressure turbines for instance) where an earlier roughness-induced transition has been shown to prevent a laminar separation on the suction surface (SS) of the aerofoil, leading to lower losses than a smooth (separated) aerofoil [42, 60, 62].

We can differentiate between studies in which the surface roughness of the entire aerofoil is varied evenly to represent possible manufacturing routes [50, 58, 59, 60, 61], and those in which the roughness on only part of the surface is varied [48, 57]. These latter studies are more representative of in-service roughening which appears to preferentially affect the pressure surface (PS) and early SS.

Erickson et al. [48] performed aerodynamic surveys a quarter of an axial chord downstream of smooth and realistically roughened uncooled vanes in a linear cascade. The Reynolds number (based on tangential chord) range was $0.50 \times 10^6 < \mathrm{Re} < 2.0 \times 10^6$ and there was three turbulence intensities: low turbulence (0.7 %); grid turbulence (8.5 %); and aerocombustor turbulence (13.5 %). The entire pressure side and the first 10 % of the SS were roughened to simulate typical in-service deterioration. The suction side and the endwalls were considered aerodynamically smooth (roughness height not reported). k_s/C of the rough surface

was 9.75×10^{-4}. Figure 2.9 shows the mass-flux-averaged total pressure loss coefficient downstream of the smooth and rough vane as a function of Reynolds number and turbulence intensity. Surface roughness has a greater impact on loss at lower turbulence intensity because it initiated an earlier laminar-turbulent boundary layer transition. The impact of surface roughness on loss is also a very light function of Reynolds number. The study also showed that the increased roughness had almost no impact on flow turning: a result that would probably have been expected.

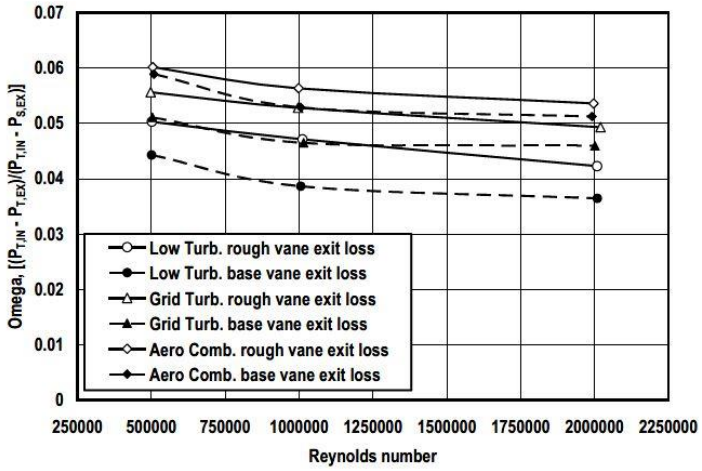


Figure 2.9: Mass-flux-averaged total pressure loss coefficient as a function of Reynolds number and turbulence intensity [48].

Matsuda et al. [57] performed aerodynamic surveys 0.165 tangential chords downstream of a linear cascade of vanes to study the impact of aerofoil and endwall roughness on profile loss and *net secondary loss*. Net secondary loss was defined as the difference between the total pressure loss measured in the secondary flow region, and the estimated profile loss (based on mid-span measurements). The exit Re (based on tangential chord) range was $0.30 \times 10^6 < \text{Re} < 1.0 \times 10^6$ and inlet turbulence intensity (Tu) was 0.43 %. They took aerodynamic measurements with various surface finishes (identified as C1 to C7, with C7 being the roughest), with a R_z/C range of $0.80 \times 10^{-5} < R_z/C < 8.4 \times 10^{-4}$. They also looked at the impact of the location (PS, SS and endwalls) of roughness on secondary loss.

Figure 2.10 shows the net secondary loss as a function of roughness height and location. For Re = 0.87 × 10^6 and a surface roughness of R_z/C = 8.4 × 10^{-4} (C7) on the PS and endwalls (smooth SS), they found that the net secondary loss increased by approximately 80 % compared to the smooth (C1) PS and endwalls.

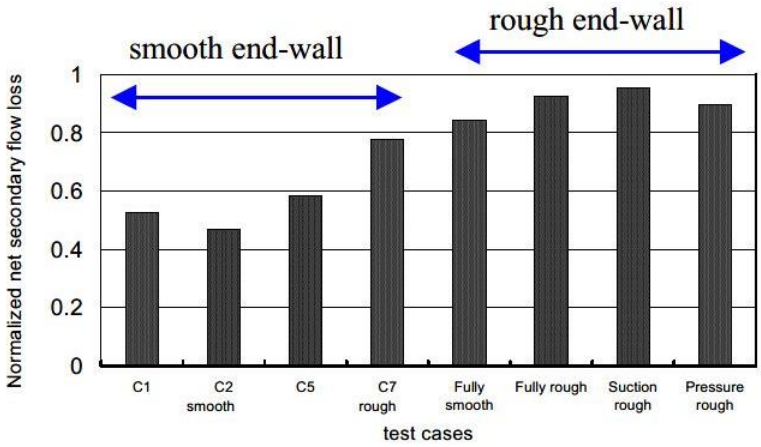


Figure 2.10: Net secondary loss as a function of roughness height and location [57].

2.2.3. Surface Roughness Effects on External Heat Transfer Coefficient

There have been a number of cascade experiments to assess the impact of surface roughness on the external HTC distribution of turbine components [63–73]. As described in Bons [42] review paper, the consensus is that an increase in surface roughness causes an increase in external HTC due to both earlier laminar-turbulent boundary layer transition and enhanced mixing in the turbulent boundary layer. Most studies [65, 66, 67, 50, 70, 72, 73] suggest that increased roughness does not significantly impact heat transfer in the laminar region of the boundary layer.

Erickson et al. [73] studied the impact of surface roughness on the external HTC with the same roughened vane presented in the previous section (see review of [48]). In agreement with other literature, they measured increased HTC on the vane, attributed this to both earlier laminar-turbulent boundary layer transition and enhanced mixing in the turbulent boundary layer. This is shown in Figure 2.11. At Re = 1.60 × 10^6 (interpolated, Re of the present study) and Tu = 13.5 %, they measured increases in area-average HTC (with respect to the reference

vane, and ignoring very local excursions) of approximately 25 % and 35 % on the PS and early SS, respectively. No significant change in HTC was observed on the late SS (for high Tu). They additionally found that that the boundary layer transition onset was independent of the turbulence level, and that the heat transfer in the laminar boundary layer was unaffected by roughness.

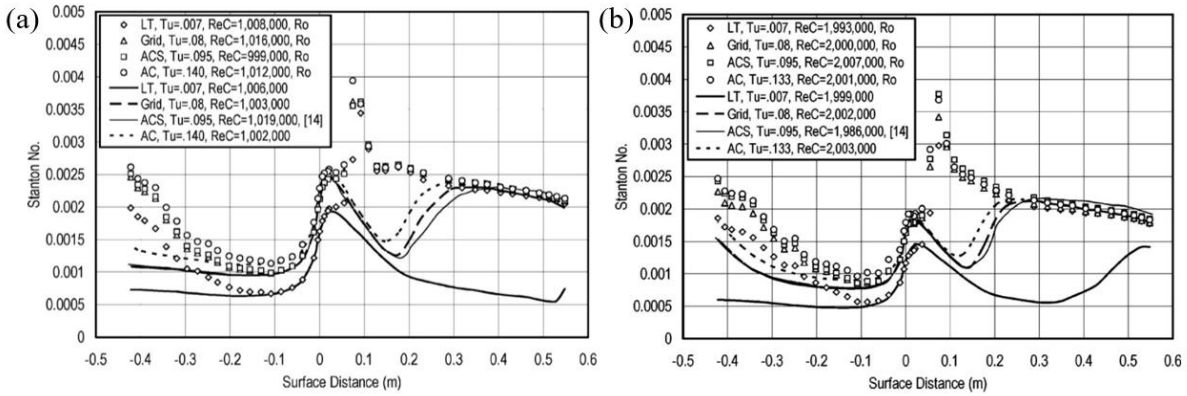


Figure 2.11: Rough vane heat transfer compared with smooth vane distributions: (a) Re = 1,000,000; (b) Re = 2,000,000 [73].

2.2.4. Surface Roughness Effects on Adibatic Film Cooling Effectiveness

Experiments have been performed using flat plates [74–78] and linear cascades [68, 79] to evaluate the impact of surface roughness on adiabatic film cooling effectiveness η_f. The general trend reported is that an increase in surface roughness upstream of a film cooling row leads to a thicker boundary layer and hence a higher *effective local* blowing ratio *B* (or, by the same token, momentum flux ratio *I*) which increases the tendency for film lift-off (separation). Increased surface roughness downstream of a film cooling row was found to reduce η_f at low *B* due to enhanced near-wall roughness-induced turbulent mixing between coolant and mainstream flows. At high *B*, increased surface roughness downstream of a film cooling row was less detrimental to film cooling performance, and in certain cases increased η_f. This was thought to be the result of enhanced early mixing reducing penetration of the jet into the mainstream. The most relevant study to the present study is now reviewed in more detail.

Rutledge et al. [68] investigated the impact of surface roughness on adiabatic film cooling effectiveness and external HTC on the SS of a vane in a low-speed linear cascade. The exit Re (based on tangential chord) was 1.06×10^6, the inlet Tu was 21 % and the blowing ratio range was $0.3 < B < 1.4$. The SS was cooled with a cooling row with cylindrical holes and located at a normalized surface distance $L/C = 0.208$. Two types of surface were considered in the study: an *aerodynamically smooth* surface (roughness height not reported); and a *rough* surface which consisted of a simulated array of cones with $k_s/C = 0.842 \times 10^{-3}$. Four surface roughness configurations were studied: a *smooth* configuration in which the entire aerofoil was aerodynamically smooth; an *upstream rough* configuration with a rough surface upstream of the film cooling row; a *downstream rough* configuration with a rough surface downstream of the film cooling row; and an *all rough* configuration with a rough surface upstream and downstream of the film cooling row. Their results are presented in Figure 2.12. For $B = 0.3$, they reported decreases (with respect to smooth configuration) in area-average adiabatic film cooling effectiveness ($\bar{\bar{\eta}}_f$) of 29 %, 25 % and 31 % for the upstream, downstream and all rough configurations, respectively. In contrast, for $B = 1.4$, they reported increases in $\bar{\bar{\eta}}_f$ of 11 %, 73 % and 86 % for the upstream, downstream and all rough configurations, respectively. The effect of roughness on $\bar{\bar{\eta}}_f$ was found to be minimal for $B = 0.85$. This contrary behaviour was explained by roughness-induced mixing in the case of films already attached ($B = 0.3$), and a roughness-induced decreased tendency to detach at higher blowing ratio ($B = 1.4$). At the intermediate condition ($B = 0.85$) it might be assumed that the two effects are opposite in direction but similar in magnitude. They also reported that roughness caused an increase in external surface heat flux (driven by changes in both η_f and HTC) of 30–70 % under their operating conditions.

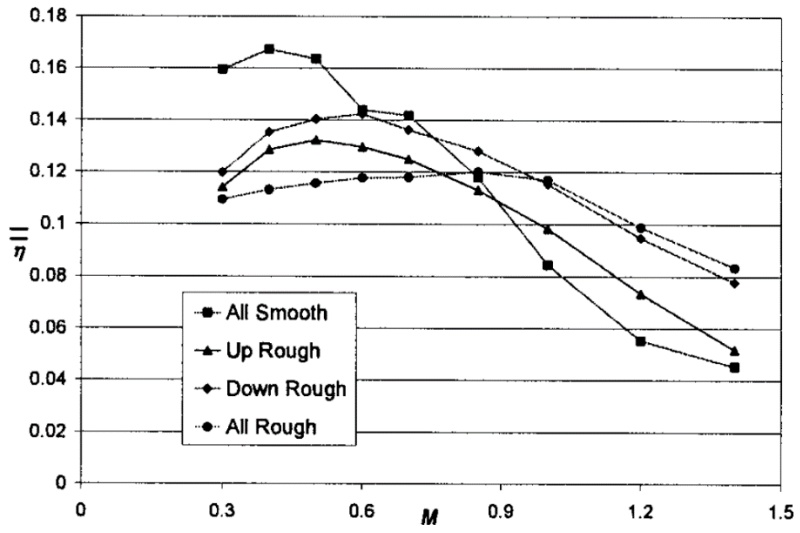


Figure 2.12: Area-average adiabatic film cooling effectiveness versus blowing ratio for all the roughness configurations under high mainstream Tu [68].

2.2.5. Impact of in-service TBC deterioration on wall thermal resistance

We now consider the in-service deterioration of TBC and its impact on heat transfer in turbine components. There are three primary deterioration mechanisms of TBC prior to mechanical failure (i.e. spallation): sintering [80]; erosion [81, 82]; local impact damage [81, 82]. We now briefly review these mechanisms. The type of TBC considered is yttria-stabilized zirconia (YSZ) produced by electron-beam physical vapor deposition (EB-PVD). This is the TBC type used on the vanes in the current study.

Rätzer-Scheibe and Schulz [80] studied the effect of sintering on the thermal conductivity of EB-PVD YSZ TBC. They exposed a 280 μm thick coating to air at a temperature of 1100 °C (engine-representative surface temperature) for 100 and 200 hours. They found that this temperature exposure had raised the thermal conductivity of the TBC (κ_{TBC}) from κ_{TBC} = 1.34 W m^{-1} K^{-1} (new) to κ_{TBC} = 2.01 W m^{-1} K^{-1} after 100 hours (measured at 30 °C, i.e. representative of lab conditions), an increase of approximately 50 %. There was no significant change in κ_{TBC} between 100 and 200 hours.

Wellman and Nicholls [81] and Darolia [82] reviewed the literature (to 2007 and to 2013, respectively) related to erosion and impact damage of TBC, including EB-PVD TBC. They

reported that TBC can be significantly eroded by ingested particles during engine operation. Erosion rates were greater at the leading edge (LE) and on the SS, than on the PS. They also reported that the impact of particles under a high temperature can compact the TBC. Erosion and impact damage during service therefore act to reduce the thermal resistance of the TBC by reducing its thickness. The results vary widely with service environment and duration—with erosion between 0 and 100 % of original coating thickness—and therefore it is hard to draw generalized quantitative conclusions.

2.2.6. Impact of Trailing Edge Damage on Turbine Vane Aerodynamics

We now review the literature on the impact of TE damage on the aerodynamic characteristics of turbine components. Sjolander et al. [83] studied the impact of a semi-circular cutout in the TE of a turbine blade (to simulate damage caused by burn-back or erosion) on loss and flow turning angle. Using a low-speed linear cascade, they did aerodynamic surveys downstream of an undamaged blade and two blades with a semi-circular cutout in their TE (Figure 2.13) with a diameters equivalent to 15 and 25 % of the blade tangential chord. Results showed that the wake downstream of the cutout was significantly modified, with local under-turning of the flow (up to 4.2° yaw angle deficit compared to a new blade) in the cutout region. They also observed the formation of counter-rotating streamwise vortices at the edges of the cutout, driven by the sharp gradients (with radius) in yaw angle. Similar flow structures have been observed in CFD studies of vanes with TE damage by Di Mare et al. [84] and Meyer et al. [85]. Sjolander et al. [83] reported that the mass-flux-averaged total pressure profile loss coefficient increased by 56 % (compared to undamaged blade) for the deepest cutout.

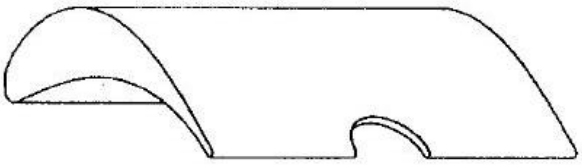


Figure 2.13: Trailing edge circular cutout [83]

Bouchard et al. [86] did aerodynamic surveys downstream of full rings of uncooled new and in-service deteriorated engine vanes in a transonic annular cascade. The vanes were those of a Rolls-Royce A-250 engine. The TE of the deteriorated vanes had small chordwise cracks, and some TE were significantly thermally distorted as marked in Figure 2.14. No surface roughness measurements were reported in the paper. Profile loss measurements were taken one half of an axial chord downstream of the vanes at exit Mach number M = 1.2. The exit Reynolds number was not reported. They reported an increase in profile loss of 51 % for the deteriorated vane ring.

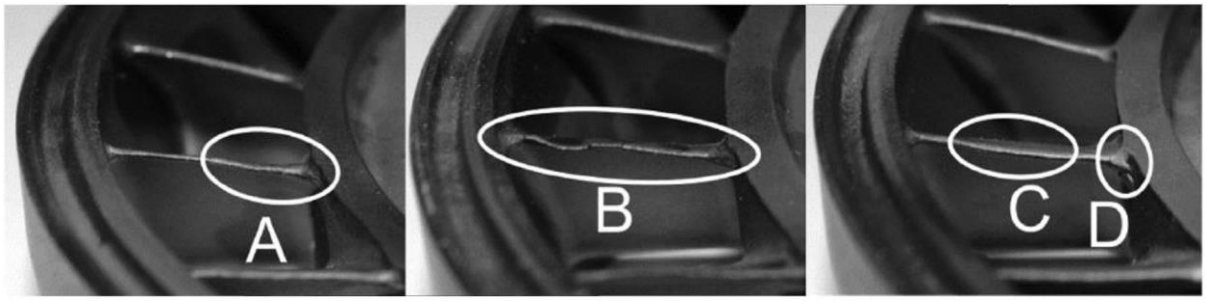


Figure 2.14: Bends and cracks on the trailing edges of the in-service deteriorated vanes [86].

3. Annular Dump Diffuser and Deswirl System for Back-pressure Control in an Engine-scale Transonic Annular Cascade

This chapter consists of a preprint journal paper describing the design and commissioning of a combined annular dump diffuser and deswirl system for back-pressure control. The new system was installed in the ECAT facility to independently control the Mach number and Reynolds number of the cascade. The new system allows to operate the facility and validate the aerothermal performance of HP NGVs at different engine representative operating conditions (cruise and max-take-off, MTO). The new system also allow to isolate Mach number and/or Reynolds number effects during more fundamental research programs. The nomenclature and references included in this chapter are self-contained and differ in numbering compared to the overall thesis.

ANNULAR DUMP DIFFUSER AND DESWIRL SYSTEM FOR BACK-PRESSURE CONTROL IN ENGINE-SCALE TRANSONIC ANNULAR CASCADE

Mathias Michaud, Francesco Ornano and Thomas Povey*

Department of Engineering Science, University of Oxford, Parks Road, Oxford, OX1 3PJ, UK

ABSTRACT

This paper describes the design and commissioning of a combined annular dump diffuser and deswirl system for back-pressure control in environments with high-whirl transonic flow. The particular application was an annular cascade of nozzle guide vanes from a current civil engine. The purpose was to provide independent control of Mach number and Reynolds number, by controlling the back-pressure in the intermediate annular plenum which forms the dump diffuser. The dump diffuser is necessary to facilitate optical and probe access (without interaction effects) and to reduce the risk of exit static pressure disturbances (due to particular duct design). The system has been installed and validated in the Engine Component AeroThermal (ECAT) facility at the University of Oxford. In this implementation of the system, the high-whirl transonic flow from the nozzle guide vanes passes through a short, parallel annular duct, and is dumped into an annular plenum, before being re-accelerated into a deswirl vane ring. The deswirl ring turns the flow to the axial direction. The flow is then discharged through a variable choke plate into a silencer. Conditioning the flow to have zero whirl at the choke plate reduces the sensitivity of the choke plate effective blockage to the whirl angle. The design, deswirl vane aerodynamic performance, and overall system performance are assessed with detailed experiments and 3D unsteady computational fluid dynamics predictions. The control of high-whirl transonic flow is notoriously challenging, and the deswirl system has application to exhaust conditioning in a number of applications including annular cascade experiments and rocket turbo-pump exhaust systems.

INTRODUCTION AND RELATED LITERATURE

To fully match non-dimensional conditions relevant to aerodynamic and heat transfer testing of turbomachinery components, it is necessary to provide independent control of exit Mach number and Reynolds number. This is achieved by having independent control of the inlet total pressure and exit static pressure. Control of the inlet total pressure is normally via compressor control (in continuously running facilities) or a combination of regulators and limiters (in blowdown facilities). Most continuously running facilities control the exit static pressure using a vacuum pump [1–3], or a vacuum pump in combination with a throttle [4–7]. In blowdown facilities, control of the exit static pressure is normally achieved with an exit throttle, both for atmospheric-back-pressure [8–10] and evacuated-tank [11–16] facilities. In transonic blowdown *linear* cascades, simple valves and nozzles have be used for back-pressure control, typically integrated into the exit duct of the cascade [17,18]. In transonic blowdown *annular* cascades (both rotating and non-rotating) accurate back-pressure control with an area-limiting device is complicated by the swirling motion of the flow. This is particularly true in high-pressure (HP) nozzle guide vane (NGV) cascades or 1.5 stage turbine configurations [19,20] in which there is a high exit swirl angle (typically above 70°). Back-pressure control in single stage turbine configurations is often relatively simpler because exit swirl angles are typically below 30° [8,11]. In cases with high exit swirl angle, traditional choke plates (see, for example [11,12]) might be expected both to have extremely high minimum blockage—even in the fully open position—on account of gross separation from the individual radial elements, and to have high sensitivity to the swirl angle. Thus, more sophisticated back-pressure control systems may be required. To overcome the problems associated with traditional choke plates, three alternative concepts have been deployed: the radial-flow sleeve throat [13]; the *annular second throat* (an adjustable annular nozzle) [6,14,15 and discussion in 9] and the deswirl vane with choke plate combination [9,10,19,20, and present study]. Table 1 summarizes the major transonic annular turbine cascade facilities (continuous running and blowdown) and their back-pressure control systems.

We review the annular nozzle and deswirl vane concepts briefly. The adjustable annular nozzle is conceptually simple, and—provided the mean radius of the flow path is well-matched—is unlikely to have unusual swirl sensitivity. A significant disadvantage, however, is the necessity of providing a support structure for the inner-radius parts of the system. In a turbine system with shaft support structure this may be easily accommodated (the downstream end of the turbine shaft is normally supported by a series of structural struts), but in a NGV cascade this requirement is likely to add significant complexity, weight, axial length and cost.

The deswirl vane with choke plate combination works on the principle of first removing the swirl, then throttling the flow. This allows for low minimum blockage and low sensitivity of the choke plate to the swirl angle. Such systems have been deployed successfully in annular sector cascades [10] and fully annular cascades [19,20], and have been proven to provide excellent fine control of back-pressure. The disadvantage, of course, is the relative complexity of the aerodynamic design, and the fact that such systems have relatively high sensitivity to swirl angle *changes*: that is, the deswirl vane is optimized for a particular

cascade exit angle. Previous systems have been designed with unseparated intermediate ducts (both annular sector [10], and fully annular [19,20]). Although this leads to the lowest total pressure loss (in principle, zero loss) connection between the cascade exit and the choke plate—and therefore allows for the most compact deswirl vane—there are two disadvantages: the further design requirement for the interconnecting duct; and the residual problem of high *local* back-pressure sensitivity to blockage within the duct (from probes or cameras, for example). By employing a dump diffuser, the local back-pressure sensitivity is removed, allowing greater freedom for downstream traverse systems and camera instrumentation.

This first known implementation of a combined dump-diffuser deswirl-vane control system is presented in this paper. The system was installed and validated on the Engine Component AeroThermal (ECAT) facility at the University of Oxford, a transonic, fully-annular, engine-scale HP NGV cascade. Detailed experimental measurements at a wide range of operational conditions are combined with 3D unsteady computational fluid dynamics (CFD) predictions to understand the performance of this new flow control system.

Table 1: List of the back-pressure control systems used in major transonic turbine annular cascades.

Facility name	Cascade type	Institution	Back-pressure control system
TTTF [1]	Rotating	TU Graz	Vacuum pump
HSAC [2]	Annular	Cambridge	Vacuum pump
HWRT [3]	Rotating	P&WC	Vacuum pump
NDTL [4]	Rotating	Notre-Dame	Valve & vacuum pump
ASC [5]	Annular sector	KTH	Butterfly valve & vacuum pump
ORF [11]	Rotating	Oxford	Choke plate
CT3 [12]	Annular/ Rotating	VKI	Choke plate
BTF [13]	Rotating	MIT	Sleeve throat
TTF [14]	Rotating	Ohio State	Annular nozzle
PETAL [15]	Rotating	Purdue	Annular nozzle
OTRF [8]	Rotating	Oxford	Annular nozzle
OTRF [9]	Rotating	Oxford	Deswirl & choke
Sector [10]	Annular sector	Oxford	Deswirl & choke
ECAT/ECAT+ (present study)	Annular	Oxford	Deswirl & choke
NG-Turb [6]	Rotating	DLR	Vaccum pump & shutters
RGG [7]	Rotating	DLR	Vaccum pump & shutters

OVERVIEW OF THE EXPERIMENTAL FACILITY

The ECAT facility at the University of Oxford is a semi-transient fully annular cascade of real engine HP NGVs [21]. Figure 2 shows a cross-sectional schematic of the ECAT facility. The original facility is identified with solid hatching lines while the new deswirl module is identified with the dashed hatching lines. The measurement stations of the facility are identified in Figure 2: (1) upstream of the HP NGVs; (2) downstream of the HP NGVs; (3) HP NGV exit duct outlet; (4) upstream of the deswirl vanes; (5) downstream of the deswirl vanes (detuner). We will refer to these stations in later sections. During a test, the high-pressure air stored in large tanks is discharged through the cascade in regulated or blowdown mode (more details later). In the original facility (without back-pressure control), the air exits the NGVs and passes through a short parallel annular duct (to maintain pressure gradients similar to those in an engine) before being dumped into a large detuner at atmospheric conditions. The facility achieves a high degree of non-dimensional similarity to engine operating conditions by matching the NGV exit Mach number M_2, NGV exit Reynolds number Re_2 (based on NGV true chord) near cruise and coolant-to-mainstream pressure ratio. Nominal operating conditions are given in Table 2.

The facility was developed for extremely accurate measurement of overall cooling effectiveness [21], aerodynamic performance [21,22], and capacity [23–25]. Further details of the general capability can be found in [21]. To perform these measurements it is necessary to have optical access from both upstream and downstream (infrared cameras and traverse probes), and a radial back-pressure condition typical of that in the engine situation.

The M_2-Re_2 characteristic of the HP NGVs develops naturally, and it is fortuitous that at typical cold-rig and warm-rig operating conditions M_2 and Re_2 are simultaneously well-matched to engine cruise conditions with atmospheric back-pressure. The facility is currently being upgraded for operation at engine realistic coolant-to-mainstream temperature ratios (known as the ECAT+ facility) [26], a condition at which the natural Re_2 is less well matched. The *natural characteristics* (without the deswirl module installed) at typical cold-, warm-, and hot-rig conditions along with typical engine operating points (max-take-off, MTO, and cruise) of are shown in Figure 1 for the ECAT+ facility.

The purpose of the dump diffuser and deswirl system is to extend the operating range of the facility to higher Re_2 (at a given M_2), by means of back-pressure control, without limiting instrumentation access to the facility (optical and traverse). The maximum operating total pressure upstream of the NGVs (p_{01}) is 6 bar [26]. The maximum operating temperature (T_{01}) with extended temperature range is 600 K [26]. With the operating envelope in pressure and temperature defined for the ECAT+ facility (Table 2), the M_2-Re_2 operating space with the deswirl module at cold-, warm- and hot-rig operating conditions are delimited by the shaded area in Figure 1.

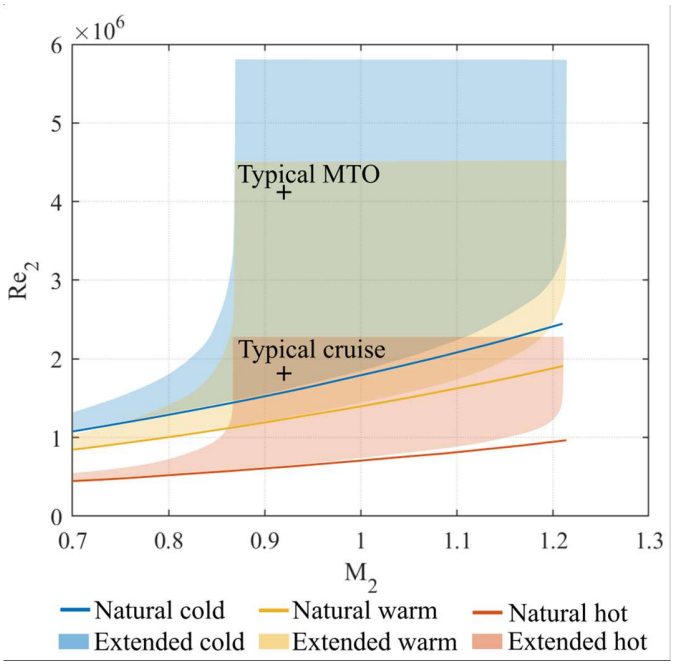


Figure 1: Natural operating characteristics for the ECAT+ facility in cold-, warm- and hot-rig operation; extended operating range with deswirl module; engine cruise and MTO conditions.

BACK-PRESSURE CONTROL SYSTEM DESIGN

In this section we describe the design of the back-pressure control system for the ECAT and ECAT+ facilities. The purpose is to provide independent control of the NGV cascade Reynolds and Mach numbers.

The general concept is shown in sectional view in Figure 2. Downstream of the test NGV cascade (the ECAT or ECAT+ *module*) there is a dump diffuser followed by a ring of deswirl vanes with a downstream adjustable choke plate. The NGV cascade is typically operated in the transonic regime with high exit whirl angle (typically $\beta_2 > 70°$). To reduce the chance of separation of the hub boundary layer at the vane exit plane, and to provide an axial region for downstream traversing, the flow first passes through a parallel duct (typically 2 to 2.5 axial chords in length) before being dumped into the intermediate annular plenum (the dump diffuser). The flow is then re-accelerated through an inlet contraction into a deswirl vane ring. The deswirl vanes turn the flow to the axial direction and the flow is then discharged through a variable choke plate into a detuner at atmospheric pressure. The dump diffuser allows significant freedom for a downstream traverse system and infrared cameras.

We now consider the following topics in more detail: deswirl vane conceptual design; preliminary aerodynamic design and capacity setting; deswirl vane count; the mechanical design; and the choke plate design.

Table 2: ECAT+ facility operating conditions

Parameter	Cold	Warm	Hot
Extended inlet total pressure, p_{01} [bara]	1–6	1–6	1–6
Extended inlet total temperature, T_{01} [K]	285	345	600
Vane exit Mach number, M_2	0.70–1.21	0.70–1.21	0.70–1.21
Natural exit Reynolds number at $M_2 = 1$, Re_2	1.81×10^6	1.39×10^6	0.69×10^6
Extended maximum exit Reynolds number at $M_2 = 1$, $Re_{2,max}$	5.79×10^6	4.51×10^6	2.27×10^6

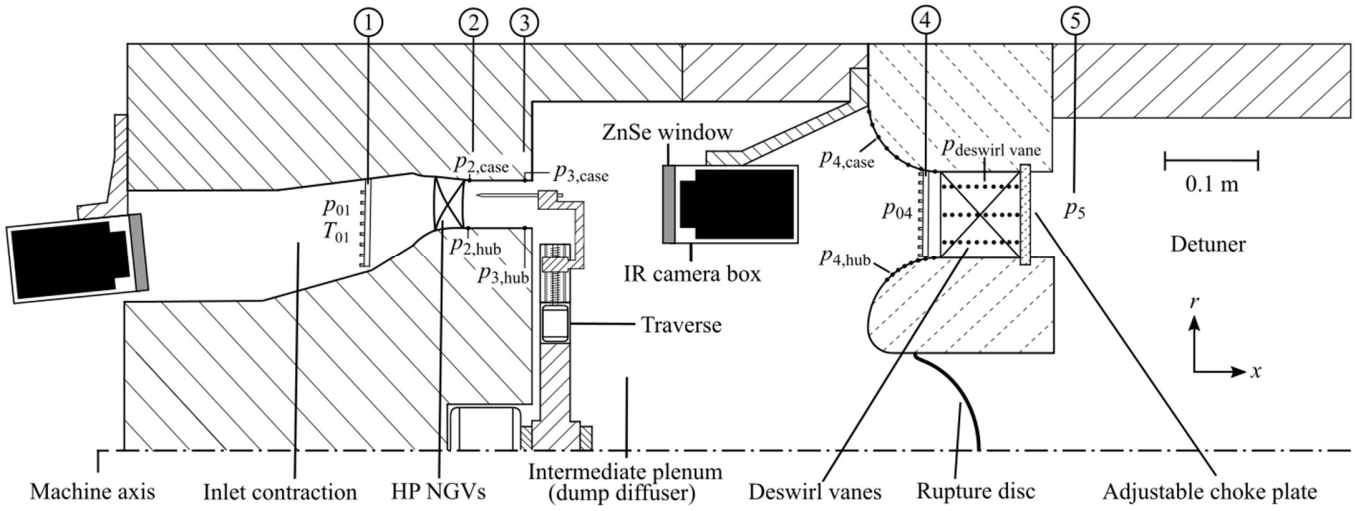


Figure 2: Sectional schematic of the ECAT/ECAT+ facility with the new deswirl module.

Deswirl vane conceptual design

A schematic of the deswirl vane concept is shown in Figure 3b. The concept is an impulse-type transonic turbine blade (Figure 3a) truncated at half chord, where the flow direction is approximately axial. The leading edge (LE) is relatively sharp (circular arc of 0.5 mm radius), to avoid detached shocks in mildly supersonic regions. The passage is of constant area design, to turn the flow without diffusion, thus reducing the chance of boundary layer separation and associated blockage. Deswirl vanes of similar design have been successfully used for high-whirl transonic flow control in fully annular cascades of intermediate-pressure nozzle guide vanes [19,20,9], annular sectors of HP NGVs [10,27] and also in rocket turbo-pump exhaust systems.

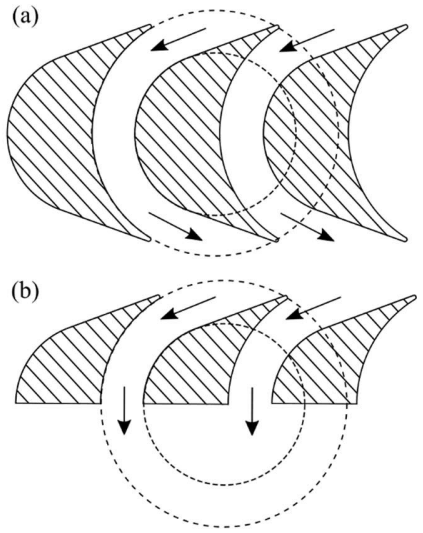


Figure 3: (a) Impulse turbine blade design; (b) impulse-type deswirl vane based on [9].

Preliminary aerodynamic design and capacity setting

The mean metal angle of the LE of the deswirl vanes was chosen to have a small nominal positive incidence angle. The logic is that a separation bubble on the uncovered suction surface (SS) surface is likely to collapse before the flow enters the covered passage, leading to relatively low blockage and loss, but a separation bubble on the pressure surface (PS) would more directly impact the vane aerodynamics. For the first implementation of the system (a typical ECAT HP NGV test module), the mass-flux-averaged exit yaw angle from the HP NGVs was $\beta_2 = 75.8°$ (see Figure 10b). The corresponding CFD-predicted mass-flux-averaged yaw angle at the deswirl vane inlet plane was 77.0° (discussed in context of Figure 16). The deswirl vane nominal LE metal angle before the LE radius was applied was 74.0° leading to a nominal incidence angle (for area-ratio calculations) of 3.0° based on the CFD-evaluated angle, or a capacity increase based on area (for a given span) of 14 %. This reduces the required span of the deswirl vane necessary to maintain an adequate *capacity overhead*: that is, sufficiently larger area that even accounting for all total pressure loss between the NGV exit and deswirl vane inlet a low minimum back-pressure can be achieved with the system installed. The LE cutback decreases the PS metal angle to 70.0°, leading to a nominal predicted PS incidence angle of 7.0° (SS metal angle is unchanged at 74.0°).

The deswirl vane mean radius was chosen to be similar to that of the NGV (360 mm versus 371 mm), but the span was increased (100 mm compared to 53 mm for the NGV) to allow sufficient *capacity overhead*. Using the deswirl vane PS metal angle, this gives an *ideal* deswirl-to-NGV capacity ratio $\Gamma_{4,\mathrm{ideal}}/\Gamma_1 = 2.57$. Assuming a deswirl vane capacity deficit ζ (effective blockage factor to account for secondary flow and loss *within* the deswirl vane passage) of 0.20 we estimate a *predicted* effective deswirl-to-NGV capacity ratio of $\Gamma_{4,\mathrm{predicted}}/\Gamma_1 = 2.06$.

We now define a mass-flux-averaged dump diffuser total pressure loss coefficient by

$$Y_{p,\mathrm{DD}} = \frac{\bar{p}_{02} - \bar{p}_{04}}{\bar{p}_{02} - p_2} \tag{1}$$

where $\bar{p}_{02}$ is the mass-flux-averaged total pressure downstream of the NGVs, p_2 is the static pressure downstream of the NGVs and $\bar{p}_{04}$ is the mass-flux-averaged total pressure upstream of the deswirl vanes. For preliminary design a value $Y_{p,\mathrm{DD}} = 0.5$ was assumed. In analogy, we define a similar total pressure loss coefficient for the NGV

$$Y_{p,\mathrm{NGV}} = \frac{p_{01} - \bar{p}_{02}}{p_{01} - p_2} \tag{2}$$

where p_{01} is the total pressure upstream of the vane. For design, we take a value—from experiment—of $Y_{p,\mathrm{NGV}} = 0.05$.

We now specify the following nominal operating conditions for the zero blockage at the deswirl vane exit plane: atmospheric pressure (p_5 = 1 bar); a Mach number of unity at the NGV exit ($M_2 = 1$, or $p_{01}/p_2 = 1.89$); $\Gamma_{4,\mathrm{predicted}}/\Gamma_1 = 2.06$; $Y_{p,\mathrm{DD}} = 0.5$; $Y_{p,\mathrm{NGV}} = 0.05$. Using these values with *locally* (NGV row or deswirl row in isolation) isentropic capacity characteristics, we can back-calculate the following: deswirl vane inlet total pressure, p_{04}; intermediate plenum static pressure, p_2; NGV downstream and upstream total pressures, p_{02} and p_{01} respectively; and NGV Reynolds number, Re_2. The resulting values are summarized in Figure 4 and Table 3.

The minimum NGV Reynolds number with the system installed was $\mathrm{Re}_2 = 1.87 \times 10^6$, 3.32 % higher than without a back-pressure control system ($\mathrm{Re}_2 = 1.81 \times 10^6$). The conclusion based on the preliminary design values is that the capacity overhead is sufficient to provide flexibility for low-Re conditions. The maximum Re_2 is determined either by the design pressure capability of the upstream vessel (10 bar for ECAT and 15 bar for ECAT+), or the maximum mass flow rate with the current metering system (equivalent to upstream total pressure of 4.0 bar for ECAT and 6.0 bar for ECAT+, for typical NGV capacity).

For the NGV ring used in this study (which is typical of large civil engines) the increase in Re_2 above the minimum value to match the cruise and MTO operating points at M_2 = 0.92 (see Figure 1) were 15.3 % and 162 % respectively. At cold-ECAT conditions, upstream total pressures of 1.95 bar and 4.41 bar—respectively—are necessary. Using the prelim-design method, this is equivalent to choke plate blockage factors of 0.30 and 0.37, respectively. To provide additional headroom, the maximum choke plate blockage factor was set to 0.50. At this value the predicted total pressure upstream of the NGV is p_{01} = 5.85 bar, well below the design pressure (10 bar).

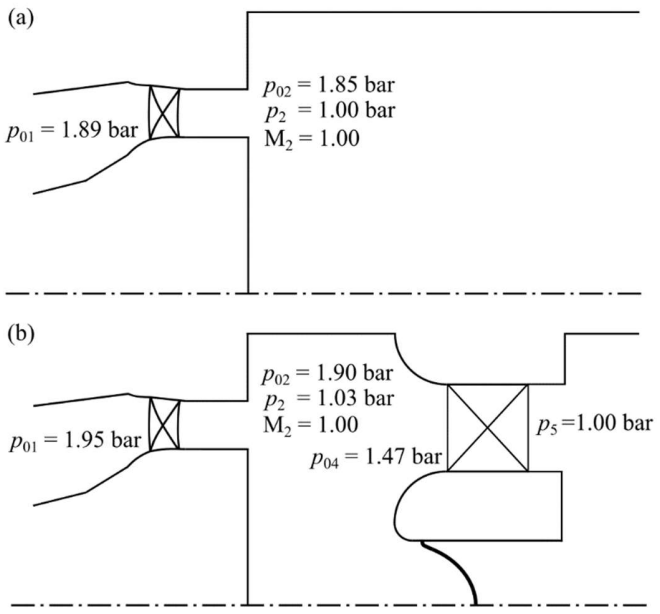


Figure 4: Summary of preliminary design operating points without back-pressure control system installed, and with the system installed with choke plate fully open.

Table 3: Preliminary design input and output parameters with zero choke plate blockage ratio.

Preliminary design input parameter	NGV	Deswirl
Midspan radius, [mm]	371	360
Span, [mm]	53	100
Ideal capacity ratio, $\Gamma_{4,\mathrm{ideal}}/\Gamma_1$	2.57	
Assumed deswirl vane capacity deficit, ζ	0.20	
Predicted capacity ratio, $\Gamma_{4,\mathrm{predicted}}/\Gamma_1$	2.06	
Dump diffuser loss coefficient, $Y_{p,\mathrm{DD}}$	0.50	
NGV loss coefficient, $Y_{p,\mathrm{NGV}}$	0.05	
NGV exit Mach number, M_2	1.00	
System back-pressure, p_5 [bar]	1.00	
Preliminary design output parameter		
Deswirl vane inlet total pressure, p_{04} [bar]	1.47	
Intermediate plenum static pressure, p_2 [bar]	1.03	
NGV exit total pressure, p_{02} [bar]	1.90	
NGV upstream total pressure, p_{01} [bar]	1.95	
Minimum Re_2 with deswirl system	1.87×10^6	
Reference values without deswirl system		
Minimum Re_2 without deswirl system	1.81×10^6	
Increase in minimum Re_2 with deswirl, [%]	3.32	

Deswirl vane count

For a given deswirl vane midspan radius, span, and specified metal angle, the capacity ratio is unaffected by the vane count. The axial chord of the deswirl vane is proportional to vane count. Lower vane count therefore implies: stiffer vanes (important if the vane is to be used structurally as a blisk); lower total pressure loss (same wetted surface area, but reduced average shear); higher weight (approximately inversely proportional to vane count); longer range LE potential field interaction. A vane count of 30 was chosen, which is a compromise between these competing design requirements. For NGV rings with 40 vanes (typical installation) this gives a beat count of 10, suggesting low potential field interaction effects at the NGV exit plane.

Mechanical design

Figure 5 shows the front and back views of the deswirl module. The deswirl vane ring was machined as a blisk, providing structural support for the hub components and burst disk. The blisk was machined from 17-4 PH stainless steel (H900 condition), which is high temperature capable. The working section and intermediate plenum were rated to a design pressure of 10 bar, and protected (in the event of full blockage of the deswirl vane ring) by a 400 mm in diameter stainless steel rupture disc with a burst pressure of 10 bar. The stiffness of the blisk was such that at 600 K and 10 bar, the maximum deflection of the hub components was predicted to be 0.4 mm, with a minimum safety factor of 3.0 at the peak stress location within the blisk. By using the blisk structurally, it removes the need for a separate support structure for the hub components. The total mass of the module was approximately 750 kg.

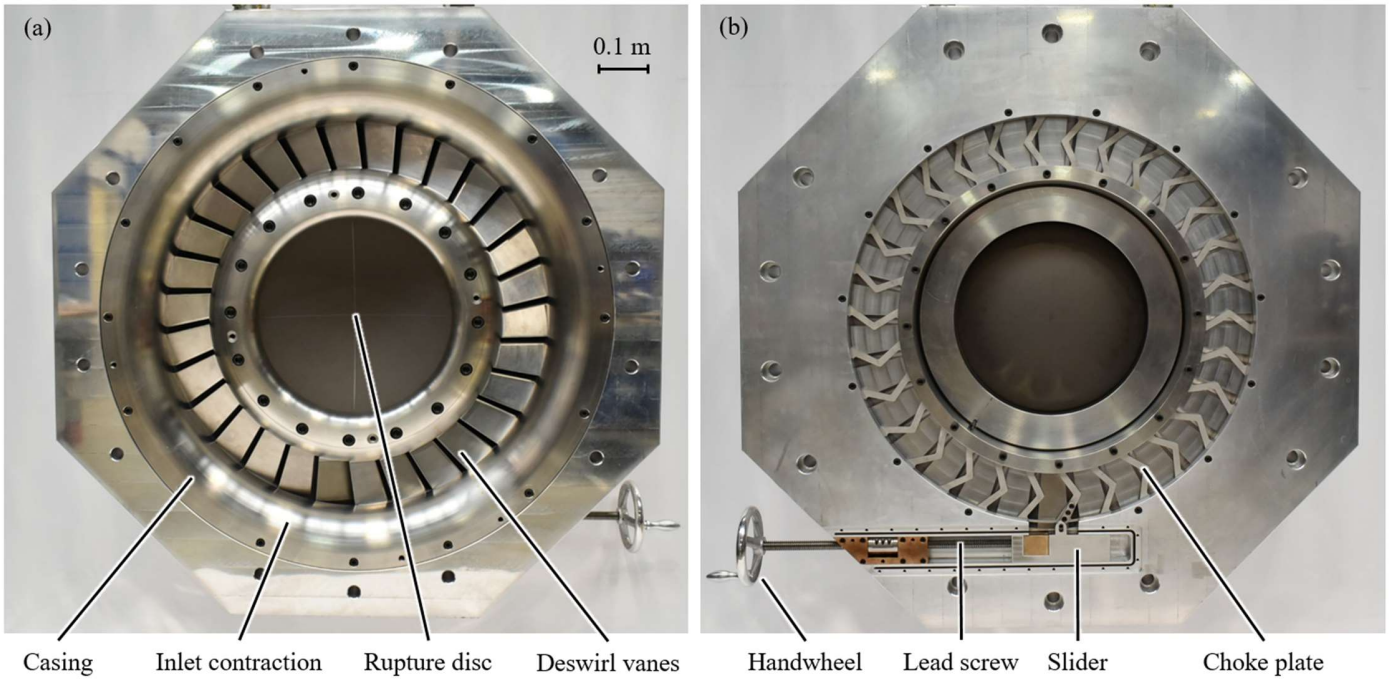


Figure 5: View of the deswirl module (deswirl vane ring; choke plate; rupture disk) hardware from: (a) upstream; (b) downstream.

Choke plate design

An adjustable choke is integrated into the deswirl vane module, rotatable by a geared handwheel with a sealed shaft extending to the outside of the facility. The choke plate has 30 webs (see Figure 5b) designed to give a blockage ratio B of up to 0.5. The web shape (a profiled arrow shape) was designed to give a profile of blockage ratio as a function of deswirl vane pitch (rotation angle) that offered good control. This profile is shown in Figure 6 (note fine control at low blockage ratio).

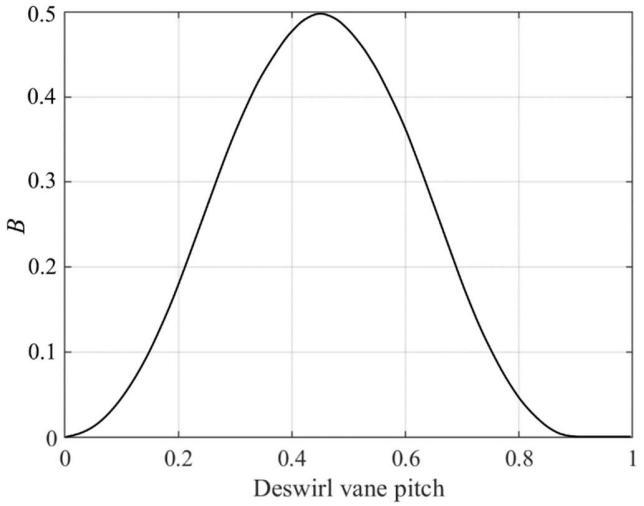


Figure 6: Blockage ratio B as a function of deswirl vane pitch.

EXPERIMENTAL METHODS

Operational modes

During the commissioning of the deswirl module, the ECAT facility was operated in two modes: valve-controlled mode and regulated mode. These modes of operation are described in more detail in [21]. In valve-controlled mode, the mass flow rate is controlled with a butterfly valve at inlet to the flow conditioning and metering pipework for the facility, and a wide range of facility pressure ratios can be achieved in single run. We define the facility pressure ratio (p_{01}/p_5) as the ratio of total pressure upstream of the NGVs (p_{01}) and the atmospheric pressure in the detuner (p_5). A typical valve-controlled facility pressure ratio characteristic is shown by the dashed line in Figure 7. The through-flow time (time for complete air exchange in the facility) ranges between 2.5–30 ms. This can be taken as proxy for the flow time-constant. In this time the maximum percentage change in facility pressure ratio is 3.9×10^{-3} %. The flow is therefore quasi-steady. This operational mode was used for determining the approximate capacity characteristics for the facility at a range of blockage ratio (positions of the choke plate). True steady operation (up to 60 s) can be achieved by using regulated mode (pressure regulator at inlet). A typical steady facility pressure ratio characteristic is shown by the solid line in Figure 7. This mode was used for aerodynamic measurements and for flow visualization measurements.

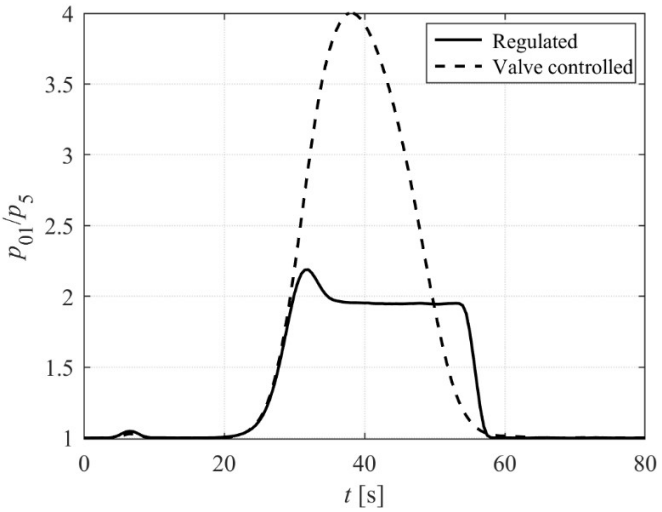


Figure 7: Typical facility overall pressure ratio characteristics (p_{01}/p_5) during valve-controlled and regulated operation.

Instrumentation

To measure the deswirl vane inlet radial total pressure distribution, a radial total pressure rake was installed 0.2 deswirl vane axial chords upstream of the deswirl vanes as shown in Figure 8.

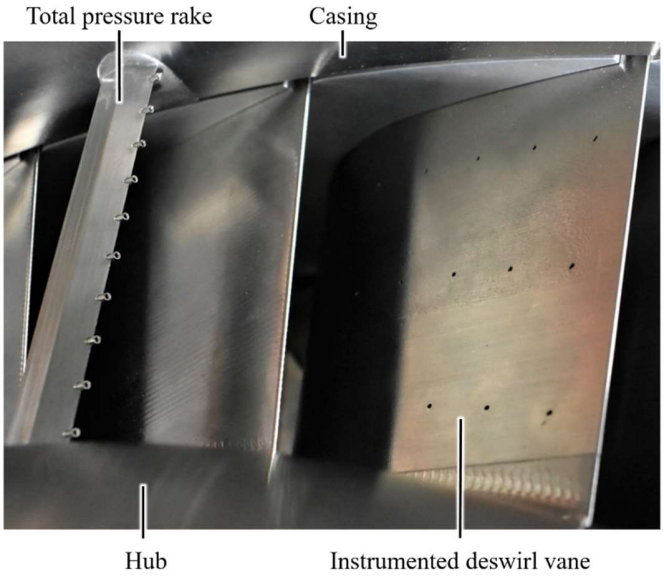


Figure 8: Upstream total pressure rake and instrumented deswirl vane.

This probe had 8 beveled-inlet pitot probes oriented at a pitch angle of 0° and a yaw angle of 77°. The angle was chosen based on the nominal flow whirl angle from CFD. To measure the deswirl vane pressure distribution, an instrumented deswirl vane was installed with 60 static pressure tappings (10 each on SS and PS surfaces at each of 20, 50 and 80 % span). The instrumented vane was laser sintered in stainless steel with integral internal channels, and post-machined to ensure the same surface finish as the non-instrumented vanes. The deswirl vane inlet contraction had eight static pressure tappings on each of the hub and casing walls. The location of all instrumentation is shown in Figure 2.

Flow visualization method

A mixture clear vegetable oil and fluorescent powder paint was used to visualize the streamlines on the deswirl vanes and the endwalls. The paint mixture was applied with a brush everywhere on 5 deswirl vanes (red paint), on the hub inlet contraction and passages (green paint), and on the casing inlet contraction and passages (blue paint). The facility was then ran in regulated mode (steady-state) at the nominal facility pressure ratio ($p_{01}/p_5 = 1.974$) with zero blockage ratio for 20 s. Photographs of the streamlines were taken immediately after the run in a dark room under an ultraviolet light.

NUMERICAL METHODS

Solver settings

Simulations were performed using ANSYS CFX, with Unsteady Reynolds Averaged Navier-Stokes (URANS) settings and high resolution discretization (second order accurate) for both advection and turbulence terms. A second order discretization scheme was also used for the time derivative. The k-ω shear stress transport (SST) turbulence model with automatic wall functions and the reattachment prediction model were selected. The time step was based on typical values of the Strouhal number for trailing edge (TE) vortex shedding. According to Sieverding and Heinemann [28], for turbulent boundary layers on both PS and SS, the Strouhal number (defined by $\mathrm{St} = fL/U$, where f is the vortex shedding frequency, U is the mass-averaged velocity at the deswirl vanes exit plane, and L is the TE thickness) is below 0.25. The calculated characteristic vortex shedding frequency f was approximately 3.3 kHz, corresponding to a cycle time period of approximately 3.1×10^{-4} s. A time step of 10^{-5} s was chosen (approximately 30 time steps per cycle). Unsteady simulations were initialized with results from a converged steady simulation and run for sufficient time steps to flush through initial transients. Monitor points in the wake region were used to test convergence of the simulations to a quasi-periodic state. The solution was converged for at least five periods of the velocity signal with the lowest frequency. In this time window, the solution at each mesh node was acquired every 20 time steps. This corresponds to a sampling time of approximately every 2×10^{-4} s, compared with the dominant periodic time period of 2×10^{-3} s, associated with the time cycle of a large separation in the hub region of the deswirl vane inlet.

Mesh and boundary conditions

Meshing was performed using ANSYS ICEM-CFD. The domain included the intermediate plenum (including the NGV exit duct), the deswirl vane and the detuner. A sector comprising 1/30th of the full annulus was modelled (one deswirl vane passage), and periodic boundary conditions were applied to both sides of the domain. The mesh is shown in Figure 9. The three subdomains (plenum, deswirl vane and detuner) were meshed independently with local refinement to enhance mesh quality. The plenum

domain was discretized with a fully-structured hexahedral mesh, whereas both the deswirl vane and the detuner were meshed using unstructured tetrahedrons. The subdomains were connected via non-conformal general grid interfaces (GGI). Grid density was kept high at mesh interfaces to minimize interpolation errors. However, the authors acknowledge that the high grid density in the main jet was not ideal in terms of simulation time. The overall mesh had approximately 14.7 million hybrid cells (hexahedral and tetrahedral). In the near wall region, the grid was refined with 15 prism layers with an expansion ratio of 1.2. The value of the non-dimensional wall distance (y^+) was below 10 on most of the wetted surfaces (maximum value below 30). The value of $y+$ was overlooked during this study and the authors acknowledge that a value $y+$ in the range <10–30 is not ideal.

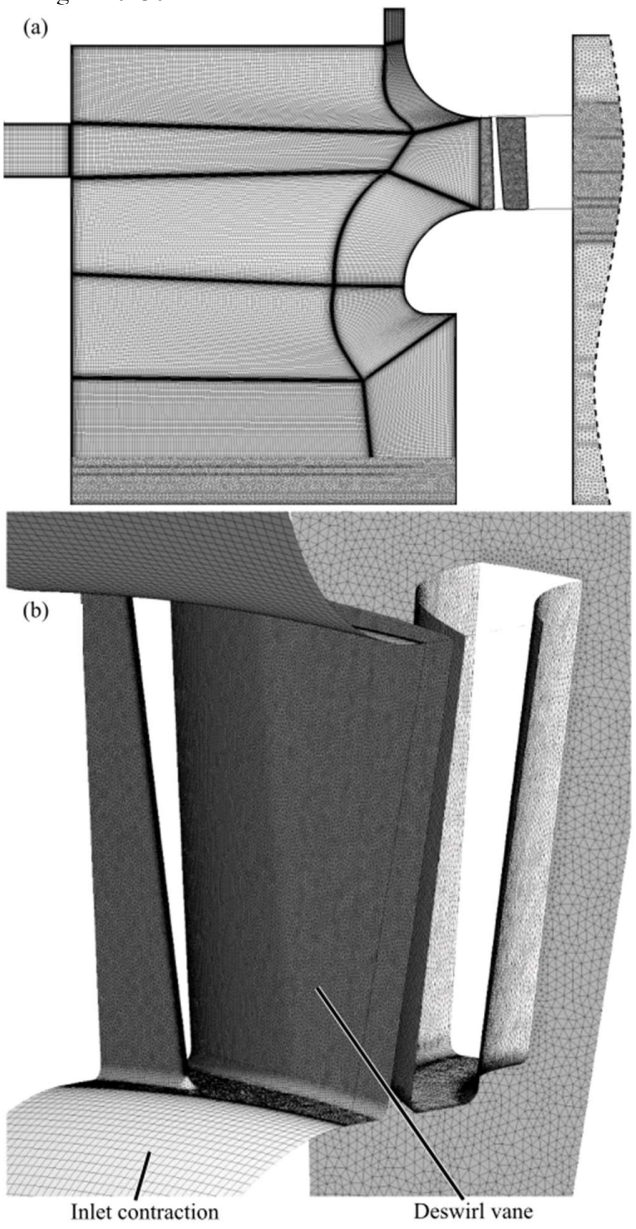


Figure 9: Computational domain and mesh: (a) cross-section; (b) detailed view of the deswirl vane.

An inflow boundary condition was imposed at the domain inlet, with specified total pressure, total temperature, flow direction, and turbulence intensity (Tu = 10 %). Inlet total pressure and yaw angle were specified as circumferential mass-flux-averaged distributions based on traverse measurement performed at the NGV exit plane, at nominal test conditions (M_2 and Re_2). The measured profiles of total pressure and yaw angle at the NGV exit (domain inlet) are shown in Figure 10. The mean Mach number during the measurement and yaw angle were $M_2 = 0.97$ and $\beta_2 = 75.8°$, respectively. At the domain outlet (detuner) the static pressure was set to atmospheric pressure. A radial equilibrium condition was applied. All wetted surfaces were adiabatic.

It should be noted that changes in facility pressure ratio p_{01}/p_5 in the experiments were achieved by varying the facility inlet total pressure p_{01}, for a fixed detuner static pressure p_5 (equal to atmospheric pressure). In CFD, however, the facility pressure ratio was changed by varying the detuner exit static pressure, p_5 (from the nominal atmospheric pressure condition), for a fixed domain inlet total pressure, p_{02}. This strategy was more computationally efficient. Simulations performed in this way are on a single Re_2-M_2 characteristic, however, and neglect the possibility of Reynolds-dependent loss mechanisms in the dump-diffuser. As the flow is dominated by a swirling separated jet, this was taken to be unimportant. We review this assumption later in the paper. The inlet boundary conditions of total pressure and yaw angle are given in Figure 10. To back-calculate the equivalent facility pressure ratio, p_{01}/p_5, for the CFD simulations (for comparison with experimental data) the approximate measured value of NGV total pressure loss coefficient $Y_{p,\mathrm{NGV}} = 0.05$ (see Equation 2) was taken.

In all, five simulations were run, with equivalent overall pressure ratios of for p_{01}/p_5 = 1.716, 1.794, 1.974, 2.193 and 2.322. These are shown in Re_2-M_2 space, in Figure 21.

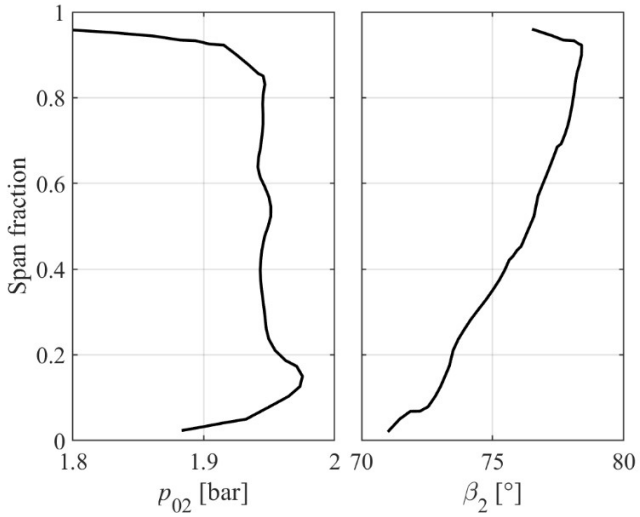


Figure 10: Spanwise distributions of (a) total pressure, and (b) flow yaw angle, used as boundary conditions to the CFD domain.

ANALYSIS OF FLOW STRUCTURE

In this section, we examine the measured and predicted flow properties (pressures, flow angles and velocities) and streamlines in the HP NGV exit duct, intermediate plenum (dump diffuser) and in the deswirl vane passage to understand the flow structure within the system.

General description of flow

Figure 11 shows the predicted time-averaged cross-sectional streamline pattern in the intermediate plenum at the nominal facility pressure ratio ($p_{01}/p_5 = 1.974$) with zero blockage ratio ($B = 0$). The corresponding absolute velocity distribution (we choose this in place of Mach number because of significant total pressure variations) is shown in Figure 12.

The flow is well-behaved (no separation; no significant modification to the radial pressure field) in the short (2.3 NGV axial chords) parallel exit duct downstream of the HP NGVs. This is important, because the deswirl module is designed to control intermediate plenum static pressure without disturbing the radial pressure field at the vane outlet.

In the intermediate plenum the flow pattern is dominated by a high-velocity central jet (Figure 11 and Figure 12) with shear layers on either side, driving strong recirculations at both casing and hub. The principal recirculations are marked A and B in Figure 11; secondary recirculations (driven by the principal recirculations) are marked C and D. It is recalled that the mean flow yaw angle at domain inlet is $\beta_2 = 75.8°$—the recirculations are toroidal in shape with a net recirculation in the whirl direction of the vane.

In the intermediate plenum the jet is unconstrained and moves to slightly higher radius. This causes a reduction in tangential velocity to as a requirement of angular momentum conservation. Friction at the free shear layer also slows the jet. These combined actions explain the slight divergence of the streamlines in the central jet in the downstream direction. This is also clearly observed in the absolute velocity distribution in Figure 12.

As the flow enters the deswirl module inlet contraction, it is simultaneously forced to lower radius (causing an increase in the tangential velocity) and accelerated (contraction of annulus). As the flow gets deeper into the deswirl vane passage (not shown) the radial pressure field is weakened (reduction of whirl angle), causing a favourable pressure gradient for the casing flow and and an adverse pressure gradient at the hub.

It is interesting to note the recirculation B extends into the deswirl vane passage, with inflow (at the deswirl vanes inlet plane) from the recirculation between approximately 20 % and 35 % span, and outflow between 0 % and 20 % span. The driving mechanism is a follows: the entire recirculation (between 0 and 35 % span at deswirl vanes inlet) is a region of low total pressure inclined to be overturned (towards the hub) by the radial pressure gradient established in the central jet; as the main flow enters the deswirl vane passage the radial pressure gradient is weakened (by taking turning out of the flow), creating and adverse pressure gradient for streamlines in the hub region; the flow between 20 % and 30 % span is turned down towards the hub, reverses, and flows back out of the passage into hub recirculation B. We examine this effect in greater detail in later sections.

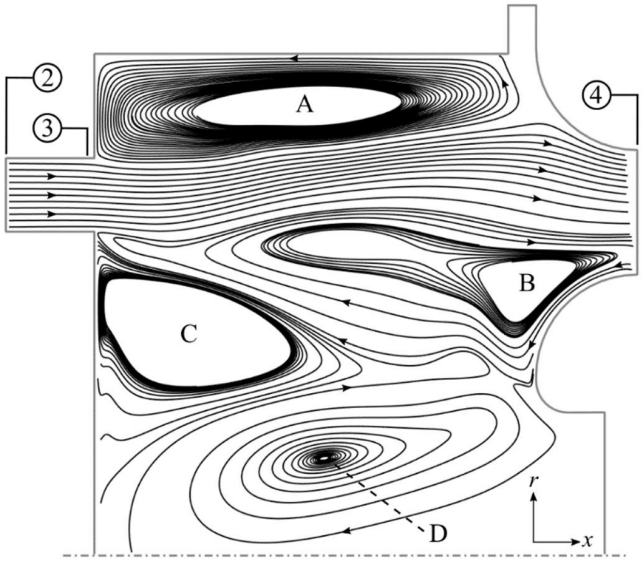


Figure 11: Predicted time-averaged cross-sectional streamline pattern in the intermediate plenum at nominal pressure ratio and zero blockage ratio.

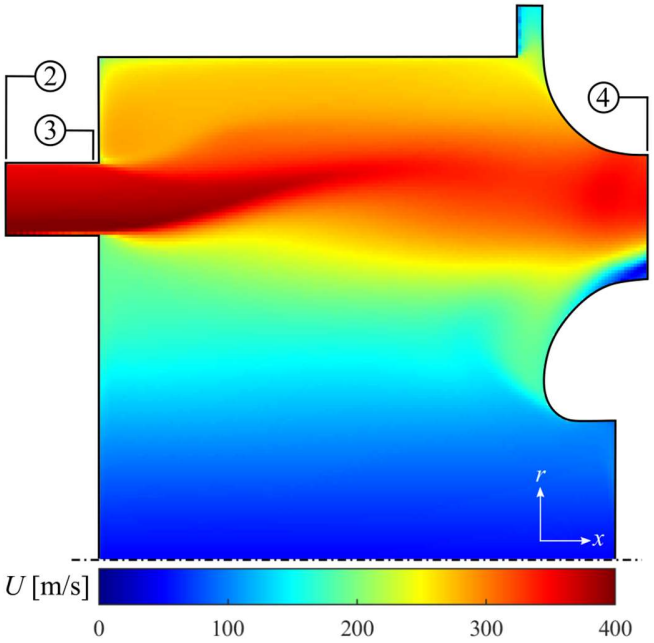


Figure 12: Predicted time-averaged absolute velocity distribution in the intermediate plenum at nominal pressure ratio and zero blockage ratio.

HP NGV exit duct behavior

Figure 13 shows measured and predicted normalised static pressures at the HP NGV exit plane (station 2; see Figure 2) and at the end of the parallel duct (station 3; see Figure 2), 2.3 axial chords downstream of the NGV exit plane. Local static pressures are normalised by the upstream total pressure (or implied—via assumed value of $Y_{p,\mathrm{NGV}}$ = 0.05—upstream total pressure in the case of the CFD), and plotted as a function of the mean vane isentropic Mach number, $M_{2,is}$. Presented in this way, the radial pressure gradients at the two stations are most apparent. In the case of the experiment the facility pressure ratio was adjusted by varying both the choke plate blockage *and* the upstream total pressure. The data therefore cover a wide range of Re_2 for a given M_2 (see Figure 21). The data across the entire Re_2-M_2 space overlay very precisely, showing that the ratios p_2/p_{01} and p_3/p_{01} are essentially independent of Re_2 over the range tested. Data without the back-pressure control module are also presented, marked *natural* in the figure. In the CFD data, only the system back-pressure (p_5) was varied, as a proxy for varying the choke plate blockage, for fixed inlet total pressure. The CFD data are therefore for a single Re_2-M_2 characteristic in the Re_2-M_2 space. In the experimental data, p_2 values are the average of 12 tappings each at hub and case, and p_3 values are based on a single tapping. In the CFD data averages were taken across the entire sector at each location.

Looking first experimental data at the NGV exit plane (station 2), we see a well-behaved radial pressure gradient that increases in magnitude with increasing Mach number. The introduction of the back-pressure control module has a negligible effect on the radial pressure gradient in this location: i.e. it appears to be unaffected by the flow structure that develops in the dump diffuser (compared to exhausting directly into the detuner). This confirms that the back-pressure control module does not affect the NGV exit boundary condition. At the same location, the CFD data with deswirl system installed (for p_{01}/p_5 = 1.716, 1.794, 1.974, 2.193 and 2.322) is in almost identical agreement with the experimental data. This is expected because the inlet boundary of the CFD (imposed boundary conditions from experiment) is very close to station 2.

Looking now at the station 3 data (end of exit duct), we see that in the subsonic range ($0.7 < M_{2,is} < 1.0$) the experimental data shows well-behaved radial pressure distributions at all Mach numbers, with slightly lower pressure gradient (relaxation from forced to free vortex, and flow accommodating to relatively constant static pressure condition in plenum) and slightly lower absolute pressure than at station 2. In the transonic range ($1.0 < M_{2,is} < 1.2$) the casing static pressure trend is modified by the introduction of the deswirl system. This effect is almost completely insensitive to deswirl vane blockage (data not shown), and is thought to be caused by a modification of the intensity of the casing vortex (marked A in Figure 11) due to a global change secondary flow structure in the dump diffuser (compared with the exhaust duct). The CFD data at station 3 (with deswirl system installed) agree almost exactly with the station 2 data. That is, unlike the experimental data, there is almost no predicted development (relaxation of radial pressure gradient) of the vortex through the exit duct.

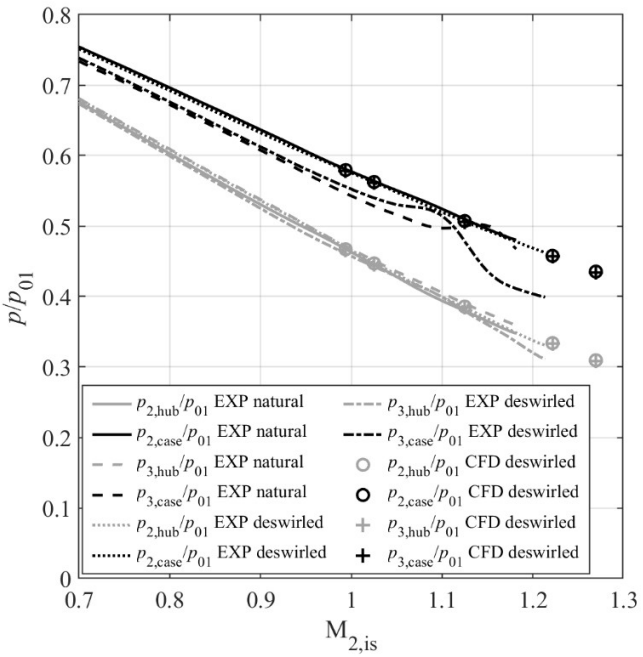


Figure 13: Measured and predicted normalised static pressures at station 2 (NGV exit plane) and station 3 (duct exit) as a function of NGV isentropic exit Mach number.

Flow visualization results

Experimental flow visualization results are presented in Figure 14, and compared to predicted surface streamlines (4th order Runge-Kutta path integrals of time-averaged near-wall velocity field). For clarity, companion line drawings of streamline patterns have been recreated for the experimental data by carefully examining the photographs of the parts. We will consider the pressure surface, suction surface, hub and case walls in turn.

On the PS, the flow is well-behaved in both the experiment and CFD. There is moderate downwash of streamlines caused by slight negative pitch angle at the inlet (note the 5° downflow of the central jet in Figure 11), and moderate spreading of streamlines caused by positive incidence at the LE (mean design incidence of 3°)—we examine this in more detail later. The experimental and CFD flow patterns are broadly extremely similar, with slightly exaggerated downwash in the CFD in the lower forward half of the vane. Both show a hub recirculation region, but the exaggerated downwash in the case of CFD enhances this effect leading to a larger predicted hub recirculation region than seen in the experiment.

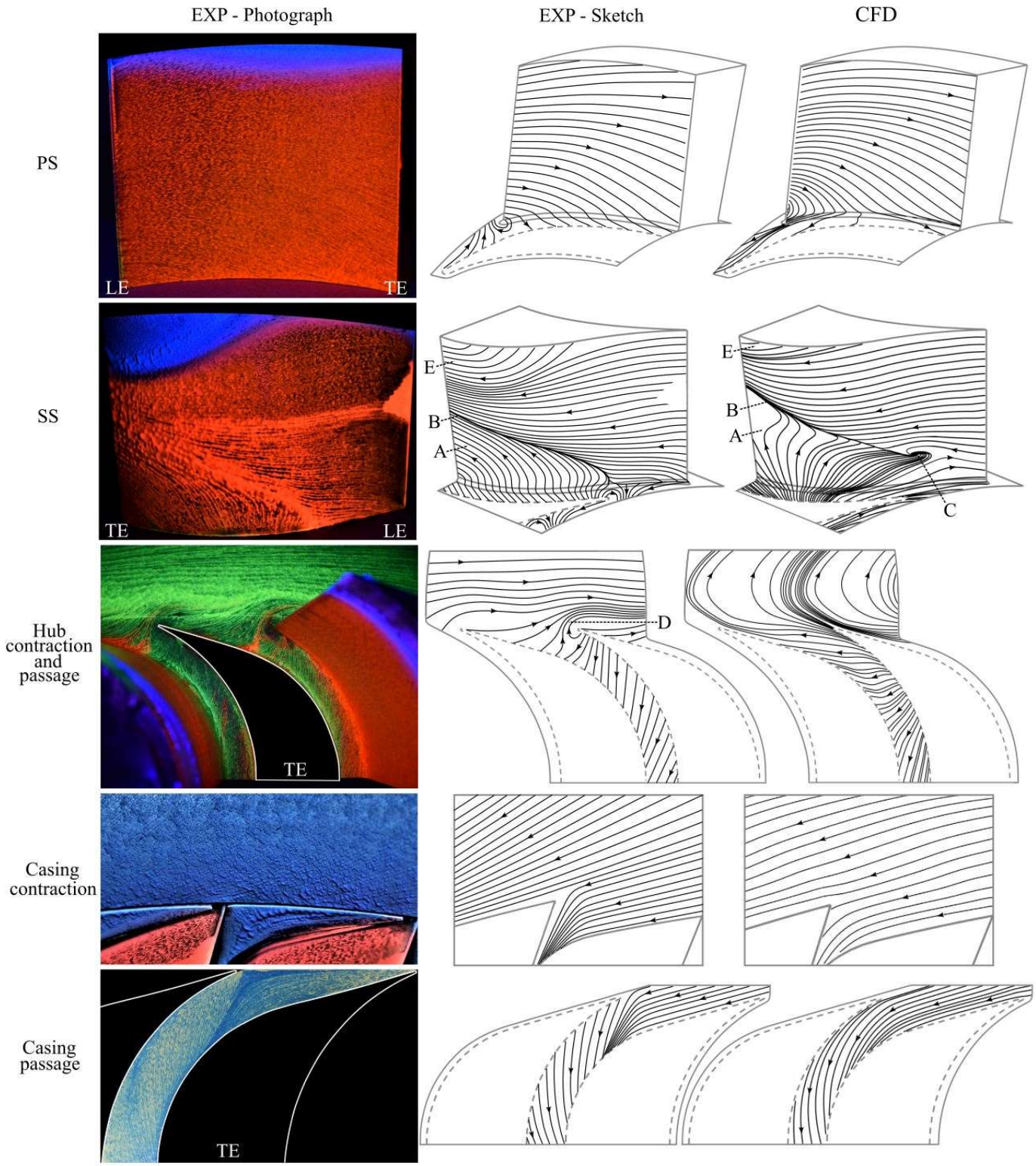


Figure 14: Comparison of experimental and CFD flow visualization at the nominal pressure ratio and zero blockage ratio.

Now consider the SS of the vane. The flow pattern is dominated by strong secondary flows, particularly pronounced at the hub, where the cross-passage flow (driven by the extreme cross-passage pressure gradients expected in an impulse-type design) climbs up the SS (marked A) to 50 % span at the TE in the case of the experiment, and 70 % span in the case of the CFD. Here the flow meets the main flow, and there is a well-defined lift-off line (marked B) marked by counter-rotating vortices (marked C). This is most clearly shown by considering the secondary flows within the passage visualized using the λ_2 method in Figure 15. Here we see the significant growth of the hub passage vortex driving upwash of streamlines on the SS at the hub. There is a similar, but smaller, casing passage vortex which drives mild downwash.

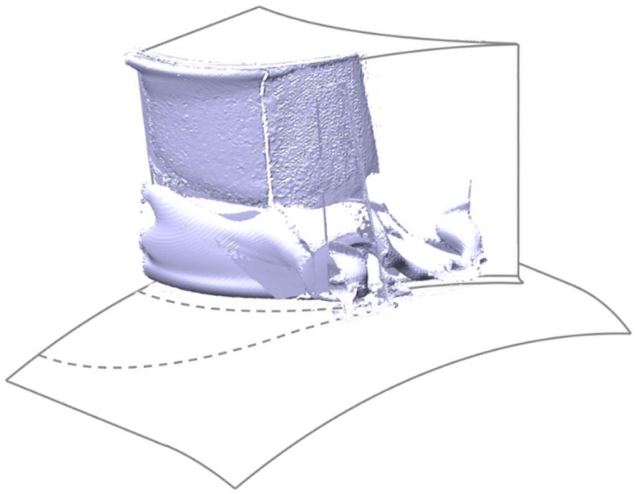


Figure 15: Predicted time-averaged secondary flows within the deswirl vane passage visualized using the λ_2 method at the nominal facility pressure ratio and zero blockage ratio.

On the hub surface (viewed from the gas path to the wall), in both the experiment and the CFD there is a region of reversed flow in the near-endwall region in the leading part and forward of the deswirl vane. This is the same feature as vortex B in Figure 11. In the case of the experiment the reversed flow feature seems to be confined to an extremely small span adjacent to the endwall. Downwash and flow reversal causes the flow on the leading SS of the vane to *spill* around the PS of the LE into the adjacent passage (marked D). The same feature is apparent in the CFD, but with substantially greater depth in the spanwise (flow reversal up to 20 % span; see also Figure 11) and chordwise directions (reversed flow up to approximately 30 % axial chord).

On the casing inlet contraction surface (viewed from the gas path to the wall), the flow is well-behaved in both the experiment and CFD. There is mild negative incidence due to the constant LE metal angle (with span) and decreasing flow yaw angle towards the case (Figure 16d). This negative incidence angle is more pronounced in the experiment (approximately –4.0°) than in CFD (–1.8°).

On the casing passage surface (viewed from the gas path to the wall), there is significant over-turning of the low-momentum endwall boundary layer fluid, leading to cross-passage migration of streamlines from the PS to the SS of the vane. This effect is more pronounced in the experiment than predicted, leading to a roll-up into a passage vortex that climbs down on to the SS of the vane at approximately 40 % axial chord. By the TE of the deswirl vane this secondary flow feature extends between approximately 100 % and 75 % span (marked E). The same features are apparent in the CFD but the point at which the endwall secondary flow climbs down on to the vane surface is less distinct, and the passage vortex fills only the uppermost 15 % of the span.

Deswirl system inlet conditions

We now consider the inlet conditions to the deswirl vanes. Figure 16 shows the measured and predicted (time-averaged) flow properties at the deswirl vane inlet plane (station 4; see Figure 2) for the zero blockage ratio case. Results are presented for five overall facility pressure ratios p_{01}/p_5 = 1.716, 1.794, 1.974, 2.193 and 2.322 with zero blockage.

Figure 16a shows the normalised radial total pressure profiles. CFD-predicted pressures were evaluated at the same locations as the pitot probes. Although the NGV outlet flow has relatively constant total pressure (see Figure 10a), the general trend at the deswirl vane inlet is higher a total pressure towards the casing than the hub. This is broadly consistent with the general flow pattern of Figure 11, in which there is a separated mixing jet with mass flow biased towards the casing (representing lower sensitivity to loss in mixing shear layers), and higher absolute velocity (on account of the radial static pressure field) towards the hub (representing greater opportunity for loss). This trend is exaggerated in the CFD, compared to the experiment, suggesting the CFD underpredicts the jet mixing (a common problem with the URANS method), and overpredicts the migration of the jet towards the casing. There is a reduction in normalised total pressure with increasing facility pressure ratio, consistent with higher vane exit Mach number, and higher associated absolute loss. In a later section we qualify this loss using a loss coefficient for the dump diffuser.

Figure 16b shows the radial profiles of normalised static pressure upstream of the deswirl vanes. The experimental profiles were measured with the first spanwise row of pressure tappings on the SS of the instrumented deswirl vane (see Figure 8) and pressure tappings on the hub and casing upstream of the deswirl vanes (see Figure 2). The incidence angle is non-zero, and therefore the leading SS static pressures are an imperfect proxy for the undisturbed static pressure (i.e., that *upstream* of the deswirl vanes). A small correction is required, the method for which is summarized in the appendix. The measured and predicted profiles have a similar shape, with an approximately linear trend between 100 % and 20 % span (consistent with highly whirling flow) and approximately constant static pressure below 20 % span. For the predicted results, the constant static

pressure below 20 % span is in agreement with the large separation in this region (see Figure 11). The CFD departs from the experiment in that it significantly underpredicts the mean static pressure at all facility pressure ratios (p_{01}/p_5). Taken in combination with a higher mass-flux-averaged total pressure (or lower dump diffuser loss coefficient; see Figure 17), this suggests significantly lower local *effective* area than in the experiment. This could be the result of a higher predicted whirl angle, or a jet that is more constrained in the radial direction.

Figure 16c shows the predicted time-averaged radial pitch angle distribution at the location of the rake. The pitch angle is negative (range between −4° and −8°) between 20 % and 100 % span, caused by the downward deflection of the primary jet (see Figure 11). In the hub region (0–20 % of the span), the flow is separated, and the predicted pitch angle tends to values close to 180°, corresponding to reverse flow along the hub wall (see Figure 11).

Figure 16d shows the predicted time-averaged radial yaw angle distribution at the location of the rake. Comparing to Figure 10b (yaw at NGV exit) we see that the mass-flux-averaged yaw angle at the deswirl vane inlet plane is 77.0° compared with 75.8° at the NGV exit. Interestingly—but not surprisingly—there is a reversal of the gradient of the yaw angle with radius: at the NGV exit the yaw angle increases with radius (forced vortex created by the NGV), but at the deswirl vane inlet plane the yaw angle decreases with radius (similar trend to free vortex, in which the tangential velocity is proportional to 1/*r*). Between the NGV and the deswirl vane the separated jet *relaxes* from a forced to a free vortex. Below 20 % span the flow is separated (large, separated recirculation, marked B in Figure 11) and reversed.

The pitch and yaw angles are (on the basis of the CFD predictions) relatively independent of the overall facility pressure ratio in the range $1.716 < p_{01}/p_5 < 2.322$, varying by on average ±0.71° between 20 and 100 % span. In addition, the pitot probes (pre-pitch of 0° and pre-yaw of 77°) are within a compound incidence angle of less than 13° across the 20–100 % span range, leading to errors in uncorrected total pressure measurements of less than 1.00 % for beveled-inlet pitot probes [29]. We therefore take the experimental deswirl vane inlet total pressure data of Figure 16 to be unaffected by probe incidence effects in the 20–100 % span range.

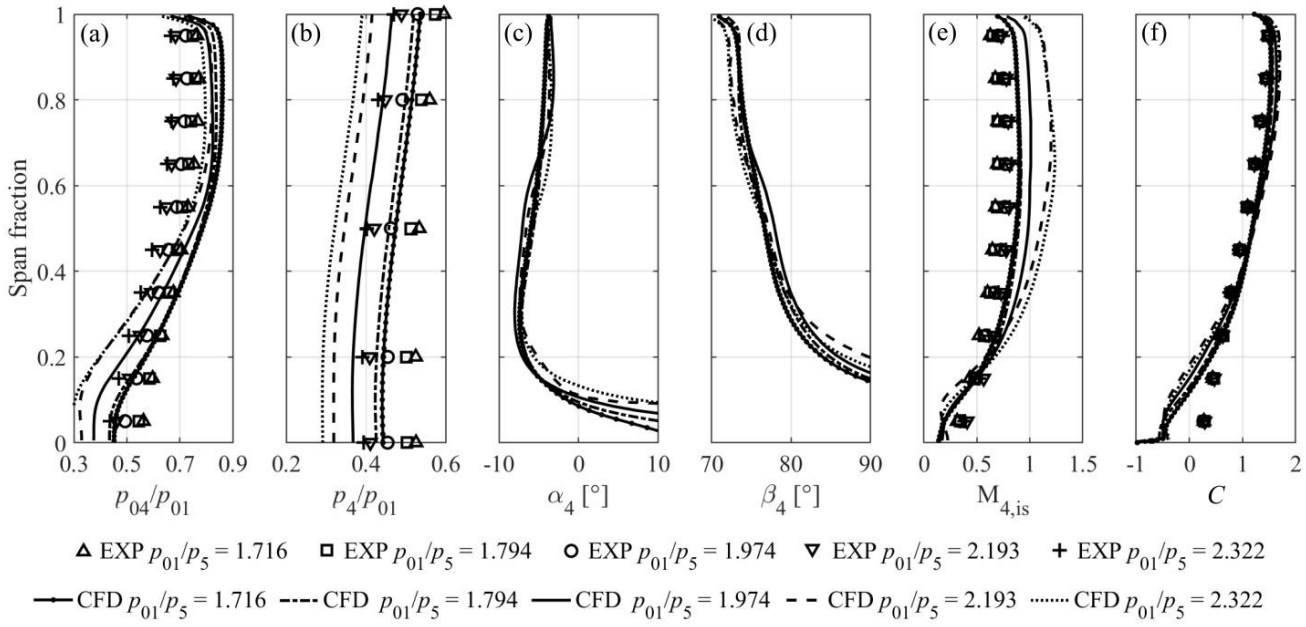


Figure 16: Measured and predicted (time-averaged) flow properties upstream of the deswirl vanes for different facility pressure ratios and zero blockage ratio: (a) normalised total pressure; (b) normalised static pressure; (c) pitch angle; (d) yaw angle; (e) isentropic Mach number; (f) normalised mass flux.

Figure 16e shows the experimentally-inferred and predicted isentropic Mach number distributions at the deswirl vane inlet plane ($M_{4,is}$). The experimentally-inferred $M_{4,is}$ was calculated using the total and static pressures measured (p_{04}) and inferred (p_4; see appendix for method) upstream of the deswirl vanes. Looking at the experimental data, we see a relatively constant $M_{4,is}$ between 35 % and 95 % span, with $M_{4,is}$ increasing with overall facility pressure ratio. At the nominal facility pressure ratio the mass-flux-averaged $M_{4,is}$ was 0.71. The corresponding value (at same facility pressure ratio) predicted by CFD was 0.84: a moderate overprediction. The overprediction of $M_{4,is}$ is a result of the combined effect of the underprediction of the both the dump diffuser static pressure and the total pressure loss coefficient.

Figure 16f shows a distribution of a *normalised mass flux function* upstream of the deswirl vanes: specifically, the local mass flow rate per unit of local geometric passage area ($\dot{m}_{4,l}/A_{4,g,l}$) normalised by the mean value of the same, or—equivalently— the ratio of the total mass flow rate and total area ($\dot{m}_4/A_{4,g}$). That is, we define the normalised mass flux function by:

$$C = (\dot{m}_{4,l}/A_{4,g,l})/(\dot{m}_4/A_{4,g}) \quad (3)$$

where the local mass flow rate $\dot{m}_{4,l}$ was calculated from the spanwise distributions static pressure (p_4) and total pressure (p_{04}), and the predicted flow angles (α_4 and β_4; values in the 0–20 % span region were extrapolated from the rest of the span). This normalised mass flux function has the following properties: it has an average value of unity across the span; values above unity show regions where the local mass *flux* (i.e. the area-independent mass flow rate) is higher than average; values below unity show the reverse. In a uniform flow a constant value of unity would be expected and the purpose in the definition is to allow description of deviations from that state.

In both the experimental and CFD data we see a significantly casing-loaded normalised mass flux function, with average experimental values in the range 1.3–1.5 near the casing and approximately 0.3–0.5 (i.e. a mean ratio of approximately 3.5) near the hub. This is partly explained both by the central jet (Figure 11 and Figure 12) carrying significantly high total pressure (Figure 16a) in the near-casing region, but is also associated with the effective blockage caused both by large scale separations within the deswirl vane passage near the hub (0–20 % span in the case of CFD), and secondary flows extending between 0 and 50 % span (Figure 15). Although both experiment and CFD have similar trends, the CFD trend is exaggerated on account of reversed flow in 20 % span region nearest the hub.

Dump diffuser loss coefficient

To better understand the total pressure data of Figure 16a, and to retrospectively evaluate the assumptions about dump diffuser loss used for capacity setting of the deswirl vane, we now calculate the dump diffuser total pressure loss coefficient ($Y_{p,\mathrm{DD}}$) as a function of the NGV isentropic exit Mach number for both the experimental and CFD data.

Taking Equation 1, $\bar{p}_{02}$ was calculated from p_{01} (measured) using an assumed (from traverse measurements [22]) NGV total pressure loss coefficient $Y_{p,\mathrm{NGV}} = 0.05$. $\bar{p}_{04}$ was calculated by averaging the spanwise distribution of p_{04} weighted by the local mass flow rate ($\dot{m}_{4,l}$) at each span position. The resulting trend of $Y_{p,\mathrm{DD}}$ with NGV isentropic exit Mach number, $\mathrm{M}_{2,\mathrm{is}}$, is presented in Figure 17 for both experimental and CFD data. The experimental data are presented for both zero and 0.25 choke plate blockage ratio (representing a range of $1.51 \times 10^6 < \mathrm{Re}_2 < 3.48 \times 10^6$ at $\mathrm{M}_{2,\mathrm{is}} = 0.9$). It is recalled that the CFD simulations were performed for a single Re_2-M_2 characteristic. The experimental data for $Y_{p,\mathrm{DD}}$ are in the range $0.59 < Y_{p,\mathrm{DD}} < 0.71$ over a fairly wide range of $\mathrm{M}_{2,\mathrm{is}}$ and Re_2. The loss coefficient increases slightly with $\mathrm{M}_{2,\mathrm{is}}$ for $\mathrm{M}_{2,\mathrm{is}} > 0.4$, but is relatively insensitive to Re_2. This justifies the CFD method that was used. The CFD data shows lower loss (underprediction of the jet mixing rate) and less sensitivity to $\mathrm{M}_{2,\mathrm{is}}$, with all loss coefficients in the range $0.34 < Y_{p,\mathrm{DD}} < 0.37$ over a Mach number range $1.00 < \mathrm{M}_{2,\mathrm{is}} < 1.29$. The preliminary design value of $Y_{p,\mathrm{DD}} = 0.5$ appears to have been a reasonable choice for setting the deswirl vane capacity.

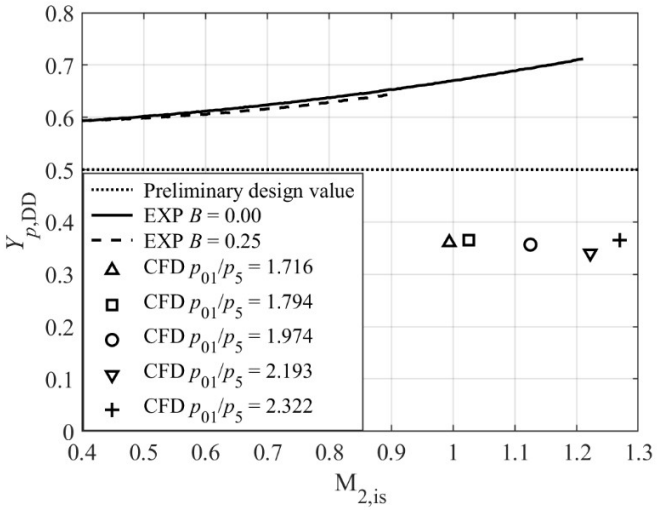


Figure 17: Measured and predicted dump diffuser mass-flux-averaged total pressure loss coefficient as a function of NGV isentropic exit Mach number based on rake measurements.

Deswirl vane aerodynamics

We now consider the deswirl vane aerodynamics. Figure 18 shows the measured and predicted (time-averaged) isentropic Mach number (M_{is}) distributions at 20, 50 and 80 % span. Data are presented for the nominal facility pressure ratio, $p_{01}/p_5 = 1.974$, and zero blockage ratio. For the experimental data, M_{is} was calculated using local surface static pressure (Figure 8) and the span-relevant total pressure measured using the upstream rake. An identical process was used in CFD, with the additional step of time-averaging the unsteady flow at each location.

We first analyse the CFD data. To aid interpretation, we also consider the corresponding time-averaged area-distributions of M_{is} at 50 and 80 % span. These are shown in Figure 19. For the particular operating condition, the flow upstream of the vanes is high-subsonic, with $\mathrm{M}_{\mathrm{is}} = 0.98$ and $\mathrm{M}_{\mathrm{is}} = 0.99$ at 50 and 80 % span respectively. This is shown in the radial distributions of $\mathrm{M}_{4,\mathrm{is}}$ in Figure 16e, and in the contour plot of Figure 19. With respect to the mean LE metal angle, the local incidence angles at 50 and 80 % span are 5.4° and 2.2°, respectively. Taking account of the LE radius, the corresponding local turning angles on the SS of the vane are 3.4° and 0.2°, at 50 % and 80 % span respectively, and 7.4° and 4.2° on the PS. At both 50 % and 80 % span we see a local acceleration (caused by positive incidence) round the SS LE tip, leading to a locally supersonic patch (marked A in Figure 18 and Figure 19) extending between 0 and approximately 15 % surface distance. Excluding the LE spike,

the peak Mach number in this region is approximately 1.30 at 50 % span, and 1.15 at 80 % span. Beyond this local *suction peak*, the flow appears to isentropically diffuse back to a Mach number of approximately unity (i.e. close to the inlet Mach number). At approximately 40 % surface distance on the SS there is a local acceleration and diffusion (marked B in Figure 18 and Figure 19). This is located at the blend point between the flat and curved (constant radius) sections that form the vane SS construction. The pressure disturbance is thought to arise because of the discontinuity in the surface curvature at this point [30]. On the remainder of the SS there is a relatively constant M_{is} distribution for the 80 % span section, and a slight reduction in M_{is} with surface distance for the 50 % span section. On the PS of the vane M_{is} has an almost constant value at approximately 0.75. The pressure difference across the passage is therefore relatively constant with surface distance, consistent with constant PS curvature and constant turning rate within the passage (impulse-type vane). The 20 % span CFD pressure distribution is primarily within a separated region and is presumably primarily driven by the pressure distribution of the nearby non-separated flow.

Looking now at the experimental data, we observe similar general trends but different absolute magnitude. At the 50 and 80 % span sections, the pressure gradient across the passage is similar to the CFD, but with average SS M_{is} of 0.72 and 0.77 respectively. This is consistent with the lower-than-predicted measured Mach numbers in Figure 16e. At 20 % span the pressure distribution is consistent with attached flow within the passage, but at very low local Mach number or total pressure (see Figure 16a and Figure 16e). This is also consistent with the flow visualization results (Figure 14) which show only a local reversed flow region near the LE of the vane in the experimental data, but a larger scale reversed flow region in the CFD.

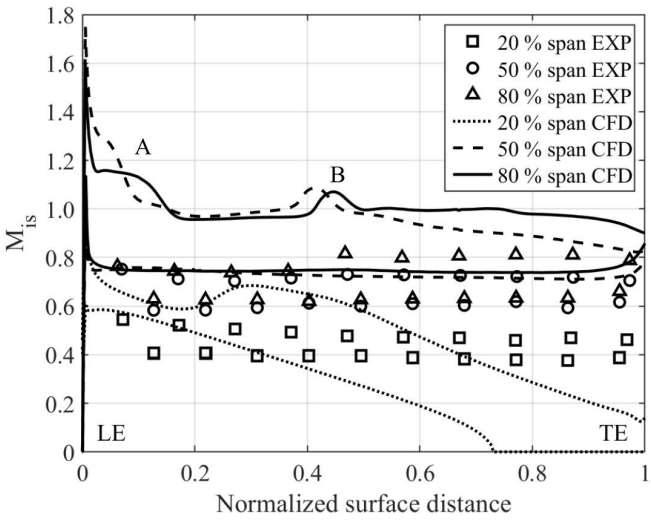


Figure 18: Measured and predicted distributions of deswirl vane surface isentropic Mach number at the nominal facility pressure ratio and zero blockage ratio.

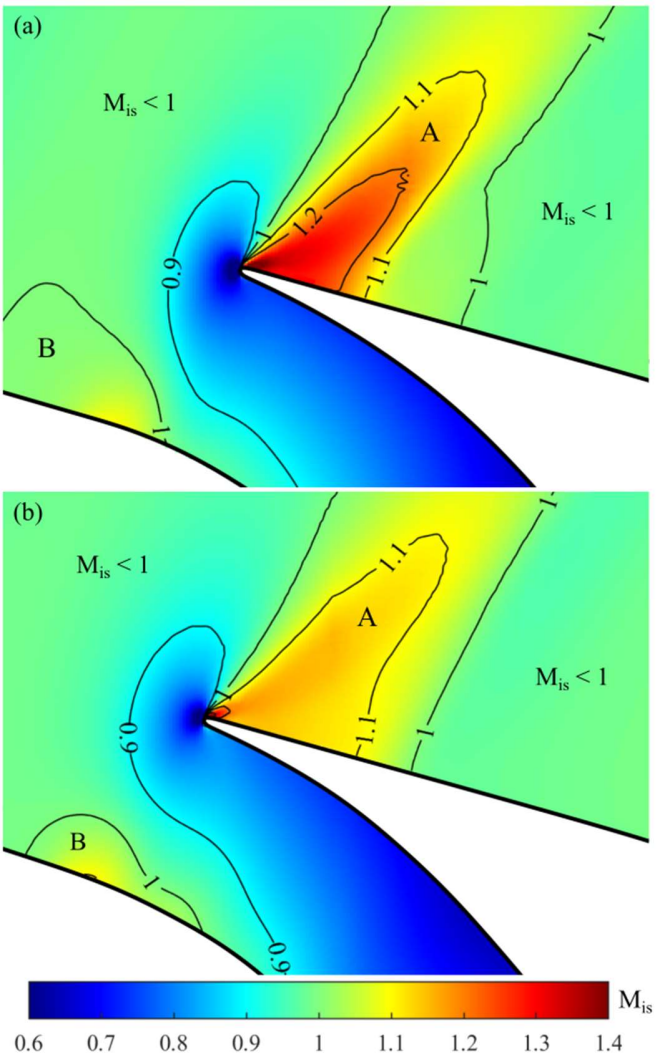


Figure 19: Time-averaged predicted isentropic Mach number distributions at the leading edge of a deswirl vane at the nominal facility pressure ratio and zero blockage ratio: (a) 50 % span; (b) 80 % span.

BACK-PRESSURE CONTROL; TOTAL PRESSURE LOSS; CAPACITY RELATIONSHIP

We now consider the performance of the system for the purpose of back-pressure control, and attempt to understand the system characteristics by considering the dump diffuser total pressure loss and the deswirl vane capacity.

Back-pressure control

In this section, we look at the HP NGV back-pressure as a function of facility pressure ratio using experimental data. Blockage ratio was evaluated geometrically (see Figure 6).

Figure 20 shows measured span-averaged NGV exit isentropic Mach number characteristics as a function of facility pressure ratio for various blockage ratios. The *natural* (no deswirl module) operating characteristic, and the characteristics

for 11 blockage ratios are shown. As a discussion example, we consider operation at $M_2 = 1$. Condition A (marked in Figure 20) is the natural operating point with no deswirl module. Condition B represents the minimum facility pressure ratio (and associated Re_2) that can be achieved with the deswirl module installed: that is a blockage ratio of zero. Increasing the blockage ratio (moving between B and C) leads to an increase in Re_2. In this blockage range, the *deswirl vane* mean inlet Mach number increases from high-transonic to choked. In the region between C and D (and beyond) both the NGV *and* the deswirl vane are choked and indefinite further increases in overall facility pressure ratio (and therefore NGV Re_2) are possible at the same blockage ratio without affecting the NGV exit Mach number.

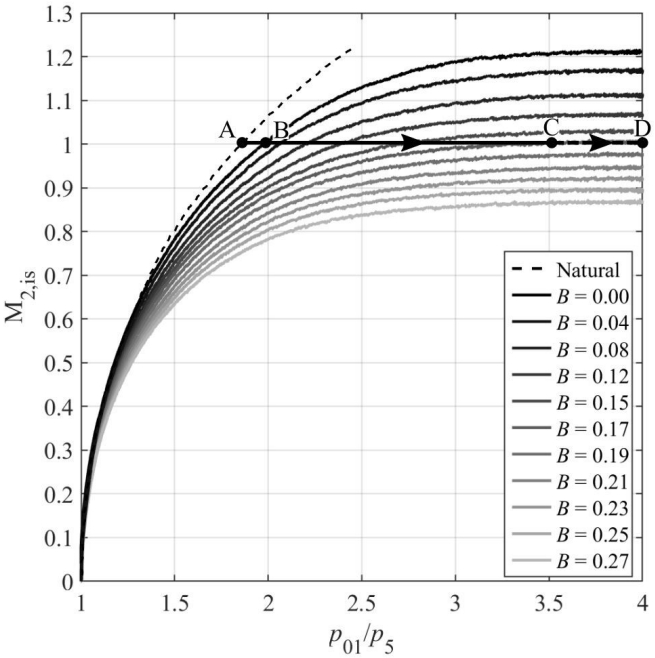


Figure 20: Experimentally measured HP NGV exit isentropic Mach number characteristics as a function of facility pressure ratio for various blockage ratios.

The overall performance curves for the deswirl module are most compactly represented as M_2-Re_2 characteristics. These are shown in Figure 21, marking in particular: the natural operating characteristic; eleven characteristics at particular blockage ratios; and the M_2-Re_2 conditions for the five particular CFD simulations. The conclusion is that excellent M_2-Re_2 control can be achieved with good sensitivity over a wide range. The deswirl module works well for the intended purpose providing precise control of operating point. Taking the nominal operating point as $M_{2,is} = 1$, the experimentally measured minimum value of Re_2 was 1.84×10^6, or 1.66 % greater than the natural operating point. This compares well with the predicted increase in minimum Reynolds number of 3.32 %, partially validating assumptions made in setting the required capacity overhead during preliminary design.

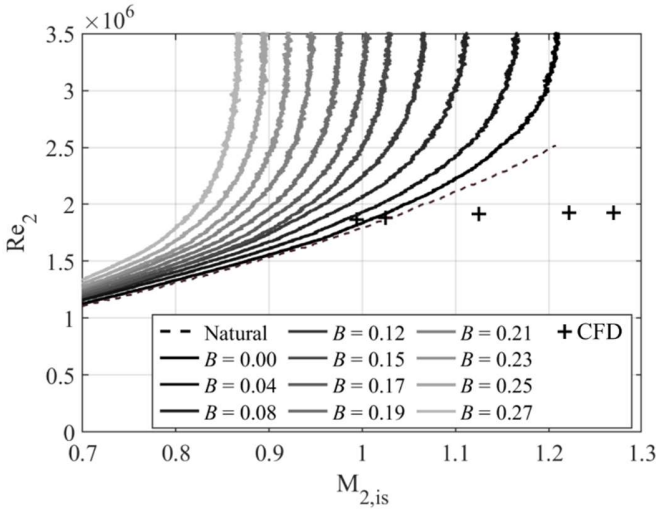


Figure 21: Experimentally measured M_2-Re_2 relationship for the HP NGVs as a function of blockage ratio. Individual CFD simulations are also marked.

Total pressure loss

To understand the deswirl vane capacity deficit (discussed in the next section) we calculate the experimentally evaluated mass-flux-averaged dump diffuser total pressure loss coefficient at every *system operating point* $Y_{p,\mathrm{DD}}(p_{01}/p_5, B)$. We present the results in this form—as opposed to the more natural co-ordinate system $Y_{p,\mathrm{DD}}(p_{02}/p_2)$—to allow us to calculate the capacity deficit at every system operating point. $Y_{p,\mathrm{DD}}$ was defined according to Equation 1, using the mass-flux-averaged total pressure upstream of the deswirl vane (calculated by averaging the spanwise distribution of p_{04} weighted by the local mass flow rate $\dot{m}_{4,l}$ at each span position). The results are presented in Figure 22.

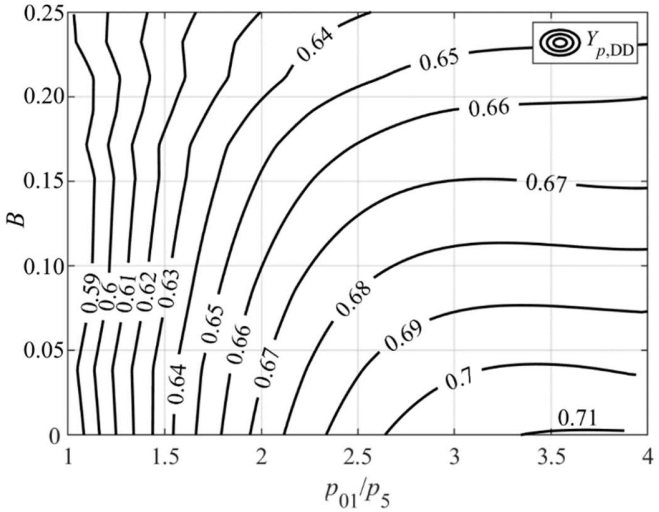


Figure 22: Experimentally determined dump diffuser mass-flux-averaged total pressure loss coefficient as a function of facility pressure ratio and blockage ratio.

Over a very wide range of facility pressure ratio ($1.0 < p_{01}/p_5 < 4.0$) and blockage ratio ($0 < B < 0.25$) the total pressure loss coefficient varies in the range $0.59 < Y_{p,\mathrm{DD}} < 0.71$: a relatively limited range. The value of $Y_{p,\mathrm{DD}} = 0.59$ can be taken as the incompressible limit, with $Y_{p,\mathrm{DD}} = 0.71$ corresponding to $M_{2,is} = 1.2$, the highest isentropic Mach number tested. Vertical contours at low values of p_{01}/p_5 indicate a slow increase in the value of $Y_{p,\mathrm{DD}}$ with increasing compressibility. Independence of $Y_{p,\mathrm{DD}}$ on pressure ratio for high values of p_{01}/p_5 (horizontal contours) occurs when the deswirl vane is choked, setting a particular NGV exit Mach number (both subsonic or mildly supersonic) for a given blockage ratio. In this region increasing blockage lowers the NGV exit Mach number, and lowers the corresponding value of $Y_{p,\mathrm{DD}}$. In the next section we consider the implied capacity deficit based on geometric area.

Deswirl vane capacity deficit

Using the results of Figure 22 as a representation of $\bar{p}_{04}$ (see Equation 1), we can compute the *measured* deswirl vane capacity $\Gamma_4\,(\bar{p}_{04}/p_5, B)$

$$\Gamma_4(\bar{p}_{04}/p_5, B) \;=\; \frac{\dot{m}\sqrt{T_{04}}}{\bar{p}_{04}} \tag{4}$$

We can also define an isentropic geometric capacity function [25] $\Gamma_{4,\mathrm{is}}(\bar{p}_{04}/p_5, B)$ using the full geometric passage area, $A_{4,g}$, and the blockage (see Figure 6), as

$$\Gamma_{4,\mathrm{is}}(\bar{p}_{04}/p_5, B) = (1-B)A_{4,g}\sqrt{\frac{\gamma}{R}}\left(\frac{p_5}{\bar{p}_{04}}\right)^{\frac{\gamma+1}{2\gamma}} \left\{\left[\left(\frac{p_5}{\bar{p}_{04}}\right)^{(1-\gamma)/\gamma} - 1\right]\frac{2}{\gamma-1}\right\}^{1/2} \tag{5}$$

Noting that the deswirl vane pressure ratio ($\bar{p}_{04}/p_5$) is uniquely defined by the overall facility pressure ratio (p_{01}/p_5) and the blockage ratio (B)—that is $\bar{p}_{04}/p_5 = f(p_{01}/p_5, B)$—we can make the co-ordinate transform in Equations 4 and 5 between $\Gamma(\bar{p}_{04}/p_5, B)$ and $\Gamma(p_{01}/p_5, B)$. Doing so allows us to define a capacity deficit function $\zeta(p_{01}/p_5, B)$ by

$$\zeta(p_{01}/p_5, B) \;=\; \frac{\Gamma_{4,\mathrm{is}}(p_{01}/p_5, B) \;-\; \Gamma_4(p_{01}/p_5, B)}{\Gamma_{4,\mathrm{is}}(p_{01}/p_5, B)} \tag{6}$$

This expresses the *effective blockage* in the deswirl vane due to the combined effects of: inlet separation; secondary flow within the vane; shock loss; the exit vena contracta effect. A plot of $\zeta(\bar{p}_{04}/p_5, B)$ is presented in Figure 23.

Over the range of facility pressure ratio ($1.0 < p_{01}/p_5 < 4.0$) and blockage ratio ($0 < B < 0.25$), the deswirl vane capacity deficit varies in the range $0.125 < \zeta < 0.180$—a relatively narrow range—decreasing slightly with increasing p_{01}/p_5. Over most of this range, ζ is essentially independent of blockage, with only slight dependence for $p_{01}/p_5 > 3.5$.

The conclusion is that the capacity deficit (or effective blockage) due to secondary effects within the deswirl vane is essentially constant (at approximately 0.15) across an extremely wide range of operating conditions of overall facility pressure ratio and choke plate blockage. This make operation relatively linear, and leads to easy preliminary design of future systems. The experimentally determined value of 0.15 justifies the use of the value of 0.2 during the preliminary design phase. It is noteworthy that this value is high in comparison to typical HP NGVs, which are typically in the range 0.05–0.12, the lower limit being capped by total pressure loss coefficients ($Y_{p,\mathrm{NGV}} \sim 0.05$ for transonic vanes), and the upper end of the range typically only applying for heavily aft-loaded vanes with significant static pressure variation across the controlling region [24]. This is perhaps unsurprising because of the extreme secondary flows within the impulse-turbine-type passage.

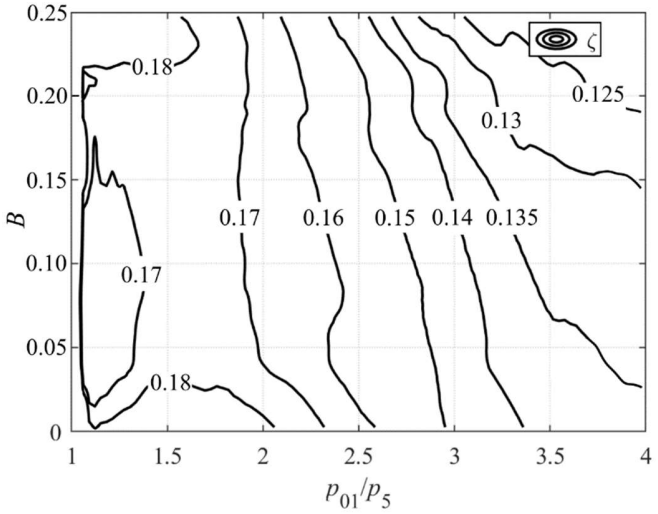


Figure 23: Capacity deficit function as a function of facility pressure ratio and blockage ratio.

CONCLUSIONS

In this paper, we present the design and commissioning of a novel back-pressure control system which combines an annular dump-diffuser and deswirl system with integrated choke plate. The purpose of the system is to facilitate precise back-pressure control whilst maintaining access for traverse and optical equipment. The application is in annular cascades in which there is a requirement for independent control of Reynolds and Mach numbers. The new system is uniquely compact, and—by virtue of being manufactured as a blisk—does not require an additional hub support structure. Using experimental and CFD data we perform a comprehensive analysis of the flow that develops in the annular dump-diffuser, and within the deswirl vane ring.

A preliminary design method is described which will help designers of future systems. This considers both local aerodynamic aspects, and overall capacity-loss relationships, leading to a required *capacity overhead* for a specified increase in minimum Reynolds number with the introduction of the

system. In the case of the present system the a priori prediction was for a 3.32 % increase in minimum Reynolds numbers: a value of 1.66 % was achieved in practice, the slight discrepancy arising because of conservativism in design assumptions. An experimentally-determined total pressure loss coefficient for the dump diffuser is calculated, as is the capacity deficit function for the deswirl vane ring (characterizing the impact of secondary flows and loss within the deswirl vane passage), allowing greater precision in preliminary design of future systems.

The new system has a number of installation and control advantages over previous systems, and it is hoped that this analysis will prove useful to designers of future facilities.

ACKNOWLEDGEMENTS

The financial support of Rolls-Royce plc is gratefully acknowledged. Nafiz Chowdhury is thanked for his support with the experiments.

NOMENCLATURE

Acronyms

AFRL	Air Force Research Laboratory
ASC	Annular Sector Cascade
BTF	Blowdown Turbine Facility
CFD	computational fluid dynamics
DLR	German Aerospace Center
ECAT	Engine Component AeroThermal (Facility)
EXP	experiment
HP	high-pressure
HSAC	High Speed Annular Cascade
HWRT	High Work Research Turbine
IR	infrared
KTH	Royal Institute of Technology
LE	leading edge
MIT	Massachusetts Institute of Technology
MTO	maximum take-off
NDTL	Notre-Dame Turbomachinery Laboratory
NGV	nozzle guide vane
ORF	Oxford Rotor Facility
OTRF	Oxford Turbine Research Facility
PETAL	Purdue Experimental Turbine Aerothermal Laboratory
PS	pressure surface
P&WC	Pratt & Whitney Canada
RGG	Rotating Cascade Tunnel in Göttingen
SS	suction surface
TE	trailing edge
TRF	Turbine Research Facility
TTF	Turbine Test Facility
TTTF	Transonic Turbine Test Facility
URANS	unsteady Reynolds-averaged Navier-Stokes
VKI	von Karman Institute

Greeks

α	pitch angle
β	yaw angle
γ	ratio of specific heat capacities
Γ	capacity
ζ	capacity deficit

Romans

A	area
B	deswirl vane passage area blockage ratio
C	normalised mass flux function
f	frequency
i	incidence angle
L	characteristic length
$\dot{m}$	mass flow rate
M	Mach number
p	static pressure
p_0	total pressure
$\bar{p}_0$	mass-flux-averaged total pressure
r	radial position
R	ideal gas constant
Re	Reynolds number
St	Strouhal number
t	time
T_0	total temperature
Tu	turbulence intensity
U	velocity
x	axial position
y+	non-dimensional wall distance
Y_p	total pressure loss coefficient

Subscripts

1	station 1 (upstream of the HP NGVs)
2	station 2 (downstream of the HP NGVs)
3	station 3 (HP NGV exit duct outlet)
4	station 4 (upstream of the deswirl vanes)
$4'$	static pressure tappings at LE SS on deswirl vane
5	station 5 (downstream of the deswirl vanes)
DD	dump diffuser
g	geometric
is	isentropic
l	local

Superscript

*	sonic condition

REFERENCES

[1] Erhard, J., and Gehrer, A., 2000, "Design and Construction of a Transonic Test-Turbine Facility," Proceedings of the ASME Turbo Expo, Munich, Germany, paper no. 2000-GT-0480.

[2] Dominy, R. G., 1988, "The Whittle Laboratory Transonic Annular Cascade Wind Tunnel," Proceedings of the 9th Symposium on Measuring Techniques for Transonic and Supersonic Flow in Cascades and Turbomachines, Oxford, UK.

[3] Vlasic, E. P., Girgis, S., and Moustapha, S. H., 1996, "The Design and Performance of a High Work Research Turbine," ASME Journal of Turbomachinery, 118(4): 792–799.

[4] Bernardini, C., Takakura, T., Perez, E., Cameron, J. D. and Morris, S. C., 2019, "Development of a 10 MW Facility for

Gas Turbine Engine and Component Testing," AIAA Propulsion and Energy Forum, Indianapolis, Indiana, USA, paper no. 2019-4001.
[5] Wiers, S. H. and Fransson, T. H., 1998, "A New Annular Sector Cascade Test Facility to Investigate Steady State Cooling Effects," Proceedings of the 14th Symposium on Measuring Techniques for Transonic and Supersonic Flow in Cascades and Turbomachines, Limerick, Ireland.
[6] Rehder, H, Pahs, A, Bittner, M, and Kocian, F., 2017, "Next Generation Turbine Testing at DLR," Proceedings of the ASME Turbo Expo 2017, Charlotte, North Carolina, USA, paper no. GT2017-64409.
[7] Kost, F. and Giess, P.-A., 2004, "Experimental Turbine Research at DLR Goettingen", Journal of the Gas Turbine Society of Japan, Vol. 32, No. 6.
[8] Hilditch, M. A., Fowler, A., Jones, T. V., Chana, K. S., Oldfield, M. L. G., Ainsworth, R. W., Hogg, S. I., Anderson, S. J., and Smith, G. C., 1994, "Installation of a Turbine Stage in the Pyestock Isentropic Light Piston Facility," Proceedings of the ASME Turbo Expo 1994, The Hague, Netherlands, paper no. 94-GT-277.
[9] Povey, T., Chana, K. S., Jones, T. V., and Oldfield, M. L. G., 2003, "The Design and Performance of a Transonic Flow Deswirling System—An Application of Current CFD Design Techniques Tested Against Model and Full-Scale Experiments," Advances of CFD in Fluid Machinery Design, IMechE Professional Engineering Publishing, pp. 65–94. ISBN 1 8058 353 9.
[10] Povey, T., Jones, T. V., and Oldfield, M. L. G., 2004, "On a Novel Annular Sector Cascade Technique," ASME Journal of Turbomachinery, 129(1): 175–183.
[11] Ainsworth, R. W., Schultz, D. L., Davies, M. R. D., Forth, C. J. P., Hilditch, M. A., Oldfield, M. L. G., and Sheard, A. G., 1988, "A Transient Flow Facility for the Study of the Thermofluid-Dynamics of a Full Stage Turbine Under Engine Representative Conditions," Proceedings of the ASME 1988 International Gas Turbine and Aeroengine Congress and Exposition, Amsterdam, Netherlands, paper no. 88-GT-144.
[12] Sieverding, C. H. and Arts, T., 1992, "The VKI Compression Tube Annular Cascade Facility CT3," Proceedings of the ASME 1992 International Gas Turbine and Aeroengine Congress and Exposition, Cologne, Germany, paper no. 92-GT-336.
[13] Epstein, A. H., Guenette, G. R. and Norton, R. J. G., 1984, "The MIT Blowdown Turbine Facility," Proceedings of the ASME 1984 International Gas Turbine Conference and Exhibit, Amsterdam, Netherlands, paper no. 84-GT-116.
[14] Dunn, M. and Mathison, R., 2014, "History of Short-Duration Measurement Programs Related to Gas Turbine Heat Transfer, Aerodynamics, and Aeroperformance at Calspan and The Ohio State University," ASME Journal of Turbomachinery, 136(4): 041004.
[15] Paniagua, G., Cuadrado, D., Saavedra, J., Andreoli, V., Meyer, T., Solano, J. P., Herrero, R., Meyer, S., and Lawrence, D., 2018, "Design of the Purdue Experimental Turbine Aerothermal Laboratory for Optical and Surface Aerothermal Measurements," ASME Journal of Engineering for Gas Turbines and Power, 141(1): 012601.
[16] Haldenan, C.W., Dunn, M. G., MacArthur, C. D. and Murawski, C. G., 1992, "The USAF Advanced Turbine Aerothermal Research Rig (ATARR)." AGARD Conference Proceedings, Propulsion and Energetics Panel 80th Symposium, Antalya, Turkey.
[17] Parker, J., A., Romero, E., and Povey, T., 2019, "A Modular Transonic Turbine Cascade for Cooled Rotor Metal Effectiveness Investigations," Proceedings of the ASME Turbo Expo 2019, Phoenix, Arizona, USA, paper no. GT2019-91697.
[18] Povey, T., Oldfield, M. L. G. and Haselbach, F., 2008, "Transonic turbine vane tests in a new miniature cascade facility," Proceedings of the Institution of Mechanical Engineers Part A Journal of Power and Energy, 222(5), 529–539.
[19] Chana, K. S., Singh, U. K., and Povey, T., 2004, "Turbine Heat Transfer and Aerodynamic Measurements and Predictions for a 1.5 Stage Configuration," Proceedings of the ASME Turbo Expo 2004, Vienna, Austria, paper no. GT2004-53951.
[20] Beard, P. F., Adams, M. G., Nagawakar, J. R., Stokes, M. R., Wallin, F., Cardwell, D. N., Povey, T. and Chana, K. S., 2019, "The LEMCOTEC 1½ Stage Film-Cooled HP Turbine: Design, Integration and Testing in the Oxford Turbine Research Facility," Proceedings of 13th European Conference on Turbomachinery Fluid Dynamics & Thermodynamics, Lausanne, Switzerland.
[21] Kirollos, B., Lubbock, R., Beard, P., Goenaga, F., Rawlinson, A., Janke, E., and Povey, T., 2017, "ECAT: An Engine Component Aerothermal Facility at the University of Oxford," Proceedings of the ASME Turbo Expo 2017, Charlotte, North Carolina, USA, paper no. GT2017-64736.
[22] Burdett, D. and Povey, T., 2021, "Experimental and Numerical Analysis of Loss Characteristics of Cooled Transonic Nozzle Guide Vane," (under review).
[23] Burdett, D., Hambidge, C., and Povey, T., 2020, "Analysis of ultra-low uncertainty gas turbine flow capacity measurement techniques," Proceedings of the Institution of Mechanical Engineers, Part A: Journal of Power and Energy.
[24] Burdett, D., Goenaga, F., and Povey, T., 2021, "Understanding Capacity Sensitivity of Cooled Transonic Nozzle Guide Vanes: A Parametric Experimental and Computational Study of the Impact of Trailing Edge Geometry," ASME Journal of Turbomachinery, 143(5): 051001.
[25] Povey, T., Sharpe, M., and Rawlinson, A., 2011, "Experimental Measurements of Gas Turbine Flow Capacity Using a Novel Transient Technique," ASME Journal of Turbomachinery, 133(1): 011005.
[26] Messenger, A. and Povey, T., 2020, "Calibrated Low-Order Transient Thermal and Flow Models for Robust Test

Facility Design," Journal of the Global Power and Propulsion Society, 4, 94-113.
[27] Luque, S., and Povey, T., 2010, "A Novel Technique for Assessing Turbine Cooling System Performance," ASME Journal of Turbomachinery, 133(3): 031013.
[28] Sieverding, C. H., and Heinemann, H., 1990, "The Influence of Boundary Layer State on Vortex Shedding From Flat Plates and Turbine Cascades," ASME Journal of Turbomachinery, 112(2): 181–187.
[29] Gracey, W., Letko, W. and Russell, W. R., 1950, "Wind-tunnel Investigation of a Number of Total Pressure Tubes at High Angles of Attacks," RM L50G19, National Advisory Committee for Aeronautics, Washington, D.C.
[30] Korakianitis, T., and Papagiannidis, P., 1993, "Surface-Curvature-Distribution Effects on Turbine-Cascade Performance," ASME Journal of Turbomachinery, 115(2): 334–341.

APPENDIX A: EXPERIMENTALLY-INFERRED STATIC PRESSURE UPSTREAM OF THE DESWIRL VANES

Because the flow incidence angle is non-zero at the deswirl vane LE, the leading SS static pressures (see Figure 8) are an imperfect representation of the undisturbed upstream static pressure. We now describe the correction method used to recover an inferred value for upstream static pressure. The method is as follows:

i) We assume that the flow is subsonic. This is justified by the CFD data at most operating pressure ratios, and also by inability to achieve converged solutions in a similar method to the current one in which a supersonic inlet state is assumed (with associated shock/expansion structure on the deswirl vane).
ii) We assume that the measured static pressure on the SS of the deswirl vane, $p_{4\prime}$, is equivalent to the upstream static pressure *as disturbed by a subsonic diffusion* around the LE SS of the vane. This is associated with an angle change in the flow equal to the incidence angle, i. This is shown in Figure 24.
iii) Referencing the equivalent upstream area, A_4, and equivalent downstream area, $A_{4\prime}$, to the equivalent sonic reference area A^* (we take it as the same upstream and downstream because the process is isentropic) we get

$$\frac{A_4}{A^*} = \left(\frac{A_{4\prime}}{A^*}\right)\left(\frac{\cos(\beta_4)}{\cos(\beta_4 - i)}\right) \qquad (7)$$

Using these area ratios and the area-Mach-number relationships, we calculate the inferred undisturbed upstream static-to-total pressure ratio p_4/p_{04} from the post-diffusion value $p_{4\prime}/p_{04}$.

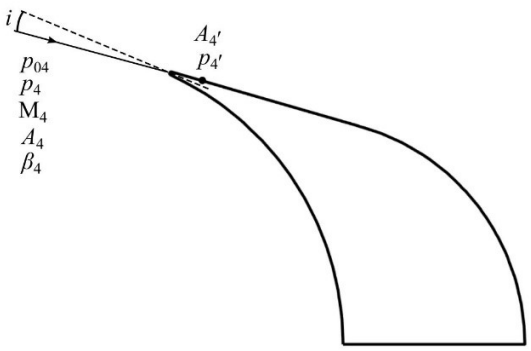


Figure 24: Schematic of deswirl vane in subsonic flow for calculation of inferred undisturbed upstream static pressure.

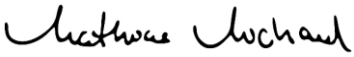
Statement of Authorship for joint/multi-authored papers for PGR thesis

To appear at the end of each thesis chapter submitted as an article/paper

The statement shall describe the candidate's and co-authors' independent research contributions in the thesis publications. For each publication there should exist a complete statement that is to be filled out and signed by the candidate and supervisor **(only required where there isn't already a statement of contribution within the paper itself).**

Title of Paper	Annular Dump Diffuser and Deswirl System for Back-Pressure Control in Engine-Scale Transonic Annular Cascade
Publication Status	□ Published ■ Accepted for Publication □ Submitted for Publication □ Unpublished and unsubmitted work written in a manuscript style
Publication Details	Michaud, M., Ornano, F. and Povey, T., 2022, "Annular Dump Diffuser and Deswirler System for Back-Pressure Control in an Engine-Scale Transonic Annular Cascade."

Student Confirmation

Student Name:	Mathias Michaud		
Contribution to the Paper	Mathias Michaud performed all the experiments, post-processed the experimental data, post-processed some of the CFD data, wrote the manuscript and contributed to the analysis. Francesco Ornano was in charge of running the CFD simulations (meshing and simulation setup) and post-processing some the CFD data. Thomas Povey provided the original research idea, contributed to the analysis and the writing of the manuscript.		
Signature 		Date	07/12/2021

Supervisor Confirmation

By signing the Statement of Authorship, you are certifying that the candidate made a substantial contribution to the publication, and that the description described above is accurate.

Supervisor name and title: Professor Thomas Povey		
Supervisor comments: I certify that the candidate made a substantial contribution to the publication, and that the description described above is accurate.		
Signature: 	Date	22/01/2022

This completed form should be included in the thesis, at the end of the relevant chapter.

4. Methodology for High-accuracy Infrared Calibration in Environments with Through-wall Heat Flux

This chapter consists of a preprint journal paper detailing the development of new instrumentation for accurate in situ IR calibration in environments with significant through-wall heat flux and surface temperature non-uniformity. The proposed sensor is particularly relevant for facilities performing overall cooling effectiveness measurements, but also for IR measurements on adiabatic surfaces with significant lateral temperature variations (e.g. film cooling effectiveness measurements). The nomenclature and references included in this chapter are self-contained and differ in numbering compared to the overall thesis.

METHODOLOGY FOR HIGH-ACCURACY INFRARED CALIBRATION IN ENVIRONMENTS WITH THROUGH-WALL HEAT FLUX

Mathias Michaud, Francesco Ornano, Nafiz H. K. Chowdhury and Thomas Povey

Department of Engineering Science, University of Oxford, Parks Road, Oxford, OX1 3PJ, UK

ABSTRACT

This paper describes a new method for accurate in situ infrared (IR) calibration in environments with significant through-wall heat flux and surface temperature non-uniformity. In the context of turbine research environments, conventional approaches for in situ IR calibrations rely on thermocouples embedded in the surface or bonded to the surface using an adhesive layer. A review of the literature points to lack of emphasis on the uncertainty in the calibration arising from the effect of the adhesive substrate and paint on the temperature measured by the thermocouple, namely that under diabatic conditions (i.e. with through-wall heat flux) the measured temperature deviates from the true surface temperature.

We present a systematic study of the sensitivity of the thermocouple temperature to installation conditions seen in typical laboratory IR calibration arrangements, and under realistic conditions of through-wall heat flux. A new technique is proposed that improves the calibration accuracy by reducing the difference between the thermocouple measurement and the external wall temperature seen by the infrared camera. The new technique has the additional advantage of reducing the uncertainty associated with selecting an appropriate pixel in the IR image, by providing a region with greater temperature uniformity especially in environments with significant underlying lateral surface temperature variation. The new approach is experimentally demonstrated and compared to more conventional measurement techniques on a heavily film-cooled nozzle guide vane assembly operated at highly engine-representative conditions. The proposed technique is demonstrated to significantly improve the measurement accuracy for IR in situ calibrations in environment with through-wall heat flux and surface temperature non-uniformity.

INTRODUCTION

As the spatial resolution and internal calibration stability of IR cameras has improved, they have become more popular as research instruments in the gas turbine heat transfer community. It is common practice to calibrate the camera (IR radiometric value) against a region of known temperature (typically by thermocouple measurement) in the field of view (FOV) of the camera. The in situ calibration, whilst typically having the disadvantage of less accurate surface temperature measurement (thermocouple instead of RTD, as it would be common in dedicated calibration instruments), has the significant advantage of directly accounting for poorly characterized target surface emissivity, angle variation and transmissivity of elements in the optical path (windows in pressure vessels typically being the most significant). This is the prime reason for it being the most common method for target surface temperature evaluation (over methods involving separate out-of-experiment calibrations, and associated correction methods). Typical methods for instrumenting the target surface include embedding a thermocouple in the surface, or adhering it to the surface by means of an adhesive layer. Data is acquired simultaneously from both the IR camera and the thermocouple at a fixed location in space (i.e. fixed pixel location for the IR camera), resulting in a direct calibration for the target surface. Any thermal resistance (an adhesive layer, for example) between the thermocouple and the target surface will lead to a measurement error by the thermocouple in situations where there is through-wall heat flux. The presence of an adhesive layer will also cause a lateral temperature disturbance locally near the thermocouple junction. This complicates the formation of an accurate calibration curve, because of the high sensitivity to the selection of the thermocouple junction location (often just a few pixels wide) in a region of high lateral temperature variation. Additional uncertainty in the calibration chain can arise if an adhesive layer forms on the outer face of the thermocouple during its installation, due to the thermal resistance between the thermocouple junction and the surface being visualized. Indeed, a similar effect is often deliberately introduced in the form of a thin paint layer, in an effort to render the entire surface of uniform emissivity.

Literature relating to practice for IR calibration experiments

In the case of highly non-uniform wall heat transfer and surface temperature gradients (typical of, for instance, film cooling environments), high spatial resolution is required to fully characterize the complex thermal field. IR thermography is a perfect candidate for this type of applications as it offers both high spatial and thermal resolution. The accuracy of quantitative IR measurements relies on calibration experiments performed to correlate the radiometric signal from the camera to a known temperature. In turbine research environments (namely, represented by wind tunnels operating at either low- or high-speed conditions, with surface temperature variations), bespoke in situ experiments are required to calibrate the IR camera at the nominal test conditions. In situ tests are performed to correct for poorly characterized target surface emissivity, view angle variation, and transmissivity of elements in the optical path.

It is common practice when carrying out in situ calibration tests to compare the radiometric data to a thermocouple temperature at the thermocouple location in the IR image. A number of thermocouples are therefore embedded or bonded to the surface with an adhesive layer, and the temperature measured by the thermocouples used for

calibration should cover the complete temperature range of interest.

Martiny et al. [1] presented an in situ calibration technique for quantitative infrared measurements. The raw detector signal from the infrared camera was compared to the temperatures measured with thermocouples. The function between raw detector value and object temperature was cast in the form of the Plank equation. The latter included three parameters, which were used for a best-fit approximation. The resulting non-linear system of equations was solved numerically and the calculated parameters were used to estimate the corrected temperature of the body.

Schulz [2] presented a quantitative infrared approach applied to film cooling research. Their work described the theoretical aspects and methods related to in situ calibrations. Examples of film cooling investigations using infrared thermography were also presented. In their experiments, a number of thermocouples were embedded in the surface and used to directly calibrate the radiometric signal from a single IR camera.

Ochs et al. [3] proposed a technique to overcome the issue related to thermocouples being located in regions of high surface temperature gradients. The technique allows for data extrapolation with improved accuracy when calibrating the radiometric data to the thermocouple temperature. The approach was based on the determination of three of four calibration parameters by a pre-calibration run and a subsequent in situ calibration to estimate the value of the fourth parameter. They claimed that fewer thermocouples were necessary for the in situ calibration, and that thermocouples did not have to cover the entire temperature operating range (making therefore possible to discard the thermocouples located in regions of high temperature gradients). The method was applied to the thermal investigation of transonic trailing edge cooling and film cooling of a flat plate.

Despite the conspicuous number of papers on the application of IR thermography on film cooling research, we can find no mention of the effect of the calibration arrangement on the accuracy of surface temperature measurements. As it will be shown later, there is a strong sensitivity of the primary sources of error in the calibration to variations in the parameters involved in the measurement setup. In fact, various parameters such as adhesive/paint thickness and thermal conductivity substantially affect the temperature measured by the thermocouple and therefore can lead to increased overall uncertainty in the calibration process.

This paper presents a parametric study on the influence of the measurement layout on the temperature measured by the thermocouple. The influence of a number of physical parameters is assessed in the context of their effect on the difference between thermocouple temperature measurement used for calibration and the temperature of the surface seen by the IR camera. A new instrumentation methodology is proposed which has significant advantages over more conventional methods, in that it mitigates the primary sources of error. The method offers a low thermocouple measurement error in the presence of through-wall heat flux and a high accuracy in localizing the reference thermocouple in regions of high surface temperature gradients. In the proposed layout, a low conductivity substrate is implemented to locally minimize the through-wall heat flux, and a high thermal conductivity layer is bonded to a thermocouple by means of thermally conductive paste. The high conductivity layer is designed to operate at low values of the Biot number, namely that uniform spatial temperature is reached during the test. An area including several pixels at uniform temperature is therefore available in the IR image, leading to substantially reduced error when calibrating the radiometric signal to the true wall temperature measured by the thermocouple.

It is hoped that results from this paper will be useful to researchers to understand the influence of the physical parameters involved in the calibration experiments, and to quantify the systematic primary error introduced by the system layout in the surface temperature measurement.

ASSESSMENT OF ERRORS ASSOCIATED WITH CONVENTIONAL MEASUREMENT SYSTEMS

We now consider typical errors in the most common thermocouple temperature measurement and calibration systems. This discussion is progressed under two headings: sensitivity of surface temperature measurement to adhesive and paint layers; and sensitivity of surface temperature measurement to pixel selection in regions of high temperature gradient.

Sensitivity of surface temperature measurement to adhesive and paints layers

In this section, we assess the sensitivity of the surface temperature measurement to the structure of the surface measurement system. In particular, we consider the effect of adhesive and paint layers on the on the temperature measured by the thermocouple. We use a one-dimensional steady-state heat transfer model to consider the impact of thermal conductivities and thickness of such layers in a number of common surface measurement systems.

Figure 1 shows three conventional surface measurement systems used for in-situ IR calibration. We refer to these as *reference systems* 1 to 3. The systems are: (1) thermocouple over adhesive; (2) over-painted thermocouple over adhesive; (3) thermocouple between adhesive layers. Reference system 1 is representative of a typical foil thermocouple (used to minimise surface aero-thermal disruption) adhered directly to a surface. Reference system 2 is a modified version of system 1, in which the foil thermocouple is additionally over-painted to render the surface of uniform emissivity. Reference system 3 represents a foil thermocouple that is adhered between adhesive layers (sometimes used either for robustness, or arising due to unintentional over-coating with glue when adhering with resin-based glue).

In the analysis of these systems, the wall is subject to a (hot) external flow at total temperature $T_{0,\mathrm{ext}}$ with heat transfer coefficient h_{ext}. The internal surface is subject to a flow of total temperature $T_{0,\mathrm{int}}$ with heat transfer coefficient h_{int}. The particular boundary conditions are summarised in Table 1, and are representative of typical laboratory turbine testing conditions with Reynolds and Mach numbers matched to engine conditions, but with temperature ratio

$T_{0,\text{ext}}/T_{0.\text{int}}$ lower than the engine situation (nominal temperature ratio). The wall properties are summarised in Table 2, and correspond to those of Inconel, which is a common material for high-pressure turbine components.

In the analysis of these systems, we differentiate between three types of measurement error: (1) error between the thermocouple measurement and the surface temperature directly above the thermocouple junction; (2) error between the thermocouple measurement and the surface temperature near the thermocouple junction; (3) the error between the thermocouple measurement and the *true undisturbed* wall temperature (without the presence of the thermocouple, or any associated surface treatment, for example thin over paint layers). Errors of type 1 are the direct error arising in the calibration process when selecting a pixel directly above the thermocouple junction to compare against the thermocouple data. This error is intrinsic in all calibration processes and is difficult to remove. Errors of type 2 arise when there is lateral surface temperature variation, when either the selected pixel in the IR image is not the one directly above the thermocouple junction, or where there is a requirement to average a region in the vicinity of the thermocouple. Errors of type 3 (between the thermocouple measurement and the true undisturbed wall temperature) are most relevant for thermal analysis of a particular component, when the effect of all instrumentation (including thin paint layers) must be accounted for.

These errors, presented in a form normalised by the total temperature difference between the streams, are defined by equations 1 to 3. The temperatures used in these definitions (except for the true undisturbed wall temperature) are defined in Figure 2. In this paper we are concerned with measurement errors of type 1 and 2 (β_1 and β_2), which lead directly to uncertainty in the IR surface calibration (IR radiometric value for a given measured wall temperature). Where the wall treatment (over-paint layer) is known, error type 3 (β_3) is relatively easy to deal with in back-analysis of a test part.

Table 1: Wall boundary conditions.

Boundary condition	Symbol	Value
External HTC	h_{ext}	1500 W m^{-2} K^{-1}
Internal HTC	h_{int}	2000 W m^{-2} K^{-1}
External flow total temperature	$T_{0,\text{ext}}$	350 K
Internal flow total temperature	$T_{0,\text{int}}$	293 K

Table 2: Wall thermal properties.

Property	Symbol	Value
Wall thickness	t_{w}	1.50 mm
Wall conductivity	k_{w}	11.7 W m^{-1} K^{-1}

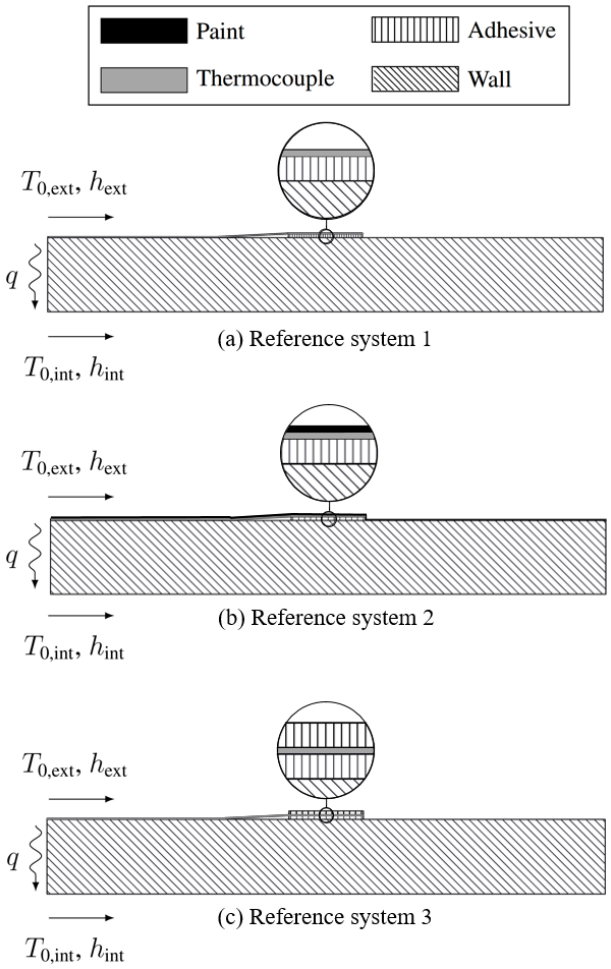


Figure 1: Diagrams of the reference systems (scale 4.5:1): (a) thermocouple over adhesive; (b) over-painted thermocouple over adhesive; (c) thermocouple between adhesive layers.

$$\beta_1 = \frac{T_{\text{w,measured by TC}} - T_{\text{w,over TC}}}{T_{0,\text{ext}} - T_{0,\text{int}}} \quad (1)$$

$$\beta_2 = \frac{T_{\text{w,measured by TC}} - T_{\text{w,next to TC}}}{T_{0,\text{ext}} - T_{0,\text{int}}} \quad (2)$$

$$\beta_3 = \frac{T_{\text{w,measured by TC}} - T_{\text{w,true}}}{T_{0,\text{ext}} - T_{0,\text{int}}} \quad (3)$$

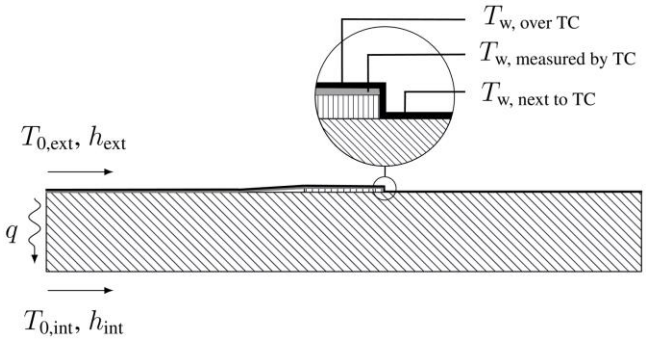


Figure 2: Diagram of gauge structure showing definitions of the temperature measurements.

Reference system 1: thermocouple over adhesive

Since the thermocouple junction in reference system 1 (Figure 1a) is exposed (not covered by paint or adhesive), the measured temperature by the thermocouple is the same as the temperature directly above the thermocouple junction. Therefore, reference system 1 is not affected by errors of type 1; i.e. β_1 is zero. We note for completeness, however, that systems of this type are rarely seen in practice, due to extreme variation in the surface emissivity when the over-paint layer of reference system 2 is omitted (most test surfaces have emissivity close to unity, but untreated foil thermocouples are highly reflective with an emissivity closer to zero).

In the presence of through-wall heat flux, the adhesive layer underneath the thermocouple causes errors of type 2 (β_2). This error becomes relevant in almost all practical situations (see later example) where it is necessary to average a number of pixels in the vicinity of the thermocouple because of the difficulty of identifying the thermocouple junction in regions of high surface temperature gradient.

Figure 3 presents β_2 as a function of the adhesive thermal conductivity and thickness underneath the thermocouple for reference system 1. It is worth nothing that only a fraction of this error that is passed into the final calibration uncertainty, but in many practical situations this fraction may either be high, or at the very least difficult to assess. The discussion is taken up in an example later in this paper.

A foil thermocouple with a standard epoxy bonding layer would typically have an adhesive layer thickness of 40.0–80.0 μm. Although epoxy adhesives offer a high bonding strength, typical thermal conductivities of these adhesives are very low: typically in the range 0.100–0.200 W m^{-1} K^{-1} [4]. This range of values is marked in the figure as (a). For the through-wall heat flux conditions considered (Table 1), the error for the worst-case estimated values of thermal conductivity and layer thickness can be up to 20.0 % of the total temperature difference between the streams. Even at the best-case end of the estimated range errors of 7.0 % are likely. It is clear that using instrumentation systems of this type it is necessary to be extremely careful with installation effects. Even so, using such systems for high-accuracy calibration systems would appear to be a risky proposition.

An alternative option would be to use a thermally conductive epoxy, which has a thermal conductivity in the range 1.00–2.00 W m^{-1} K^{-1}. This situation is marked as (b) in the figure. Even for thermally conductive epoxy, the estimated range of errors is between 0.80 and 3.00 % of the total temperature difference between the streams. Although the use of high conductivity epoxy partially mitigates the errors arising in high through-wall heat flux situations, errors can still be high in the context of high accuracy calibration requirements.

An improved option might be to use a high thermal conductivity (and low electrical conductivity) adhesive. Such adhesives would typically also have a bonding layer thickness in the range 40.0–80.0 μm, with a thermal conductivity in the range 3.50–5.00 W m^{-1} K^{-1}. This range of values is marked in the figure as (c). For best-case estimated values of thermal conductivity and layer thickness, the error is estimated to be at least 0.30 % of the total temperature difference between the streams. The measurement error can be up to 0.90 % for the worst case. However, the typical tensile strength of high thermal conductivity adhesives is considerably lower than standard epoxy resins (1.00–2.00 MPa, versus more than 20.0 MPa for more common epoxy resins) and this is a serious consideration in high-speed flow environments.

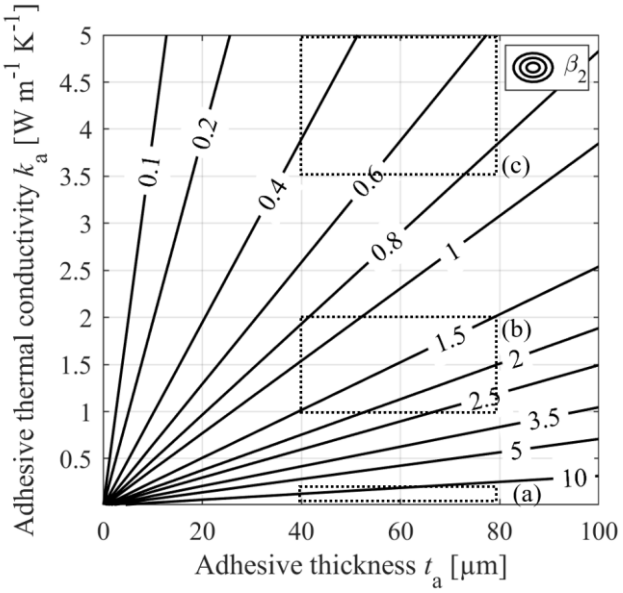


Figure 3: Analysis of reference system 1, showing β_2 (in %) as a function of adhesive thickness and conductivity.

Reference system 2: over-painted thermocouple over adhesive

It is a common practice in IR thermography to spray a thin layer of paint over the entire target surface (including the reference thermocouple) to render the surface of uniform emissivity. This situation is shown in Figure 1b. In the presence of through-wall heat flux, the over-paint layer acts as an additional thermal resistance, and raises (for higher mainstream gas temperature) the surface temperature (visualised by the IR camera) with respect to the thermocouple measurement. This leads to errors of type 1. The effect is rather different to that of underside adhesive, which raises both the thermocouple temperature and the wall temperature above it, leading to errors of type 2 where pixels near to, but not directly above the thermocouple are considered as part of the calibration process. Because nearby

pixels (not over the adhesive layer on which the thermocouple is mounted) would tend to register lower temperature in an IR image, the type 2 error is generally of opposite sign to the type 1 error.

Matt black acrylic paint is commonly used in IR thermography, and has a thermal conductivity in the range 0.500–1.50 W m^{-1} K^{-1} [5]. With well-controlled spraying, a layer thickness as low as 10.0 μm is possible. Figure 4 presents errors of type 1 and 2 (β_1 and β_2) as a function of the paint thermal conductivity and layer thickness for an adhesive with 40.0 μm thickness and thermal conductivity of 5.00 W m^{-1} K^{-1}. This adhesive layer represents the thinnest possible layer of high thermal conductivity adhesive estimated for reference system 1, corresponding to the lowest possible estimated values of β_1 and β_2 (0.00 and 0.30 % respectively). These errors are the starting point for our current calculation, and we recall the effects lead to errors with opposite sign.

Figure 4 shows type 1 and type 2 errors, β_1 and β_2, as a function of paint thickness and conductivity. So far as type 1 errors are concerned, in the presence of through-wall heat flux the temperature difference between the thermocouple and the surface directly above it increases with increasing paint thickness and with decreasing paint thermal conductivity, leading to an increase in the absolute magnitude of the error. The effect is due to the increase in wall resistance between the thermocouple junction and the surface being visualised. So far as type 2 errors are concerned, the effect is broadly similar in nature and magnitude to the type 1 error, but non-linearity in the additive effect of the wall resistances leads to slightly different trends. We observe that for the nominal paint thickness of 10.0 μm at the best-case estimated value of paint thermal conductivity, β_1 and β_2 are respectively −0.50 and −0.20 %. As for the worst-case estimate of the paint thermal conductivity, β_1 and β_2 are respectively −1.50 and −1.20 %. This demonstrates that adding paint over a reference measurement system (almost universal in practice, for reasons discussed above) can lead to significant errors. The direct calibration errors (β_1) in particular can be extremely difficult to remove.

Reference system 3: thermocouple between adhesive layers

During the thermocouple installation a layer of adhesive can form over the thermocouple junction, adding further thermal resistance. Figure 5 and Figure 6 show the contours of β_1 and β_2, respectively, as a function of the thickness and thermal conductivity of the adhesive *over* the thermocouple, for the case of a 50.0 μm thick layer of the same adhesive underneath the thermocouple.

Adhesive over the thermocouple has the effect of introducing error between the local (directly above the thermocouple) external wall temperature and the thermocouple temperature, and is a cause of β_1 error. Adhesive under the thermocouple is unimportant so far as β_1 error is concerned, but is a source of β_2 error.

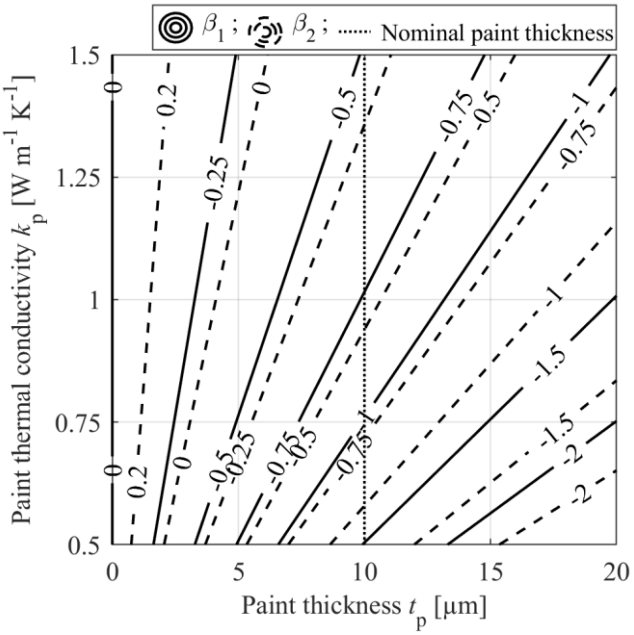


Figure 4: Analysis of reference system 2, showing β_1 and β_2 (in %) as a function of paint thickness and conductivity, for an adhesive layer with thickness 40.0 μm and thermal conductivity 5.00 W m^{-1} K^{-1}.

So far as β_2 errors are concerned, in the presence of through-wall heat flux, adhesive under the thermocouple tends to drive up the thermocouple temperature with respect to a point unaffected by the adhesive next to the thermocouple. Adhesive over the thermocouple tends to drive the thermocouple temperature down with respect to a nearby region of wall. The effects are therefore in an interesting competition, and can potentially cancel each other out.

A typical adhesive layer thickness over the thermocouple can be up to 20.0 μm. For standard epoxy adhesives (region marked as (a) in Figure 5), the direct calibration error β_1 can be as large as −10.00 % for the worst-case estimated thermal conductivity and thickness of the adhesive layer over the thermocouple. For thermally conductive epoxy (marked as (b) in Figure 5), β_1 can be as large as −1.50 % as a worst case. As for high thermal conductivity adhesive (marked as (c) in Figure 5), β_1 can reach −0.45 % for the worst case. It is clear that during thermocouple installation it is necessary to avoid the migration of adhesive over the thermocouple junction, or significant direct errors in the calibration can arise.

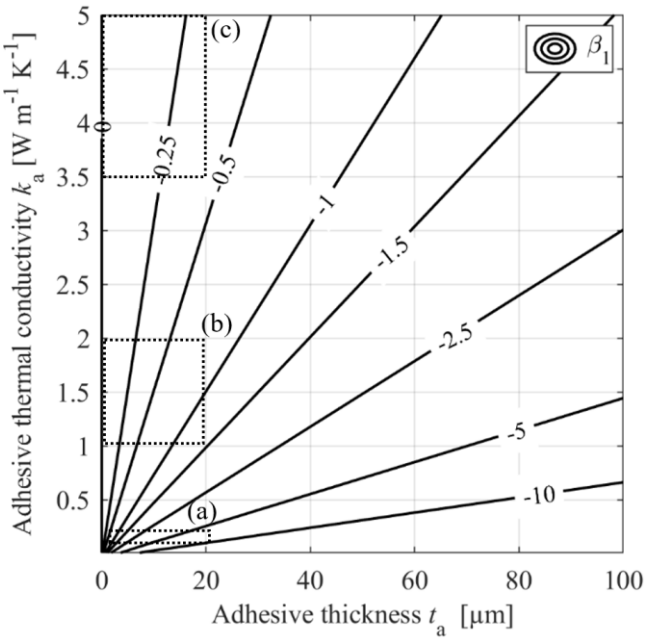


Figure 5: Analysis of reference system 3, showing β_1 as a function of adhesive thickness and conductivity over the thermocouple, for fixed adhesive layer thickness of 50.0 µm under the thermocouple.

Concerning β_2, the smallest error encountered with standard epoxy (region marked as (a) in Figure 6) is 5.00 % for the best-case estimated thermal conductivity and thickness of the adhesive layer over the thermocouple. For thermally conductive epoxy (marked as (b) in Figure 6), β_2 can be as small as 0.64 % as a best case. As for high thermal conductivity adhesive (marked as (c) in Figure 6), β_2 can reach 0.25 % for the best case. For a given adhesive thermal conductivity, the worst-case scenario corresponds to having no adhesive over the thermocouple (i.e. reference system 1 with the same adhesive layer thickness underneath the thermocouple). This shows that having a layer of adhesive over the thermocouple thinner than the layer underneath is beneficial as far as β_2 is concerned (error reduced compared to reference system 1). However, this is very hard to achieve in practice as it is very difficult to control the thicknesses of both layers adhesives.

We numerically assessed the dependency of the thermocouple temperature on the measurement layout and physical properties of the adhesive used. We observed that the measurement error strongly depends on the location, thickness and thermal conductivity of the adhesive layer in the presence of through-wall heat flux. In practice, poorly characterized adhesive/paint thermal properties and thicknesses could lead to significantly large measurement errors and increased overall calibration uncertainty.

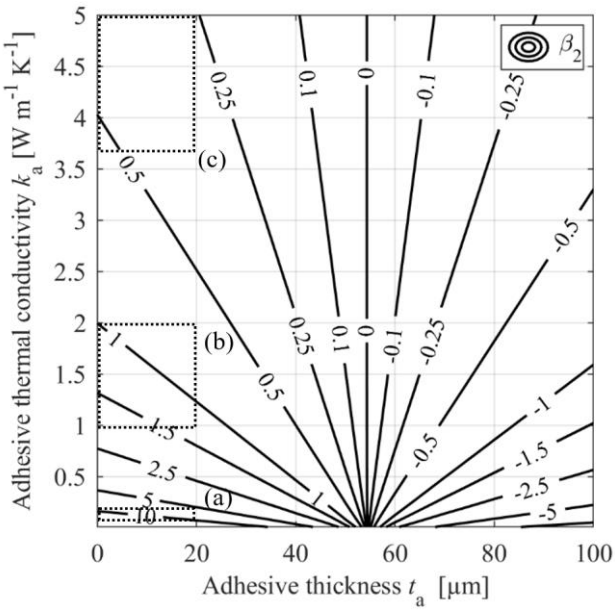


Figure 6: Analysis of reference system 3, showing β_2 as a function of adhesive thickness and conductivity over the thermocouple, for fixed adhesive layer thickness of 50.0 µm under the thermocouple.

Sensitivity of surface temperature measurement to pixel selection in regions of high temperature gradient

To calibrate IR camera output to a measured wall temperature, radiometric values are recorded against thermocouple readings. In this process it is required that the thermocouple reading is as representative as possible of the local surface temperature. If the region of the thermocouple is sufficiently isothermal, the temperature directly above the thermocouple location can be taken. Errors for this situation have been discussed. Where the surface is non-isothermal—on account of disruption by the thermocouple system for example—the error associated with region selection must also be considered. In this case, two errors must be considered: the error between the thermocouple and wall temperature directly above the thermocouple (β_1); the error between the thermocouple and the wall temperature local to but not directly above the thermocouple (β_2). These errors have been considered separately in the preceding sections.

When IR images are taken, it is typical to select a region of several pixels around the thermocouple junction location to establish an area-averaged radiometric value on the target surface. Moderate lateral temperature gradients are possible because of the nature of the components being studied, as shown, for example in the results of Kirollos et al. [6], which are reproduced in Figure 7. The figure shows a nozzle guide vane non-dimensional surface temperature presented as overall cooling effectiveness θ (the complete definition of θ is described in [6]). The part was fully cooled (both external film and internal convective cooling) and was operated at conditions non-dimensionally representative of an engine. In these demonstration measurements, a thin foil K-type thermocouple was used (indicated in Figure 7) to calibrate IR data. The thermocouple installation scheme was like

reference system 2 (Figure 1b): over-painted thermocouple over adhesive.

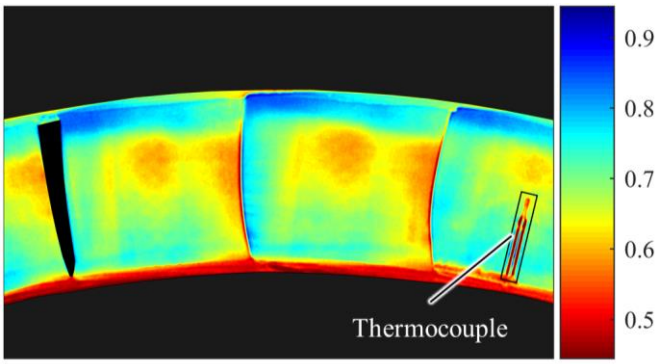


Figure 7: Example of overall cooling effectiveness (θ) measurements [6] on engine components, showing high lateral temperature variation.

The thermocouple wires are visible in Figure 7 because of the change in surface temperature due to the variation in thermal resistance with respect to the undisturbed surface. This primarily results from a thin layer of epoxy under the leads.

A detail view of the results of Figure 7 is presented in Figure 8a in terms of normalised temperature ϕ in the vicinity of the thermocouple. Here ϕ is defined by

$$\phi = \frac{T_{0,\text{ext}} - T_{\text{w,bb}}}{T_{0,\text{ext}} - T_{0,\text{int}}} \tag{4}$$

where $T_{\text{w,bb}}$ is the equivalent black body temperature of the target surface recorded by the IR camera, and $T_{0,\text{ext}}$ and $T_{0,\text{int}}$ are the mainstream total temperatures respectively (defined at vane inlet and the vane coolant plenum inlet).

It is clear that the moderate lateral temperature gradients on the vane surface are compounded by high temperature gradients local to the thermocouple, caused by the disturbance of the thermocouple construction.

This is emphasized by Figure 8b, which shows the lateral distribution of normalised temperature along the line AA' through the thermocouple junction. Individual points represent single pixels in the IR image. Significant lateral temperature variation is apparent. This situation is very common even with the most careful instrumentation scheme. In this example it is clear that two sources of error must be considered. To reiterate: we must consider the error between the thermocouple measurement and wall temperature directly above the thermocouple junction β_1 (directly relevant to the calibration error); we must consider the error between the thermocouple measurement and the wall temperature local to but not directly above the thermocouple junction β_2 on account of the averaging/region-selection problem that this example exemplifies. These sources of error can be identified in Figure 8b. Firstly, we observe that the thermocouple junction takes a low value of the non-dimensional temperature compared to the region in the vicinity (ϕ = 0.64). In fact, the structure of the thermocouple determines a change in temperature (due to flow disruption and change in thermal resistance due to adhesive underneath). Secondly, there is a significant lateral temperature variation in the region around the thermocouple (Figure 8a). This primarily affects the error β_2. The effect is visible in Figure 8b, where the lateral temperature distribution along line AA' passing through the thermocouple junction is plotted. The non-dimensional temperature ϕ takes a value of around 0.64 at the junction location and rapidly increases to the level corresponding to the undisturbed surface (ϕ = 0.69–0.71).

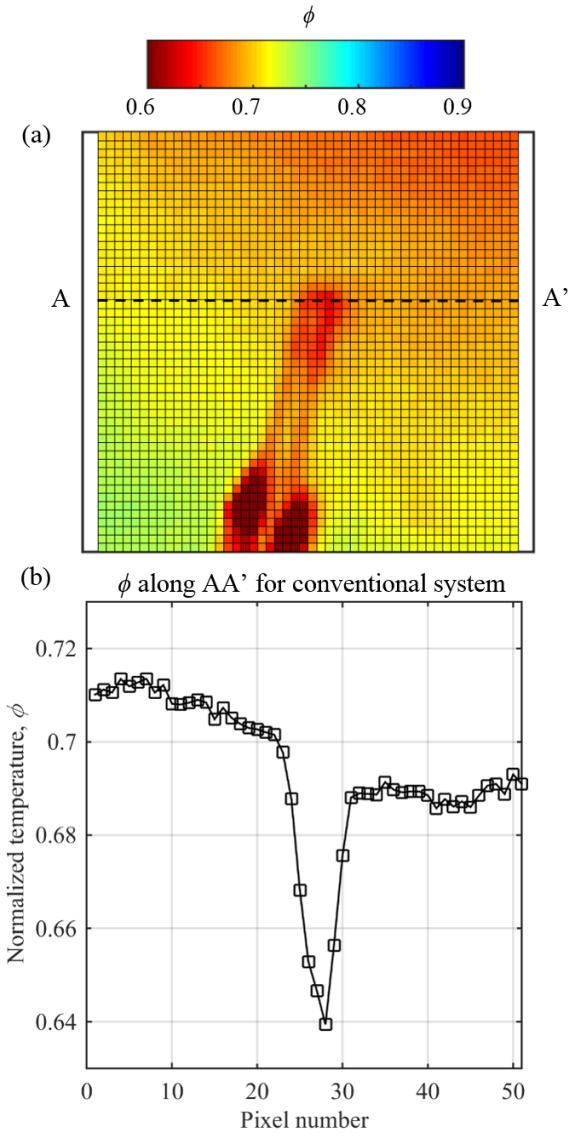


Figure 8: Conventional calibration system (reference system 2): (a) surface plot of ϕ over a 50-by-50 pixel area; (b) line-plot of ϕ (along AA') through the thermocouple junction.

PROPOSAL FOR AN IMPROVED MEASUREMENT SYSTEM

We now propose an improved measurement and calibration system (for in situ IR calibration) optimised to reduce measurement error in environments with significant through-wall heat flux and/or lateral temperature gradient. The proposed system is shown in cross-section in Figure 9. We refer to this as *reference system 4*.

In the assembly, a thin-foil K-type thermocouple is bonded between a disk of copper (high thermal conductivity) and a polyimide film (low thermal conductivity). The thermocouple is in direct contact with the bottom face of the copper disk and a layer of thermal paste is applied under the thermocouple and on its sides to adhere it to the copper disk. The copper disk is held in place using an epoxy adhesive and the whole assembly is installed at the trailing edge of the vane—a region of low surface curvature—and is arranged flush with the surface to minimize boundary layer disruption. A layer of matt black paint is applied over the calibration and the target surfaces to render them of uniform and equal emissivity. Figure 10 is a photograph (plan view) of the system assembled on the suction side of a high-pressure nozzle guide vane before over-painting. The cavity into which the assembly was assembled was machined using a 6 mm diameter flat-bottom cutter to a depth of 0.7 mm. The copper disk is 4 mm in diameter and is 0.5 mm thick. The disk geometry can be scaled to suit the application. In situations where wall thickness is limiting, where there are high lateral gradients of mainstream gas temperature, and where the surface area of the sensor cannot be sufficiently reduced (on account of the field of view and minimum desired pixel count on the sensor) to ensure a sensor aspect ratio that gives approximately isothermal conditions, a practicable sensor mounted on the surface of interest may not be sufficiently isothermal to meet the requirements of the calibration. In this unusual combination of circumstances, the sensor can be moved off the surface of interest, to another location within the field of view. Table 3 lists the thickness and thermal conductivity of each element in the assembly.

The proposed measurement system offers several advantages over conventional approaches, specifically:

(1) the low thermal conductivity of the polyimide layer reduces the through-wall heat flux, and in combination with the copper layer, reduces the temperature difference between the thermocouple junction and external surface. This reduces the error between the thermocouple and the wall temperature directly above the thermocouple (β_1).

(2) we create a region in the IR camera field of view which is both larger and more isothermal than is typically provided on the target surface with a conventional application of the thermocouple, thus reducing errors associated with thermocouple localized in regions with high temperature variation (β_2). In this arrangement the error between the thermocouple and the wall temperature local to but not directly above the thermocouple junction is no longer relevant, because we thermally isolate the calibration patch from the local environment.

(3) the thermocouple junction is protected from the testing environment, allowing the measurement system to be used in high-speed flows.

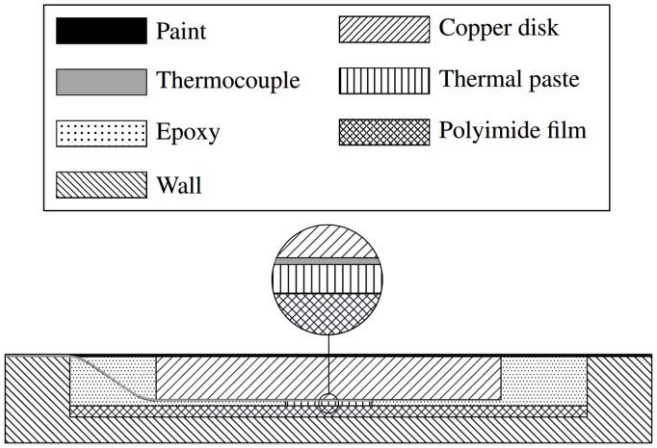


Figure 9: Cross-section of the *proposed* measurement system (scale 4.5:1)*:* reference system 4.

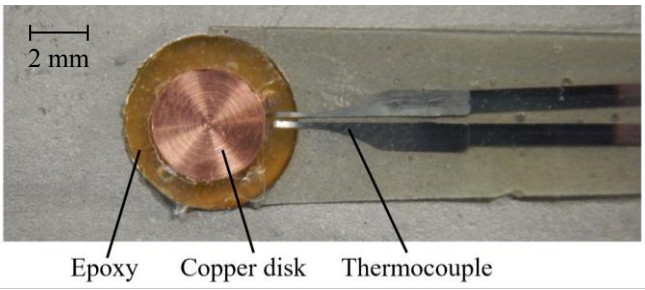


Figure 10: Photograph of the *proposed* measurement system without paint.

Table 3: Properties of the elements in the assembly.

Element	Nominal thickness	Thermal conductivity
Paint	10.0 μm	0.500–1.50 W m^{-1} K^{-1}
Copper disk	500 μm	386 W m^{-1} K^{-1}
Thermocouple	12.3 μm	11.3 W m^{-1} K^{-1}
Thermal paste	63.7 μm	3.40 W m^{-1} K^{-1}
Polyimide film	124 μm	0.120 W m^{-1} K^{-1}

DEMONSTRATION OF THE PROPOSED MEASUREMENT SYSTEM

In this section, we demonstrate how the proposed measurement system (reference system 4) provides a large isothermal region in the FOV of the IR camera, while maintaining a low measurement error of type 1 (β_1) and completely removing error of type 2 (β_2).

To assess the errors in reference system 4, we created a one-dimensional steady-state heat transfer model of the system shown in Figure 9. The main source of error in the assembly of reference system 4 is the low thermal conductivity of the matt black paint layer applied over the copper disk, which has a range 0.500–1.50 W m^{-1} K^{-1} [5]. Figure 11 presents the contours of β_1, here defined as the error between the thermocouple measurement and the temperature of the painted external surface of the copper

disk, as a function of the paint thermal conductivity and the thickness of its layer.

For a nominal paint layer thickness of 10.0 μm and the best-case estimated value of paint thermal conductivity, β_1 is at least 0.32 % of the total temperature difference between the streams. As for the worst-case estimated value of paint thermal conductivity, β_1 remains below 0.85 %. With reference system 4 we achieve $0.32 < \beta_1 < 0.85$ %: a significant improvement over system 2, which achieves $0.50 < \beta_1 < 1.50$ %. This improvement is due to the additional thermal resistance of the (124 μm) polyimide film, which is sufficient to reduce the through wall heat flux in our application by 47 %. This, in turn, reduces the temperature difference between the thermocouple measurement location and the external surface temperature seen by the IR camera. As for constructions of the type of reference system 4, β_2 errors are negligible because the calibration element (copper disk) is approximately isothermal.

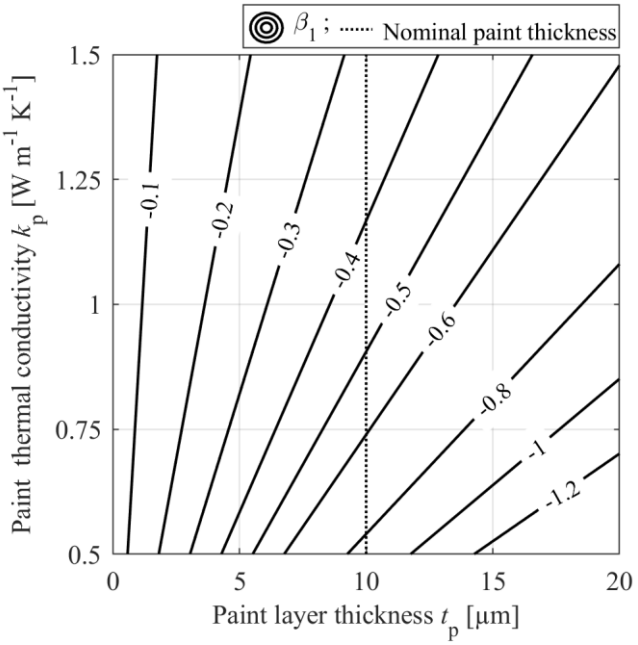


Figure 11: Analysis of reference system 4, showing difference between measured and true external surface temperature as a function of paint thickness and conductivity.

Figure 12 shows the experimental results from reference system 4 in terms of normalised temperature ϕ distribution around the exposed copper disk. It is worth mentioning that the absolute levels of ϕ differ from Figure 8a because the test were carried on different vanes. However, both measurement systems were approximately at the same location on the vane suction side. Improvements associated to the new system are observed in Figure 12a, where a uniform distribution of normalised temperature is attained on the copper disk. This is emphasized by Figure 12b, which shows the lateral distribution of normalised temperature along the line AA' through the copper disk. A circular region with a diameter of approximately 12 pixels (corresponding to the diameter of the copper disk) is found to perform with substantially uniform normalised temperature (ϕ = approximately 0.715). This arrangement, therefore, allows reducing the sensitivity to the pixel selection or averaging region, even in the case of uncertainty in the location of the thermocouple junction.

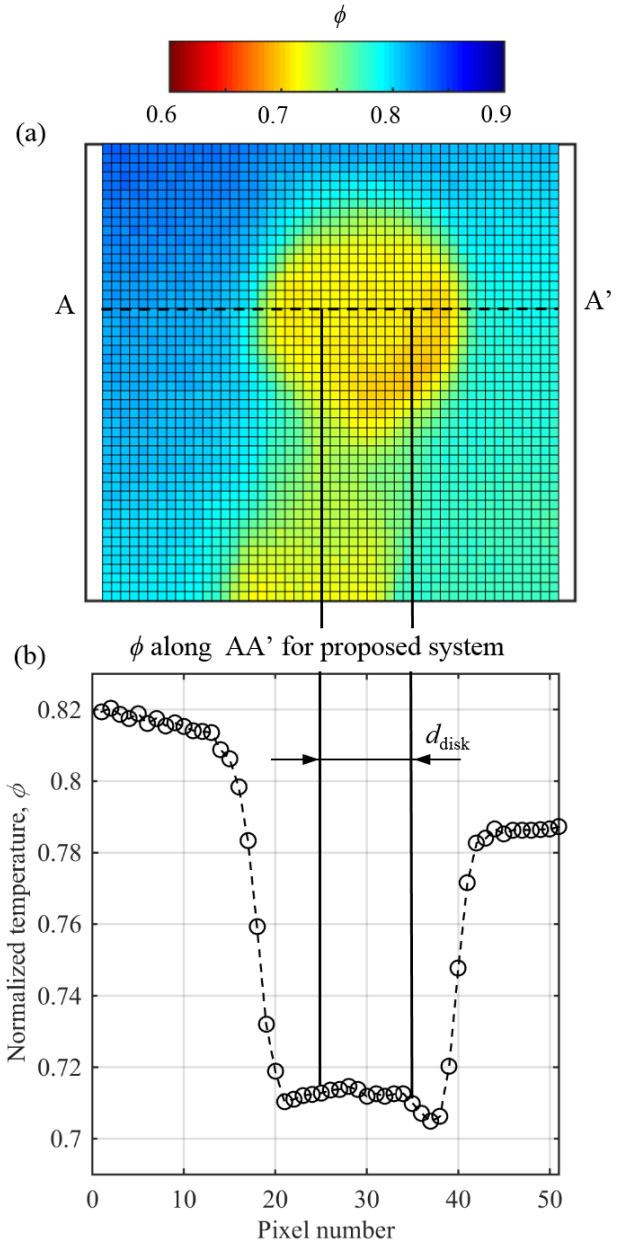


Figure 12: Proposed calibration system (reference system 4, see Figure 7): (a) surface plot of ϕ area; (b) line-plot of ϕ (along AA') through the thermocouple junction over a 50-by-50 pixel.

CONCLUSIONS

In this paper, we present a systematic study of the sensitivity of two types of measurement errors (β_1 and β_2) to installation conditions seen in typical laboratory IR calibration arrangements, and under realistic conditions of through-wall heat flux. We assess the errors arising from a number of typical in situ IR calibration arrangements by quantifying their sensitivities to the location, thickness and thermal conductivity of the adhesive used to bond the thermocouple to the surface. We define reference system 1 as

the case in which the thermocouple is only placed over an adhesive layer; reference system 2 in which the thermocouple is placed over an adhesive layer and over-painted with black paint; reference system 3 in which the thermocouple is in between two adhesive layers. An improved system (defined here as reference system 4) aimed to provide a large isothermal region the IR camera FOV, while maintaining a low measurement errors, is also presented and described in detail.

Analysis of system 1 shows a wide range of β_2 error depending on adhesive thickness and thermal conductivity. Errors can be extremely high for common adhesives such as epoxy resin, and relatively low for thin layers of high thermal conductivity adhesives, but such adhesives have low bonding strengths and are not always suitable to adhere a thermocouple on a surface subjected to high-speed flows. It is also noted that system 1 is often impracticable because of the extreme variation in surface emissivity when an over-paint layer is omitted.

Analysis of system 2 shows that paint over the thermocouple increases β_1, and can increase or decrease β_2 depending on the thermal conductivity and thickness of the paint layer with respect to the adhesive layer.

Analysis of system 3 show that an adhesive layer over the thermocouple leads to increased β_1 errors, but that it can reduce β_2 errors. However, the latter is very difficult to achieve in practical applications, as in such thin layers precise thickness control is unrealistic.

Analysis of a proposed new system (system 4) shows that β_1 is primarily dependent on the paint layer thickness and thermal conductivity, and that for typical values of these two parameters encountered in practice, the β_1 can be rendered extremely low by adoption of the proposed scheme. It was also shown that system 4 provides a large isothermal region in the FOV of the IR camera, hence reducing the uncertainty associated with the pixel selection compared to conventional measurement system (system 1 to 3).

The work of this paper is developed in response to the lack of data presented in the literature on the effect of typical calibration arrangements on the errors arising in in-situ IR calibrations in environments with high through-wall heat flux and lateral temperature gradient. It is hoped that this paper will present a framework for quantifying such errors in typical calibration arrangements, and that by adoption of the proposed technique error in the calibration process might be substantially reduced.

ACKNOWLEDGMENTS

The support of Rolls-Royce plc is gratefully acknowledged. The authors would also like to acknowledge the technicians Trevor Godfrey, Gregory King and Dominic Harris for their help in the manufacture of the new measurement system.

NOMENCLATURE

Roman

d	Diameter
h	heat transfer coefficient
k	thermal conductivity
q	heat flux
t	thickness
T	temperature

Greek

β_1	normalised measurement error of type 1
β_2	normalised measurement error of type 2
β_3	normalised measurement error of type 3
ϕ	normalised wall temperature
θ	overall cooling effectiveness

Subscripts

a	adhesive
bb	black body
ext	external side
int	internal side
p	paint
w	wall

Abbreviations

FOV	field of view
HTC	heat transfer coefficient
IR	infrared
RTD	resistance temperature detectors

REFERENCES

[1] Martiny, M., Schiele, R., Gritsch, A., Schulz, S. and Witting, S., 1996, "In Situ Calibration for Quantitative Infrared Thermography," QIRT'96 Eurotherm Seminar No. 50, Stuttgart, Germany.

[2] Schulz, A., 2000, "Infrared Thermography as Applied to Film Cooling of Gas Turbine Components," Measurement Science and Technology, 11(7), pp. 948–956.

[3] Ochs, M., Horbach, T., Schulz, A., Koch, R. and Bauer, H-J., 2009, "A Novel Calibration Method for an Infrared Thermography System Applied to Heat Transfer Experiments," Measurement Science and Technology, 20(7), pp. 075103–075112.

[4] Lee, H. and Neville, K., 1967, *Handbook of Epoxy Resins*, New York: McGraw Hill. ISBN 0070369976.

[5] Raghu, O. and Philip, J., 2006, "Thermal Properties of Paint Coatings on Different Backings using a Scanning Photo Acoustic Technique," Measurement Science and Technology, 17(11), pp. 2945–2949.

[6] Kirollos, B., Lubbock, R., Beard, P., Goenaga, F., Rawlinson, A., Janke, E. and Povey, T., 2017, "ECAT: an Engine Component Aerothermal Facility at the University of Oxford," ASME Turbo Expo 2017, Charlotte, USA, paper no. GT2017-64736.

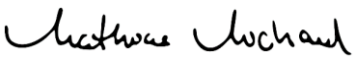
Statement of Authorship for joint/multi-authored papers for PGR thesis

To appear at the end of each thesis chapter submitted as an article/paper

The statement shall describe the candidate's and co-authors' independent research contributions in the thesis publications. For each publication there should exist a complete statement that is to be filled out and signed by the candidate and supervisor **(only required where there isn't already a statement of contribution within the paper itself).**

Title of Paper	Methodology for High-Accuracy Infrared Calibration in Environments with Through-Wall Heat Flux
Publication Status	■ Published □ Accepted for Publication □ Submitted for Publication □ Unpublished and unsubmitted work written in a manuscript style
Publication Details	Michaud, M., Ornano, F., Chowdhury, N. H. K. and Povey, T., 2019, "Methodology for High-Accuracy Infrared Calibration in Environments with Through-Wall Heat Flux," Journal of the Global Power and Propulsion Society, 4, 1-13.

Student Confirmation

Student Name:	Mathias Michaud		
Contribution to the Paper	Mathias Michaud performed the heat transfer modelling, the uncertainty analysis, led the writing of the manuscript and contributed to the analysis. Francesco Ornano was in charge of the literature review and post-processing the infrared data. Nafiz Chowdhury contributed to the analysis. Thomas Povey provided the original research idea, contributed to the analysis and the writing of the manuscript.		
Signature 		Date	07/12/2021

Supervisor Confirmation

By signing the Statement of Authorship, you are certifying that the candidate made a substantial contribution to the publication, and that the description described above is accurate.

Supervisor name and title: Professor Thomas Povey		
Supervisor comments: I certify that the candidate made a substantial contribution to the publication, and that the description described above is accurate		
Signature: 	Date	22/01/2022

This completed form should be included in the thesis, at the end of the relevant chapter.

5. Impact of In-service Deterioration on the Aerodynamic Performance of High-Pressure Nozzle Guide Vanes

This chapter consists of a preprint journal paper detailing the experimental study to evaluate the impact of in-service deterioration on the aerodynamic performance of heavily film-cooled HP NGVs. This chapter provides an example of aerodynamic research that can be performed in a high TRL research turbine facility. Although the overall impact of deterioration could reasonably be expected to be well-modelled by superposition of the individual deterioration effects, there is a lack of aerodynamic performance data when many deterioration effects are combined. The purpose of this work is to provide a reference point for whole-life aerothermal performance modelling. The nomenclature and references included in this chapter are self-contained and differ in numbering and order compared to the overall thesis.

EXPERIMENTAL STUDY OF IMPACT OF IN-SERVICE DETERIORATION ON AERODYNAMIC PERFORMANCE OF HIGH-PRESSURE NOZZLE GUIDE VANES

Mathias Michaud*, Dougal Jackson†, Frédéric Goenaga†, Thomas Povey*

*Department of Engineering Science, University of Oxford, Parks Road, Oxford, OX1 3PJ, UK
†Rolls-Royce plc, WH88, PO Box 3, Filton, BS34 7QE, United Kingdom

ABSTRACT

In this paper we experimentally evaluate the impact of in-service deterioration on the aerodynamic performance of heavily film-cooled high-pressure nozzle guide vanes from large civil jet engines. We study 15 mid-life to end-of-life parts removed from operational engines, and compare their performance to those of new parts. Deterioration features included: increased surface roughness; thermal barrier coating spallation; damaged film cooling holes; and trailing edge burn-back. We characterize and present statistics for the surface roughness. Aerodynamic measurements were performed in the high technology readiness level Engine Component AeroThermal (ECAT) facility at the University of Oxford, at engine-representative conditions of exit Mach number, exit Reynolds number, coolant-to-mainstream pressure ratio and turbulence intensity. We present detailed experimental measurements of the coolant capacity characteristics, downstream loss, and downstream flow structures. The results show that service time significantly increases the surface roughness of high pressure nozzle guide vanes, leads to reduced coolant flow capacity, increased overall aerodynamic loss, and greater downstream flow angle variation. This is one of the first significant studies of its type in the open literature, and is an important step towards whole-life engine performance assessment.

INTRODUCTION AND RELATED LITERATURE

High-pressure (HP) nozzle guide vanes (NGVs) deteriorate with service time due to (see, for example [1]) oxidation, deposition of airborne contaminants, thermal fatigue cracking (e.g., of the thermal barrier coat (TBC) layer) and erosion due to impact-abrasion [2]. These effects lead to both local changes in surface roughness, and global changes in geometry. Thermal barrier coating spallation and cracking is common, as is the partial collapse of cooling holes (smaller effective size), or the blockage or geometry change of holes due to particulate deposition. Eroded trailing edges (TE), or TE *burn-back* due to overheating are also common. These effects generally reduced the aero-thermal performance of the parts. The purpose of this paper is to perform accurate aerodynamic characterization of engine-run parts. We first review the literature related to the impact of surface roughness and TE damage on aerodynamic performance.

Impact of surface roughness

There have been several cascade experiments to assess the impact of surface roughness on the aerodynamics performance of turbine components. Most of these studies have used simple simulated roughness elements (sandgrains, hemispheres and truncated cones) [3–5] or surface finishes arising from manufacturing processes (e.g. machining processes, polishing processes and coating types) [6–11], with only one study (to the authors knowledge) attempting to simulate engine-representative roughened surfaces on an aerofoil [12]. A comprehensive review of literature (up to 2010) on effects due to roughness was provided by Bons [13]. As expected, the primary effects are earlier laminar-turbulent boundary layer transition, and an increased rate of thickening of the boundary layer (in both states), leading to higher aerodynamic loss. One exception is the case of low Reynolds number (Re) operation (low pressure turbines for instance) where an earlier roughness-induced transition has been shown to prevent a laminar separation on the suction surface (SS) of the aerofoil, leading to lower losses than a smooth (separated) aerofoil [10, 13, 14]. This general effect is—of course—well known.

We can differentiate between studies in which the surface roughness of the entire aerofoil is varied evenly to represent possible manufacturing routes [3, 4, 6–10], for example, metal printing techniques, and those in which the roughness on only part of the surface is varied [5, 11, 12]. These latter studies are more representative of in-service roughening which appears to preferentially affect the pressure surface (PS) and early SS.

Kind et al. [5] performed aerodynamic surveys 0.4 axial chords (C_{ax}) downstream of a low-speed linear cascade of turbine blades to study the impact of roughness on profile loss. The inlet Re_C (based on tangential chord) was 3.0×10^5. They tested 18 cascade configurations: one *smooth* cascade configuration in which the aerofoil surface (PS and SS) and endwalls are reported to be aerodynamically smooth (roughness height not reported) and 17 other configurations in which spanwise-oriented bands of roughness (application of sand grains) were introduced at different locations around the aerofoil. The roughness distribution most relevant to the current study was a roughened band covering approximately 30–100 % of the PS with the rest of the aerofoil being smooth. For this distribution, two sandgrain roughness heights (k) were used: $k/C = 4.5 \times 10^{-3}$ and 6.3×10^{-3}, where C is the tangential chord. They reported that at the design incidence angle the profile loss increased from the smooth configuration by approximately 30 % and 40 % for the two roughness heights, respectively.

Matsuda et al. [11] performed aerodynamic surveys 0.165 tangential chords downstream of a linear cascade of vanes to study the impact of aerofoil and endwall roughness on profile loss and *net secondary loss*. Net secondary loss was defined as the difference between the total pressure loss measured in the

secondary flow region, and the estimated profile loss (based on mid-span measurements). The exit Re_C (based on tangential chord) range was $0.30 \times 10^6 < Re_C < 1.0 \times 10^6$ and inlet turbulence intensity (Tu) was 0.43 %. They tested two configurations: a *smooth* cascade configuration in which the aerofoil surface (PS and SS) and endwalls had a normalised maximum peak-to-valley roughness height R_z/C of 5.2×10^{-5} (typical of a milled surface of a new steam turbine vane); and a *rough* cascade configuration in which the PS and endwalls had R_z/C equal to 84.0×10^{-5} (approximately 16 times larger than the smooth configuration, and typical of a shot blasted surface), and with the SS essentially unchanged from the smooth case with R_z/C equal to 6.0×10^{-5}. At $Re_C = 0.87 \times 10^6$, they found that the profile loss and net secondary loss for the rough configuration increased by approximately 36 % and 80 %, respectively, compared to the smooth configuration. The measured increase in loss was similar in magnitude to the study of Kind et al. [5], despite an almost order-of-magnitude difference in reported surface roughness height. This apparently surprising result may be explained by a combination of two factors: the peak-to-valley roughness height, R_z, and sandgrain roughness height, k, both fails to take account of shape and density of the roughness elements in the profile; the roughness types are different, one surface being artificially roughened (sand grains) and the other being the result of a manufacturing process. Differences in roughness type and quantification make the comparison between studies difficult.

Erickson et al. [12] studied the impact of in-service roughening on the aerodynamic performance of turbine vanes in a low-speed linear cascade over a wide range of Tu and Re. Because of the similarity of their study to the current experiment (in terms of roughness type, distribution, modelling method, height, and operating conditions of Re and Tu) we consider the Erickson et al. [12] study an important reference point. At the closest condition to our experiment an increase in midspan total pressure loss coefficient of 12 % was measured. We devote a later section of this paper to a more detailed comparison of our work and that of Erickson et al. [12]. The purpose is to allow detailed comparison of very similar studies, in the hope of cross-validation of the results, and in the hope of developing a benchmark loss-enhancement factor for typical engine geometries under engine realistic conditions. Comparison to existing correlations would be desirable, but is problematic, because, as demonstrated in the extensive review of Bons [13], variation in roughness type (simulated, manufacturing-related and service-related) appears to have a significant effect on the correlation, and therefore a single global correlation remains elusive. It may be the case that in the foreseeable future it is necessary to perform high-fidelity studies of the type presented in this paper, in the hope of direct rules-of-thumb for particular combinations of part-type and deterioration characteristic.

Impact of TE damage

We now review the literature on the impact of TE damage on the aerodynamic characteristics of turbine components. Sjolander et al. [15] studied the impact of a semi-circular cutout in the TE of a turbine blade (to simulate damage caused by burn-back or erosion) on loss and flow turning angle. Using a low-speed linear cascade, they did aerodynamic surveys downstream of an undamaged blade and two blades with a semi-circular cutout in their TE with diameters equivalent to 15 and 25 % of the blade tangential chord. Results showed that the wake downstream of the cutout was significantly modified, with local under-turning of the flow (up to 4.2° yaw angle deficit compared to a new blade) in the cutout region. They also observed the formation of counter-rotating streamwise vortices at the edges of the cutout, driven by the sharp gradients (with radius) in yaw angle. Similar flow structures have been observed in computational fluid dynamics (CFD) studies of vanes with TE damage by Di Mare et al. [16] and Meyer et al. [17]. Sjolander et al. reported that the mass-flux-average profile total pressure loss coefficient increased by 56 % (compared to undamaged blade) for the deepest cutout.

Bouchard et al. [18] did aerodynamic surveys downstream of full rings of uncooled new and in-service deteriorated engine vanes in a transonic annular cascade. The vanes were those of a Rolls-Royce A-250 engine. The TE of the deteriorated vanes had small chordwise cracks, and some TE were significantly thermally distorted. No surface roughness measurements were reported in the paper. Profile loss measurements were taken one half of an axial chord downstream of the vanes at exit Mach number (M) M = 1.2. They reported an increase in profile loss of 51 % for the deteriorated vane ring.

Objective of this study

Although there is a small body of literature which presents results of studies of simulated deterioration features in isolation, there are very few studies indeed [18] which characterize components with in-service deterioration. Although the overall impact of deterioration could reasonably be expected to be well-modelled by superposition of the individual deterioration effects, for the purpose of building whole-life turbine performance models it is important to characterize real engine parts at various stages through the life cycle. There is very little data available for this task. The purpose of this paper is to carefully characterize the aerodynamic performance of real-engine HP NGVs subject to various levels of in-service deterioration, to provide a reference point for whole-life performance modelling. To this end, for 15 engine-run parts, we present detailed measurements of: surface roughness; coolant capacity; and aerodynamic performance. Measurements were conducted for parts operating under engine-representative conditions of exit M and exit Re. The data are to be used to benchmark whole-life modelling codes.

CHARACTERIZATION OF TESTED COMPONENTS

In this study we experimentally characterize a total of 17 real-engine vanes. The vane design was that from a modern large civil jet engine. The vanes were divided in two sets, referred to as *set 1* and *set 2*. Set 1 was composed of one new vane and 12 mid-life vanes and set 2 was composed of one new vane and three end-of-life vanes. The new vane within each set has the same as-new geometry as the deteriorated vanes in the same set and

acts as a baseline for that set. The deteriorated vanes within each set are from the same engine, and therefore were operated in the same environment and for the same number of cycles. The two sets operated in a non-sandy, yet not identical, environment. A summary of the operation history of both sets of vanes is given in Table 2.

Table 1: Descriptive summary of the operation history of the in-service deteriorated parts in set 1 and set 2.

Parameter	Set 1	Set 2
Number of vanes	12 (+1 new)	3 (+1 new)
Position in life cycle	Mid-life.	End-of-life.
Operating environment	Non-sandy.	Non-sandy.

Although the vanes in set 1 and set 2 are from the same engine-class, they are from different generations of the same engine and have slightly different geometries. Thus, comparisons between sets should be avoided. All vanes were fully featured, including film cooling holes, TE slots and TBC. We identify individual vanes using their set number (S1 or S2) and vane number within the set (V1, V2, etc.).

Although experimental data was acquired for all vanes in both sets, in this paper we focus on data from four vanes for each set: one new vane and three deteriorated vanes. In set 1, for the focused study, we chose the vanes with the most severe TE burn-back. We refer to selected set 1 vanes as: S1-V1 (new); and S1-V2, S1-V3 and S1-V4 (mid-life). The corresponding nomenclature for set 2 is: S2-V1 (new); and S2-V2, S2-V3 and S2-V4 (end-of-life). Although we present detailed measurements for only this sample, we present statistics on the parent set of parts where space allows.

We now characterize the deterioration of the tested vanes. First we consider TE burn-back and TBC spallation, then we present surface roughness measurements.

TE burn-back and TBC spallation

Figure 1 shows a schematic of the vanes in set 1 (S1) and set 2 (S2). Film cooling holes and the TE slots are omitted for clarity. The solid black lines show the undamaged vanes. Coloured solid and dashed lines demarcate regions of TE burn-back and TBC spallation, respectively, with individual colours for particular vanes (V1, V2, etc.) within a set.

We consider first the selection of set 1 parts: one reference vane and three mid-life vanes. Vanes S1-V1 to S1-V4 are illustrated in Figure 1a. We see TE burn-back for vanes S1-V2 and S1-V3, with notches at approximately mid-span that extend to a depth equal to approximately 5 % of the tangential chord and up to 18 % of the span of the vane. There is a small region of TBC spallation at the leading edges (LE) close to the stagnation point for vanes S1-V3 and S1-V4. These regions are narrow and cover less than 10 % of the span of the vanes. The TE burn-back and TBC spallation on vanes S1-V2 to S1-V4 are representative of the damage of the other deteriorated vanes in set 1.

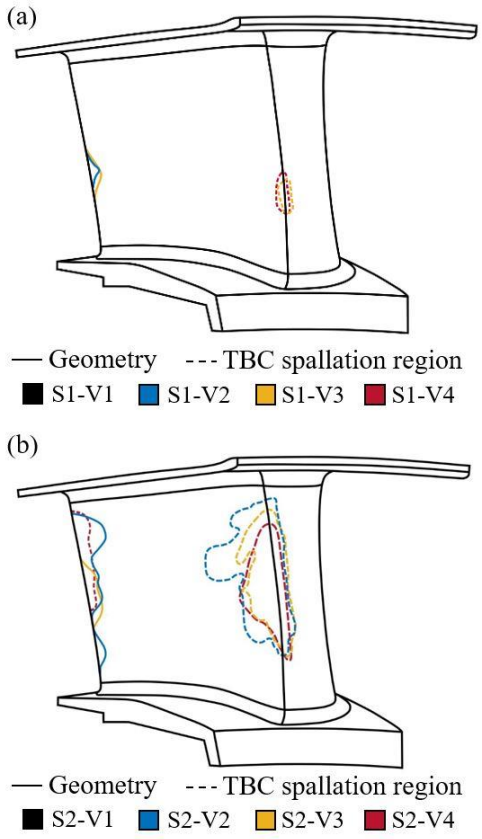


Figure 1: Deterioration characterization for a selection of vanes from: (a) set 1; (b) set 2.

Now we consider the set 2 parts: one reference vane and three end-of-life vanes. With reference to Figure 1b, we see both significant TE burn-back and significant TBC spallation. Looking first at the TE damage, vane S2-V2 was burned back up to 14.2 % of the tangential chord and the damage covers 80 % of the span of the vane. The TE of vane S2-V3 is burned back up to 9.6 % of the tangential chord at midspan and the damage covers 40 % of the span of the vane. The TE of vane S2-V4 is slightly cracked and distorted towards the SS, with TE TBC spallation on both the PS and SS extending up to 7 % of the tangential chord over 35 % of the span of the vane. It is suspected that the TE damage is the result of local overheating rather than erosion (by, for example, sand) because approximately half of the vanes from the same engine had relatively undeteriorated TE.

Now consider the LE region damage for the set 2 (end-of-life) vanes. The LE of all vanes in this set were severely damaged with TBC spallation covering up to 65 % of the span of the vanes, and extending as far as 30 % of the tangential chord on the PS of the vanes (see Figure 1b). The spallation was so severe in some places that the metal was left unprotected. This is thought to be due to a combination of thermal fatigue cracking and oxidation. In the regions of most severe deterioration, primarily in the showerhead region of the parts, there was significant collapse (shrinkage of diameter, and damage to form) of the cooling holes, and cracking between holes.

A descriptive summary of the deterioration characteristics of both sets of vanes is given in Table 2.

Table 2: Descriptive summary of deterioration characteristics of the set 1 (mid-life) and set 2 (end-of-life) parts.

Vane	LE geometry	TE geometry
S1-V1	New.	New.
S1-V2	Intact.	Small notch at midspan.
S1-V3	Minor TBC spallation.	Small notch at midspan.
S1-V4	Minor TBC spallation.	Intact.
S2-V1	New.	New.
S2-V2	Severe TBC spallation; collapsed cooling holes; cracking between holes.	Burn-back along the entire span.
S2-V3	Severe TBC spallation; collapsed cooling holes; cracking between holes.	Burn-back at midspan.
S2-V4	Severe TBC spallation; collapsed cooling holes; cracking between holes.	Minor distortion and cracking; minor TBC spallation.

Surface roughness measurements

In this section we present surface roughness measurements for the tested vanes. Profilometry measurements were performed using an Alicona InfiniteFocus profilometer (non-contact optical three-dimensional surface measurement system). Measurements were taken at three span fractions and three streamwise positions on the PS, and at three span fractions and four streamwise positions on the SS. These 21 locations are indicated in Figure 2. Each profilometry measurement covered a 500 μm × 500 μm area and consisted of 250,000 (500 × 500) discrete points. The measurement resolution in the wall-normal direction (z) direction was 0.1 μm. The macroscopic surface shape was evaluated by cubic surface fitting and was removed from the measurement to only keep the surface profile. Figure 3 shows examples of the measured and processed surface profiles. The positive streamwise direction is along the x axis. The data show good measurement resolution. New TBC (Figure 3a) is characterized with a high density of shallow and blunt valleys. Deteriorated TBC (Figure 3b) is characterized by sharper high peaks formed by deposits. The shape of the peaks appears to be independent of direction (streamwise or spanwise).

We represent roughness at the measurement locations with an *equivalent sandgrain roughness height* (k_s) using the methodology proposed by Bons [19]. We present k_s normalised by the tangential chord C of the vanes. Figure 4 shows k_s/C measured on vanes S1-V1 to S1-V4 for set 1 and S2-V1 to S2-V4 for set 2 (entire set).

Plots (a) and (b) show data for the PS of the vanes in set 1 and set 2, respectively. Plots (c) and (d) show data for the SS of the vanes in set 1 and set 2, respectively. Position labels indicate: the side of the vane (PS or SS); streamwise position (1–3 on PS and 1–4 on SS, as shown in Figure 2); and span fraction (20, 50 and 80 %). Each bar at a given position corresponds to a particular vane measurement.

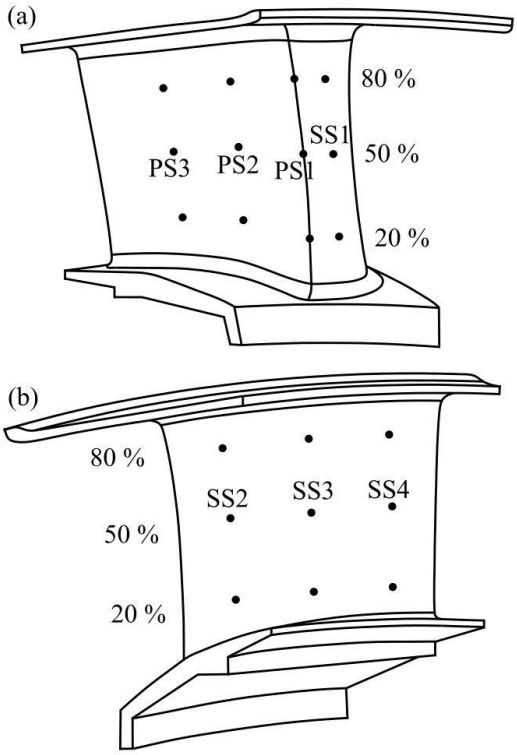


Figure 2: Profilometry measurement locations on the HP NGVs: (a) viewed from upstream; (b) viewed from downstream.

Consider first the vanes in set 1 (mid-life) part data of Figure 4a and Figure 4c. On the PS and early SS (SS/1/XX locations, where XX = 20, 50 or 80) we see a significant increase in k_s/C of the deteriorated vanes compared to the new vane. The mean increase in these 12 locations was 441 %, with a maximum increase of 1056 %. On the remainder of the SS (locations SS/2–4/XX) the deteriorated and new vanes are more similar, with a mean increase in roughness of 53.3 %, and a maximum increase of 192 %. This is in accord with the result of Bons et al. [20], who documented the surface roughness on nearly 100 in-service-deteriorated turbine components and noted that the PS and early SS suffer from in-service roughening much more than the late SS.

Now consider the set 2 (end-of-life) part data of Figure 4b and Figure 4d. The early PS (locations PS/1/XX) and early SS (locations SS/1/XX) show a significant increase in roughness compared to the new vane, with a mean increase in roughness of 104 % and a maximum increase of 723 %. In all other locations on the vane the increase in roughness is smaller, with a mean increase of 49.5 %, and a maximum increase of 201 %.

Taking all vanes within set 1 (mid-life) (entire set of 12 deteriorated vanes and one new vane), the mean values of k_s/C across all measurement points were 0.109×10^{-3} for the new vane and 0.399×10^{-3} for the deteriorated vanes (average of 12

vanes). The average increase in roughness (compared to the new vanes) was 266 %. This was strongly biased towards the PS and the early SS (locations SS/1/XX).

Taking the vanes within set 2 (end-of-life) as a whole (3 deteriorated vanes in total and one new vane), the mean values of k_s/C across all measurement points were 0.103×10^{-3} for the new vane and 0.185×10^{-3} for the deteriorated vanes (average of 3 vanes). The average increase in roughness (compared the new vanes) was 79.6 %. Again, this was strongly biased towards the PS and the early SS (locations SS/1/XX).

Although in this paper we focus on the aerofoil surface, for completeness we note that the hub and casing platforms of the deteriorated vanes of both set 1 and set 2 were qualitatively rougher than new platforms, but without major geometrical deviations.

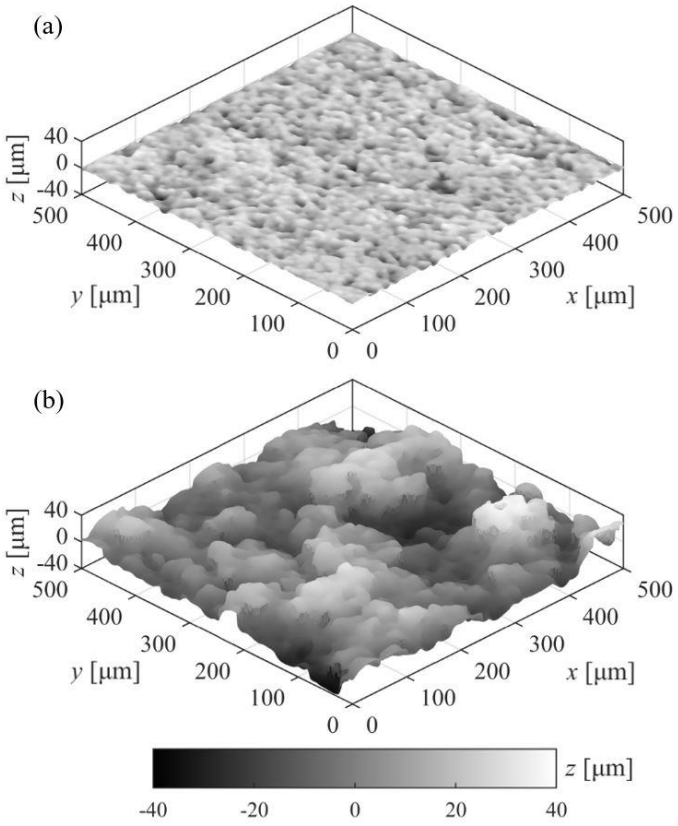


Figure 3: Examples of measured surface profiles on: (a) new TBC; (b) deteriorated TBC.

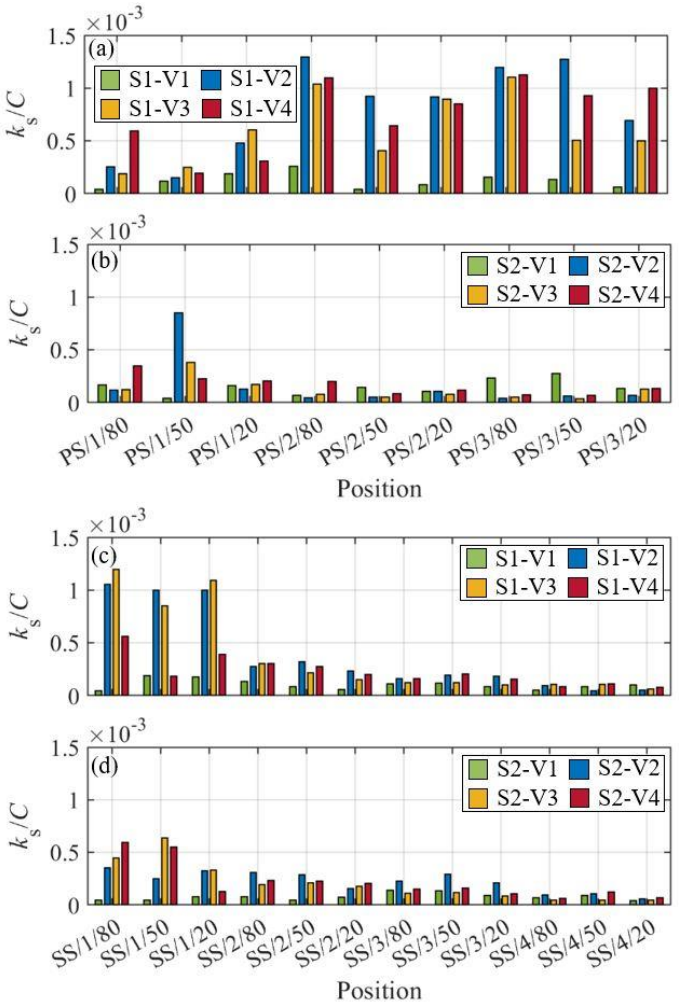


Figure 4: Normalised equivalent sandgrain roughness height: (a) PS for set 1; (b) PS for set 2; (c) SS for set 1; (d) SS for set 2.

OVERVIEW OF THE EXPERIMENTAL FACILITY

Aerodynamic measurements were conducted in the Engine Component AeroThermal (ECAT) facility at the University of Oxford [21]. This is a high technology readiness level (TRL) blowdown facility capable of testing an annular cascade of HP NGVs from operating engines at engine-representative conditions of Mach number, Reynolds number and coolant-to-mainstream pressure ratio. A schematic cross-section of the facility working section with the traverse system installed is presented in Figure 5.

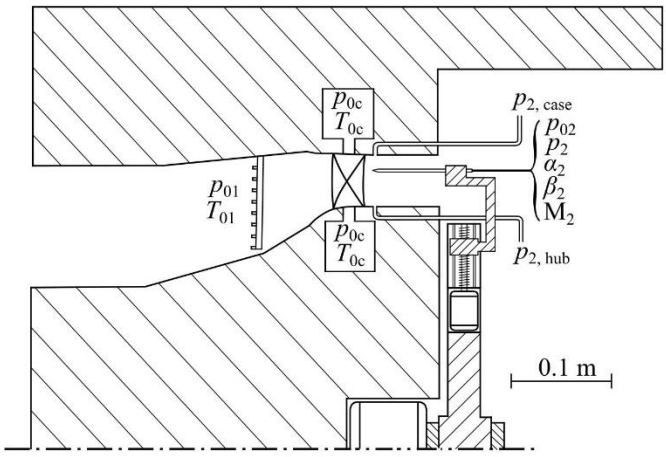


Figure 5: Schematic cross-section of the ECAT facility working section with traverse system installed.

Operating conditions

During a test, high pressure air (initially stored in large tanks) is discharged through the cascade of vanes. Steady operating conditions can be achieved for approximately 60 seconds by the action of a pressure regulator upstream of the cascade. During this time aerodynamic traverse measurements are taken. The vanes are supplied with coolant from the hub and case (see Figure 5), feeding the vane film cooling holes and the TE slot. Further details on the operation of the ECAT facility can be found in [21, 22, 23]. The operating conditions used in this study are summarized in Table 3.

Table 3: ECAT facility operating conditions for aerodynamic measurements of this study.

Parameter	Value
Mean vane pressure ratio, p_2/p_{01}	0.58
Mean vane isentropic exit Mach no., $M_{2,is}$	0.92
Exit Reynolds no., Re_C	1.60×10^6
Vane inlet turbulence intensity, Tu	12 %
Coolant-to-mainstream pressure ratio, p_{0c}/p_{01}	1.027
Coolant mass ratio, $\dot{m}_c/\dot{m}$	10 %

Instrumentation for aerodynamic measurements

Mainstream total pressure and total temperature measurements at the cascade inlet (p_{01} and T_{01}) were performed using probe rakes (approximate axial location shown in Figure 5) at four circumferential positions around the annulus. Hub and case coolant cavity total pressure and total temperature (p_{0c} and T_{0c}) were also measured at four circumferential positions. The vane exit static pressure ($p_{2,\text{hub}}$ and $p_{2,\text{case}}$) was measured on six vanes (from a total of 40) with 28 tappings per vane (84 tappings in total) located on the hub and case platform overhangs approximately 5 mm downstream of the cascade TE plane (see Figure 5).

Area surveys were conducted in an axial plane one quarter of an axial chord downstream of the HP NGV TE using an automated radial-circumferential hub-mounted traverse gear. The location and approximate geometry of the traverse is shown in Figure 5. The probe tip is approximately aligned with the mean flow angle, to ensure measurements were in the range of minimum error for the probe system. Aerodynamic measurements were taken using a five-hole probe (tip diameter 2.8 mm) calibrated over a wide Mach number range ($0.3 \leq M \leq 1.4$). The probe was calibrated to allow determination of total and static pressures, Mach number, and flow angles. Data on a full area-traverse plane is built from six discrete blocks (separate runs) which are then stitched together. A full-area traverse map contains approximately 60 traverse passes with a radial step size of approximately 1 mm. Better than 1 mm effective resolution is obtained in the circumferential direction. More details on the instrumentation, measurement processing and uncertainty in the aerodynamic measurements in the ECAT facility can be found in [21, 23, 24].

Coolant flow capacity measurement process

To understand how *in-situ* coolant capacity,

$$\Gamma_c\left(\frac{p_{0c}}{p_{01}}, \frac{p_2}{p_{01}}\right) = \frac{\dot{m}_c\sqrt{T_{0c}}}{p_{0c}} \quad (1)$$

(where $\dot{m}_c$ is the total coolant mass flow rate, and p_{0c} and T_{0c} are the total pressure and total temperature of the coolant flow in the feed plenum) was affected by in-service deterioration, accurate *ex-situ* coolant capacity measurements,

$$\Gamma_c\left(\frac{p_{0c}}{p_{atm}}\right) = \frac{\dot{m}_c\sqrt{T_{0c}}}{p_{0c}} \quad (2)$$

were performed on all 17 vanes (2 new vanes and 15 deteriorated vanes) used in this study. By ex-situ, we refer to a bench-test experiment in the absence of the potential field developed by the vane. It is necessary to perform ex-situ measurements on individual parts to separate effects on a per-vane basis. To accurately translate these measurements to in-situ coolant capacity predictions requires an aerodynamic model, individual *assumed* row-based in-situ capacity characteristics, experimental in-situ data for *checksum scaling* of the overall cascade coolant capacity, and—in a more sophisticated analysis—a coupled internal-external network loss model. These approaches are covered in [25]. Here we are primarily concerned with changes in in-situ coolant capacity from the situation for undamaged vane. At the nominal coolant-to-mainstream pressure ratio (Table 3) the coolant mass ratio (reference to the overall cascade flow) is approximately 10 %. For cascade experiments operated at fixed coolant-to-mainstream pressure ratio (pressure, as opposed to mass-flow, boundary condition), and at fixed vane overall pressure ratio, it can be assumed that for relatively small changes in row-capacity characteristics (such that the gross aerodynamic field is not disturbed) the per-row operating points on the in-situ capacity characteristics are approximately unchanged. Thus, for an individual vane, *proportional changes* in the per-row in-situ coolant mass flow rate (for the stated cascade boundary conditions) will be approximately equal to proportional changes in per-row ex-situ coolant mass flow rates.

We can express this as a proportional change (from the undamaged vane) in ex-situ per-row coolant capacity evaluated at any fixed arbitrary pressure ratio in the ex-situ environment (e.g. $\Gamma_{c,S1-VX} - \Gamma_{c,S1-V1})/\Gamma_{c,S1-V1}$, where X = 2, 3 or 4) evaluated at an arbitrary pressure ratio. The same statements are equally true for any group of cooling rows. In our particular tests we consider two groups: the TE slot; and the entire flow from 11 film cooling rows.

Bench-test measurements were taken in an experiment in which the NGV was fed from both the hub and case using custom-made (plastic printed) feed plena sealed to the vane with wax sealant (to ensure complete removal). The feed plena were pressure-balanced using variable metered feeds fed from a constant pressure (regulated) supply. Total temperature and total pressure were measured upstream of the NGV coolant inlet using measurement rakes. The flow discharged directly to atmosphere through the film cooling holes and the TE slot. Test data was taken at five coolant-to-mainstream pressure ratios, p_{0c}/p_{atm} = 1.1, 1.2, 1.4, 1.6 and 1.8. The proportional changes in capacity (e.g. $\Gamma_{c,S1-VX} - \Gamma_{c,S1-V1})/\Gamma_{c,S1-V1}$) were approximately independent of pressure ratio, and an average value (from all tested pressure ratios) was taken. Measurements were taken on each vane with all film cooling holes and the TE slot open, and also with the TE slot sealed (and films open). This allowed separation of the film capacity and the TE slot capacity.

EXPERIMENTAL RESULTS

The experimental results are now presented. We will consider: coolant capacity measurements; local kinetic energy (KE) loss coefficient distributions; plane-average and mixed-out KE loss coefficients; comparisons to open-literature data of loss enhancement due to increased surface roughness; circumferential profiles of local KE loss coefficient; and radial distributions of flow angle.

Coolant flow capacity measurements

In this section we consider the measurements of ex-situ coolant capacity which—we have explained—is a reasonable proxy for in-situ coolant capacity in our experiments. The proportional changes in coolant capacity $(\Gamma_{c,S1-VX} - \Gamma_{c,S1-V1})/\Gamma_{c,S1-V1}$ for set 1 and $(\Gamma_{c,S2-VX} - \Gamma_{c,S2-V1})/\Gamma_{c,S2-V1}$ for set 2) are presented in Table 4. The measurement process allows separation of the TE slot flow and the film flow. Proportional changes are relative to the reference (new) vane in each set.

Looking first at the set 1 data, we see a reduction in coolant capacity for all the mid-life deteriorated vanes for both film cooling holes and TE slot. For the film cooling flow the reduction in capacity is between –6.21 % and –3.87 % with an average (across three parts) of –5.15 %, and for the TE slot the reduction is between –15.0 % and −2.54 % with an average of –10.3 % (across three parts). The decrease in film coolant capacity appears to be caused by partial blockage of the holes due to particle deposition. This is marked A in Figure 6b. The condition of an undamaged film cooling hole shown in Figure 6a. Close inspection of the film cooling holes of the mid-life vanes show some level of deposition in all holes. The decrease in TE slots coolant capacity appears to be due to partial collapse of the TE slot, due to overheating and thermal distortion. This is shown in Figure 6c, marked B. Most mid-life vanes showed partial collapse in some areas, even on vanes without TE burn-back, but the effect was more advanced on vanes which also showed TE burn-back (e.g. S1-V2 and S1-V3). Taking the average across *all* vanes in set 1 (total of 12 mid-life vanes; not individually reported in Table 4) we find a mean reduction in film cooling flow capacity of –2.20 % and a mean reduction in TE flow capacity of –4.87 %. These average values are presented in Table 4. The difference in the mean reduction in film hole coolant capacity between the three selected vanes of set 1 (–5.15 %) and the parent set of 12 vanes (–2.20 %) is attributed to the random nature of the deposition process (even within the same engine), and the small sample size. Likewise the mean reduction in TE slot coolant capacity between the three selected vanes (–10.3 %) and the parent set of 12 vanes (–4.87 %) is explained by the fact that only three vanes from the parent set have TE burn-back: i.e. in selecting the vanes to be studied in detail, vanes with more significant TE burn-back were preferred, and these had greater associated collapse of the TE slot than average across the parent set.

Table 4: Proportional changes in coolant capacity.

Set 1 vane	$(\Gamma_{c,S1-VX} - \Gamma_{c,S1-V1})/\Gamma_{c,S1-V1}$ [%]	
	Film holes	TE slot
S1-V2	–5.37	–13.4
S1-V3	–6.21	–15.0
S1-V4	–3.87	–2.54
Mean S1-V(2–4)	–5.15	–10.3
Mean S1-V(2–13)	–2.20	–4.87
Set 2 vane	$(\Gamma_{c,S2-VX} - \Gamma_{c,S2-V1})/\Gamma_{c,S2-V1}$ [%]	
	Film holes	TE slot
S2-V2	–5.62	–24.7
S2-V3	–5.43	–15.9
S2-V4	–6.27	–9.79
Mean S2-V(2–4)	–5.77	–16.8

Looking now at the data for set 2 (end-of-life parts) we see a reduction in coolant capacity between –6.27 % and –5.43 % for the film cooling holes (mean of –5.77 % across three parts) and between –24.7 % and –9.79 % for the TE slot (mean of –16.8 % across three parts). In contrast to the set 1 data, the decrease in coolant capacity of the film cooling holes appears to be primarily due to shrinkage of holes in the region of spalled TBC (spallation region shown in Figure 1b), due to local over-heating of the part (similar effect to the TE slot collapse) This is shown in Figure 6d, marked C (LE of vane S2-V4). Interestingly, the effect is partially offset by enchained cracking between holes (marked D in Figure 6d), leading to weeping flow through the cracks. As for set 1 parts, the decrease in TE flow for the set 2 parts is due to partial collapse of the TE slot. The radial extent of this was, on average, greater for the set 2 parts than the set 1 parts, on account of more severe TE overheating. This is consistent with greater

radial extent of TE burn-back for the set 2 parts. Extreme burn-back (greater than the parts shown in the present study) would potentially lead to a reversing of this effect, due to an increase in slot width in the direction towards the LE of the vane. The impact of a change in film cooling flow capacity and TE flow capacity on aerodynamic loss will be considered in the next section.

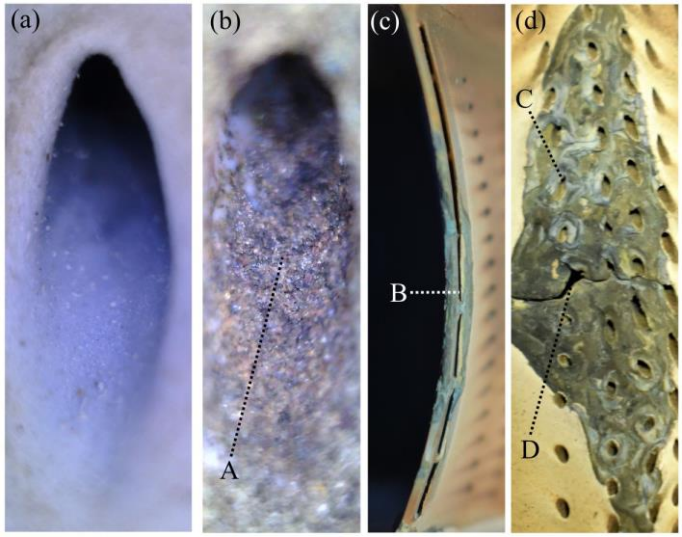


Figure 6: Photographs of: (a) new film cooling hole; (b) typical particulate deposits within a mid-life film cooling hole (chosen from set 1); (c) partial collapse of the TE slot (vane S1-V2); (d) shrinkage of LE film cooling holes and enchained cracking (vane S2-V4).

Local KE loss coefficient distributions

Results of the downstream aerodynamic surveys are now considered. We defined a local KE loss coefficient $\zeta'(r,\theta)$ by

$$\zeta'(r,\theta) = 1 - \frac{1 - \left(\frac{p_2(r,\theta)}{p_{02}(r,\theta)}\right)^{\chi}}{1 - \left(\frac{p_2(r,\theta)}{p_{01}}\right)^{\chi}} \qquad (3)$$

where $\chi = (\gamma - 1)/\gamma$ and γ is ratio of specific heats, p_{01} is the total pressure upstream of the vanes (assumed uniform), and $p_{02}(r,\theta)$ and $p_2(r,\theta)$ are the total and static pressures measured in the plane of interest downstream of the vanes. A discussion of this, and other performance metrics, is given in [23].

Figure 7 shows the local distributions of $\zeta'(r,\theta)$ downstream of the mid-life vanes S1-V1 to S1-V4 (top row, frames a–d respectively) and the end-of-life vanes S2-V1 to S2-V4 (bottom row, frames e–h respectively). Flow turning is clockwise when viewed from downstream, and data are viewed from downstream. The distribution of $\zeta'(r,\theta)$ is normalised by the maximum value of $\zeta'(r,\theta)$ measured across all the data presented.

Consider first the results for the new vanes, S1-V1 and S2-V1. There is a well-defined wake profile, which has a curve due to the compound lean in the aft region of the vane. The wake has a number of distinct maxima associated with regions of TE coolant ejection (for detailed analysis see [23]), which are intermittent on account of internal webs. The maximum value of $\zeta'(r,\theta)$ in the wake is near the hub of the vane, where the vane exit Mach number is the highest. Compound lean and sweep in the vane geometry mean the traverse plane is closest to the TE at the hub, and furthest from the vane at mid-span. This is in accord with the result that the wake towards the hub is the least mixed (a second reason for the greatest peak value in this region), and the wake in the mid-span region is most mixed.

Now consider the set 1 (mid-life) deteriorated vanes. Vanes S1-V2 and S1-V3 have only minor TE burn-back (see Figure 1a), but the distortion to the downstream wake is significant. In the region of the TE damage, the wake is under-turned with respect to the undamaged vane, leading to turning of the *passage flow* away from the SS and towards the PS. The regions of under-turned flow (co-incident with the TE burn-back regions of Figure 1a) are marked A and B in Figure 7b and Figure 7c respectively. Vane S1-V4 (Figure 7d) did not exhibit TE burn-back and the wake is deeper than that of the reference vane (Figure 7a)—due to greater surface roughness—but of relatively similar form. All of the mid-life vanes assessed had greater profile loss than the undamaged vane, which was attributed to the increased surface roughness causing greater boundary layer loss (combination of earlier transition, but also greater growth rate within the turbulent boundary layer).

The deteriorated set 2 (end-of-life) vanes have more significant TE burn-back (for extents see Figure 1b), leading to gross disruption of the wake due to severe under-turning, and—in the case of S2-V2 and S2-V3—the formation of counter-rotating vortices (marked C and D in Figure 7) either side of the more severe burnt-back regions (caused by strong radial gradient of whirl angle). Similar effects have been observed in [15, 16, 17]. Between counter-rotating vortices, there are patches of low loss between the vortices, as the lossy flow is rolled-up into the vortex. The small cracks and bends at the TE of vane S2-V4 have caused a significant local broadening of the wake (marked E in Figure 7). In the profile loss regions undisturbed by TE damage, the wake is thicker and deeper than the reference vane due to increased surface roughness of the part.

We now examine the secondary flow regions in more detail. Local distributions of $\zeta'(r,\theta)$ in the near-endwall regions are shown in Figure 8. Secondary flow loss cores in the casing region (Figure 8a–h) are difficult to identify for two reasons: they are less intense than at the hub due to the lower Mach number; there is downwash on the vane surface, spreading the boundary layer fluid throughout the wake (see e.g. [23]) and causing coalescence of the flow structures. In contrast to the casing data, in the near-hub region (Figure 8i–p) the secondary loss cores are well-defined: for the reference vanes S1-V1 (Figure 8i) and S2-V1 (Figure 8m) the SS corner vortex and passage vortex are marked A and B respectively. For the corner vortex and passage vortex, the peak measured values of local normalised KE loss coefficient were approximately 80 % and 66 %, respectively, for both reference vanes. The radial locations of the peaks were 2 % and 10 % span fraction respectively. For all deteriorated vanes the secondary loss cores are both more intense and greater in size than for their corresponding reference vane.

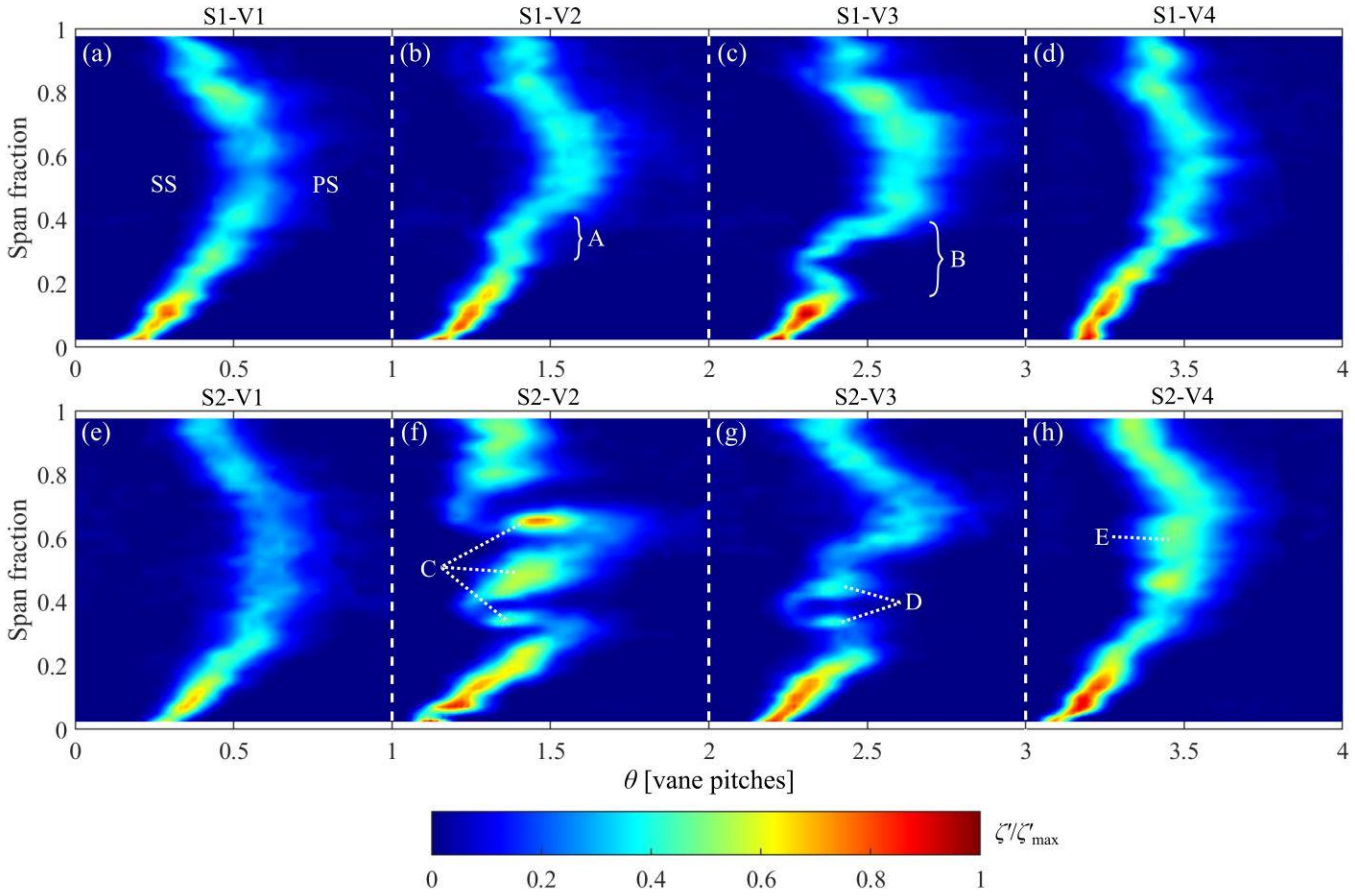


Figure 7: Local distributions of KE loss coefficient $\zeta'(r,\theta)$ for: (a)–(d) set 1; (e)–(h) set 2. Flow turning is clockwise when viewed from downstream, and data are viewed from downstream.

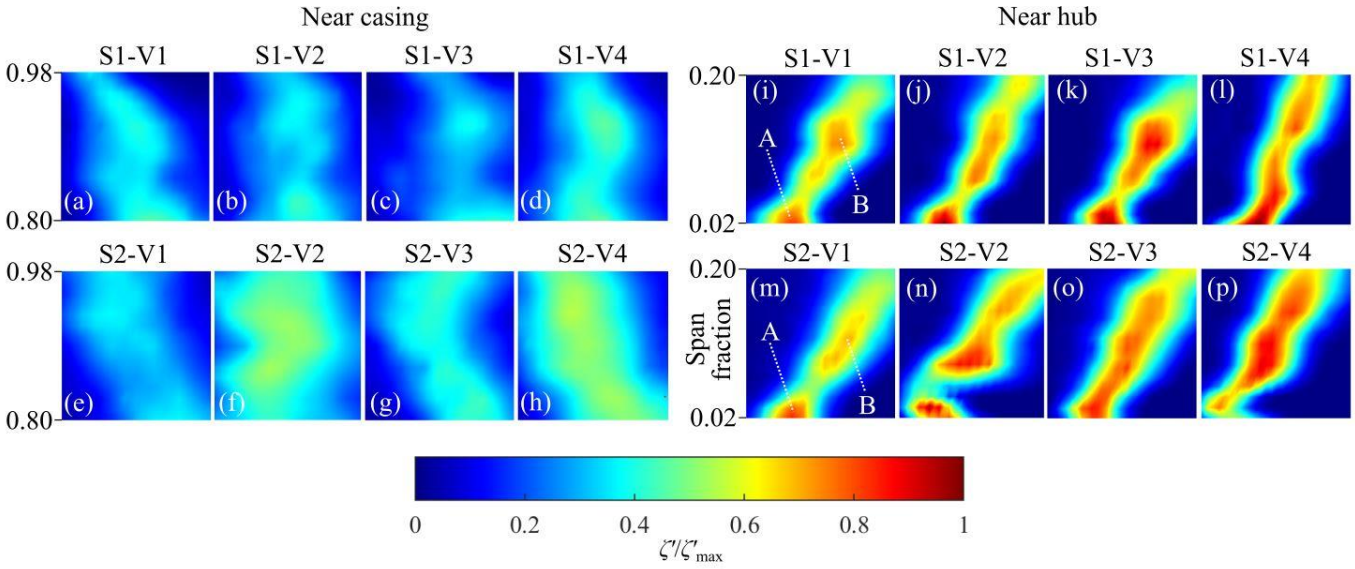


Figure 8: Comparison of secondary loss cores: (a)–(d) set 1 near-casing; (e)–(h) set 2 near-casing; (i)–(l) set 1 near-hub; (m)–(p) set 2 near-hub.

Plane-average and mixed-out KE loss coefficient

In this section we consider both plane-average KE loss coefficients, and mixed-out KE loss coefficients for the vanes. The plane-average coefficient may be taken to represent the loss *already manifested* at the measurement plane. The mixed-out KE loss coefficient can be taken to represent the sum of the loss already manifested, and the unavoidable loss as the result of the mixing out of gradients already present within the flow (and unlikely to contribute usefully to work): i.e., the secondary kinetic energy (SKE) within the flow.

Adopting the definitions of [23], we define the plane-average KE loss coefficient for a film-cooled vane by

$$\zeta'''' = 1 - \frac{(\dot{m}_\mathrm{m} + \dot{m}_\mathrm{c})\left[1 - \left(\frac{\overline{p_2}}{\overline{p_{02}}}\right)^{\chi}\right]}{\dot{m}_\mathrm{m}\left[1 - \left(\frac{\overline{p_2}}{p_{01}}\right)^{\chi}\right] + \dot{m}_\mathrm{c}\left[1 - \left(\frac{\overline{p_2}}{p_{0c}}\right)^{\chi}\right]} \qquad (4)$$

where $\dot{m}_\mathrm{m}$ and $\dot{m}_\mathrm{c}$ are the mainstream and coolant mass flow rates, respectively, and $\overline{p_{02}}$ and $\overline{p_2}$ are the mass-flux-average total pressure and area-average static pressure, respectively.

The mixed-out KE loss coefficient for a film-cooled vane is defined [23] by

$$\zeta''''' = 1 - \frac{(\dot{m}_\mathrm{m} + \dot{m}_\mathrm{c})\left[1 - \left(\frac{\overline{p_2}'}{\overline{p_{02}}'}\right)^{\chi}\right]}{\dot{m}_\mathrm{m}\left[1 - \left(\frac{\overline{p_2}'}{p_{01}}\right)^{\chi}\right] + \dot{m}_\mathrm{c}\left[1 - \left(\frac{\overline{p_2}'}{p_{0c}}\right)^{\chi}\right]} \qquad (5)$$

where $\overline{p_{02}}'$ and $\overline{p_2}'$ are the mixed-out total and static pressures, respectively, and where a prime is used to distinguish these mixed-out variables (result of mixing process) from averages resulting from the in-plane weighting (e.g. area, volume-flux or mass-flux). The definition (5) is developed in [23], and the method for calculation of the mixed-out pressures ($\overline{p_{02}}'$ and $\overline{p_2}'$) is presented in [26] and summarized in [27].

As discussed, the residual SKE is defined as the difference between the mixed-out and plane-average KE loss coefficient

$$\mathrm{SKE} = \zeta''''' - \zeta'''' \qquad (6)$$

Normalised plane-average (ζ'''') and mixed-out (ζ''''') KE loss coefficients, and corresponding residual SKE values are summarised in Table 5. The data are normalised by the mixed-out KE loss coefficient of the reference vane within each set ($\zeta'''''_{\mathrm{S1-V1}}$ and $\zeta'''''_{\mathrm{S2-V1}}$).

Consider first the data for set 1 (mid-life). For the reference vane, the normalised mixed-out KE loss coefficient is by definition unity. The normalised plane-average KE loss coefficient and SKE are 0.65 and 0.35 (sum to unity). The relatively large SKE (0.35 of the mixed-out loss) is accounted for by significant unmixed wake (traverse plane relatively close to TE). Now consider the set 1 deteriorated vanes. The average changes in ζ'''', ζ''''' and SKE for vanes S1-V(2–4) were 14.1 %, 8.72 % and –2.13 %. Corresponding values for the full set of 12 vanes—vanes S1-V(2–13)—are extremely similar: 13.6 %, 7.81 % and –2.57 %, respectively. The vane-to-vane spread in data was very low, suggesting high similarity between parts. The increase in plane-average KE loss coefficient (average of 13.6 % across all parts) is thought to be due simply to an increase in roughness, and associated boundary layer thickening. The SKE remains almost constant (average change of only –2.57 %), which is explained by the fact that the flow structure is essentially unchanged (slight change in wake thickness). The corresponding average change in mixed-out loss is 7.81 %.

Table 5: Normalised plane-average KE loss coefficient, mixed-out KE loss coefficient, and residual SKE.

Set 1 vane	$\frac{\zeta''''_{\mathrm{S1-VX}}}{\zeta''''_{\mathrm{S1-V1}}}$	$\frac{\zeta'''''_{\mathrm{S1-VX}}}{\zeta'''''_{\mathrm{S1-V1}}}$	$\frac{\mathrm{SKE}_{\mathrm{S1-VX}}}{\zeta'''''_{\mathrm{S1-V1}}}$
S1-V1	0.65	1.00	0.35
S1-V2	0.77	1.12	0.35
S1-V3	0.73	1.07	0.34
S1-V4	0.74	1.08	0.34
Mean change S1-V(2–4)	14.1 %	8.72 %	–2.13 %
Mean change S1-V(2–13)	13.6 %	7.81 %	–2.57 %
Set 2 vane	$\frac{\zeta''''_{\mathrm{S2-VX}}}{\zeta''''_{\mathrm{S2-V1}}}$	$\frac{\zeta'''''_{\mathrm{S2-VX}}}{\zeta'''''_{\mathrm{S2-V1}}}$	$\frac{\mathrm{SKE}_{\mathrm{S2-VX}}}{\zeta'''''_{\mathrm{S2-V1}}}$
S2-V1	0.65	1.00	0.35
S2-V2	0.86	1.33	0.47
S2-V3	0.72	1.12	0.40
S2-V4	0.77	1.11	0.34
Mean change S2-V(2–4)	22.7 %	18.8 %	14.9 %

Looking at the data for set 2 (end-of-life), the reference vane, has normalised plane-average KE loss coefficient and SKE values of 0.65 and 0.35. These are identical to the values for set 1 parts, suggesting high consistency between sets. Looking at the set 2 deteriorated vanes (vanes S2-V(2–4)) we find the average increase (across 3 vanes) in ζ'''', ζ''''' and SKE to be 22.7 %, 18.8 % and 14.9 %, respectively. The loss coefficients changes are significantly greater for set 2 than for set 1 both because of the flow-structure changes caused by severe TE burn-back, and the effects of increased surface roughness. The vane-to-vane spread in data is also higher that for set 1, on account of significant differences in the particular TE damage (see Figure 1b). The increase in plane-average KE loss coefficient (average of 22.7 % across all parts; approximately double that for set 1) is associated with both an increase in roughness and an increase in—already manifested—secondary flow loss at the mixing plane. In contrast to the set 1 data, the SKE change is significant (average change of 14.9 %), and is caused by significant structural changes in the flow (see discussion above, noting—in particular—streamwise vortices marked C and D in Figure 7) with the average dominated by the changes for vanes S2-V2 and

S2-V3 (these have the most significant TE burn-back; see Figure 1b), 34.3 % and 14.3 % respectively. The corresponding average change in mixed-out loss is 18.8 %, approximately double that for set 1.

So far as whole-life turbine performance modelling is concerned, we suggest preliminary (limited data sets) enhancement factors for mixed-out row loss of approximately 8 % for mid-life parts, and 19 % for end-of-life parts. Taking a typical mixed-out row total pressure loss of 6 % [23] for new parts, these would translate to approximately −0.49 % and −1.19 % on row efficiency, respectively. For *stage* loss, an additional enhancement factor might be expected for the case of end-of-life parts (but not mid-life parts) on account of the extreme yaw angle variation in the vicinity of the TE burn-back, which would be expected to cause additional losses due to incidence variation in the rotor frame.

We now consider the individual contributions of the change in film cooling flow capacity and TE slot flow capacity (due to in-service deterioration) on the overall change in aerodynamic loss. For this purpose we used the Hartsel [28] film cooling flow loss model and a TE slot flow loss model which we develop for our specific vane geometry and operating conditions.

We first consider the film cooling loss model. This model is based on that of Hartsel [28], in which the flow is considered to be comprised of a mixing layer and mainstream layer, interacting at constant static pressure in the surface normal direction, but with the possibility of acceleration in the streamwise direction. Relative row capacities were calculated using nominal hole diameters, with a scaling factor (equivalent to a common discharge coefficient) chosen to match the overall coolant capacity of the model to that measured in the experiment. In the model individual rows exhaust to particular static pressures determined using CFD (see Burdett et al. [29] for more details). Changes in film cooling flow capacity due to deterioration were assumed to affect all film cooling holes uniformly. Using the model, we can calculate the predicted change in mixed-out KE loss coefficient (normalised by $\zeta''''_{\mathrm{S1-V1}}$) as a function of a change in film cooling flow capacity: a so-called *exchange rate* between the two parameters. This function is shown in Figure 9. As expected, we observe that a reduction of film cooling flow from the design condition leads to a reduction in loss. If deterioration acts to reduce film capacity and increase roughness and TE damage, the reduced film loss acts to mitigate the increase in aerodynamic loss due to the increase surface roughness and TE burn-back.

For the set 1 parts, the mean change in film cooling flow capacity was –2.20 % (see Table 4), leading to a predicted change in mixed-out KE loss coefficient ζ'''' of –0.91 %. For the set 2 parts the mean change in film cooling flow capacity was –5.77 % (see Table 4), leading to a predicted change in mixed-out KE loss coefficient ζ'''' of –2.36 %. It should be noted that the vanes in set 2 have heavily damaged LE with distorted film cooling holes and cracks (see Figure 6d), and changes in the aerodynamics of the mixing process are beyond the scope of the model. We must regard the results for set 2 parts as therefore only indicative of likely trends rather than quantitatively robust.

We now consider the TE slot flow loss model. The model is that presented in Burdett and Povey [30], based on earlier work by Stewart [31] and then Deckers and Denton [32]. The model uses a mass-momentum control volume method to determine the mixed-out loss coefficient for a particular TE geometry and TE slot mass flow rate. We assume that the change in TE slot flow capacity due to deterioration is uniform across the entire span of the slot, and represented by the measured change in TE slot flow capacity. The predicted change in mixed-out KE loss coefficient (normalised by $\zeta''''_{\mathrm{S1-V1}}$) as a function of the change in TE slot flow capacity is shown in Figure 9. The mean changes in TE slot flow capacity for set 1 and 2 parts (see Table 4) were –4.87 % and –16.8 % respectively, leading to predicted increases in mixed-out KE loss coefficient (ζ'''') of 2.18 % and 7.62 %, respectively. For our deteriorated parts both the film capacity and TE slot flow capacity are reduced, but the modelled changes in KE loss coefficient are in opposite directions.

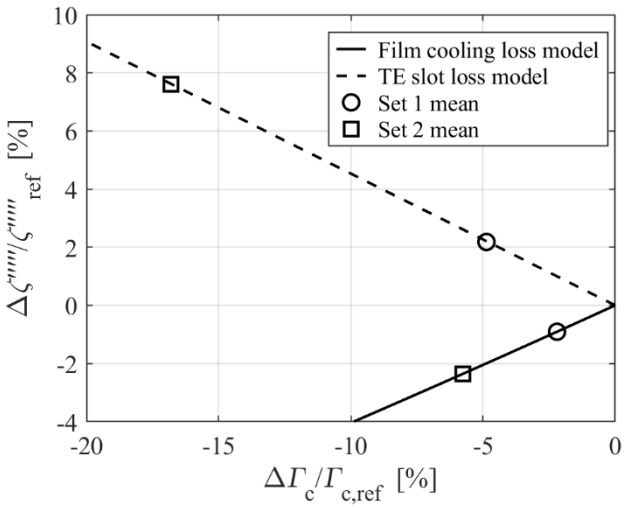


Figure 9: Predicted change in mixed-out KE loss coefficient as a function of change in coolant flow capacity calculated using film cooling loss model and TE slot loss model.

Taking the results of these models in combination with the measured overall change in mixed-out KE loss coefficient with deterioration (Table 5), we can estimate the change in mixed-out loss attributable to aerodynamic changes not included in the loss models. That is, effects such as: boundary layer changes caused by surface roughness and spalling; changes in secondary flow behaviour caused by TE burn-back; and additional loss introduced at the point of coolant injection not captured in the basic model. The estimated values for additional aerodynamic loss were 6.54 % and 13.5 % for set 1 and set 2 parts, respectively. The measured overall loss (Table 5) and the predicted (loss models) and inferred (by difference) contributions are represented diagrammatically in Figure 10.

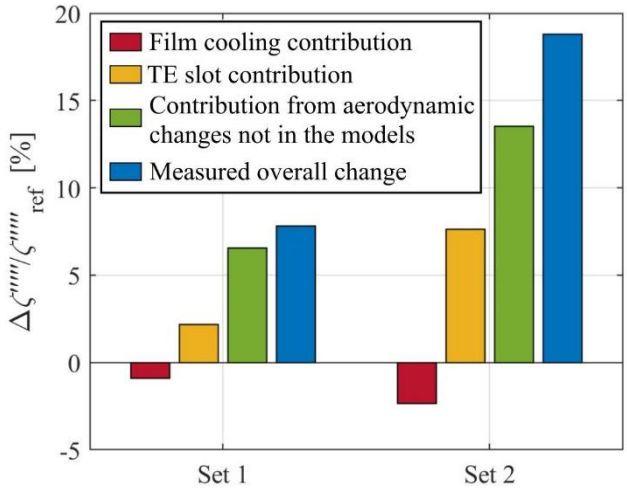


Figure 10: Summary of measured, predicted (by film and TE slot loss models, and by check-sum approach) changes in mixed-out KE loss coefficient for set 1 and set 2 parts.

Midspan profile total pressure loss: comparison with the study of Erickson et al. [12]

In this section we perform a detailed comparison of the measured changes in midspan profile total pressure loss—with increased surface roughness—to the results of study of Erickson et al. [12]. We consider this useful because of the high degree of similarity between the experiments. Erickson et al. tested two configurations: a *reference* cascade configuration in which the aerofoil surface (PS and SS) has an aerodynamically smooth surface (roughness height not reported); and a *rough* cascade configuration in which the entire PS and the first 10 % of the SS had a surface profile designed to simulate in-service roughening (the remaining SS had the same surface finish as the reference case). The reported k_s/C for the roughened surface was 0.98×10^{-3}, using the same reporting methodology as the present study [19].

For the comparison we consider only two vanes: the reference vane for set 1 (S1-V1); and vane S1-V10, which has no TE burn-back, and minimal changes in film cooling flow capacity and TE slot flow capacity (–0.31 % and –1.21 % respectively). These vanes were chosen to isolate the effect of roughness without conflating it with effects due to other deterioration features. For part S1-V10, average values of roughness were $k_s/C = 1.02 \times 10^{-3}$ for the PS and early SS, and $k_s/C = 0.29 \times 10^{-3}$ for the rest of the SS. These values were very similar to those in the Erickson et al. [12] study. Table 6 compares the two studies in terms of: experimental facility; operating conditions; details of tested components including roughness. The primary difference between the studies was unmatched exit Mach number (0.05–0.20 for Erickson et al. versus 0.92 for the present study).

We compare aerodynamic loss data using the metric of Erickson et al. [12]: a plane-average mid-span profile loss coefficient defined by

$$Y_p = \frac{p_{01} - \overline{p_{02}}}{p_{01} - \overline{p_2}} \tag{7}$$

in which $\overline{p_{02}}$ and $\overline{p_2}$ are the plane-average total and static pressures based on data in the 45–55 % span region. The method of calculation of the plane-average pressures ($\overline{p_{02}}$ and $\overline{p_2}$) is presented in [27]. For an extended discussion of relative merits of different loss coefficients see [24]. Comparison of plane-average instead of mixed-out loss coefficients is thought to be acceptable in this environment since the measurement plane for both studies is located at the same normalised axial distance from the vane TE (i.e. 0.25 C_{ax}), and therefore the result is less subject to traverse plane specification (see further discussion in [24]).

Table 6: Comparison of facility details, operating conditions and tested components between the present study and Erickson et al. [12]

Parameter	Erickson et al. [12]	Present study
Cascade type	Linear	Annular
Film cooling	No	Yes
Axial distance of measurement plane downstream of vane TE	0.25 C_{ax}	0.25 C_{ax}
Mean vane isentropic exit Mach no., $M_{2,is}$	0.05–0.20	0.92
Exit Reynolds no., Re_C	0.50×10^6–2.00×10^6	1.60×10^6
Vane inlet turbulence intensity, Tu	0.70–13.5 %	12 %
Equivalent sandgrain roughness height calculation method	Bons [19]	Bons [19]
Reference configuration		
Average equivalent sandgrain roughness height all around aerofoil, k_s/C	Not reported	0.11×10^{-3}
Rough configuration		
PS surface distance significantly roughened	0–100 %	0–100 %
SS surface distance significantly roughened	0–10 %	0–15 %
Rough surface type	Engine-representative	Engine-representative
Average equivalent sandgrain roughness height on PS and early SS, k_s/C	0.98×10^{-3}	1.02×10^{-3}
Average equivalent sandgrain roughness height on the rest of SS, k_s/C	Not reported	0.29×10^{-3}

Figure 11 shows a comparison between the change in Y_p (due to increased surface roughness) reported by Erickson et al. and reported in the present study. In the present study an increase in Y_p (from reference vane S1-V1) of 12.2 % was measured, for Tu = 12 %. Linearly interpolating the Erickson et al. data (between Tu = 8.50 % and Tu = 13.5 %, and between Re = 1.0×10^6 and Re = 2.0×10^6) gives an increase in Y_p of 15.2 %.

We take these results to be in good agreement, with the discrepancy potentially arising due to higher non-dimensional roughness for our reference ($k_s/C = 0.11 \times 10^{-3}$) than the vane used in the Erickson et al. study (reported to be aerodynamically smooth, defined by $k_s/C < 100/\mathrm{Re}_C$, i.e. $k_s/C < 0.05 \times 10^{-3}$). That is, we would expect our reference vane loss to be slightly higher than in the Erickson et al. study. We conclude the following: agreement between the results can be taken as evidence of cross-validation; from a whole-life modelling perspective, we propose profile loss enhancement factors in the range 12.2 % to 15.2 % for mid-life nozzle guide vanes with $k_s/C \sim 1.00 \times 10^{-3}$ on the PS and early SS, where the lower end of the range can be taken for parts with TBC coating, and the upper end for parts which are initially aerodynamically smooth.

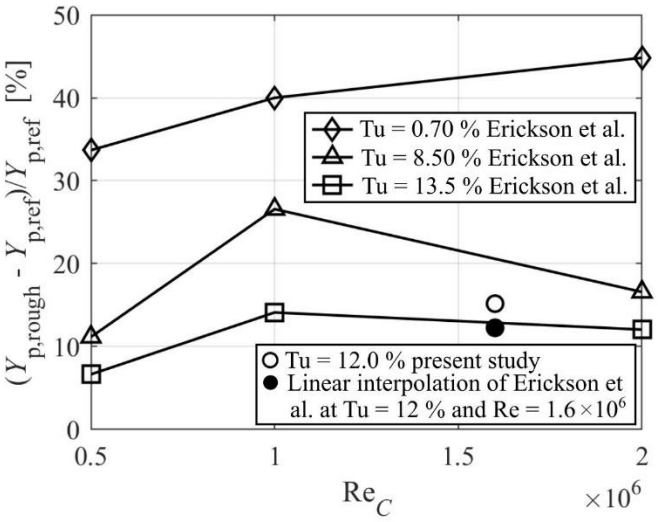


Figure 11: Comparison of the change in midspan profile total pressure loss coefficient between the present study and Erickson et al. [12].

Circumferential profiles of local KE loss coefficient

We now consider the circumferential profiles of local KE loss coefficient, $\zeta'(\theta)$, downstream of the vanes. Figure 12 and Figure 13 show the circumferential profiles of $\zeta'(\theta)$ at 10, 50 and 90 % span downstream of vanes of set 1 (S1-V1 to S1-V4) and set 2 (S2-V1 to S2-V4), respectively. Each profile is radially averaged over ±5 % at the relevant span location, and is circumferentially centered at its peak value. The distributions $\zeta'(\theta)$ are normalized by the maximum value of $\zeta'(r, \theta)$ measured across all the data presented.

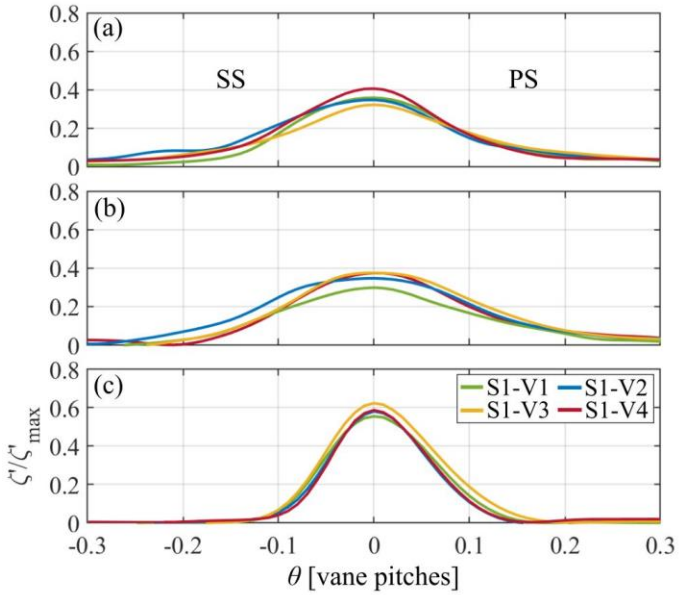


Figure 12: Circumferential profiles of $\zeta'(\theta)$ downstream of the set 1 (mid-life) vanes: (a) 90 % span; (b) 50 % span; (c) 10 % span.

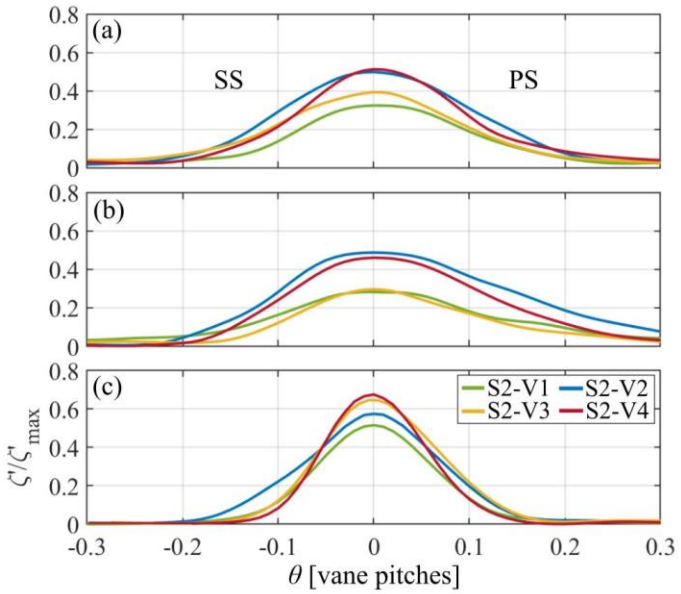


Figure 13: Circumferential profiles of $\zeta'(\theta)$ downstream of the set 2 (end-of-life) vanes: (a) 90 % span; (b) 50 % span; (c) 10 % span.

First consider the reference vanes: S1-V1 in Figure 12, and S2-V1 in Figure 13. As expected, the wake profiles have a quasi-normal distribution. The wake profiles at 10 % span are narrower and have a greater peak value of $\zeta'(\theta)$ than at 50 % and 90 % span. This is primarily due to spanwise variation of the TE position with respect to the traverse plane (see earlier discussion). The gradient of $\zeta'(\theta)$ is slightly greater moving

away from the SS than the PS. This is thought to be due to differences in the circumferential distributions of the separation loss contribution to overall loss, arising due to greater TE thickness on the PS than on the SS (design is of SS TE overhang style; see, for example, [30]). This effect opposes, and is thought to be more dominant than, the significantly larger boundary layer momentum thickness on the SS at the TE (for further discussion see [23,30]).

Now consider wake profiles for the deteriorated vanes of set 1: lines S1-V2 to S1-V4 in Figure 12. In general, the $\zeta'(\theta)$ profiles show higher peak loss, but with a similar profile shape as the undeteriorated vane. As discussed, this is due to greater profile loss and greater boundary layer thickening on account of the greater surface roughness. We characterize the circumferential profiles with three metrics: peak height (method of Burdett and Povey [23]); peak width (method of [23]); and integrated loss (IL) defined by

$$\mathrm{IL} = \int_{-0.5}^{0.5} \zeta'(\theta)/\zeta'_{\max}\,\mathrm{d}\theta \qquad (8)$$

Values for these metrics evaluated at 50 % span are presented in Table 7, both for the three deteriorated vanes of Figure 12, and for the parent set of 12 vanes. Taking an average across all 12 vanes, the mean changes in peak height, peak width, and integrated loss were 23.9 %, –1.67 % and 29.8 % respectively. That is, there is a substantial increase in overall loss, but relatively little thickening of the wake. This is because the wake width at the traverse plane is dominated by the width of the separated TE region (or *base region*), as opposed to the boundary layer thickness (more details in [23]), into which both the boundary layer loss and so-called *pressure drag* of the base region are subsumed.

Based on this statistically meaningful set of vanes (12 in total) we conclude that mid-life vanes can be characterized by a loss increase of approximately 30 %, with no substantial change in the wake width (rotor forcing implications) or profile shape. These numbers could be used in preliminary design for whole-life modelling.

Now consider the wake profiles for the deteriorated set 2 (end-of-life) vanes. For this set, the wake profile shapes for the deteriorated vanes differ from the reference vane by more than for the set 1 comparisons, on account of significant vortex activity associated with strong radial whirl angle variation in the regions of the TE burn-back. At the traverse plane, these secondary flows affect all span locations, but with a significant impact at midspan (where the burn-back is most severe). This leads to more local variation in the wake depth and width than for parts without TE burn-back. For all the three tested deteriorated vanes at all span locations, there was an increase in peak height, with the greatest increases in peak height being substantially larger than for the set 1 parts. That is, the peak loss was greater, but there was more randomness in the profile due to significant secondary flow activity. The mean changes (across three vanes) in peak height, peak width, and integrated loss were 46.7 %, –1.99 % and 24.5 % respectively. These are summarized in Table 7.

Based on the relatively small sample (three parts) we conclude that end-of-life vanes can be characterized by a loss increases in the range –20.4–61.8 % (relatively low confidence due to small statistical set). There is significant part-to-part variability in the integrated loss, but also in the radial distribution of loss, the wake shape and the associated secondary flow, leading to greater variability in the downstream rotor inlet flow.

Table 7: Metrics for wake characterization for set 1 (mid-life) and set 2 (end-of-life) vanes at 50 % span.

Vane	$\left(\zeta'/\zeta'_{\max}\right)_{\mathrm{peak}}$	Peak width	IL
S1-V1	0.299	0.225	0.0763
S1-V2	0.348	0.246	0.1071
S1-V3	0.376	0.223	0.0967
S1-V4	0.375	0.202	0.0952
Mean change S1-V(2–4)	22.5 %	–0.64 %	30.3 %
Mean change S1-V(2–12)	23.9 %	–1.67 %	29.8 %
S2-V1	0.283	0.245	0.0940
S2-V2	0.488	0.279	0.1521
S2-V3	0.297	0.203	0.0748
S2-V4	0.461	0.237	0.1244
Mean change S2-V(2–4)	46.7 %	–1.99 %	24.5 %

Radial distributions of flow angles

We now consider radial flow-angle distributions downstream of the vanes. Pitch and yaw angles (α_2 and β_2, respectively) are defined in Figure 14.

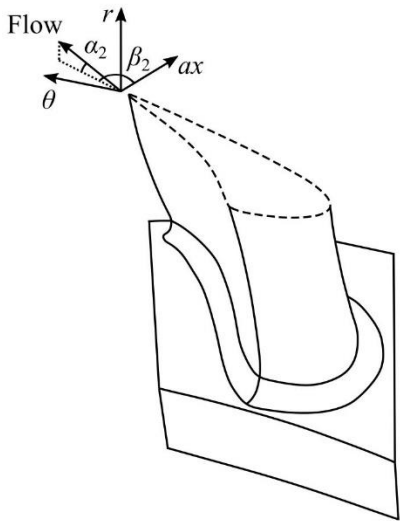


Figure 14: Flow angles definition diagram.

Spanwise distributions of circumferentially mass-flux-average flow angle (pitch angle, $\bar{\alpha}_2$, and yaw angle, $\bar{\beta}_2$) downstream of vanes in set 1 (S1-V1 to S1-V4) and set 2 (S2-V1 to S2-V4) are presented in Figure 15 and Figure 16 respectively.

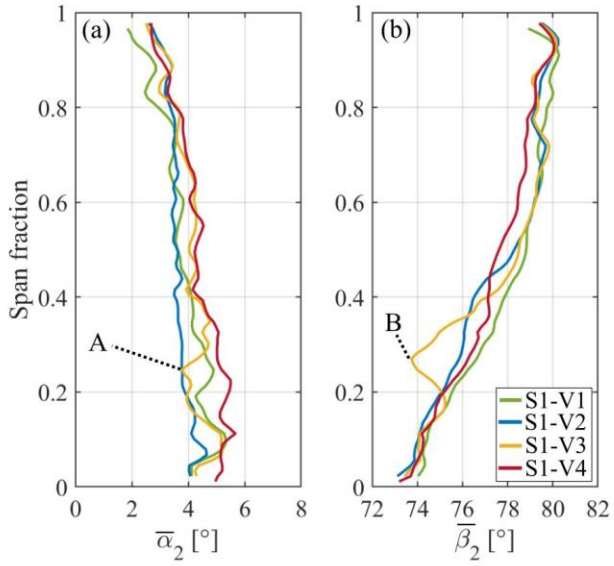


Figure 15: Radial profiles of circumferentially mass-flux-average flow angle downstream of set 1 vanes: (a) pitch angle; (b) yaw angle.

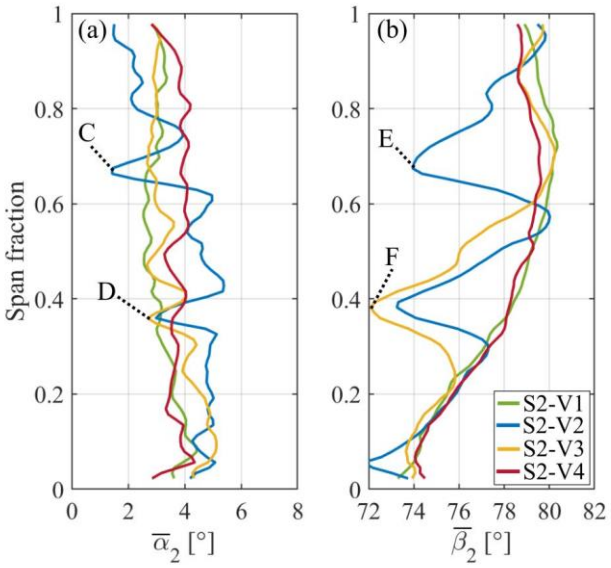


Figure 16: Radial profiles of circumferentially mass-flux-average flow angle downstream of set 2 vanes: (a) pitch angle; (b) yaw angle.

First consider the pitch angle results for the set 1 (mid-life) vanes (Figure 15). Radial distributions of pitch angle, $\bar{\alpha}_2$, are shown in Figure 15a. For the reference vane (S1-V1) pitch angle is small and positive and decreases slowly with increasing radius. This is thought to be due to the more prominent annulus hade at the hub than the case. That is, an overall annulus contraction, dominated by the hub annulus line hade (see Figure 2). The pitch angle trend is approximately linear with radius, varying between $1.9° < \bar{\alpha}_2 < 5.3°$. The mid-life vanes (S1-V2 to S1-V4) have the following characteristic differences from the reference vane: slightly greater mean pitch angle (by 0.2° on average); slightly lower spanwise variation (by –1.1° per unit of span on average); and slightly greater local variability from a linear trend (mean RMS variation of 0.5° from a linear trend compared to 0.4° for the reference vane). The small increase in both mean pitch angle and radial variation of pitch angle are not thought to arise from deterioration effects, but rather are thought to be due to quasi-random variation in the manufacturing of the vanes. The increased local variation is thought to arise from increased secondary flow activity, associated with surface defects, increased boundary layer thickness (and associated intensification of vortex features), and TE notching. Vane S1-V3 has the largest region of TE burn-back (see Figure 1a), and this is clearly associated with a local deviation in $\bar{\alpha}_2$. This is marked A in Figure 15a. The estimated value of $\Delta\bar{\alpha}_2$ (deviation from a locally linear trend for the particular vane) is $\Delta\bar{\alpha}_2 = –0.7°$.

Now consider radial yaw angle distribution for the mid-life vanes (Figure 15b). Looking at the reference vane, yaw angle increases with radius according to the particular forced vortex design of the vane, varying approximately linearly between $74.1° < \bar{\beta}_2 < 80.3°$. The effect of deterioration (S1-V2 to S1-V4) is threefold: to very slightly decrease the mean yaw angle (by 0.5° on average); to cause slightly more local variation in hub and case secondary flow regions (2–10 % span; 90–98 % span); and to cause strong local deviations in regions of TE burn-back. An example of this last effect is marked B in Figure 15b, for which the deviation from the locally linear trend for the particular vane was approximately $\Delta\bar{\beta}_2 = –1.9°$.

Now consider the corresponding results for the set 2 (end-of-life) vanes. The flow angle distributions downstream of the baseline vane (S2-V2) have similar trends to the baseline vane of set 1 (S1-V1). The aerodynamic vane standard was essentially identical so this was expected. For the deteriorated vanes, in regions of severe TE burn-back (see Figure 1b) there are significant variations in both pitch and yaw angles. The yaw angle variation arises because of under turning in regions of burn-back (see, for example, features E and F in Figure 16b). Pitch angle variation arises because of significant secondary flow associated with the strong shear (and associated secondary flow formation) at the edges of the burn-back regions (see, for example, features C and D in Figure 16a). For the most severe burn-back (vane S2-V2) the local under turning (deviation from local trend) was estimated to be $\Delta\bar{\beta}_2 = –6.1°$. The corresponding variation in local pitch angle was estimated to be $\Delta\bar{\alpha}_2 = –1.8°$.

We now consider the relationship between maximum yaw angle deviation, $(\Delta\bar{\beta}_2)_{\max}$, measured downstream of a particular burn-back feature, and the corresponding maximum depth of TE burn-back feature, $D_{\max}/C$. Three data points from set 1 parts (mid-life) and three data points from set 2 parts (end-of-life) are

presented in Figure 17. The data for both sets of parts were well-correlated with a linear trend of form

$$(\Delta\bar{\beta}_2)_{\max} = -47 D_{\max}/C \quad (9)$$

The trend was constrained to go through the origin for obvious physical reasons. A slightly better fit of set 1 data than set 2 data, and a slightly higher gradient for set 2 data than set 1 data (when individually fitted, not shown) may be explained by the greater radial extent of set 2 burn-back features, leading to less diminution of the yaw angle deviation effect in the intermediate mixing process (between vane TE and measurement plane). The empirical correlation (9) is proposed for preliminary whole-life performance assessment. The correlation would be improved with further experimental data taking separate account of both burn-back depth and radial extent.

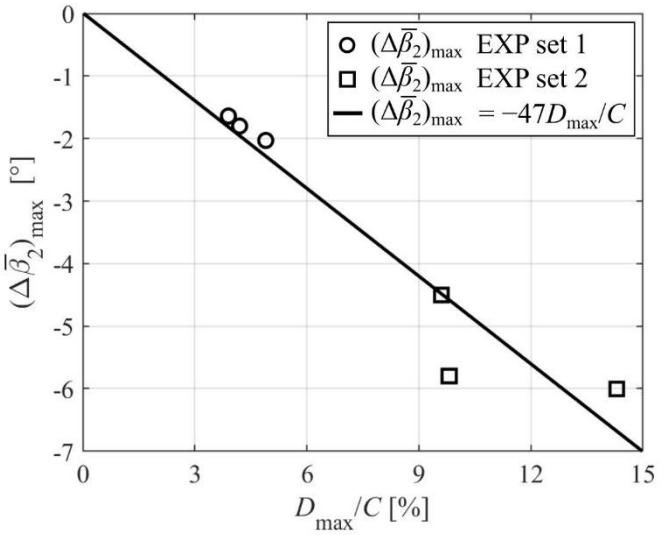


Figure 17: Maximum yaw angle deviation as a function of the maximum TE burn-back depth.

CONCLUSIONS

In this paper, 15 real-engine in-service-deteriorated HP NGVs with a broad variety of deterioration features were studied for the purpose of describing and quantifying their aerodynamic performance, as a step towards whole-life engine modelling. The deterioration features included increased surface roughness; thermal barrier coating spallation; damaged film cooling holes; and trailing edge burn-back. The study was split into six areas, from which the following conclusions were drawn:

1) *Surface roughness*. In-service roughening was found to primarily affect the PS and early SS, but not the late SS. For vanes initially coated with TBC, typical mean equivalent sandgrain roughness height was found to increase on the PS and early SS from $k_s/C = 0.109 \times 10^{-3}$ for new vanes, to $k_s/C = 0.590 \times 10^{-3}$ and $k_s/C = 0.222 \times 10^{-3}$ for mid-life and end-of-life vanes, respectively. These are increases of 441 % and 104 %—on average—for mid-life and end-of-life vanes in this study.
2) *Coolant flow capacity*. Coolant flow capacity decreased with service time both due to accumulation of deposits in the film cooling holes, and partial collapse of film cooling holes and TE slots due to overheating. For mid-life vanes, the mean change in coolant capacity was –2.20 % for the film cooling holes and –4.87 % for the TE slots. Corresponding values for end-of-life vanes were –5.77 % and –16.8 % respectively.
3) *Overall aerodynamic loss*. In-service deterioration was found to increase aerodynamic loss. The overall mean enhancement for mixed-out row KE loss was found to be approximately 8 % for mid-life vanes, and 19 % for end-of-life vanes. We propose these enhancement factors as rules of thumb for whole-life engine modelling. Mechanisms for increased mixed-out loss include: boundary layer thickening on the vane surface and endwalls due to increased surface roughness, causing change in transition point, and change in rate of growth of the boundary layer; streamwise vortex generation (and associated higher residual SKE) in the downstream wake caused by TE burn-back leading to high gradients of yaw angle; reduction in TE slot flow leading to increased base loss. In addition to these effects it is believed that the reduced cooling flow reduces loss, partly mitigating these increases (but leading to excessive part temperature).
4) *Separated loss components.* Using film cooling and TE slot loss models we show that of the 7.81 % and 18.8 % loss enhancements associated with mid-life and end-of-life deterioration, changes of –0.91 % and –2.36 % can be attributed to reduced film cooling flow (reduced loss), and 2.18 % and 7.62 % can be attributed to reduced TE flow (increased loss). The remaining 6.54 % and 13.5 %, respectively, are attributable to aerodynamic changes not included in the loss models, for example: boundary layer changes caused by surface roughness and spalling; changes in secondary flow behaviour caused by TE burn-back; and additional loss introduced at the point of coolant injection not captured in the basic model.
5) *Profile loss for undamaged mid-life parts.* Taking the results of the present study, and the study of Erickson et al. [12] together, we conclude that in-service deterioration increase profile loss of mid-life undamaged parts with $k_s/C \sim 1.00 \times 10^{-3}$ on their PS and early SS by between 12.2 % and 15.2 %, where the lower value corresponds to parts initially TBC coated, and the upper value for parts which were initially aerodynamically smooth.
6) *Downstream flow angles*: TE burn-back was found to locally reduce downstream pitch and yaw flow angles. A simple empirical correlation between maximum yaw angle deviation and maximum TE burn-back depth was presented, and is proposed for preliminary whole-life performance assessment (stage modelling).

This paper addresses a gap in literature, by providing the first detailed analysis of the *overall* impact of combined in-service deterioration features on the overall aerodynamic performance

of HP NGVs. It is hoped that the results from this paper will be a useful step towards whole-life engine performance modelling and assessment.

ACKNOWLEDGEMENTS

The financial support of Rolls-Royce plc is gratefully acknowledged. Nafiz Chowdhury and Daniel Burdett are thanked for their support with the experiments. David Newman is thanked for his support with the coolant capacity measurements and technical advice. The Laboratory for In-situ Microscopy and Analysis (LIMA) at the University of Oxford is also thanked for support of the surface roughness measurements.

NOMENCLATURE

Acronyms

CFD	computational fluid dynamics
ECAT	Engine Component AeroThermal (facility)
EXP	experiment
HP	high pressure
KE	kinetic energy
LE	leading edge
NGV	nozzle guide vane
PS	pressure surface
SS	suction surface
TBC	thermal barrier coating
TE	trailing edge
TRL	technology readiness level

Greek

α	pitch angle, °
$\bar{\alpha}$	circumferentially mass-flux-average pitch angle, °
β	yaw angle, °
$\bar{\beta}$	circumferentially mass-flux-average yaw angle, °
γ	ratio of specific heat capacities, –
Γ	capacity, kg s^{-1} $K^{1/2}$ Pa^{-1}
ζ	kinetic energy loss coefficient, –
ζ'	local kinetic energy loss coefficient, –
ζ''''	plane-average kinetic energy loss coefficient, –
ζ''''	mixed-out kinetic energy loss coefficient, –
θ	normalised (by vane pitch) circumferential position, –
χ	$(\gamma - 1)/\gamma$, –

Roman

ax	axial position, m
C	tangential chord, m
C_{ax}	axial chord, m
D	trailing edge damage depth, m
D_{max}	maximum trailing edge damage depth, m
IL	integrated loss, –
k	sandgrain roughness height, m
k_{s}	equivalent sandgrain roughness height, m
$\dot{m}$	mass flow rate, kg s^{-1}
M	Mach number, –
p	static pressure, Pa
p_0	total pressure, Pa
$\bar{p}$	plane-average static pressure, Pa
$\overline{p_0}$	plane-average total pressure, Pa
$\bar{p}'$	mixed-out static pressure, Pa
$\overline{p_0}'$	mixed-out total pressure, Pa
r	radial position, m
Re_C	exit Reynolds number based on tangential chord, –
R_{z}	maximum peak-to-valley roughness height, m
SKE	secondary kinetic energy, –
T	static temperature, K
T_0	total temperature, K
Tu	inlet turbulence intensity, –
x	streamwise distance, m
y	spanwise distance, m
Y_{p}	plane-average total pressure loss coefficient, –
z	wall-normal distance, m

Subscripts

1	upstream of HP NGVs
2	downstream of HP NGVs
atm	atmospheric
c	coolant
is	isentropic
ref	reference

REFERENCES

[1] Kurz, R., and Brun, K, 2001, "Degradation in Gas Turbine Systems." ASME Journal of Engineering for Gas Turbines and Power, 123(1): 70–77.

[2] Ozgurluk, Y., Doleker, K. M., Ahlatci, H., and Karaoglanli, A. C., 2018, "Investigation of Hot Corrosion Behavior of Thermal Barrier Coating (TBC) Systems With Rare Earth Contents." Arabian Journal of Geosciences, 11:267.

[3] Lorenz, M., Schulz, A., and Bauer, H., 2012, "Experimental Study of Surface Roughness Effects on a Turbine Airfoil in a Linear Cascade—Part II: Aerodynamic Losses." ASME Journal Turbomachinery, 134(4): 041007.

[4] Yun, Y. I., Park, I. Y., and Song, S. J., 2005, "Performance Degradation due to Blade Surface Roughness in a Single-Stage Axial Turbine." ASME Journal of Turbomachinery, 127(1): 137–143.

[5] Kind, R. J., Serjak, P. J., and Abbott, M. W. P., 1998, "Measurements and Prediction of the Effects of Surface Roughness on Profile Losses and Deviation in a Turbine Cascade." ASME Journal of Turbomachinery, 120(1): 20–27.

[6] Boyle, R. J., and Senyitko, R. G., 2003, "Measurements and Predictions of Surface Roughness Effects on the Turbine Vane Aerodynamics." Proceedings of the ASME Turbo Expo 2003, Atlanta, Georgia, USA, paper no. GT2003-38580.

[7] Hummel, F., Lötzerich, M., Cardamone, P., and Fottner, L., 2005, "Surface Roughness Effects on Turbine Blade Aerodynamics." ASME Journal of Turbomachinery, 127(3): 453–461.

[8] Abuaf, N., Bunker, R. S., and Lee, C. P., 1998, "Effects of Surface Roughness on Heat Transfer and Aerodynamic Performance of Turbine Airfoils." ASME Journal of Turbomachinery, 120(3): 522–529.

[9] Bammert, K., and Sandstede, H., 1976, "Influences of Manufacturing Tolerances and Surface Roughness of Blades on the Performance of Turbines." ASME Journal of Engineering for Gas Turbines and Power, 98(1): 29–36.

[10] Vera, M., Zhang, X. F., Hodson, H., and Harvey, N., 2007, "Separation and Transition Control on an Aft-Loaded Ultra High-Lift LP Turbine Blade at Low Reynolds Numbers: High-Speed Validation." ASME Journal of Turbomachinery, 129(2): 340–347.

[11] Matsuda, H., Otomo, F., Kawagishi, H., Inomata, A., Niizeki, Y., and Sasaki, T., 2006, "Influence of Surface Roughness on Turbine Nozzle Profile Loss and Secondary Loss." Proceedings of the ASME Turbo Expo 2006, Barcelona, Spain, paper no. GT2006-90828.

[12] Erickson, E. L., Ames, F. E., and Bons, J. P., 2010, "Effects of a Realistically Rough Surface on Vane Aerodynamic Losses Including the Influence of Turbulence Condition and Reynolds Number." Proceedings of the ASME Turbo Expo 2010, Glasgow, UK, paper no. GT2010-22173.

[13] Bons, J. P., 2010, "A Review of Surface Roughness Effects in Gas Turbines." ASME Journal of Turbomachinery, 132(2): 021004.

[14] Vazquez, R., Torre, D., Partida, F., Armananzas, L., and Antoranz, A., 2011, "Influence of Surface Roughness on the Profile and End-Wall Losses in Low Pressure Turbines." Proceedings of the ASME Turbo Expo 2011, Vancouver, Canada, paper no. GT2011-46371.

[15] Sjolander, S., Isaacs, D., and Klein, W., 1993, "Aerodynamics of Turbine Blades With Trailing-Edge Damage: Measurements and Computations." XI International Symposium on Air Breathing Engines, Tokyo, Japan, paper no. ISABE 93-7130.

[16] Di Mare, L., Imregun, M., Smith, A., and Elliott, R., 2007, "A Numerical Study of High Pressure Turbine Forced Response in the Presence of Damaged Nozzle Guide Vanes." The Aeronautical Journal, 111(1125), 751-757.

[17] Meyer, M, Parchem, R, and Davison, P., 2011, "Prediction of Turbine Rotor Blade Forcing due to In-Service Stator Vane Trailing Edge Damage." Proceedings of the ASME Turbo Expo 2011, Vancouver, Canada, paper no. GT2011-45204.

[18] Bouchard, D., Asghar, A., LaViolette, M., Allan, W. D. E., and Woodason, R., 2014, "Experimental Evaluation of Service-Exposed Nozzle Guide Vane Damage in a Rolls Royce A-250 Gas Turbine." ASME Journal of Engineering for Gas Turbines and Power, 136(10): 102601.

[19] Bons, J., 2005, "A Critical Assessment of Reynolds Analogy for Turbine Flows." ASME Journal of Heat Transfer, 127(5): 472–485.

[20] Bons, J. P., Taylor, R. P., McClain, S. T., and Rivir, R. B., 2001, "The Many Faces of Turbine Surface Roughness." ASME Journal of Turbomachinery, 123(4): 739–748.

[21] Kirollos, B., Lubbock, R., Beard, P., Goenaga, F., Rawlinson, A., Janke, E., and Povey, T., 2017, "ECAT: An Engine Component Aerothermal Facility at the University of Oxford." Proceedings of the ASME Turbo Expo 2017, Charlotte, North Carolina, USA, paper no. GT2017-64736.

[22] Burdett, D., Hambidge, C., and Povey, T., 2020. "Analysis of Ultra-low Uncertainty Gas Turbine Flow Capacity Measurement Techniques." Proceedings of the Institution of Mechanical Engineers, Part A: Journal of Power and Energy, 235(5), 1053–1079.

[23] Burdett, D. and Povey, T., 2022, "Experimental and Numerical Analysis of Loss Characteristics of Cooled Transonic Nozzle Guide Vane." ASME Journal of Turbomachinery, 144(5): 051009.

[24] Burdett, D., and Povey, T., 2022, "Analysis of Averaging Methods for Nonuniform Total Pressure Fields." ASME Journal of Turbomachinery, 144(5): 051011.

[25] Kirollos, B., and Povey, T., 2017, "Method for Accurately Evaluating Flow Capacity of Individual Film-Cooling Rows of Engine Components." ASME Journal of Turbomachinery, 139(11): 111004.

[26] Dzung, L.S., 1971, Konsistente Mittlewerte in der Theorie der Turbomaschinen für Kompressible Medien; BBC-Mitt., Vol. 58, pp. 485–492.

[27] Day, C.R.B., Oldfield, M.L.G. and Lock, G.D., 2000, "Aerodynamic Performance of an Annular Cascade of Film Cooled Nozzle Guide Vanes Under Engine Representative Conditions." Experiments in Fluids, Vol. 29, pp.117–129.

[28] Hartsel, J. E., 1972, "Prediction of Effects of Mass-Transfer Cooling on the Blade-Row Efficiency of Turbine Airfoils." AIAA Tenth Aerospace Sciences Meeting, San Diego, California, USA, AIAA Paper No. 72-11.

[29] Burdett, D., Goenaga, F., and Povey, T., 2021, "Understanding Capacity Sensitivity of Cooled Transonic Nozzle Guide Vanes: A Parametric Experimental and Computational Study of the Impact of Trailing Edge Geometry." ASME Journal of Turbomachinery, 143(5): 051001.

[30] Burdett, D., and Povey, T., 2021, "Impact of Trailing Edge Overhang Length on the Loss Characteristics of Fully Cooled Transonic Nozzle Guide Vanes." (accepted – awaiting full ref).

[31] Stewart, W. L., 1955, "Analysis of Two-Dimensional Compressible-Flow Loss Characteristics Downstream of Turbomachine Blade Rows in Terms of Basic Boundary Layer Characteristics." NACA Technical Note 3515.1955.

[32] Deckers, M, and Denton, J. D., 1997, "The Aerodynamics of Trailing-Edge-Cooled Transonic Turbine Blades: Part 2 — Theoretical and Computational Approach." Proceedings of the ASME 1997 International Gas Turbine and Aeroengine Congress and Exhibition, Orlando, Florida, USA. Paper no. 97-GT-519.

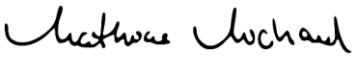
Statement of Authorship for joint/multi-authored papers for PGR thesis

To appear at the end of each thesis chapter submitted as an article/paper

The statement shall describe the candidate's and co-authors' independent research contributions in the thesis publications. For each publication there should exist a complete statement that is to be filled out and signed by the candidate and supervisor **(only required where there isn't already a statement of contribution within the paper itself).**

Title of Paper	Experimental Study of Impact of In-Service Deterioration on Aerodynamic Performance of High-Pressure Nozzle Guide Vanes
Publication Status	□ Published □ Accepted for Publication ■ Submitted for Publication □ Unpublished and unsubmitted work written in a manuscript style
Publication Details	Michaud, M., Jackson, D., Goenaga, F., and Povey, T., 2022, "Experimental Study of Impact of In-service Deterioration on Aerodynamic Performance of High-Pressure Nozzle Guide Vanes."

Student Confirmation

Student Name:	Mathias Michaud		
Contribution to the Paper	Mathias Michaud performed all the experiments, post-processed all the data, led the writing of the manuscript and contributed to the analysis. Dougal Jackson and Frederic Goenaga contributed to the analysis. Thomas Povey provided the original research idea, contributed to the analysis and the writing of the manuscript.		
Signature 		Date	07/12/2021

Supervisor Confirmation

By signing the Statement of Authorship, you are certifying that the candidate made a substantial contribution to the publication, and that the description described above is accurate.

Supervisor name and title: Professor Thomas Povey		
Supervisor comments: I certify that the candidate made a substantial contribution to the publication, and that the description described above is accurate.		
Signature: 	Date	22/01/2022

This completed form should be included in the thesis, at the end of the relevant chapter.

6. Impact of In-service Deterioration on the Thermal Performance of High-Pressure Nozzle Guide Vanes

This chapter consists of a preprint journal paper detailing the experimental study to evaluate the impact of in-service deterioration on the thermal performance of heavily film-cooled HP NGVs. This chapter provides an example of heat transfer research that can be performed in a high TRL research turbine facility. Although the overall impact of deterioration could reasonably be expected to be well-modelled by superposition of the individual deterioration effects, there is a lack of overall cooling effectiveness data when many deterioration effects are combined. The purpose of this work is to provide a reference point for whole-life aerothermal performance modelling. The nomenclature and references included in this chapter are self-contained and differ in numbering and order compared to the overall thesis.

EXPERIMENTAL STUDY OF IMPACT OF IN-SERVICE DETERIORATION ON THERMAL PERFORMANCE OF HIGH-PRESSURE NOZZLE GUIDE VANES

Mathias Michaud, Nafiz H. K. Chowdhury and Thomas Povey*

Department of Engineering Science, University of Oxford, Parks Road, Oxford, OX1 3PJ, UK

ABSTRACT

In this paper we analyse the impact of in-service deterioration on the overall thermal performance (*metal effectiveness*) of heavily-cooled high-pressure nozzle guide vanes, of a design typical of large civil jet engines. We study 15 deteriorated parts (increased surface roughness; thermal barrier coating spallation and sintering; damaged film cooling holes; and trailing edge burn-back) from operational engines, and compare their thermal performance to that of equivalent new parts. Overall cooling effectiveness measurements were performed in the Engine Component AeroThermal (ECAT) facility at the University of Oxford, at engine-representative conditions of Mach number, Reynolds number, coolant-to-mainstream pressure ratio, and turbulence intensity. We characterize the degradation of overall cooling effectiveness with service time; this is an important result for whole-life modelling. In the analysis we attempt to decouple the contributions from independent deterioration effects, and compare the philosophy of this *top-down* approach to the *bottom-up* approach in which effects are studied in isolation then superposed in modelling. A companion paper [1] focuses on the *aerodynamic* impact of in-service deterioration.

INTRODUCTION AND RELATED LITERATURE

High-pressure (HP) nozzle guide vanes (NGVs) operate in a hostile environment and deteriorate with service time due to oxidation [2], deposition of airborne and fuel contaminants [3], thermal fatigue cracking [4] (e.g., of the thermal barrier coating (TBC) layer) and erosive impact-abrasion [5]. These deterioration mechanisms cause local changes in surface roughness, and global changes in geometry [6, 7]. TBC spallation and cracking at the leading edge (LE) is common, and TBC sintering due to long exposure to high temperature can cause an increase in thermal conductivity [8]. The partial or complete collapse of cooling holes (smaller effective size) is common, as is partial blockage or geometry change of holes due to internal or external particulate deposition [9]. Partial collapse of trailing edge (TE) slots due to overheating can cause reduced TE slot coolant flow capacity. These deterioration features can exist in isolation or, more commonly, in parallel to varying degrees, but with complex interactive effects. Here we must recall that the vane has both an internal-cooling and (external) film-cooling system, and acts as a complex heat exchanger, with both forward-pass and reverse-pass elements [10–12]. The vane must properly, therefore, be regarded as highly coupled both locally in the through-wall direction, and globally at the system-level of the vane. Because of this coupling, the physical changes associated with deterioration mechanisms impact the thermal performance of the vane in an extremely complex manner. For this reason, it is particularly important to benchmark whole-life engine models with assessments of engine-run parts performed in an engine-realistic environment, in a so-called *top-down* approach. This is, of course, complementary to existing studies in the open literature related to: impact of surface roughness on external heat transfer coefficient (HTC) and on adiabatic film cooling effectiveness; and the impact of in-service TBC deterioration on the vane wall thermal resistance. We review this literature now.

Impact of surface roughness on external heat transfer coefficient

There have been a number of cascade experiments to assess the impact of surface roughness on the external HTC distribution of turbine components. The majority of these studies have used either simulated roughness (sandgrain, hemisphere, and truncated cone) [13–18] or surface finishes arising from manufacturing processes (e.g. milling, polishing and coating) [19–22]. There is only one study—to the authors' knowledge—in which an engine-representative surface roughness distribution was simulated [23]. Bons [7] provides a comprehensive review of gas-turbine-relevant roughness literature up to 2010. So far as turbine component external HTC is concerned, the consensus is that an increase in surface roughness causes an increase in external HTC due to both earlier laminar-turbulent boundary layer transition and enhanced mixing in the turbulent boundary layer. This is, of course, unsurprising. Most studies [15, 16, 17, 19, 20, 22, 23] suggest that increased roughness does not significantly impact heat transfer in the laminar region of the boundary layer.

Erickson et al. [23] performed a study similar to the present one in terms of: operating conditions, roughness type, roughness modelling, roughness height and roughness distribution around the aerofoil (see [1]). Using a low-speed linear cascade, the authors measured the external heat transfer distribution on two vanes: a *reference* vane which has an aerodynamically smooth (roughness height not reported) surface; and a *rough* vane which has the entire PS and the first 10 % of the suction surface (SS) roughened with a surface profile generated by an accelerated deposition facility to simulate in-service roughening, and with the remaining SS of the same surface finish as the reference case. The normalized (by tangential chord C) equivalent sandgrain roughness height (k_s) of the roughened surface was $k_s/$

$C = 0.98 \times 10^{-3}$. Measurements were taken over an exit Re (based on tangential chord) range $0.50 \times 10^6 < \mathrm{Re} < 2.0 \times 10^6$ and Tu range 0.70 % < Tu < 13.5 %. In agreement with other literature, they measured increased HTC on the vane, attributed this to both earlier laminar-turbulent boundary layer transition and enhanced mixing in the turbulent boundary layer. At $\mathrm{Re} = 1.00 \times 10^6$ and Tu = 13.5 %, they measured area-average increases in HTC (with respect to the reference vane) up to approximately 25 % and 35 % on the PS and early SS, respectively. No significant change in HTC was observed on the late SS. They additionally found that that the boundary layer transition onset was independent of the turbulence level, and that the heat transfer in the laminar boundary layer was unaffected by roughness.

Impact of surface roughness on adiabatic film cooling effectiveness

We now review the literature on the impact of surface roughness on adiabatic film cooling effectiveness, η_f. Experiments have been performed using flat plates [24–28] and linear cascades [18, 29]. The general trend reported is that an increase in surface roughness upstream of a film cooling row leads to a thicker boundary layer and hence a higher *effective local* blowing ratio B (or, by the same token, momentum flux ratio I) which increases the tendency for film lift-off (separation). Increased surface roughness downstream of a film cooling row was found to reduce η_f at low B due to enhanced near-wall roughness-induced turbulent mixing between coolant and mainstream flows. At high B, increased surface roughness downstream of a film cooling row was less detrimental to film cooling performance, and in certain cases increased η_f. This was thought to be the result of enhanced early mixing reducing penetration of the jet into the mainstream. We now review the most relevant study in more detail.

Rutledge et al. [18] investigated the impact of surface roughness on adiabatic film cooling effectiveness and external HTC on the SS of a vane in a low-speed linear cascade. The exit Re (based on tangential chord) was 1.06×10^6, the inlet Tu was 21 % and the blowing ratio range was $0.3 < B < 1.4$. The SS was cooled with a cooling row with cylindrical holes and located at a normalized surface distance $l/C = 0.208$. Two types of surface were considered in the study: an *aerodynamically smooth* surface (roughness height not reported); and a *rough* surface which consisted of a simulated array of cones with $k_s/C = 0.842 \times 10^{-3}$. Four surface roughness configurations were studied: a *smooth* configuration in which the entire aerofoil was aerodynamically smooth; an *upstream rough* configuration with a rough surface upstream of the film cooling row; a *downstream rough* configuration with a rough surface downstream of the film cooling row; and an *all rough* configuration with a rough surface upstream and downstream of the film cooling row. For $B = 0.3$, they reported decreases (with respect to smooth configuration) in area-average adiabatic film cooling effectiveness ($\bar{\bar{\eta}}_f$) of 29 %, 25 % and 31 % for the upstream, downstream and all rough configurations, respectively. In contrast, for $B = 1.4$, they reported increases in $\bar{\bar{\eta}}_f$ of 11 %, 73 % and 86 % for the upstream, downstream and all rough configurations, respectively. The effect of roughness on $\bar{\bar{\eta}}_f$ was found to be minimal for $B = 0.85$. This contrary behavior was explained by roughness-induced mixing in the case of films already attached ($B = 0.3$), and a roughness-induced decreased tendency to detach at higher blowing ratio ($B = 1.4$). At the intermediate condition ($B = 0.85$) it might be assumed that the two effects are opposite in direction but similar in magnitude. They also reported that roughness caused an increase in external surface heat flux (driven by changes in both η_f and HTC) of 30–70 % under their operating conditions.

Impact of in-service TBC deterioration on wall thermal resistance

We now consider the in-service deterioration of TBC and its impact on heat transfer in turbine components. There are three primary deterioration mechanisms of TBC prior to mechanical failure (i.e. spallation): sintering [30]; erosion [8, 31]; local impact damage [8, 31]. We now briefly review these mechanisms. The type of TBC considered is yttria-stabilized zirconia (YSZ) produced by electron-beam physical vapor deposition (EBPVD). This is the TBC type used on the vanes in the current study.

Rätzer-Scheibe and Schulz [30] studied the effect of sintering on the thermal conductivity of EBPVD YSZ TBC. They exposed a 280 μm thick coating to air at a temperature of 1100 °C (engine-representative surface temperature) for 100 and 200 hours. They found that this temperature exposure had raised the thermal conductivity of the TBC (κ_{TBC}) from $\kappa_{\mathrm{TBC}} = 1.34$ W m^{-1} K^{-1} (new) to $\kappa_{\mathrm{TBC}} = 2.01$ W m^{-1} K^{-1} after 100 hours (measured at 30 °C, i.e. representative of lab conditions), an increase of approximately 50 %. There was no significant change in κ_{TBC} between 100 and 200 hours.

Wellman and Nicholls [31] and Darolia [8] reviewed the literature (to 2007 and to 2013, respectively) related to erosion and impact damage of TBC, including EBPVD TBC. They reported that TBC can be significantly eroded by ingested particles during engine operation. Erosion rates were greater at the LE and on the SS, than on the PS. They also reported that the impact of particles under a high temperature can compact the TBC. Erosion and impact damage during service therefore act to reduce the thermal resistance of the TBC by reducing its thickness. The results vary widely with service environment and duration—with erosion between 0 and 100 % of original coating thickness—and therefore it is hard to draw generalized quantitative conclusions.

Objective of this study

Current understanding of the impact of deterioration on the thermal performance of turbine components is based on a series of simplified studies in which individual deterioration features are isolated, modelled and tested. In this bottom-up approach (see discussion in [32]) it is necessary to build a model in which individual effects are superposed. This approach introduces error in the superposition (reliance on many individual correlations), and does not allow for the possibility of coupling. An alternative approach is the top-down approach, in which a statistically-

relevant set of real engine parts subject to in-service deterioration are directly characterized at engine conditions. This approach has the advantage of providing direct assessment of the change in performance, suitable—for example—for building whole-life engine models, but the disadvantage that it is relatively difficult to de-couple individual effects. In this study we take the latter approach, and characterize—in detail—the change in overall cooling effectiveness (so-called *metal effectiveness*) with in-service deterioration. We do this using a set of 15 engine-run parts and two new parts, in a test at engine-representative conditions of exit Mach number, Reynolds number, and coolant-to-mainstream pressure ratio. We use supplementary testing (coolant capacity measurements, for example) and modelling to provide insight into the driving mechanisms for the observed changes in performance.

CHARACTERIZATION OF TEST COMPONENTS

We now characterize the vanes that were used for this study. Two sets of real-engine in-service-deteriorated vanes from modern large civil jet engines were used. Set 1 was composed of 12 mid-life parts and one reference part. Set 2 consisted of 3 end-of-life parts and one reference part. The vanes in set 1 and 2 are from the same engine class, but had slightly different as-new geometries: comparison between sets should therefore be avoided. All the vanes are fully featured, including film cooling holes, TE slots and thermal barrier coatings (TBC). The deteriorated vanes in a particular set were from the same engine, and therefore had been operated in the same environment and have the same number of cycles. A summary of the operation history of both sets of vanes is given in Table 1. Individual vanes are identified using their set number (S1 or S2) and vane number within the set (V1, V2, etc.).

Table 1: Descriptive summary of the operation history of the in-service-deteriorated parts, and corresponding reference parts, in set 1 and set 2.

Parameter	Set 1	Set 2
Number of vanes	12 (+1 new)	3 (+1 new)
Position in life cycle	Mid-life.	End-of-life.
Operating environment	Non-sandy.	Non-sandy.

Experimental data was acquired for all the vanes within set 1 and set 2. In this paper we present detailed measurements for only four vanes within each set (one new vane and three deteriorated vanes), but high-level statistical data for the entire set. We refer to selected set 1 vanes as: S1-V1 (new); and S1-V2, S1-V3 and S1-V4 (mid-life). The corresponding nomenclature for set 2 is: S2-V1 (new); and S2-V2, S2-V3 and S2-V4 (end-of-life). In set 1, we chose the deteriorated vanes that were the most representative of the set.

We now characterize the deterioration features of the tested vanes. We consider the changes in geometry, surface roughness, and coolant capacity. A more detailed description of the same data is presented in a companion paper [1] which deals with characterization of the aerodynamic performance of the vanes.

TBC spallation and TE burn-back

We now summarize the geometry changes with deterioration. Figure 1 shows a schematic of the geometry of set 1 (mid-life) vanes S1-V1 to S1-V4 and set 2 (end-of-life) vanes S2-V1 to S2-V4. Film cooling holes and the TE slot are omitted for clarity.

First consider the deteriorated vanes of set 1 (mid-life vanes). The mid-life vanes have only minor geometry changes. There are some very narrow (in the streamwise direction) bands of TBC spallation at the LE of some vanes, covering less than 10 % of the span of the vanes (see Figure 1a). Most of the mid-life vanes had suffered partial collapse of the TE slot due to overheating and thermal distortion. Some vanes had notch-like TE burn-back, with notches extending to 18 % of the span of the vane and to a depth of 5 % of the tangential chord (see Figure 1a). Film cooling holes were partially blocked due to particle deposition (see [1]), but internal cooling passages were essentially the same as new parts.

The set 2 (end-of-life) vanes exhibited more significant geometry changes. The LE of these vanes were severely damaged, with regions of TBC spallation extending up to 65 % of the span and 30 % of the tangential chord (see Figure 1b). In the showerhead region there was significant collapse (reduction in diameter) of the film cooling holes, and enchained cracking between holes (see [1]). The TE of the end-of-life vanes had severe TE burn-back, with the damage extending across 80 % of the span and to a depth of 14.2 % of the tangential chord. Despite the relatively severe external damage, the internal cooling passages were essentially the same as new parts.

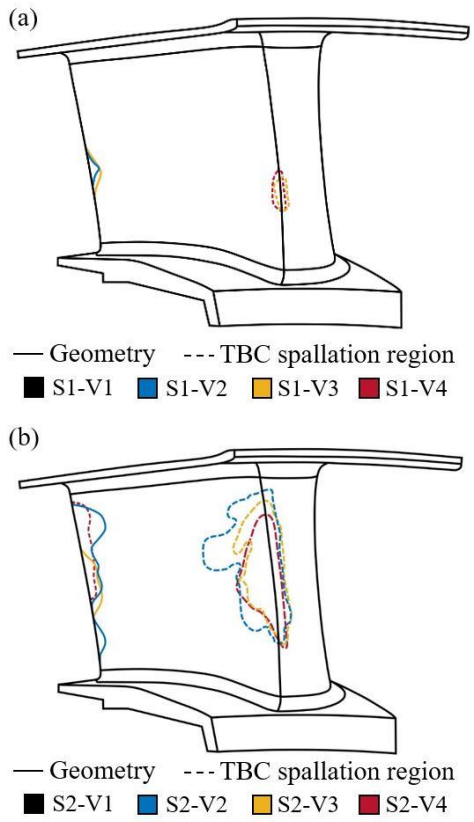


Figure 1: Deterioration characterization for a selection of vanes from: (a) set 1; (b) set 2.

Coolant capacity

We now summarize the change in coolant capacity due to in-service deterioration. Coolant capacity is defined

$$\Gamma_c = \frac{\dot{m}_c \sqrt{T_{0c}}}{p_{0c}} \quad (1)$$

where $\dot{m}_c$ is the total coolant mass flow rate, and p_{0c} and T_{0c} are the total pressure and total temperature of the coolant flow in the feed plenum (see Figure 2a). Measurements of coolant capacity were performed ex-situ (i.e. in the absence of the potential field developed by the vane) on individual vanes in a bench-test experiment to separate effects on a per-vane basis. Measurements were taken with all film cooling holes and the TE slot open, and also with the TE slot sealed but films open. This allowed separation of the film coolant capacity and the TE slot coolant capacity. By using a low order model which takes the in situ aerodynamic field as one of its inputs, it is possible to infer the in-situ coolant capacity from the ex-situ measurements. The process is explained in more detail in [1].

Taking all 12 deteriorated vanes within set 1 (mid-life), the mean proportional changes in coolant capacity with respect to the reference vane were –2.20 % for the film holes and –4.87 % for the TE slot. The changes appeared to be primarily associated with particle deposition (blockage) within the film holes, and partial collapse of the TE slot due to overheating. Photographs of these effects are shown in [1].

Taking the 3 deteriorated vanes of set 2 (end-of-life) the mean proportional changes in coolant capacity with respect to the reference vane were –5.77 % for the film holes and –16.8 % for the TE slot. For the end-of-life vanes, the decreased coolant capacity appears to be primarily associated with collapse of the film cooling holes in the region of spalled TBC (local overheating), an effect which is partially offset by weeping cracks in the same region. The decrease in TE slot coolant capacity was caused by the same mechanism as for mid-life vanes (partial collapse associated with overheating) but the severity and radial extent of damage were significantly greater.

Changes in coolant capacity for individual vanes are presented and analysed in the companion paper [1].

Surface roughness measurements

In this section we summarize changes in surface roughness with in-service deterioration. Profilometry measurements were performed using an Alicona InfiniteFocus profilometer (non-contact optical three-dimensional surface measurement system) at 21 locations around each vane. Each profilometry measurement was used to calculate an equivalent sandgrain roughness height, k_s. Results are normalized by the tangential chord, C, of the vanes. In-service roughening was found to be most significant on the PS and early SS of the vanes, and was primarily attributed to particle deposition rather than oxidation. The late SS was found to be only slightly rougher for deteriorated parts than new TBC. Table 2 summarizes mean values of k_s/C measured on the PS and early SS (12 measurement regions), and on the late SS (9 measurement regions). More details of the measurement method, roughness modelling and spatial distribution of k_s/C on individual vanes can be found in [1].

Table 2: Normalized equivalent sandgrain roughness measurements for set 1 and set 2 parts.

Vane	k_s/C ($\times 10^{-6}$)	
	PS & early SS	Late SS
Reference vane S1-V1	109	107
Mean S1-V(2–13)	590	164
Mean change S1-V(2–13)	441 %	53 %
Reference vane S2-V1	111	109
Mean S2-V(2–4)	226	163
Mean change S2-V(2–4)	104 %	50 %

EXPERIMENTAL FACILITY AND MEASUREMENT TECHNIQUES

Overall cooling effectiveness measurements were conducted in the Engine Component AeroThermal (ECAT) facility at the University of Oxford [32]. This is a high technology readiness level (TRL) blowdown facility capable of testing an annular cascade of HP NGVs at engine-representative conditions of Mach number, Reynolds number and coolant-to-mainstream total pressure ratio. Much of the research in the facility is focused

on vanes from operating engines. Figure 2a shows a schematic cross-section of the facility working section with the infrared (IR) cameras installed and Figure 2b shows an unwrapped schematic of the cascade. In this campaign, the overall cooling effectiveness was measured on the PS and early SS of the vanes by the upstream IR camera, and on the late SS of the vanes by the downstream camera.

Facility operation and test conditions

During a test, high-pressure air stored in large (60 m^3) tanks is discharged through the cascade. For overall cooling effectiveness measurements, the facility is operated in regulated blowdown mode, with a constant inlet supply pressure allowing quasi-steady conditions for approximately 60 seconds. The time constant of the part is approximately 3 second, and therefore quasi-steady-state is achieved in a small fraction of the overall run time. The mainstream air is heated using two 1 MW air heaters, which increase the mainstream temperature by approximately 50 K above ambient. Coolant air is drawn from the same system, feeding independent hub and case manifolds (see Figure 2a). For this particular campaign, measurements were taken at a coolant-to-mainstream total pressure ratio $p_{0c}/p_{01} = 1.027$. The facility operating conditions are summarized in Table 3.

Table 3: ECAT facility operating conditions for the current study.

Parameter	Value
Mainstream inlet total temperature, T_{01}	350 K
Mainstream inlet total pressure, p_{01}	1.90 bar
Mean vane pressure ratio, p_2/p_{01}	0.58
Mean vane isentropic exit Mach no., $M_{2,is}$	0.92
Vane exit Reynolds number, Re_C	1.60×10^6
Vane inlet turbulence intensity, Tu	12 %
Operating temperature ratio, T_{01}/T_{0c}	1.20
Operating pressure ratios, p_{0c}/p_{01}	1.027
Coolant mass fractions, $\dot{m}_c/\dot{m}$	10 %

Instrumentation for overall cooling effectiveness measurements

Mainstream total pressure and total temperature measurements upstream of the cascade (p_{01} and T_{01}) were performed using probe rakes (approximate axial location shown in Figure 2a). Hub and case coolant cavity total pressure and total temperature (p_{0c} and T_{0c}) were measured at four circumferential positions. The vane exit static pressure ($p_{2,hub}$ and $p_{2,case}$) was measured on six vanes (from a total of 40), with tappings located on the hub and case platform overhangs approximately 5 mm downstream of the cascade TE plane. Each of the six vanes was instrumented with six tappings at the hub and eight at the case (i.e. 84 tappings in total).

The external surface temperature of the vanes was measured using two IR cameras (FLIR A655sc) which are located within the main pressure vessel (see Figure 2a), as shown in Figure 2b. One camera is located 10 axial chords upstream of vane LE and views the entire PS and early SS of three vanes. A second camera is located seven axial chords downstream of the vane annulus and is able to view the late SS of three vanes. The cameras are installed within protective housings, sealed from the high-pressure working gas, but connected to atmosphere via a vent line. The housings have zinc selenide (ZnSe) windows with anti-reflective coatings. The cameras can be rotated to any circumferential position in the annulus, allowing the entire vane ring to be studied.

To allow in-situ calibration of the IR measurement-chain, we use a bespoke calibration system placed in the field of view (FOV) of each IR camera, and assembled on to the NGV surface. The system consists of a 4 mm diameter disk of copper (approximately 0.5 mm thick) mounted over polyimide film (low thermal conductivity). The copper disk has an underside surface thermocouple. This provides a region of uniform temperature, installed so as not to disturb the flow, and with low measurement error even in regions of significant through-wall and/or lateral temperature gradient (e.g. real engine vanes). A detailed assessment of the system is provided in [33]. As shown in Figure 2b, two surface thermocouples are installed on a *calibration vane* (CV) adjacent to the *studied vane* (SV). This is to avoid any surface disruption on the studied vane. The surface thermocouples are installed on the early PS and late SS of the calibration vane, in the fields of view of the IR cameras.

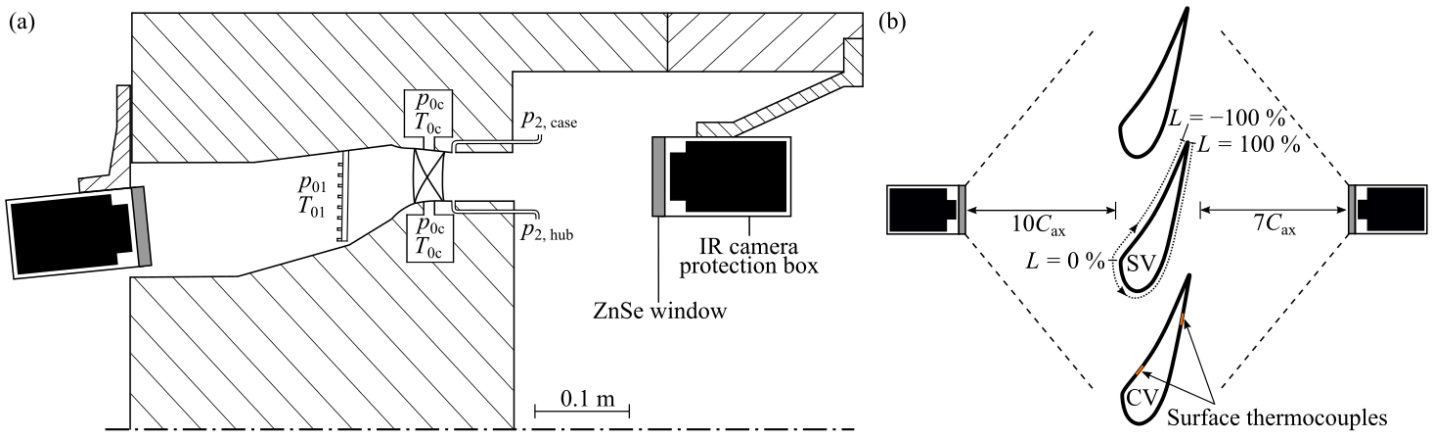


Figure 2: (a) Schematic cross-section of the ECAT facility working section showing infrared cameras locations; (b) two-dimensional unwrapped schematic of the cascade.

Infrared thermography

We now consider the details regarding IR thermography. With reference to Figure 3 and based on the work of Kirollos and Povey [34], the IR cameras record at each pixel in their FOV the total incoming radiance, q_{cam}. This is the sum of three terms

$$q_{\mathrm{cam}} = q'_{\mathrm{w}} + q''_{\mathrm{s}} + q_{\mathrm{opt}} \qquad (1)$$

where q'_{w} is the radiance emitted from the vane external surface transmitted through the ZnSe window, q''_{s} is the radiance emitted from the surrounding surfaces (e.g. the internal surfaces of the working section) reflected from the vane external surface and transmitted through the ZnSe window, and q_{opt} is the radiance emitted from the ZnSe window. Equation 1 can be written as

$$\sigma T_{\mathrm{bb}}^4 = \sigma\tau_{\mathrm{opt}}\varepsilon_{\mathrm{w}}T_{\mathrm{w}}^4 + \sigma\tau_{\mathrm{opt}}(1-\varepsilon_{\mathrm{w}})T_{\mathrm{s}}^4 + \sigma(1-\tau_{\mathrm{opt}})T_{\mathrm{opt}}^4 \qquad (2)$$

where T_{bb} is the equivalent black-body temperature recorded by the camera (obtaianed from a traceable black-body calibration process), σ is the Stefan-Boltzmann constant, τ is the transmissivity of the ZnSe window, ε_{w} is the emissivity of the vane external surface, T_{w} is the temperature of the vane external surface, T_{s} is the effective temperature of the surrounding surfaces and T_{opt} is the temperature of the ZnSe window. We can cast Equation 2 as

$$q_{\mathrm{cam}} = q'_{\mathrm{w}} + q^* \qquad (3)$$

where $q^* = q''_{\mathrm{s}} + q_{\mathrm{opt}}$ is called the *total surrounding radiance*.

The surface thermocouple (isothermal patch method of [33], shown in Figure 2b and Figure 3) provides a location on the vane surface at which the surface temperature is known at all instants in time. Provided the emissivity of the isothermal patch is known, this allows q^* to be determined using the method proposed by Kirollos and Povey [34]. Taking the assumption that q^* is uniform across the FOV (accurate for a diffusely reflecting—Lambertian—surface with relatively uniform background temperature) we can determine (Equation 3) the local surface radiance, q'_{w}, and so the true local surface temperature, T_{w}. The main advantage of this calibration method over using an ex-situ detector black body calibration coupled with a modelling of the other terms (surface emissivity and window transmissivity)—as far as the ECAT facility is concerned—is that the surrounding radiance (emitted by the hot internal surfaces of the rig) reflected on the target surface back into the detector are accounted for.

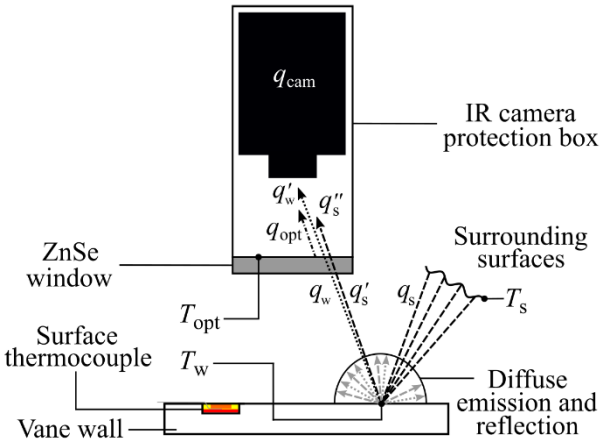


Figure 3: Schematic of the in-situ radiation calibration system.

The surface thermocouple on the calibration vanes were overpainted with a thin layer of high-emissivity matt black paint to render the system of uniform emissivity. The matt black paint has an emissivity of 0.98 [34]. On the studied vanes, four types of (unpainted) surface are encountered in this study: as-sprayed TBC; heat-exposed TBC; deteriorated TBC; and exposed metal (in the spalled TBC region). As-sprayed TBC is found on new vanes (PS and SS) and has an emissivity of 0.98 [35, 36] in the

spectral range of the IR cameras (7.5–14.0 μm) [37]. Heat-exposed TBC subject to sintering (high temperatures in engine) is found on the late SS of the deteriorated vanes (viewed by downstream IR camera, see Figure 2b): here the emissivity is taken to be 0.98 [38] in the spectral range of the IR cameras. Deteriorated TBC is found on the PS and early SS (viewed by upstream IR camera) of the deteriorated vanes and its emissivity was found to be 0.98 using the method described in Appendix B. The mean transmissivity of the ZnSe windows was $\tau_{\mathrm{opt}} = 0.95$ (manufacturer data) in the spectral range of our IR cameras. These data are summarized in Table 4.

The emissivity of the exposed metal in the spalled TBC is known to be strongly affected by surface finish and oxidation level [39–41]. It can be shown that inferred metal effectiveness is a relatively strong function of emissivity, and for this reason data reduction in the spalled region was not attempted (uncertainty too high for data to be of value). This explains regions of missing overall cooling effectiveness data for three end-of-life vanes in the region of TBC spallation.

Table 4: Emissivity of surfaces and transmissivity of ZnSe window.

Parameter	Value
Emissivity of matt black paint, ε_{p}	0.98
Emissivity of as-sprayed TBC, $\varepsilon_{\mathrm{TBC,as}}$	0.98
Emissivity of heat-exposed TBC, $\varepsilon_{\mathrm{TBC,he}}$	0.98
Emissivity of deteriorated TBC, $\varepsilon_{\mathrm{TBC,det}}$	0.98
Transmissivity of the ZnSe window, τ_{opt}	0.95

Overall cooling effectiveness measurement process

We now consider the process by which overall cooling effectiveness (so-called *metal effectiveness*) was evaluated. Overall cooling effectiveness θ_{w} is defined by

$$\theta_{\mathrm{w}}(L,S) = \frac{c_{\mathrm{m}}(L,S)T_{01} - T_{\mathrm{w}}(L,S)}{c_{\mathrm{m}}(L,S)T_{01} - c_{\mathrm{c}}(L,S)T_{0\mathrm{c}}} \tag{4}$$

where T_{01} and $T_{0\mathrm{c}}$ are the mainstream and coolant total temperatures upstream of the vanes, respectively, $T_{\mathrm{w}}(L,S)$ is the vane external surface temperature map (as a function of streamwise surface length fraction, L, and span fraction, S), and $c_{\mathrm{m}}(L,S)$ and $c_{\mathrm{c}}(L,S)$ are the mainstream and coolant recovery ratios, respectively, defined by

$$c(L,S) = \frac{1 + r\dfrac{\gamma-1}{2}\mathrm{M}(L,S)^2}{1 + \dfrac{\gamma-1}{2}\mathrm{M}(L,S)^2} \tag{5}$$

where M is the external Mach number distribution on the vane obtained from CFD [43] and r is the recovery factor, which is a function of the Prandtl number (Pr). For a turbulent boundary layer, r is taken to be approximately equal to $\mathrm{Pr}^{1/3}$, where Pr is calculated based on the mainstream or coolant fluid properties (see, for example, [42]).

The literature is not in complete consensus on the best definition of θ_{w}, and the definition in Equation 4 deviates slightly from other definitions in common use. We justify this form on the simple basis that—for a system with both internal and film cooling—it is the only definition that sets the theoretical range of θ_{w} to be between the exact limits 0 and 1. We discussed this point in Appendix D.

In our experiments, $T_{\mathrm{w}}(L,S)$ is a time-average over a short period (typically 10 images, acquired a 50 Hz frequency) near the end of an experimental run, at a point in time when the mainstream-to-coolant temperature difference is largest (typically 60 K) and most settled (metal effectiveness quasi-steady). Details of the facility operation and method are discussed in [32]. Examples of full-surface θ_{w} maps measured on HP NGVs in the ECAT facility are presented in [32]. The uncertainty analysis on θ_{w} is described in Appendix C.

EXPERIMENTAL RESULTS

The experimental results are now presented. We consider: the streamwise distribution of overall cooling effectiveness (three span fractions); the area-average overall cooling effectiveness; and the individual contribution of particular deterioration features to the change in overall cooling effectiveness.

Overall cooling effectiveness distribution

The distributions $\theta_{\mathrm{w}}(L)$, at three span fractions (S = 10, 50 and 90 %), are presented in Figure 4. Data for the set 1 vanes S1-V1 to S1-V4 are shown in the top row (frames a–c, respectively) and data for set 2 vanes S2-V1 to S2-V4 are shown in the bottom row (frames d–f, respectively). Here we are concerned with changes associated with deterioration, so data within a particular set of parts (set 1 or set 2) are normalized by the maximum value of $\theta_{\mathrm{w}}(L,S)$ measured within that entire set ($\theta_{\mathrm{w,max}}$): in practice the normalization values are close to unity, and associated with overcooled platform regions of the part (not studied in this paper). The PS is the range $L < 0$ % and the SS is the range $L > 0$ %.

Consider first the results for the PS of reference vanes S1-V1 and S2-V1. Pressure side distributions of $\theta_{\mathrm{w}}(L)$ at 10, 50 and 90 % span are broadly similar for both reference parts. At the LE (L = 0 %), there is a region of high external HTC (thin boundary layer) which causes a trough in θ_{w}. Directly downstream of the LE, θ_{w} rises as the boundary layer develops as coolant is introduced from the PS showerhead. There is a trend of gradually rising θ_{w} in the range $0 < L < 60$ %, with local peaks in θ_{w} associated with additional mid-PS cooling films are introduced. The rate of increase in θ_{w} is moderated by mildly increasing HTC. Towards the TE, and after the last row of film cooling holes ($L < -60$ %), we observe a decrease in θ_{w}, due to streamwise reduction in film cooling effectiveness as the coolant mixes with the mainstream flow.

Now consider the results for the SS ($L > 0$ %) of reference vanes S1-V1 and S2-V1. There is a steep rise in θ_{w} between L = 0 % until L = 15 %. This is driven by strongly increasing film effectiveness in the showerhead region, and a reduction in HTC as the boundary layer develops. The SS shoulder

(15 % < L < 40 %) faces normal to the line of sight of the cameras (see Figure 2b) and there is a small region in which data cannot be captured. On the late SS (L > 40 %), we observe a decrease in θ_w due to the streamwise reduction in film cooling effectiveness. A small local peak in θ_w at L = 75 % is due to presence of the internal TE pedestal bank, which enhances the internal HTC.

Now consider the deteriorated parts of set 1 (mid-life vanes). In the early PS and early SS region (−15 % < L < 15 %) distributions of θ_w are similar for the deteriorated parts and the reference part, with no consistent change due to deterioration. This result is not surprising, because in this region there are a number of effects in competition. Based on the literature we might expect the following: eroded (thinner) and more conductive TBC (due to sintering) at the LE could cause an increase in θ_w; an increase in film cooling effectiveness might be expected with increasing roughness (true for $B \cong 1.00$ and high inlet Tu; see, e.g. [18, 27]), which would increase θ_w; and a reduction in film coolant capacity due to deposition within holes would decrease film effectiveness and so decrease θ_w. For completeness, we note that we would expect little impact of increased surface roughness on external HTC in any laminar boundary layer region [15, 16, 17, 19, 20, 22, 23], so little impact on θ_w, but further note the debate about the existence of a laminar region for heavily cooled NGVs with high inlet turbulence, for which it is appears likely the classical laminar-then-turbulent development (applicable to smooth flat plates with low turbulence) is inapplicable. Over the rest of the PS (L < −15 %), there is a distinct reduction in θ_w for the mid-life vanes compared to the reference vane. This is driven by the increase in external HTC due to increased surface roughness (see e.g. [23]) and a reduction in film and TE slot coolant capacities caused by deposition and partial collapse, respectively. The decrease in θ_w is expected to be mitigated by an increase in TBC thermal conductivity. A similar effect is observed on the late SS (L > 40 %): a small reduction in θ_w for the mid-life vanes compared to the reference vane. Mechanisms for this are thought to be the same as for the PS changes.

Now consider the deteriorated parts of set 2 (end-of-life vanes). Looking at the early PS and early SS region (−15 % < L < 15 %), we see a distinct reduction in θ_w between the end-of-life vanes and the reference vane. This is in contrast to the set 1 data, and is thought to be due to the shrinkage and partial collapse of the film cooling holes in the showerhead region, reducing film coolant capacity (average capacity reduction of –5.77 %) and causing significantly lower film effectiveness and in-hole convective heat transfer. Photographs showing these effects are shown in the companion paper [1]. On the rest of the PS (L < −15 %), θ_w distributions for end-of-life parts are similar in trend to the reference part, but the absolute values of θ_w are smaller. This result is similar to, but of greater magnitude than, that for the mid-life parts. The mechanisms for the offset are thought to be the same. On the late SS (L > 40 %), the decrease in θ_w for the end-of-life vanes compared to their reference vane is similar to the corresponding result for mid-life vanes (similar increase in surface roughness on the late SS: see Table 2). The late SS film cooling holes (located just before the SS shoulder) are well outside the TBC spallation region (where film cooling holes are heavily damaged) and therefore the flow capacity of these holes would be expected to be similar to mid-life vanes: i.e. reduced only due to deposition within holes, and not due to partial collapse. We might have expected to see a greater reduction in θ_w on the late SS for end-of-life vanes compared to mid-life vanes due to a greater reduction in TE slot flow capacity (TE slot flow capacity reduction of –4.87 % for mid-life vanes, and –16.8 % for end-of-life vanes) causing a reduction in internal cooling mass flow in the TE-circuit. This effect was not conclusively observed, however.

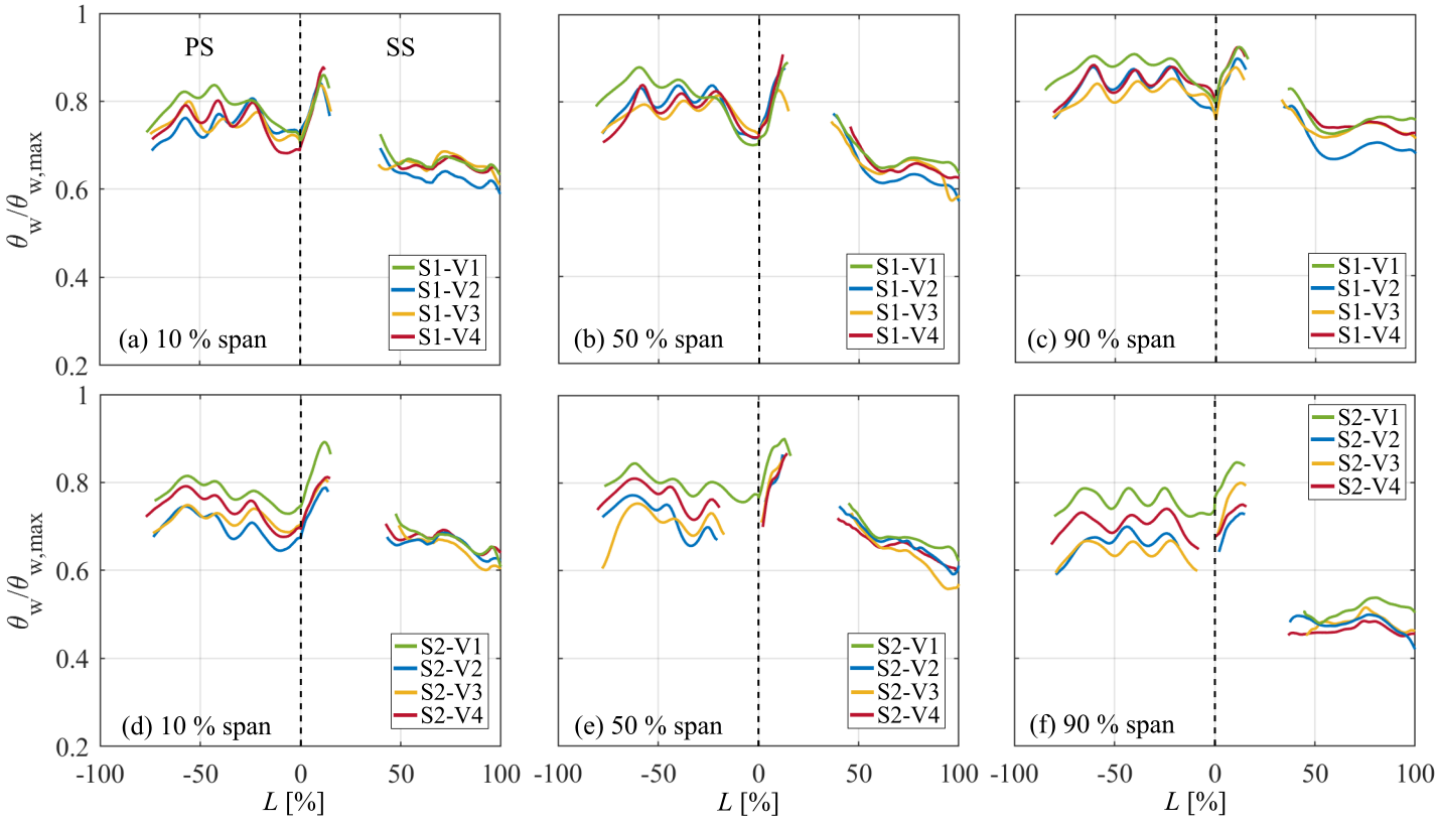


Figure 4: Streamwise distributions of overall cooling effectiveness at 10, 50 and 90 % span for: (a)–(c) set 1 vanes; (d)–(f) set 2 vanes.

Area-average overall cooling effectiveness

We now consider the area-average overall cooling effectiveness ($\bar{\bar{\theta}}_w$) of the vanes. The normalized area-average overall cooling effectiveness $\bar{\bar{\theta}}_w/\theta_{w,max}$ and the mean changes in $\bar{\bar{\theta}}_w$ between the deteriorated and reference vanes are listed in Table 5. The data are separated into the following regions: PS ($-80 < L < -0$ % for mid-life and $-80 < L < -30$ % for end-of-life); early SS ($0 < L < 15$ %); and late SS ($40 < L < 100$ %).

Consider first the data for set 1 (mid-life). For the reference vane (S1-V1), $\bar{\bar{\theta}}_w/\theta_{w,max}$ takes values of 0.80 and 0.81 on the heavily film-cooled PS and early SS, respectively, and 0.67 on the late SS. On the PS of the mid-life vanes, we observed an average reduction in $\bar{\bar{\theta}}_w$ of −1.65 % for the sample vanes S1-V(2-4) and −1.83 % for the entire set S1-V(2-13). On the early SS, we see an increase in $\bar{\bar{\theta}}_w$ of +1.24 % for the sample vanes and +1.58 % for the entire set. On the late SS, corresponding values are a decrease in $\bar{\bar{\theta}}_w$ of −0.78 % for the sample vanes and −1.32 % for the entire set. Overall, the vane-to-vane spread in the data is very low, suggesting high similarity between parts, and high similarity in the effects of degradation on the parts. Scaling the results to typical nominal engine conditions ($T_{01} = 1800$ K, $T_{0c} = 900$ K and $\theta_w = 0.70$), the measured mean change in $\bar{\bar{\theta}}_w$ for the entire set of parts (12 vanes) would correspond to changes in T_w of +11.53 K, −9.95 K and +8.31 K on the PS, early SS and late SS, respectively.

Now consider the data for set 2 (end-of-life) parts. We observe a significant decrease in $\bar{\bar{\theta}}_w$ with in-service deterioration on the PS and early SS in particular. The mean changes in $\bar{\bar{\theta}}_w$ for deteriorated set 2 parts (3 vanes) with respect to the reference part were −10.41 %, −8.53 % and −1.15 % on the PS, early SS and late SS, respectively. Scaling the results to typical engine conditions, these measured mean changes in $\bar{\bar{\theta}}_w$ correspond to a change in T_w of +65.58 K, +53.74 K and +7.24 K on the PS, early SS and late SS, respectively. This is entirely in-line with the acceleration effect.

Table 5: Area-average overall cooling effectiveness and external wall temperature changes (with respect to reference part) for set 1 (mid-life) and set 2 (end-of-life) parts.

Vane	PS $-80 < L < 0$ %	Early SS $0 < L < 15$ %	Late SS $40 < L < 100$ %	Vane	PS $-80 < L < -30$ %	Early SS $0 < L < 15$ %	Late SS $40 < L < 100$ %
$\bar{\bar{\theta}}_w/\theta_{w,max}$ for set 1 parts				$\bar{\bar{\theta}}_w/\theta_{w,max}$ for set 2 parts			
S1-V1 (Ref.)	0.80	0.81	0.67	S2-V1 (Ref.)	0.77	0.83	0.61
S1-V2	0.80	0.82	0.65	S2-V2	0.67	0.73	0.61
S1-V3	0.78	0.81	0.68	S2-V3	0.68	0.77	0.59
S1-V4	0.79	0.83	0.67	S2-V4	0.73	0.78	0.61
Mean change S1-V(2–4)	−1.65 %	+1.24 %	−0.78 %	Mean change S2-V(2–4)	−10.41 %	−8.53 %	−1.15 %
Mean change S1-V(2–13)	−1.83 %	+1.58 %	−1.32 %				
ΔT_w at nominal engine conditions (T_{01} = 1800 K and T_{0c} = 900 K) for set 1 parts				ΔT_w at nominal engine conditions (T_{01} = 1800 K and T_{0c} = 900 K) for set 2 parts			
Mean change S1-V(2–13)	+11.53 K	−9.95 K	+8.31 K	Mean change S2-V(2–4)	+65.58 K	+53.74 K	+7.24 K

DECOUPLING OF EFFECTS OF INDIVIDUAL DETERIORATION FEATURES ON OVERALL COOLING EFFECTIVENESS

In this section we attempt to quantify the effects of particular deterioration features on overall cooling effectiveness, θ_w. For this purpose, we use a one-dimensional steady-state heat transfer model of our parts, with boundary conditions taken from open-literature data. We consider four effects: the change in external HTC caused by increased surface roughness; the change in adiabatic film cooling effectiveness caused by increased surface roughness; the change in film coolant capacity; and the change in vane wall thermal resistance due to TBC sintering. Effects such as the redistribution of coolant caused by damaged film cooling holes, cracking, TBC erosion and increased surface roughness within film cooling holes are not explicitly modelled, and are assumed in aggregate to explain the balancing change in overall cooling effectiveness between that modelled and that measured.

The heat transfer model and the nominal boundary conditions are described in Appendix A. Two regions of the vane are modelled: the PS ($-80 < L < 0$ %) and late SS ($40 < L < 100$ %). Using representative values for all other boundary conditions, the internal heat transfer coefficient in the model is varied so that θ_w is matched to the experimental area-average value of θ_w for reference vane S1-V1, $\bar{\bar{\theta}}_{w,ref}$, for the appropriate region. To study each deterioration effect, we then change a particular boundary condition from its nominal value (to represent a change due to deterioration) and calculate the resulting change in $\bar{\bar{\theta}}_w$ (i.e. $\Delta\bar{\bar{\theta}}_w$). The predicted changes in $\bar{\bar{\theta}}_w$ arising from each deterioration effect are compared with the overall change in $\bar{\bar{\theta}}_w$ due to deterioration measured between reference vane S1-V1 and the mid-life vane S1-V10. This particular mid-life vane was chosen because it has an undamaged LE and TE, and an increased surface roughness (with respect to the reference vane) similar to studies in the open literature from which typical boundary conditions for the model were taken. For vane S1-V10, average values of roughness were $k_s/C = 1.02 \times 10^{-3}$ for the PS and early SS, and $k_s/C = 0.29 \times 10^{-3}$ for the rest of the SS. The measured relative changes in $\bar{\bar{\theta}}_w$ for vane S1-V10 (with respect to reference vane) were −1.47 % on the PS and −1.01 % on the late SS.

We now consider the predicted change in overall cooling effectiveness associated with each of the four deterioration effects (boundary condition) in turn.

Effect 1: contribution to change in external HTC (h) from increased surface roughness. Here we only consider the PS because of the scarcity of available data in the open literature relating to change in h due to (small) surface roughness changes on the late SS (as vane S1-V10). At $Re = 1.60 \times 10^6$ (interpolated) and Tu = 13.5 %, Erickson et al. [23] reported an increase in $\bar{\bar{h}}$ over the PS (with respect to the reference vane) of 25 %. The associated predicted change in $\bar{\bar{\theta}}_w$ (result of one-dimensional model at otherwise unchanged boundary conditions) is −7.84 %. This is summarized in Table 6.

Effect 2: contribution to change in adiabatic film cooling effectiveness (η_f) from increased surface roughness. At $Re = 1.06 \times 10^6$, Tu = 21 % and B = 1.0, Rutledge et al. [18] and Bogard et al. [29] (same experiment, data split between the two papers) reported a change in area-averaged η_f ($\bar{\bar{\eta}}_f$) of +40 % due to increased surface roughness upstream and downstream of cooling holes (like on the PS), and +16 % due to increase surface roughness only upstream of the film cooling holes (like on the late SS). The associated changes in $\bar{\bar{\theta}}_w$ are +4.44 % and +1.80 % on the PS and late SS, respectively.

Effect 3: contribution to change in adiabatic film cooling effectiveness of change in film coolant capacity ($\Gamma_{c,film}$). For this

purpose, we use a linear model in which we assume that the change in $\Gamma_{c,film}$ corresponds to an equal change in coolant mass flow rate entering the mixing layer. It is assumed that the mass flow rate of hot gas entering the mixing layer remains the same. At the nominal operating point, an enthalpy balance shows that a 1.00 % change in $\Gamma_{c,film}$ corresponds to an approximate change of 0.85 % in $\bar{\bar{\eta}}_f$. The change in $\Gamma_{c,film}$ for vane S1-V10 (with respect to reference vane S1-V1) is −0.31 %, corresponding to a change in $\bar{\bar{\eta}}_f$ of −0.26 % and leading to a change in $\bar{\bar{\theta}}_w$ of −0.02 % and −0.02 % on the PS and late SS, respectively. This effect appears to be extremely small and can be considered negligible in our particular case.

Effect 4: effect of change in TBC thermal conductivity due to sintering. Rätzer-Scheibe and Schulz [30] reported an increase from κ_{TBC} = 1.34 W m^{-1} K^{-1} to κ_{TBC} = 2.01 W m^{-1} K^{-1} after 100 hours at 1100 °C for EBPVD YSZ TBC (without further increase in κ_{TBC} after 100 hours of heat treatment). The associated predicted change in $\bar{\bar{\theta}}_w$ is +1.04 % and +1.48 % on the PS and late SS, respectively. This is summarized in Table 6.

Table 6: Summary of contributions from particular deterioration effects.

Deterioration effect	Boundary condition change on PS	Boundary condition change on late SS	$\Delta\bar{\bar{\theta}}_w$ PS	$\Delta\bar{\bar{\theta}}_w$ SS
Change in $\bar{\bar{h}}$ due to increased surface roughness	$\Delta\bar{\bar{h}}$ = +25 %	-	−7.84 %	-
Change in $\bar{\bar{\eta}}_f$ due to increased surface roughness	$\Delta\bar{\bar{\eta}}_f$ = +40 %	$\Delta\bar{\bar{\eta}}_f$ = +16 %	+4.44 %	+1.80 %
Change in $\bar{\bar{\eta}}_f$ due to reduced $\Gamma_{c,film}$	$\Delta\bar{\bar{\eta}}_f$ = −0.26 %	$\Delta\bar{\bar{\eta}}_f$ = −0.26 %	−0.02 %	−0.02 %
Change in κ_{TBC} due to sintering	$\Delta\kappa_{TBC}$ = +50 %	$\Delta\kappa_{TBC}$ = +50 %	+1.04 %	+1.48 %

The predicted contributions from each of these four modelled deterioration effects (Table 6) are visualized in Figure 5. The measured overall change in $\bar{\bar{\theta}}_w$ and the balancing term (difference between sum of modelled terms and measured overall change) are also shown. The balancing term can be regarded as the sum of contributions of effects not modelled. On the PS, the sum of the contributions of the modelled deterioration effects on $\bar{\bar{\theta}}_w$ differs from the measured overall change in $\bar{\bar{\theta}}_w$ by +0.91 % (i.e. overprediction of the reduction in $\bar{\bar{\theta}}_w$). This is likely to be due to an overprediction of the increase in $\bar{\bar{h}}$ due to increased surface roughness (largest term), but errors may also arise because of the inherent lack of coupling in the model.

On the SS, the sum of the contributions of the modelled deterioration effects on $\bar{\bar{\theta}}_w$ differs from the measured overall change in $\bar{\bar{\theta}}_w$ by −4.27 % (i.e. underprediction of the reduction in $\bar{\bar{\theta}}_w$). This is likely to be due to the unmodelled effect of an increase in surface roughness on the late SS (lack of available data) and the unmodelled effect of a reduction in TE slot coolant capacity (i.e. reduction in SS internal cooling).

Although this attempted decoupling goes some way to demonstrating the likely magnitude of individual uncoupled terms, and gives some insight into sensitivities, the relatively poor reconciliation with measured results highlights the challenges associated with the bottom-up superposition approach, in which individual effects are studied in isolation and combined via a model. In this approach—common in turbomachinery research—errors arise for three reasons: inadequate boundary condition specification in the individual studies; lack of coupling of more complex effects; and errors or assumptions in the superposition method. In the top-down approach (style of present study, and reason for the ECAT facility, as discussed in detail [32]) the combined result can be accurately characterized, but with relatively limited insight into the driving factors. Clearly both approaches are important for the development of understanding, but arguably the latter approach is more suited for accurate evaluation of aero-thermal performance of turbine components.

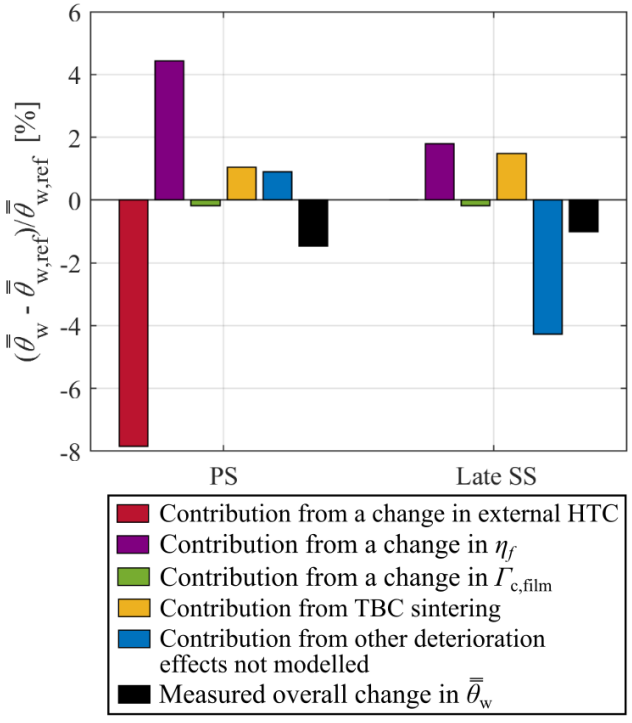


Figure 5: Modelled and measured changes in overall cooling effectiveness, and balancing term associated with effects not modelled, including coupling effects.

CONCLUSIONS

In this paper, 15 in-service-deteriorated HP NGVs representing mid-life and end-of-life parts from operational engines were studied for the purpose of describing and quantifying their overall thermal performance. The deterioration features included: thermal barrier coating spallation; damaged film cooling holes; increased surface roughness; and trailing edge burn-back. The study focused on quantifying changes in overall cooling effectiveness and on separating the effects associated with particular deterioration features.

For the mid-life vanes, the mean (12 vanes) changes in area-average overall cooling effectiveness were found to be −1.83 %, +1.58 % and −1.32 % on the PS, early SS and late SS, respectively. The corresponding implied changes in metal temperature at engine conditions (T_{01} = 1800 K and T_{0c} = 900 K) are +11.53 K, −9.95 K and +8.31 K. For the end-of-life vanes, the mean (3 vanes) changes in area-averaged overall cooling effectiveness were found to be −10.41 %, −8.53 % and −1.15 % on the PS, early SS and late SS. The corresponding implied changes in metal temperature at engine conditions are +65.58 K, +53.74 K and +7.24 K. We propose these effectiveness changes and implied temperature changes at a typical engine condition as rules-of-thumb for whole-life engine modelling.

Using a simple one-dimensional heat transfer model, decoupling of contributions from particular deterioration effects was attempted. The purpose both to get insight into particular sensitivities, but also to reflect on the philosophy of the top-down approach (present study) as compared to more conventional bottom-up approach in which effects are studied in isolation then superposed in modelling. We found that despite careful choice of boundary conditions, it was difficult to reconcile the modelled effect of individual deterioration features (combined via linear superposition) with the overall change in overall cooling effectiveness measured in the experiment. Whilst some insight into the likely magnitude of individual effects was provided, confidence in the superposed result was low. This somewhat justifies the importance of top-down studies for this type of investigation.

This paper addresses an important literature-gap by providing the first detailed analysis of the overall impact of combined in-service deterioration features on the overall thermal performance of HP NGVs. It is hoped that the results from this paper will be a useful step towards whole-life engine performance modeling and assessment.

ACKNOWLEDGEMENTS

The financial support of Rolls-Royce plc and the Aerospace Technology Institute are gratefully acknowledged. Technical discussions with James Cartlidge regarding appendix D are also gratefully acknowledged.

NOMENCLATURE

Acronyms

CV	calibration vane
EBPVD	electron-beam physical vapor deposition
ECAT	Engine Component AeroThermal (facility)
EXP	experiment
FOV	field of view
HP	high-pressure
HTC	heat transfer coefficient
IR	infrared
LE	leading edge
LHR	linearity, hysteresis, and repeatability
NGV	nozzle guide vane
PS	pressure surface
SLE	special limits of error
SS	suction surface
SV	studied vane
TBC	thermal barrier coating
TC	thermocouple
TE	trailing edge
TRL	technology readiness level
YSZ	yttria-stabilized zirconia
ZnSe	zinc selenide

Greek

β	bias uncertainty, –
γ	ratio of specific heat capacities, –
Γ	capacity, kg s^{-1} K$^{1/2}$ Pa^{-1}
ε	emissivity, –
η_f	adiabatic film cooling effectiveness, –
$\bar{\eta}_f$	laterally-average adiabatic film cooling effectiveness,–
$\bar{\bar{\eta}}_f$	area-average adiabatic film cooling effectiveness, –
θ_{bb}	black body effectiveness, –
θ_{w}	overall cooling effectiveness, –
$\bar{\bar{\theta}}_{\mathrm{w}}$	area-average overall cooling effectiveness, –
$\Delta\bar{\bar{\theta}}_{\mathrm{w}}$	change in area-average overall cooling effectiveness, –
κ	thermal conductivity, W m^{-1} K^{-1}
σ	Stefan-Boltzmann constant, –
τ	transmissivity, –

Roman

B	blowing ratio, –
c	recovery ratio, –
C	tangential chord, m
C_{ax}	axial chord, m
D	diameter of film cooling hole, m
h	heat transfer coefficient, W m^{-2} K^{-1}
$\bar{\bar{h}}$	area-averaged heat transfer coefficient, W m^{-2} K^{-1}
I	momentum flux ratio, –
k_{s}	equivalent sandgrain roughness height, m
l	streamwise surface length, m
L	streamwise surface length fraction, –
M	Mach number, –
$\dot{m}$	mass flow rate, kg s^{-1}
p	static pressure, Pa
p_0	total pressure, Pa
Pr	Prandtl number, –
q_{cam}	total radiance measured by IR camera, W m^{-2} sr^{-1}

q_{opt}	emitted ZnSe window radiance, W m^{-2} sr^{-1}
q_{w}	emitted vane external wall radiance, W m^{-2} sr^{-1}
q'_{w}	transmitted vane external wall radiance, W m^{-2} sr^{-1}
q_{s}	emitted surrounding surface radiance, W m^{-2} sr^{-1}
q'_{s}	reflected radiance from surrounding surfaces, W m^{-2} sr^{-1}
q''_{s}	reflected and transmitted radiance from surrounding surfaces, W m^{-2} sr^{-1}
q^*	total surrounding radiance ($q''_{\mathrm{s}} + q_{\mathrm{opt}}$), W m^{-2} sr^{-1}
r	recovery factor, –
R_{a}	centerline average roughness height, m
Re_C	exit Reynolds number based on tangential chord, –
S	span fraction, –
t	thickness, m
T	temperature, K
T_0	total temperature, K
$T_{0,\mathrm{mixed}}$	total temperature of mixing layer, K
T_{bb}	equivalent black body temperature, K
T_{opt}	ZnSe window temperature, K
T_{s}	temperature of surrounding surfaces, K
T_{w}	evaluated vane external surface temperature, K
Tu	inlet turbulence intensity, –

Subcripts

1	upstream of HP NGVs
2	downstream of HP NGVs
as	as-sprayed
ax	axial
bb	black body
c	coolant
cam	camera
det	deteriorated
he	heat-exposed
is	isentropic
opt	optic
p	paint
ref	reference
s	surrounding

REFERENCES

[1] Michaud, M., Jackson, D., Goenaga, F., and Povey, T., 2022, "Experimental Study of Impact of In-Service Deterioration on Aerodynamic Performance of High-Pressure Nozzle Guide Vanes." (under review).

[2] Ozgurluk, Y., Doleker, K. M., Ahlatci, H. and Karaoglanli, A. C., 2018, "Investigation of Hot Corrosion Behavior of Thermal Barrier Coating (TBC) Systems With Rare Earth Contents." Arabian Journal of Geosciences, 11:267. DOI: 10.1007/s12517-018-3625-0.

[3] Prenter, R., Ameri, A., and Bons, J. P., 2016, "Deposition on a Cooled Nozzle Guide Vane With Nonuniform Inlet Temperatures." ASME Journal of Turbomachinery, 138(10): 101005. DOI: 10.1115/1.4032924.

[4] Gell, M., Eric, J., Krishnakumar, V., McCarron, K., Barber, B., Sohn, Y.-H., and Tolpygo, V. K., 1993, "Bond Strength, Bond Stress and Spallation Mechanisms of Thermal Barrier Coatings." Surface and Coatings Technology, 120–121: pp. 53–60.

[5] Hamed, A. A., Tabakoff, W., Rivir, R. B., Das, K., and Arora, P., 2005, "Turbine Blade Surface Deterioration by Erosion." ASME Journal Turbomachinery, 127(3): pp. 445–452. DOI: 10.1115/1.1860376.

[6] Kurz, R., and Brun, K, 2001, "Degradation in Gas Turbine Systems." ASME Journal of Engineering for Gas Turbines and Power, 123(1): pp. 70–77. DOI: 10.1115/1.1340629.

[7] Bons, J. P., 2010, "A Review of Surface Roughness Effects in Gas Turbines." ASME Journal of Turbomachinery, 132(2): 021004. DOI: 10.1115/1.3066315.

[8] Darolia, R., 2013, "Thermal Barrier Coatings Technology: Critical Review, Progress Update, Remaining Challenges and Prospects." International Materials Reviews, 58(6): pp. 315–348. DOI: 10.1179/1743280413Y.0000000019.

[9] Bogard, D. G., Schmidt, D. L., and Tabbita, M., 1998, "Characterization and Laboratory Simulation of Turbine Airfoil Surface Roughness and Associated Heat Transfer." ASME Journal of Turbomachinery, 120(2): pp. 337–342. DOI: 10.1115/1.2841411.

[10] Kirollos, B., and Povey, T., 2014, "Reverse-Pass Cooling Systems for Improved Performance." ASME Journal of Turbomachinery, 136(11): 111004. DOI: 10.1115/1.4028161.

[11] Kirollos, B., and Povey, T., 2016, "Cooling Optimization Theory—Part I: Optimum Wall Temperature, Coolant Exit Temperature, and the Effect of Wall/Film Properties on Performance." ASME Journal of Turbomachinery, 138(8): 081002. DOI: 10.1115/1.4032612.

[12] Kirollos, B., and Povey, T., 2016, "Cooling Optimization Theory—Part II: Optimum Internal Heat Transfer Coefficient Distribution." ASME Journal of Turbomachinery, 138(8): 081003. DOI:10.1115/1.4032613.

[13] Turner, A. B., Tarada, F. H. A., and Bayley, F. J., 1985, "Effects of Surface Roughness on Heat Transfer to Gas Turbine Blades." AGARD Heat Transfer and Cooling in Gas Turbines, 9, pp. 1–10.

[14] Bunker, R. S., 1997, "Separate and Combined Effects of Surface Roughness and Turbulence Intensity on Vane Heat Transfer." Proceedings of the ASME 1997 International Gas Turbine and Aeroengine Congress and Exhibition, Orlando, Florida, USA. Paper no. 97-GT-135. DOI: 10.1115/97-GT-135.

[15] Stripf, M., Schulz, A., and Wittig, S., 2005, "Surface Roughness Effects on External Heat Transfer of a HP Turbine Vane." ASME Journal of Turbomachinery, 127(1): pp. 200–208. DOI: 10.1115/1.1811101.

[16] Lorenz, M., Schulz, A., and Bauer, H., 2012, "Experimental Study of Surface Roughness Effects on a Turbine Airfoil in a Linear Cascade—Part I: External Heat Transfer." ASME Journal of Turbomachinery, 134(4): 041006. DOI: 10.1115/1.4003234.

[17] Blair, M. F., 1994, "An Experimental Study Heat Transfer in a Large-Scale Turbine Rotor Passage." ASME Journal of

Turbomachinery, 116(1): pp. 1–13. DOI: 10.1115/1.2928273.

[18] Rutledge, J. L., Robertson, D., and Bogard, D. G., 2006, "Degradation of Film Cooling Performance on a Turbine Vane Suction Side due to Surface Roughness." ASME Journal of Turbomachinery, 128(3): pp. 547–554. DOI: 10.1115/1.2185674.

[19] Abuaf, N., Bunker, R. S., and Lee, C. P., 1998, "Effects of Surface Roughness on Heat Transfer and Aerodynamic Performance of Turbine Airfoils." ASME Journal of Turbomachinery, 120(3): pp. 522–529. DOI: 10.1115/1.2841749.

[20] Hoffs, A., Drost, U., and Bölcs, A., 1996, "Heat Transfer Measurements on a Turbine Airfoil at Various Reynolds Numbers and Turbulence Intensities Including Effects of Surface Roughness." Proceedings of the ASME 1996 International Gas Turbine and Aeroengine Congress and Exhibition, Birmingham, UK. Paper no. 96-GT-169. DOI: 10.1115/96-GT-169.

[21] Boyle, R. J., and Senyitko, R. G. "Effects of Surface Roughness on Turbine Vane Heat Transfer." Proceedings of the ASME Turbo Expo 2005, Reno, Nevada, USA. Paper no. GT2005-69133. DOI: 10.1115/1.2841749.

[22] Bacci, T., Picchi, A., Lenzi, T., Facchini, B., and Innocenti, L., 2021, "Effect of Surface Roughness and Inlet Turbulence Intensity on a Turbine Nozzle Guide Vane External Heat Transfer: Experimental Investigation on a Literature Test Case." ASME Journal of Turbomachinery, 143(4): 041006. DOI: 10.1115/1.4049917.

[23] Erickson, E. L., Ames, F. E., and Bons, J. P., 2012, "Effects of a Realistically Rough Surface on Vane Heat Transfer Including the Influence of Turbulence Condition and Reynolds Number." ASME Journal of Turbomachinery, 134(2): 021013. DOI: 10.1115/1.4003026.

[24] Barlow, D. N., and Kim, Y. W., 1995, "Effect of Surface Roughness on Local Heat Transfer and Film Cooling Effectiveness." Proceedings of the ASME 1995 International Gas Turbine and Aeroengine Congress and Exposition, Houston, Texas, USA. Paper no. 95-GT-014. DOI: 10.1115/95-GT-014.

[25] Lawson, S. A., and Thole, K. A., 2011, "Effects of Simulated Particle Deposition on Film Cooling." ASME Journal of Turbomachinery, 133(2): 021009. DOI: 10.1115/1.4000571.

[26] Goldstein, R. J., Eckert, E. R. G., Chiang, H. D., and Elovic, E., 1985, "Effect of Surface Roughness on Film Cooling Performance." ASME Journal Engineering of Gas Turbines and Power, 107(1): pp. 111–116. DOI: 10.1115/1.3239669.

[27] Schmidt, D. L., and Bogard, D. G., 1996, "Effects of Free-Stream Turbulence and Surface Roughness on Film Cooling." Proceedings of the ASME 1996 International Gas Turbine and Aeroengine Congress and Exhibition, Birmingham, UK. Paper no. 96-GT-462. DOI: 10.1115/96-GT-462.

[28] Schmidt, D. L., Sen, B., and Bogard, D. G., 1996, "Effects of Surface Roughness on Film Cooling." Proceedings of the ASME 1996 International Gas Turbine and Aeroengine Congress and Exhibition, Birmingham, UK. Paper no. 96-GT-299. DOI: 10.1115/96-GT-299.

[29] Bogard, D. G., Snook, D., and Kohli, A., 2003, "Rough Surface Effects on Film Cooling of the Suction Side Surface of a Turbine Vane." Proceedings of the ASME 2003 International Mechanical Engineering Congress and Exposition, Washington, D. C., USA. Paper no. IMECE2003-42061. DOI: 10.1115/IMECE2003-42061.

[30] Rätzer-Scheibe, H.-J., and Schulz, U., 2007, "The Effects of Heat Treatment and Gas Atmosphere on the Thermal Conductivity of APS and EB-PVD PYSZ Thermal Barrier Coatings." Surface & Coatings Technology, 201(18): pp. 7880–7888. DOI: 10.1016/j.surfcoat.2007.03.028.

[31] Wellman, R. G., and Nicholls, J. R., 2007, "A Review of the Erosion of Thermal Barrier Coatings." Journal of Physics D: Applied Physics, 40(16): pp. 293–305. DOI:10.1088/0022-3727/40/16/R01.

[32] Kirollos, B., Lubbock, R., Beard, P., Goenaga, F., Rawlinson, A., Janke, E., and Povey, T., 2017, "ECAT: An Engine Component Aerothermal Facility at the University of Oxford." Proceedings of the ASME Turbo Expo 2017: Charlotte, North Carolina, USA. Paper no. GT2017-64736. DOI: 10.1115/GT2017-64736.

[33] Michaud, M., Ornano, F., Chowdhury, N. H. K., and Povey, T., 2020, "Methodology for High-Accuracy Infrared Calibration in Environments with Through-Wall Heat Flux." Journal of the Global Power and Propulsion Society, 4, pp. 1–13. DOI: 10.33737/jgpps/118091.

[34] Kirollos, B., and Povey, T., 2017, "Laboratory Infrared Thermal Assessment of Laser-Sintered High-Pressure Nozzle Guide Vanes to Derisk Engine Design Programs." ASME Journal of Turbomachinery, 139(4): 041009. DOI: 10.1115/1.4035074.

[35] Liebert, C. H., 1978, "Emittance and Absorbance of NASA Ceramic Thermal Barrier Coating System." NASA Technical Paper 1190.

[36] González-Fernández, L., del Campo, L., Pérez-Sáez, R. B., and Tello, M. J., 2012, "Normal Spectral Emittance of Inconel 718 Aeronautical Alloy Coated With Yttria Stabilized Zirconia Films." Journal of Alloys and Compounds, 513, pp. 101–106. DOI: 10.1016/j.jallcom.2011.09.097.

[37] FLIR, 2018, "FLIR Product Catalog 2018." FLIR System, Inc., Wilsonville, OR, USA. Publication No. T559480.

[38] Manara, J., Arduini-Schuster, M., Rätzer-Scheibe, H.-J., and Schulz, U., 2009, "Infrared-optical Properties and Heat Transfer Coefficients of Semitransparent Barrier Coatings." Surface & Coatings Technologies, 203, pp. 1059–1068. DOI: 10.1016/j.surfcoat.2008.09.033.

[39] Keller, B. P., Nelson, S. E., Walton, K. L., Ghosh, T. K., Tompson, R. V., and Loyalka, S. K., 2015, "Total Hemispherical Emissivity of Inconel 718." Nuclear Engineering and Design, 287, pp. 11–18. DOI: 10.1016/S0894-1777(00)00021-2.

[40] Greene, G. A., Finfrock, C. C., and Irvine, T. F., 2000, "Total Hemispherical Emissivity of Oxidized Inconel 718 in the Temperature Range 300–1000°C." Experimental Thermal and Fluid Science, 22, pp. 145–153. DOI: 10.1016/S0894-1777(00)00021-2.

[41] Del Campo, L., Pérez-Sáez, R. B., González-Fernández, L., Esquisabel, X., Fernández, I., González-Martín, P., and Tello, M. J., 2010, "Emissivity Measurements on Aeronautical Alloys." Journal of Alloys and Compounds, 489(2), pp. 482–487. DOI: 10.1016/j.jallcom.2009.09.091.

[42] Eckert, E. R. G., and Drake, R. M., 1972, "Analysis of Heat and Mass Transfer." McGraw-Hill, New York. ISBN 978-0070189256.

[43] Burdett, D., Goenaga, F., and Povey, T., 2021, "Understanding Capacity Sensitivity of Cooled Transonic Nozzle Guide Vanes: A Parametric Experimental and Computational Study of the Impact of Trailing Edge Geometry." ASME Journal of Turbomachinery, 143(5): 051001. DOI: 10.1115/1.4050068.

[44] Wee S., Do J., Kim K., Lee C., Seok C., Choi B.-G., Choi Y., and Kim W., 2020, "Review on Mechanical Thermal Properties of Superalloys and Thermal Barrier Coating Used in Gas Turbines." Applied Sciences, 10(16): 5476. DOI: 10.3390/app10165476.

[45] Qureshi, I., Smith, A. D., and Povey, T., 2013, "HP Vane Aerodynamics and Heat Transfer in the Presence of Aggressive Inlet Swirl." ASME Journal of Turbomachinery, 135(2): 021040. DOI: 10.1115/1.4006610.

[46] Ames, F. E., 1998, "Aspects of Vane Film Cooling With High Turbulence: Part II—Adiabatic Effectiveness." ASME Journal of Turbomachinery, 120(4): 777–784. DOI: 10.1115/1.2841789.

[47] Raghu, O., and Philip, J., 2006, "Thermal Properties of Paint Coatings on Different Backings Using a Scanning Photo Acoustic Technique." Measurement Science and Technology, 17(11), pp. 2945–2949. DOI: 10.1088/0957-0233/17/11/012.

[48] Naidu, A., Rey, L., Chowdhury, N. H. K., and Povey, T., 2022, "Design and Optimization of Direct Metal Laser Sintered Cooled Camera Housing for High-Temperature Turbomachinery Application." (paper under review).

[49] Parker, J., and Povey, T., 2022, "Method for Determining Adiabatic Film Effectiveness in Presence of Thermal Boundary Layer." (accepted – awaiting full ref).

APPENDIX A: 1D HEAT TRANSFER MODEL

In this section we introduce the steady one-dimensional heat transfer model and the associated nominal boundary conditions used to decouple the effect of individual deterioration features. A schematic of the model is shown in Figure 6. It consists of a two-layer vane wall (metal and TBC) subjected to a hot external flow with heat transfer coefficient h, and an internal coolant flow at temperature T_{0c} with heat transfer coefficient h_c. The external surface has a mixing film cooling layer, which entrains mainstream gas at temperature T_{01}, and which is described by an adiabatic film cooling effectiveness, η_f. This gives us the total temperature of the mixing layer

$$T_{0,\mathrm{mixed}} = T_{01} - \eta_f (T_{01} - T_{0c}) \qquad \text{(A1)}$$

The temperature of the mixing layer ($T_{0,\mathrm{mixed}}$) is the external driving temperature. Heat conduction is one dimensional in the through-wall direction.

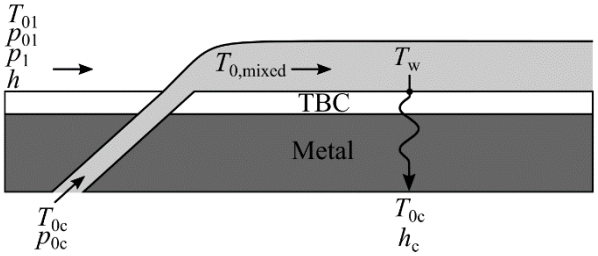


Figure 6: Schematic of the heat transfer model (not to scale).

The nominal temperatures T_{01} and T_{0c} are those of a typical run and are listed in Table 3. The model was run for boundary conditions typical of the pressure side ($-80 < L < 0$ %) and late suction side ($40 < L < 100$ %). Nominal external HTCs (h_{PS} and h_{SS}) and adiabatic film cooling effectiveness values ($\eta_{f,\mathrm{PS}}$ and $\eta_{f,\mathrm{SS}}$) for each region are average values (over the entire region) obtained from the open literature. These are listed in Table 7 with the original source for the values. Wall thermal properties and physical parameters are also listed. The nominal thermal conductivity of the TBC ($\kappa_{\mathrm{TBC,as}}$) is representative of its as-sprayed condition [30] and the thermal conductivity of the metal is typical of a nickel-based superalloy (commonly used in turbine components) [44]. Values for internal HTCs ($h_{\mathrm{c,PS}}$ and $h_{\mathrm{c,SS}}$) were taken to be those that reconcile the output of the one-dimensional thermal model with measured average values of overall cooling effectiveness on the vane. This ensures accuracy of the decoupling process.

Table 7: Boundary conditions and constants used in the one-dimensional heat transfer model.

Property	Value	Source
h_{PS}	625 W m^{-2} K^{-1}	[45]
h_{SS}	900 W m^{-2} K^{-1}	[45]
$h_{\mathrm{c,PS}}$	2000 W m^{-2} K^{-1}	-
$h_{\mathrm{c,SS}}$	2500 W m^{-2} K^{-1}	-
$\eta_{f,\mathrm{PS}}$	0.25	[46]
$\eta_{f,\mathrm{SS}}$	0.20	[46]
t_{TBC}	0.15 mm	-
κ_{TBC}	1.34 W m^{-1} K^{-1}	[30]

t_{metal}	1.50 mm	-
κ_{metal}	8.00 W m^{-1} K^{-1}	[44]

APPENDIX B: EMISSIVITY OF DETERIORATED TBC

There are numerous papers which consider the emissivity of as-sprayed (new) and heat-exposed (but otherwise not deteriorated) TBC [35–38], but there is a lack of data regarding the emissivity of deteriorated TBC subject to significant oxidation and deposition (and associated discolouration).To the authors' knowledge, the only open-literature study is that of Liebert [35], who found no change in emissivity of the TBC of a turbine component after 150 hours of engine operation: this is a relatively short operating time compared to the engine-run vanes in the present study. A method was therefore developed to provide an estimate of the emissivity of the deteriorated TBC of the vanes in the present study. The method was validated by application to heat-exposed but otherwise non-deteriorated TBC, for which the emissivity is independently known.

A photograph of the calibration system and corresponding IR image are shown in Figure 7 (frames a and b, respectively), applied to the heat-exposed but otherwise non-deteriorated TBC reference surface. An identical system was used on the deteriorated TBC to be calibrated. The IR image was captured during a run (situation with high through-wall heat flux) and presented in terms of black-body effectiveness defined by

$$\theta_{\text{bb}} = \frac{T_{01} - T_{\text{bb}}}{T_{01} - T_{0\text{c}}} \tag{B1}$$

The calibration system comprises: an isothermal calibration patch, marked A, which is of known uniform temperature (thermocouple) and known emissivity (overpainted with matt black paint); a proximate matt black paint patch, marked B, of known emissivity but unknown temperature; and a surrounding surface region (C or D, for the two example cases) for which the surface effectiveness is to be evaluated. Further discussion around the necessity for an isothermal calibration patch can be found in [33].

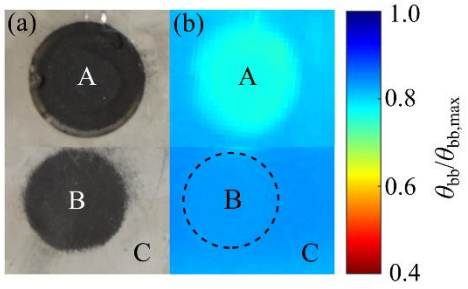


Figure 7: (a) Photograph of calibration system on surface with heat-exposed but otherwise non-deteriorated TBC; (b) black-body effectiveness map of same under conditions of high through-wall heat flux.

Examining Figure 7b, we see no visible difference between θ_{bb} on the paint patch, B, and surrounding surface, C. The maximum difference in θ_{bb} between the paint patch and the surrounding surface was measured to be 0.2 %. This was true also for the case of the deteriorated TBC to be calibrated. That is—in both cases—the equivalent black-body temperature (T_{bb}) of the paint patch and proximate TBC surface were essentially the same. We now compute the maximum difference in surface emissivity (between B and C) that is possible under the condition $T_{\text{bb,B}} = T_{\text{bb,C}}$.

For $T_{\text{bb,B}} = T_{\text{bb,C}}$, it is possible to show (Equation 2) that the effectiveness values at B and C (ε_{B} and ε_{C}, respectively) must be related by

$$\frac{\varepsilon_{\text{B}}}{\varepsilon_{\text{C}}} = \frac{T_{\text{w,C}}^4 - T_{\text{s}}^4}{T_{\text{w,B}}^4 - T_{\text{s}}^4} \tag{B2}$$

in which T_{s} is the equivalent temperature of the surrounding surfaces, which can be found by applying Equation 2 to the isothermal calibration patch A, for which both surface temperature ($T_{\text{w,A}}$) and emissivity (ε_{A}) are known (see [33]). The temperature of the ZnSe window (T_{opt}) is known by measurement (see [48]). Evaluating T_{s} in this way we get

$$T_{\text{s}} = \sqrt[4]{\frac{T_{\text{bb,A}}^4 - \tau_{\text{opt}}\varepsilon_{\text{A}}T_{\text{w,A}}^4 - (1-\tau_{\text{opt}})T_{\text{opt}}^4}{\tau_{\text{opt}}(1-\varepsilon_{\text{A}})}} \tag{B3}$$

We now calculate the relationship between $T_{\text{w,B}}$ and $T_{\text{w,C}}$ using a simple 1D heat transfer model. Taking local estimates for quasi-steady-state through wall heat flux, and noting the thermal resistance of the additional paint layer (10 μm thick; κ_{p} = 1.00 W m^{-1} K^{-1} [47]), it is possible to show using a 1D heat transfer model that for identical values of T_{bb} (i.e. $T_{\text{bb,B}} = T_{\text{bb,C}}$) the external surface temperature $T_{\text{w,B}}$ is higher than $T_{\text{w,C}}$ by approximately 0.04 %, that is $T_{\text{w,B}} \cong T_{\text{w,C}} \times 1.0004$. The small temperature increase is caused by the additional thermal resistance of the paint layer in the presence of the estimated through-wall heat flux.

Combining Equation B3 and Equation B2, for the condition $T_{\text{w,B}} \cong T_{\text{w,C}} \times 1.0004$, we get $\varepsilon_{\text{B}} \cong \varepsilon_{\text{C}} \times 1.002$. That is, when indistinguishable equivalent black-body temperatures are measured on the paint patch (B) and the surrounding surface (C), the implication (in our system) is that the emissivities are the same to within 0.2 %. As this condition ($T_{\text{bb,B}} = T_{\text{bb,C}}$) was met for both the heat-exposed but otherwise non-deteriorated TBC reference surface, and for the deteriorated TBC to be calibrated, we conclude that in both instances the emissivities are effectively the same as that of matt black paint, i.e. $\varepsilon_{\text{B}} = \varepsilon_{\text{C}} = 0.98$.

APPENDIX C: BIAS UNCERTAINTY ANALYSIS

The bias uncertainty in measured and derived quantities is now considered.

The mainstream flow total temperature (T_{01}) was measured by 32 K-type thermocouples each with a quoted bias uncertainty of ±1.1 K (special limits of error, SLE), or ±0.31 % (350 K nominal). The bias uncertainty in measured temperature (average of 32 measurements) was therefore estimated to be $\beta^{\%}_{T_{01}} = \pm 0.31/\sqrt{32}$ % = ±0.06 % to 95 % confidence (see Table 8). The coolant flow total temperature (T_{0c}) was measured using 8 K-type thermocouples each with a quoted bias uncertainty of ±1.1 K (SLE), or ±0.38 % (290 K nominal). The bias uncertainty in the mean of all the 8 measurements was therefore estimated to be $\beta^{\%}_{T_{0c}} = \pm 0.38/\sqrt{8}$ % = ±0.13 % to 95 % confidence.

The equivalent black-body surface temperature (T_{bb}) was measured by an IR camera calibrated in-situ against a calibration system with a single K-type thermocouple. The error in T_{bb} is therefore dominated by the thermocouple uncertainty, which was estimated as ±1.1 K (SLE), or ±0.35 % (310 K nominal). The processing method is such that at the location of the calibration patch T_{bb} is real-time-normalized to the value measured by the calibration thermocouple. Thus, we take the uncertainty in T_{bb} at the location of the calibration patch to be ±0.35 % (310 K nominal). At other locations on the vane surface, where the surface temperature is different than that at the calibration system, an additional uncertainty is introduced due to errors in linearity, hysteresis and repeatability (LHR) of the IR camera black-body calibration. This is estimated by the IR camera manufacturer to be ±0.05 % of the measured T_{bb} [50]. The worst-case bias uncertainty in T_{bb} is therefore estimated to be $\beta^{\%}_{T_{bb}}$ = ±0.40 % to 95 % confidence.

The bias uncertainty in the transmissivity of the ZnSe window (τ_{opt}) is quoted to ±3.00 % by the window manufacturer. The uncertainty in the emissivity of as-sprayed TBC ($\varepsilon_{TBC,as}$) and heat-exposed but otherwise not deteriorated TBC ($\varepsilon_{TBC,he}$) is not reported in the open literature, but a survey of the reported emissivities from three papers [35, 36, 38] shows that the emissivity is typically in the range $0.97 < \varepsilon_{TBC,as/he} < 0.99$ and we therefore take the uncertainty in $\varepsilon_{TBC,as/he}$ to be ±0.01 or ±1.02 % with a nominal value of 0.98. We have demonstrated (Appendix B) that the observed difference in emissivity between deteriorated TBC and non-deteriorated TBC was negligible, and we therefore take the uncertainty $\varepsilon_{TBC,det}$ to be the same as $\varepsilon_{TBC,as}$ and $\varepsilon_{TBC,he}$. These values are summarized in Table 8.

Performing a Monte Carlo simulation with the uncertainties in the directly measured quantities listed in Table 8 as inputs, we estimate the bias uncertainty in evaluated external wall temperature (T_w) to be ±0.51 %. Although we are primarily interested in the *change* in area-averaged overall cooling effectiveness, $\Delta\bar{\bar{\theta}}_w$ (defined as the difference in $\bar{\bar{\theta}}_w$ between a new reference vane and a deteriorated vane), we also perform crude estimates of the absolute errors in local and area-averaged overall cooling effectiveness values θ_w and $\bar{\bar{\theta}}_w$ arising from errors in T_w and M (from CFD, and affecting c_m and c_c). Estimating the error (difference between CFD and experiment) in the local value M to be 2.00 %, this gives errors in the *absolute* values θ_w and $\bar{\bar{\theta}}_w$ of 2.83 % (based on nominal values of 0.70). So far as interpreting the normalized data of Figure 4 is concerned, the error in the *change* in area-averaged overall cooling effectiveness, $\Delta\bar{\bar{\theta}}_w$, is more important. Here we can assume that spatial distributions of c_m and c_c are essentially the same for all vanes. Additionally, the uncertainties in T_{01}, T_{0c}, τ_{opt} and ε (used to calculate the uncertainty in T_w) are relatively highly correlated between vanes (same instrumentation and material property uncertainties). Taking a worst-case assumption that all errors are uncorrelated, however, we obtain an upper-bound estimate of the uncertainty in $\Delta\bar{\bar{\theta}}_w$ as ±3.73 % of the nominal value of $\bar{\bar{\theta}}_w$. This is dominated by uncertainty in T_{bb}.

Table 8: Summary of bias uncertainty (to 95 % confidence) in directly measured and derived quantities.

Quantity	$\beta^{\%}$	Nominal value
T_{01}	±0.06 %	350 K
T_{0c}	±0.13 %	290 K
T_{bb}	±0.40 %	310 K
τ_{opt}	±3.00 %	0.95
$\varepsilon_{TBC,as}$	±1.02 %	0.98
$\varepsilon_{TBC,he}$	±1.02 %	0.98
$\varepsilon_{TBC,det}$	±1.02 %	0.98
T_w	±0.51 %	310 K
θ_w	±2.83 %	0.70
$\bar{\bar{\theta}}_w$	±2.83 %	0.70
$\Delta\bar{\bar{\theta}}_w$	±3.73 %	0.70

APPENDIX D: DEFINITION OF OVERALL COOLING EFFECTIVENESS

A common definition of overall cooling effectiveness θ_w is

$$\theta_w = \frac{c_m T_{01} - T_w}{c_m T_{01} - T_{0c}} \qquad \text{(C1)}$$

where the local recovery ratio c_m is used to account for compressibility effects associated with the mainstream gas at the vane external Mach number, but we do not account for similar effects associated with the coolant stream. This—we could argue—on the basis that the mainstream flow, being confined exclusively to the external compressible flow field, is unavoidably subject to a reduction in temperature due to recovery effects in the near wall region. This definition suffers from the obvious problem that it is not necessarily limited to the range $0 \le \theta_w \le 1$. Indeed, for a perfectly effective cooling system (i.e. infinite coolant flow, infinite internal HTC and adiabatic film effectiveness at unity), the theoretical lowest temperature in the system is $c_c T_{0c}$, where the local recovery ratio c_c is that associated with the vane external Mach number and the coolant

gas temperature is that at inlet to the vane. In the limit $T_{\mathrm{w}} \rightarrow c_c T_{0\mathrm{c}}$, it is clear that $\theta_{\mathrm{w}} > 1$ is possible in the definition of equation C1. A remedy is to additionally include a local recovery ratio term for the coolant stream temperature, giving

$$\theta_{\mathrm{w}} = \frac{c_{\mathrm{m}} T_{01} - T_{\mathrm{w}}}{c_{\mathrm{m}} T_{01} - c_{\mathrm{c}} T_{0\mathrm{c}}} \qquad \text{(C2)}$$

This has the advantage of limiting the theoretical range of θ_{w} to between zero and unity (i.e. $0 \leq \theta_{\mathrm{w}} \leq 1$) for the situation of combined internal and film cooling. This is the form we use in the present paper. We justify it on the basis that the coolant flow is also subject to the external compressible flow field on the external surface of the vane (in the mixing layer).

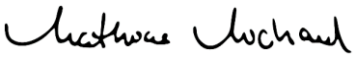
Statement of Authorship for joint/multi-authored papers for PGR thesis

To appear at the end of each thesis chapter submitted as an article/paper

The statement shall describe the candidate's and co-authors' independent research contributions in the thesis publications. For each publication there should exist a complete statement that is to be filled out and signed by the candidate and supervisor **(only required where there isn't already a statement of contribution within the paper itself).**

Title of Paper	Experimental Study of Impact of In-Service Deterioration on Thermal Performance of High-Pressure Nozzle Guide Vanes
Publication Status	□ Published □ Accepted for Publication ■ Submitted for Publication □ Unpublished and unsubmitted work written in a manuscript style
Publication Details	Michaud, M., Chowdhury, N. H. K., and Povey, T., 2022, "Experimental Study of Impact of In-service Deterioration on Thermal Performance of High-Pressure Nozzle Guide Vanes."

Student Confirmation

Student Name:	Mathias Michaud		
Contribution to the Paper	Mathias Michaud performed all the experiments, post-processed all the data, led the writing of the manuscript and contributed to the analysis. Nafiz Chowdhury assisted the experimental campaign and contributed to the analysis. Thomas Povey provided the original research idea, contributed to the analysis and the writing of the manuscript.		
Signature 		Date	

Supervisor Confirmation

By signing the Statement of Authorship, you are certifying that the candidate made a substantial contribution to the publication, and that the description described above is accurate.

Supervisor name and title: Professor Thomas Povey		
Supervisor comments: I certify that the candidate made a substantial contribution to the publication, and that the description described above is accurate		
Signature: 	Date	22/01/2022

This completed form should be included in the thesis, at the end of the relevant chapter.

7. Methods to Extract Underlying Boundary Conditions from Transient Overall Cooling Effectiveness Measurements

This chapter consists of a preprint journal paper detailing a new post-processing method to extract the heat transfer coefficients (internal and external) from transient overall cooling effectiveness measurements on internally cooled components (like most turbine components). While the proposed method is still at an early stage in its development, it provides a first step towards the decoupling of the underlying boundary conditions in highly coupled environment (e.g. high TRL experiments). A complete uncertainty analysis on the method is presented. The nomenclature and references included in this chapter are self-contained and differ in numbering and order compared to the overall thesis.

METHODS TO EXTRACT UNDERLYING BOUNDARY CONDITIONS FROM TRANSIENT OVERALL COOLING EFFECTIVENESS MEASUREMENTS

Mathias Michaud and Thomas Povey

Department of Engineering Science, University of Oxford, Parks Road, Oxford, OX1 3PJ, UK

ABSTRACT

Overall cooling effectiveness measurements (or metal effectiveness measurements) are becoming increasingly used to understand complex coupled systems in gas turbine experimental research. Unlike traditional techniques in which individual boundary conditions are measured in isolation and superposed using a thermal model, overall cooling effectiveness measurements give the final result of a complex coupled system. In correctly scaled experiments this allows aerothermal performance at near-engine conditions to be evaluated directly, and is thus powerful both as a research technique and for de-risking engine development programs. The technique is particularly useful for evaluating the thermal performance of internally cooled turbine components, because of the complexity and degree of interaction of the underlying boundary conditions. An intrinsic limitation of overall cooling effectiveness measurement data is that the individual boundary conditions (the internal and external heat transfer coefficients, for example) cannot be directly obtained from the final measurement. Decoupling of these boundary conditions would allow deeper understanding of the systems which are the subject of experiments. The objective of this paper is to present methods to extract the individual underlying boundary conditions from data available in typical overall cooling effectiveness experimental measurements, and to assess the uncertainty associated with decoupling techniques. Although we reference experimental data from advanced facilities for overall cooling effectiveness research throughout, much of the analysis is performed using a low-order heat transfer model to allow the impact of experiment design and measurement errors to be clearly separated at each stage of the analysis.

INTRODUCTION

Research investment in overall cooling effectiveness measurement techniques has been driven by the desire to accurately assess the overall thermal performance of nozzle guide vanes or turbine blades at engine-realistic conditions [1–6]. The traditional approach of predicting overall thermal performance of such parts from a thermal model with boundary conditions obtained from separate experiments [7–10] has the disadvantage that errors in underlying measurements can accumulate in the final result. Additionally, certain coupling terms are inherently absent in the separated experiments, limiting the accuracy of the predicted performance even in the absence of experimental errors. Overall cooling effectiveness techniques are arguably more suited to overall performance assessment than the traditional method. One limitation, however, is that underlying boundary conditions are not automatically determined from the overall cooling effectiveness measurement. Doing so would present a number of advantages to both researchers and engine designers, but is not an entirely straightforward process, not least because of the relative complexity of establishing (and even describing) confidence limits on the decoupled variables. Consider, for example, that the relationship—ratios of values, for example—between a number of variables may be known with a considerably higher degree of confidence than the value of any single variable, and that this information in itself may be of considerable value in solving certain types of problems. We refer to this as the *decoupling problem*. The objective is to present methods to decouple the individual underlying boundary conditions (both internal and external heat transfer coefficients) using data from a typical unsteady experimental measurement of overall cooling effectiveness. We also assess the uncertainty associated with the decoupling techniques we discuss. The paper is structured around various simplified elemental problems, designed to typify certain aspects of the overall problem in such a way that the behaviour of the system can be understood. These are:

1) *Impact of precision and bias errors in a one-dimensional system subject to a step change in the external flow temperature*. We use this idealized system to understand the impact of precision and bias errors in measurements of external flow temperature, internal flow temperature, and external wall temperature on the accuracy with which the underlying (extracted) boundary condition values of h_1 and h_2 can be determined.
2) *Impact of time constant of the external temperature rise in a one-dimensional system subject to a rise in external flow temperature*. We use this idealized system to understand the impact of experimental design (in terms of realistically achievable time constants) on the accuracy with which the underlying (extracted) boundary condition values of h_1 and h_2 can be determined.
3) *Practical applications*. We consider specific examples on how we can extract and use the underlying boundary conditions from an overall cooling effectiveness experiment.

MODELLING

In this section, we introduce the low-order one-dimensional heat transfer model used as the basis for the results in this paper. The model is represented in Figure 1. It consists of a wall subjected to a hot external flow with temperature $T_{01}(t)$ and heat transfer coefficient h_1, and an internal flow of temperature

$T_{02}(t)$ and with the internal wall subject to heat transfer coefficient h_2. Heat conduction is one-dimensional in the through-wall direction, represented by the nodes shown in Figure 1.

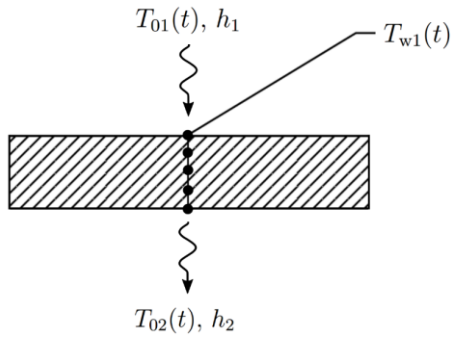


Figure 1: One-dimensional heat transfer model.

To represent typical overall cooling effectiveness experiments, we set $T_{01}(t)$ to be an exponential temperature rise (Equation 1) of time constant τ_{rise} with magnitude ΔT_{01} (where $\Delta T_{01} = T_{01}|_{t=\infty} - T_{01}|_{t=0}$), that is

$$T_{01}(t) = \Delta T_{01}(1 - e^{-t/\tau_{\text{rise}}}) + T_{01}(0) \quad (1)$$

In all our simulations we assume that the coolant temperature, $T_{02}(t)$, remains constant with time at a typical ambient temperature. The wall thermal properties correspond to those of Inconel, which is a common material for high-pressure turbine parts. Values are listed in Table 1. Despite the relative ease of implementation of temperature-dependent wall properties in the model, constant wall properties were chosen so as to keep the problem in its simplest form and isolate the impact that bias and precision errors in temperature measurement (specifically $T_{01}(t)$, $T_{02}(t)$ and $T_{w1}(t)$) have on the uncertainty of the extracted boundary conditions (h_1 and h_2).

Table 1: Wall properties.

Property	Symbol	Value
Wall conductivity	k_w	11.7 W m^{-1} K^{-1}
Wall thermal diffusivity	α_w	3.13 × 10^{-6} m^2 s^{-1}
Wall thickness	b_w	2.00 × 10^{-3} m
Wall specific heat capacity	c_w	440 J kg^{-1} K^{-1}
Wall density	ρ_w	8.280 × 10^3 kg m^{-3}

For given boundary conditions on each side of the wall, the transient thermal response of the wall is solved using a finite difference approach to approximate the temporal and spatial derivatives of the 1D heat equation (Equation 2). The solving methodology was the one proposed by Bergman [11]. The wall was spatially discretized into n nodes as shown in Figure 2 and an energy balance was applied to each node, which allows the temperature of any node j, $T_{w,j}^{p+1}$, to be calculated at the next time step. We distinguish three types of node: the exterior surface node ($j = 1$); interior nodes ($j = 2, \ldots, n-1$); and the internal surface node ($j = n$). These nodes are solved using Equations 3 to 5, respectively. The simulation parameters are listed in

Table 2. The number of nodes (n = 41) was chosen to have a wall discretization Δy (Equation 6) fine enough for the result of the simulation to be independent of the node count. The time interval Δt was set to the maximum value Δt that satisfied the stability condition for all node types, i.e. the minimum value of the three conditions expressed in Equation 7.

$$\frac{1}{\alpha_w}\frac{\partial T_w}{\partial t} = \frac{\partial^2 T_w}{\partial y^2} \quad (2)$$

$$T_{w,1}^{p+1} = \frac{2h_1\Delta t}{\rho_w c_w \Delta y}\left(T_{01}^p - T_{w,1}^p\right) + T_{w,1}^p + \frac{2\alpha_w \Delta t}{\Delta y^2}\left(T_{w,2}^p - T_{w,1}^p\right) \quad (3)$$

$$T_{w,j}^{p+1} = T_{w,j}^p + \frac{k_w \Delta t}{\rho_w c_w \Delta y^2}\left(T_{w,j-1}^p + T_{w,j+1}^p - 2T_{w,j}^p\right) \quad (4)$$

$$T_{w,n}^{p+1} = \frac{2h_2\Delta t}{\rho_w c_w \Delta y}\left(T_{02}^p - T_{w,n}^p\right) + T_{w,n}^p + \frac{2\alpha_w \Delta t}{\Delta y^2}\left(T_{w,n-1}^p - T_{w,n}^p\right) \quad (5)$$

$$\Delta y = b_w/(n-1) \quad (6)$$

$$\Delta t = \min\left\{\frac{k_w(\Delta y)^2}{2\alpha_w(k_w + h_1\Delta y)}, \frac{(\Delta y)^2}{2\alpha_w}, \frac{k_w(\Delta y)^2}{2\alpha_w(k_w + h_2\Delta y)}\right\} \quad (7)$$

Table 2: Simulation parameters.

Parameter	Symbol	Value
Number of nodes	n	41
Wall discretization	Δy	50.0 × 10^{-6} m

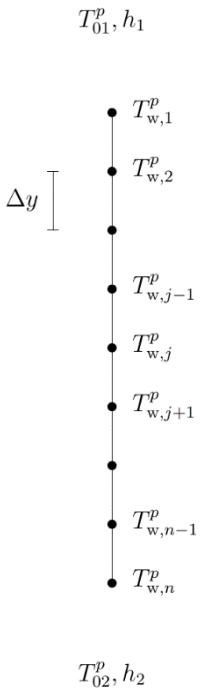


Figure 2: Discretization of the wall.

METHOD FOR EXTRACTING UNDERLYING BOUNDARY CONDITIONS

Consider the external wall thermal response T_{w1} to a step change (in time) in external flow temperature (τ_{rise} = 0.00 s). This is presented in a normalised form—ϕ_{w1} (Equation 8)—in Figure 3, for the nominal boundary conditions listed in Table 3 (typical of lab experiments in which Reynolds number is matched, but in which temperature ratio T_{01}/T_{02} is lower than the engine situation). To extract the underlying boundary conditions (h_1 and h_2) from this external wall thermal response, we find the combination of h_1 and h_2 that minimizes the RMS value $\Delta T_{\mathrm{w1,RMS}}$ (Equation 9) between a particular prediction $T_{\mathrm{w1,prt}}(t)$ (made using any given combination of h_1 and h_2, and the $T_{01}(t)$ and $T_{02}(t)$ traces associated with the target external wall response) and the target external wall response $T_{\mathrm{w1,trg}}(t)$ (Figure 3). In making the particular prediction of the external wall temperature ($T_{\mathrm{w1,prt}}(t)$), the initial temperature of the wall is set to be uniform (with surface depth) at the initial temperature of the target external wall thermal response ($T_{\mathrm{w1,trg}}|_{t=0}$). Justifying this choice is somewhat subtle, and this is discussed in Appendix A. The minimization of $\Delta T_{\mathrm{w1,RMS}}$ is performed using the Nelder-Mead algorithm, which is a common derivative-free simplex method to find the arguments minimizing the objective function $\Delta T_{\mathrm{w1,RMS}}(h_1, h_2)$.

$$\phi = \frac{T - T_{02}}{\Delta T_{01}} \tag{8}$$

$$\Delta T_{\mathrm{w1,RMS}} = \sqrt{\frac{1}{(t_{\mathrm{e}} - t_{\mathrm{s}})}\int_{t_{\mathrm{s}}}^{t_{\mathrm{e}}} \left(T_{\mathrm{w1,trg}} - T_{\mathrm{w1,prt}}\right)^2 \mathrm{d}t} \tag{9}$$

Table 3: Nominal boundary conditions.

Parameter	Symbol	Value
External HTC	$h_{1,\mathrm{nom}}$	3000 W m^{-2} K^{-1}
Internal HTC	$h_{2,\mathrm{nom}}$	6000 W m^{-2} K^{-1}
External flow rise time constant	τ_{rise}	0.00 s
Step change magnitude	ΔT_{01}	50.0 K
Internal total temperature	$T_{02}(t)$	298 K

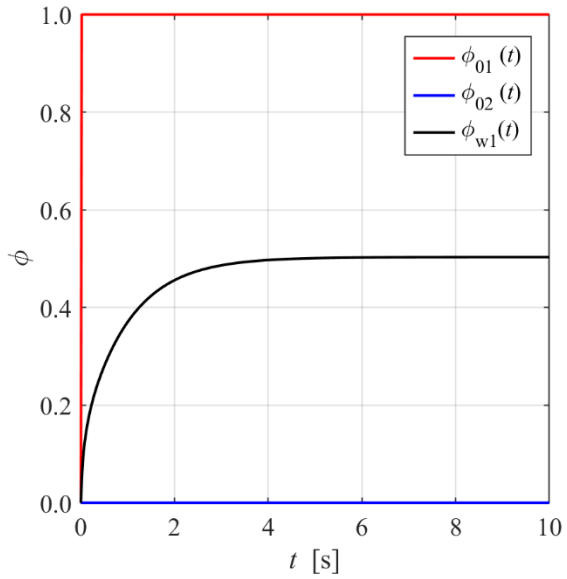


Figure 3: Normalised external wall thermal response to a perfect step change (in time) in external flow temperature.

In evaluating the RMS temperature difference ($\Delta T_{\mathrm{w1,RMS}}$) between a particular combination h_1-h_2 and the target combination h_1-h_2, a choice must be made about the averaging window (in time) to use, $t_{\mathrm{s}} < t < t_{\mathrm{e}}$. The purpose is to define both the best fit combination h_1-h_2 and to quantify an increase in $\Delta T_{\mathrm{w1,RMS}}$ as we move away from the best fit combination. We therefore choose a period $t_{\mathrm{s}} < t < t_{\mathrm{e}}$ which minimises a threshold contour of $\Delta T_{\mathrm{w1,RMS}}$ on a map of $\Delta T_{\mathrm{w1,RMS}}(h_1, h_2)$. This is done by creating maps of $\Delta T_{\mathrm{w1,RMS}}(h_1, h_2)$, for every combination t_{s}, t_{e}, and calculating the area enclosed by a threshold contour. The converged values t_{s} and t_{e} are insensitive to the particular threshold error that is chosen ($\Delta T_{\mathrm{w1,RMS}}$ = 0.5 K, 1 K, 2 K, etc.), provided that it is in the vicinity of the best fit pair (low absolute threshold). Arbitrarily, a threshold of $\Delta T_{\mathrm{w1,RMS}}$ = 1 K was chosen.

The converged values of t_s and t_e are respectively 0.25 s and 5.00 s for a perfect step change in the external flow temperature and the final map of $\Delta T_{w1,RMS}(h_1, h_2)$ for this particular case is shown in Figure 4. This time window covers the initial part of the rise (0.25–3.00 s, see Figure 3) of $T_{w1}(t)$, which is dominated by h_1 and $T_{01}(t)$, up to the approximately steady state region (3.00–5.00 s, see Figure 3) of $T_{w1}(t)$, which is also dependent on h_2 and $T_{02}(t)$. This allows us to study the influence of h_1, h_2, $T_{01}(t)$ and $T_{02}(t)$ on $\Delta T_{w1,RMS}$.

To explain why the optimal value of t_s is not 0.00 s but takes a small non-zero value (t_s = 0.25 s for τ_{rise}/τ_w = 0.00), consider two external wall responses under the same $T_{01}(t)$, $T_{02}(t)$ and h_2, but different h_1, the expression ($T_{w1,trg} - T_{w1,prt}$) in Equation 9 will be nonzero only for $t \neq 0.00$ s. So—rather trivially—the point t_s = 0.00 s provides no information to the problem. Perhaps more importantly, for external wall responses with the same $T_{01}(t)$, $T_{02}(t)$ and h_1 but different h_2, the expression ($T_{w1,trg} - T_{w1,prt}$) grows from an initial value of zero at t_s = 0.00 s, to values meaningfully separated in temperature at a time which depends on τ_{rise}/τ_w. Including times very close to the zero-point constrains h_1 but does not meaningfully constrain h_2. Thus, the optimal constraint *on the solution-pair* h_1-h_2 occurs for t_s > 0.00 s (result of Figure 3).

To explain why the optimal value of t_e is not arbitrarily large, but rather takes a value near the end of the unsteady rise, we note that in the approximately steady region (t > 5.00 s in Figure 3) there are infinitely many combinations of h_1 and h_2 that satisfy $T_{w1}(t)$ for the given boundary conditions $T_{01}(t)$ and $T_{02}(t)$. That is, although in the steady period the *ratio* h_1/h_2 is defined by the combination $T_{w1}(t)$, $T_{01}(t)$ and $T_{02}(t)$, individual values of h_1 and h_2 are not constrained. Thus, for a given ratio τ_{rise}/τ_w, there is a particular value of t_e that is optimal in terms of separating individual values of h_1 and h_2.

When the target temperature trace $T_{w1}(t)$ and input temperature traces $T_{01}(t)$ and $T_{02}(t)$, have no bias or precision errors, then the combination of h_1 and h_2 corresponding to the target external wall response can be extracted without any error. That is, $\Delta T_{w1,RMS}(h_1, h_2)$ = 0 for the best fit pair (h_1, h_2). This is marked by the "+" symbol in Figure 4.

The form of Figure 4 is interesting. Moving away from the best fit h_1-h_2 solution-pair (marked by the "+" symbol), the gradient of the error ($\Delta T_{w1,RMS}$) in the h_1 direction is approximately 4 times greater than in the h_2 direction. This is manifested by highly elongated ellipse-like contours on the map of $\Delta T_{w1,RMS}(h_1, h_2)$. Because of the thermal resistance and thermal capacity of the wall, the initial rise (0.25–3.00 s) of $T_{w1}(t)$ is more strongly influenced by h_1 than it is by h_2 (and so far as the dimensional result is concerned, and for the given temperature boundary conditions, influenced more by $T_{01}(t)$ than $T_{02}(t)$, but this dependency drops out when results are put in non-dimensional form). The settled value in the quasi-steady-state region (3.00–5.00 s) is essentially a function of the ratio h_1/h_2, and is therefore equally influenced by both h_1 and h_2. The net result is that when the entire time window is considered (0.25–5.00 s), the error ($\Delta T_{w1,RMS}$) is more strongly influenced by h_1 than by h_2. This is one of the reasons why we have high aspect ratio quasi-elliptical (rather than circular) shape of the solution region for low error ($\Delta T_{w1,RMS}$) thresholds.

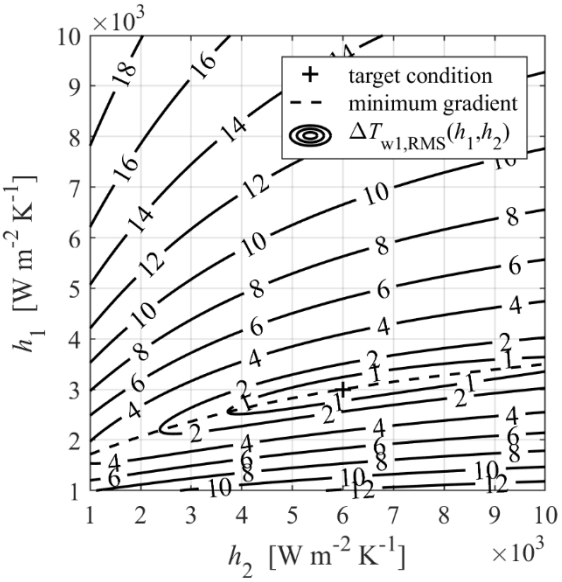


Figure 4: $\Delta T_{w1,RMS}$ (in K) at all combinations h_1, h_2 and the target wall response $T_{w1}(t)$ for a perfect step change in the external flow temperature.

IMPACT OF PRECISION AND BIAS ERRORS

In laboratory experiments in which overall cooling effectiveness is measured, there will be a finite measurement uncertainty associated with each of the three temporal responses $T_{w1}(t)$, $T_{01}(t)$ and $T_{02}(t)$. The purpose of this section is to consider the impact of those errors on the accuracy with which boundary conditions h_1 and h_2 can be determined. We do this by considering a distribution of temporal responses $T_{w1}(t)$, $T_{01}(t)$ and $T_{02}(t)$ that have the same mean as those shown in Figure 3, but with normally distributed bias and precision errors.

The bias error, β, is introduced by applying a temperature offset to all the temperature traces. The value of the bias error for each temperature trace is randomly picked from a population that is normally distributed with a mean, μ, equal to 0 and a standard deviation, σ, equal to the half of the desired maximum error amplitude, which is expressed as a fraction δ of the external flow temperature rise magnitude ΔT_{01} (e.g. $\sigma = \delta\Delta T_{01}/2$). Thus, 95 % of the normally distributed curves lie in a range $T(t) - \delta\Delta T_{01} < T(t) < T(t) + \delta\Delta T_{01}$. Throughout the paper, the presented values of bias errors are normalised by ΔT_{01}.

Precision error, ε, is introduced as random white noise of a given amplitude superimposed on the clean temperature traces. The noise maximum amplitude is expressed as a fraction δ of

the external flow temperature rise magnitude ΔT_{01} (e.g. $\varepsilon = \delta\Delta T_{01}$). Throughout the paper, the presented values of precision errors are normalised by ΔT_{01}.

To quantify the effect of bias and precision errors, the temperature signals are modified with bias and/or precision errors, creating a set of simulated experimental output signals $T_{01}(t)$, $T_{02}(t)$ and $T_{\mathrm{w1,trg}}(t)$. With the modified $T_{01}(t)$ and $T_{02}(t)$, we can simulate a particular external wall response $T_{\mathrm{w1,prt}}(t)$ by setting particular values of h_1 and h_2 and then compare (in terms of $\Delta T_{\mathrm{w1,RMS}}$) this particular external wall response to the target one ($T_{\mathrm{w1,trg}}(t)$). By minimising $\Delta T_{\mathrm{w1,RMS}}$, we can find the best fit h_1-h_2 solution-pairs for the input bias and/or precision errors. This process is repeated many times in the form of a Monte Carlo simulation to determine the range of values h_1 and h_2 can take for a given bias and/or precision error range.

We now compute the 95 % confidence regions for the h_1-h_2 solution-pairs obtained from Monte Carlo simulations for a number of simulated bias and/or precision errors applied to the input temperature signals. All simulations were for a perfect step change ($\tau_{\mathrm{rise}}/\tau_{\mathrm{w}} = 0.00$) in the external flow temperature. To compute the output error maps (95 % confidence regions) 10,000 simulations were performed for each combination of error amplitudes, to represent the statistical distribution of errors around the mean value. The resulting h_1-h_2 solution-pairs are not normally distributed, and therefore the 95 % confidence region (in h_1-h_2 space) is not a perfect ellipse. A somewhat arbitrary choice must therefore be made about how to define this region. The high density of the h_1-h_2 solution-pairs allows a definition based on a minimum-area to be used. We calculate the shape of the region containing 95 % of the output pairs, which has minimum area, but which is constrained with a limit on the minimum allowable radius of curvature—i.e. the shape must be smooth. The output 95 % confidence regions take the form of distorted ellipses. The form of these is justified in the following sections.

The results of this analysis are presented in Figure 5 to Figure 7, which deal in turn with: precision error only; bias error only; combined precision and bias error. In all three cases, the area enclosed by the 95 % confidence region grows approximately as the fourth power of the error amplitude. Accordingly, because the output (h_1-h_2 solution-pairs) 95 % error contours are approximately self-similar in shape, across a range of input (precision; bias; or combined precision and bias) error amplitudes, the output error in either h_1 or h_2 grows as approximately the second power of the input error amplitude.

For all three error inputs (precision; bias; or combined precision and bias) we note that h_1 is better constrained than h_2 across the entire range of input error amplitude. Some of the underlying reasons for this have been discussed.

Figure 5 shows results when only a precision error is introduced. The shape of the 95 % confidence regions (in h_1-h_2) are similar in form to the contours of constant $\Delta T_{\mathrm{w1,RMS}}$ shown in Figure 4: high aspect ratio quasi-elliptical shapes. This is explained by the fact that when a precision error (noise) is applied to the temperature signals, it removes the gradient of $\Delta T_{\mathrm{w1,RMS}}$ along the minimum gradient curve (see Figure 4) near the target condition, which causes the map of $\Delta T_{\mathrm{w1,RMS}}$ to be flat in that region. Consequently, the output h_1-h_2 solution-pairs to best fit the noisy signals will all lie on the flat region since the minimization algorithm is unable to find an absolute minimum of $\Delta T_{\mathrm{w1,RMS}}$.

Figure 6 shows results when only a bias error is introduced. It is notable that the high aspect ratio quasi-elliptical shapes lie along a different major axis to those for the simulations with only precision error (almost perpendicular trends, in fact). Indeed, the individual impact of bias errors on each of the input $T_{01}(t)$, $T_{02}(t)$ or $T_{\mathrm{w1}}(t)$ traces, are characteristically different. The impact on each of the three input traces is shown in Figure 8.

With reference to Figure 8, when a bias error (distribution) is applied to only $T_{01}(t)$, output h_1-h_2 combinations are distributed along the red dashed line in Figure 8. Similarly, when a bias error is applied to only $T_{02}(t)$, h_1-h_2 solution-pairs lie along the blue dashed line. Finally, for bias applied to $T_{\mathrm{w1}}(t)$, solutions lie along the black dashed line. The compound effect of normally distributed bias errors (of a given magnitude) applied to all three input temperature trends, is the quasi-elliptical 95 % confidence region delimited by the solid black line. By visualizing the three input components (lines of h_1-h_2 solution-pairs, for each of $T_{01}(t)$, $T_{02}(t)$ and $T_{\mathrm{w1}}(t)$) we can go some way to checking the final form of the confidence region. Justifying the rotational orientation of this region is more difficult, and requires many individual cases to be examined. Particular cases will be considered in subsequent sections.

When the precision and the bias errors are both applied to the input temperature signals, their effects on the output values of h_1 and h_2 are combined to create a large elliptical confidence region as shown in Figure 7. This figure shows well how measurement errors (bias and precision) can lead to large uncertainty in the extracted values of h_1 and h_2. For example, when the precision and bias errors are of ±0.1 (black contour in Figure 7), h_1 that has a range of 1500–4500 W m^{-2} K^{-1} can deviate by up to 1500 W m^{-2} K^{-1} from the nominal h_1 value, while h_2 that has a range 2500–12,500 W m^{-2} K^{-1} can deviate by up to 6500 W m^{-2} K^{-1} from the nominal h_2.

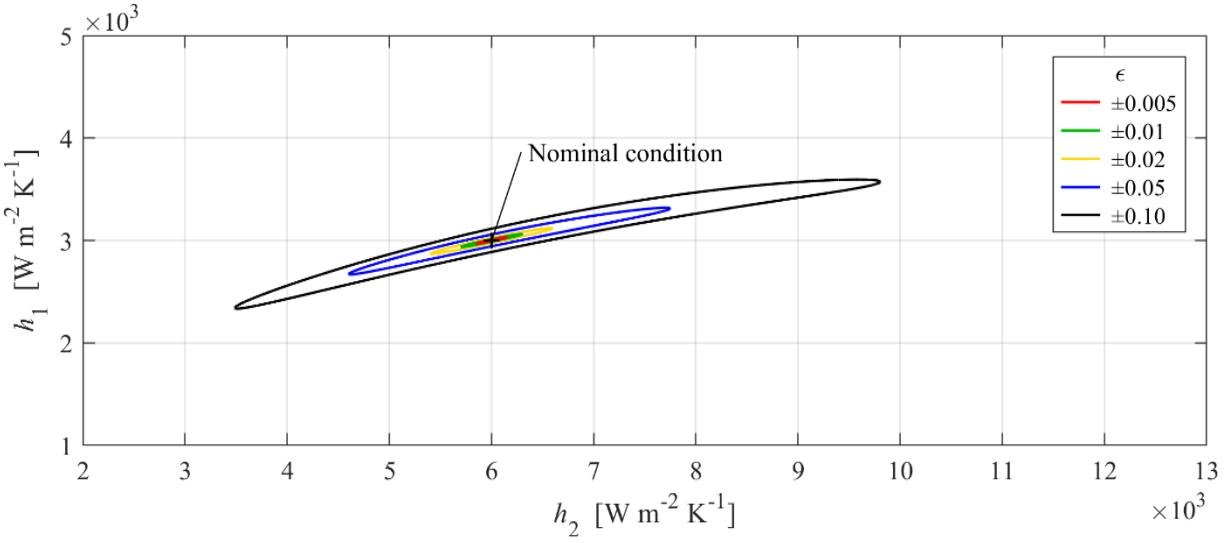


Figure 5: 95 % confidence region for extracted h_1-h_2 solution-pairs for a perfect step change in the external flow temperature with precision errors.

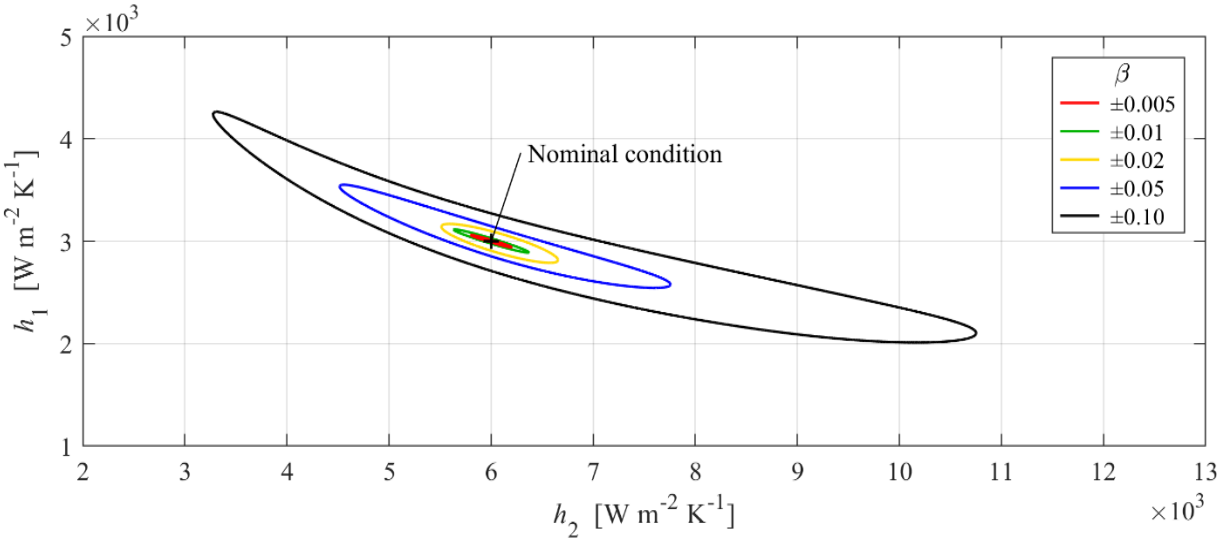


Figure 6: 95 % confidence region for extracted h_1-h_2 solution-pairs for a perfect step change in the external flow temperature with bias errors.

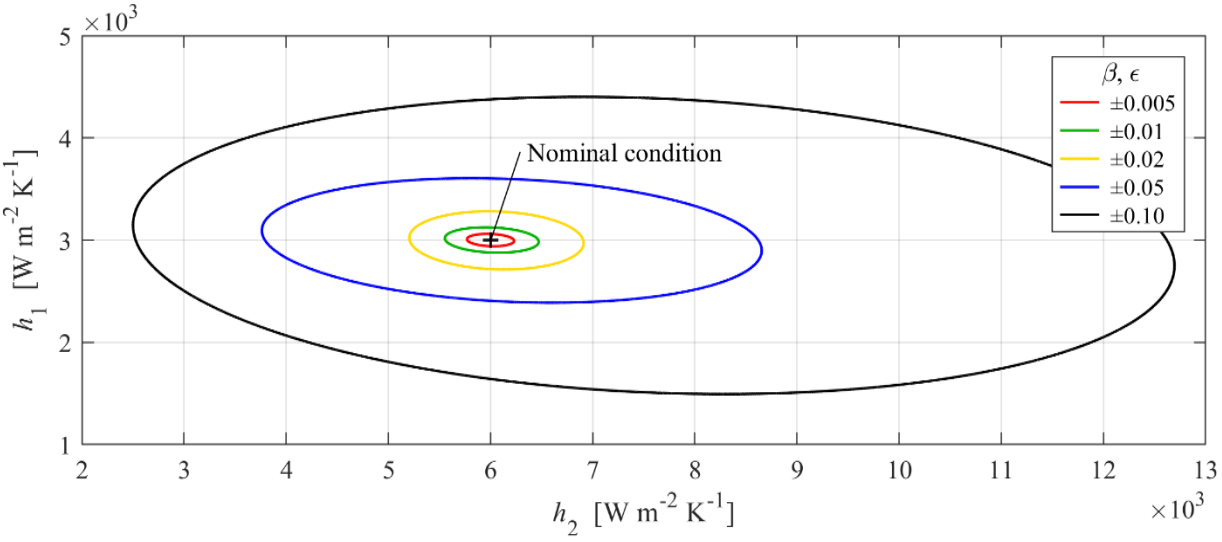


Figure 7: 95 % confidence regions for extracted h_1-h_2 solution-pairs for a perfect step change in the external flow temperature with bias and precision errors.

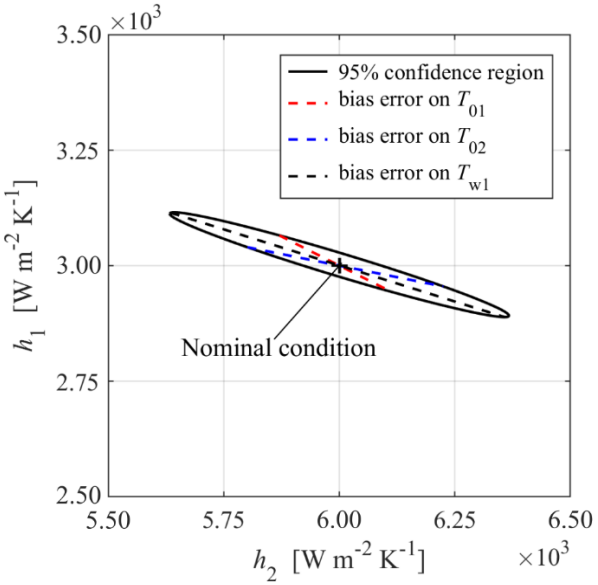


Figure 8: 95 % confidence region for h_1-h_2 solution-pairs for bias errors β = ±0.01 and the line of h_1-h_2 solution-pairs for each temperature signal.

Figure 9 shows the individual PDFs of h_1 and h_2 at the nominal condition for the 3 error inputs (precision; bias; and combined precision and bias) of amplitude ±0.01.

Table 4 lists the 95 % confidence intervals of the PDFs shown in Figure 9. Each PDF of h_1 was calculated from the h_1-h_2 solution-pairs within the band $h_{2,\text{nom}}$ ±0.2 % for each error type, and vice-versa for the PDFs of h_2. Figure 9 shows that h_1 is well constrained when only precision errors are considered (±10 W m^{-2} K^{-1} to 95 % confidence). When only bias errors with the same distribution are considered, the 95 % confidence interval for h_1 is approximately twice the one when only the precision errors are considered. When precision and bias errors are combined, the 95 % confidence interval for h_1 grows to more than 11 times the length of the confidence interval when only precision errors are considered. As for h_2, when precision errors, bias errors or combined errors are considered, the 95 % confidence intervals are respectively 7, 8 and 43 times longer than the 95 % confidence interval for h_1 with only precision errors. For this particular case (perfect step change in the external flow temperature), we see again that h_1 is better constrained than h_2 for a given error type. We also see that the precision errors have a lesser impact on the uncertainty in a given extracted boundary condition than bias errors with the same distribution. When both type of errors are combined, we observe an important increase in the uncertainty of the extracted boundary conditions.

Table 4: 95 % confidence intervals of h_1 and h_2 at the nominal condition for different error inputs.

Variable	Input error range	95 % confidence interval, W m^{-2} K^{-1}
h_1	$\varepsilon = \pm 0.01$	[2991, 3011]
h_1	$\beta = \pm 0.01$	[2982, 3023]
h_1	$\varepsilon = \beta = \pm 0.01$	[2883, 3113]
h_2	$\varepsilon = \pm 0.01$	[5936, 6068]
h_2	$\beta = \pm 0.01$	[5919, 6077]
h_2	$\varepsilon = \beta = \pm 0.01$	[5569, 6439]

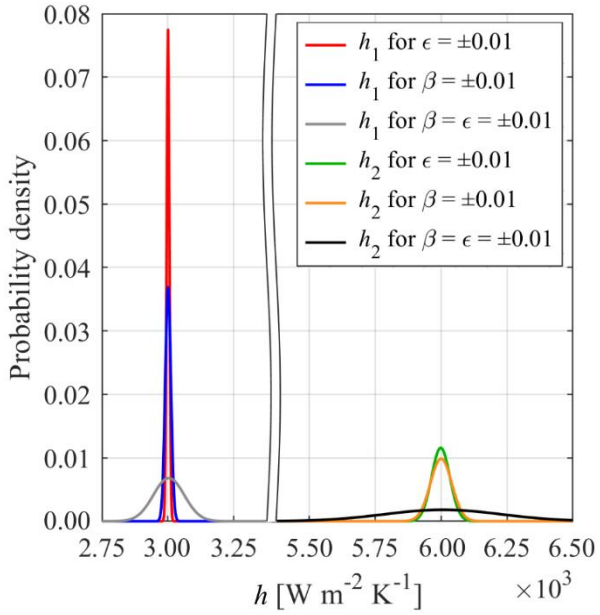


Figure 9: Probability density functions at the nominal condition.

IMPACT OF THE TIME CONSTANT OF THE EXTERNAL FLOW TEMPERATURE RISE

To assess the impact of the external flow temperature rise time constant on the 95 % confidence regions for the h_1-h_2 solution-pairs, the procedure to obtain the confidence regions with a perfect step change in external flow temperature is repeated with exponential external flow temperature rises of different time constants τ_{rise}. The normalised external flow temperature rises are presented in Figure 10, where their respective time constants normalised by the thermal time constant of the wall τ_{w}. The latter corresponds to the time constant of the best exponential fit of the external wall thermal response to a perfect step change in the external flow temperature as shown in Figure 3. The Annular Sector Heat Transfer facility [2] and the Engine Component Aerothermal facility [5] (facilities performing overall cooling effectiveness measurements at the University of Oxford) can achieve external flow temperature rises of time-constant ratios ($\tau_{\text{rise}}/\tau_{\text{w}}$) of 0.25 and 15 respectively.

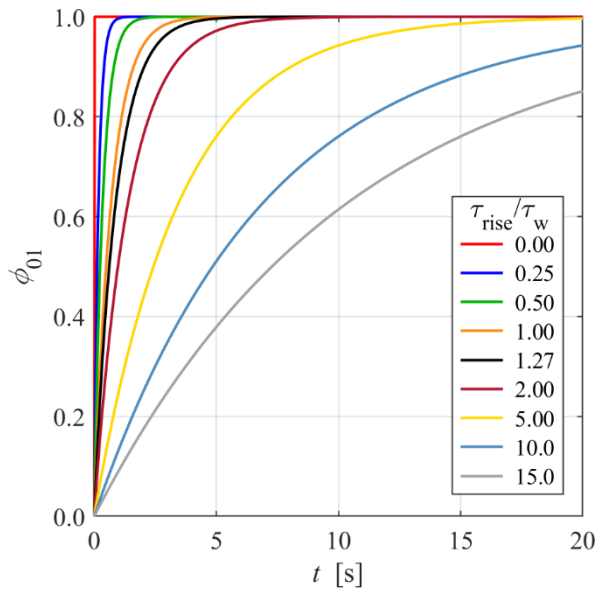


Figure 10: Normalised external flow temperature rise $\phi_{01}(t)$ for a number of time-constant ratios.

We present results for two error distributions in the normalised input temperatures: firstly, normally distributed bias error with a 95 % confidence interval of ±0.01; secondly, normally distributed bias and precision errors (here precision is distinguished from bias by being randomly distributed in time) each with 95 % confidence intervals of ±0.01 and uncorrelated between all temperature signals. The 95 % confidence regions of output h_1-h_2 solution-pairs for the first error distribution are shown in Figure 11. The equivalent plot for the second error distribution is shown in Figure 12. For completeness we note that results for the case of only precision error are not presented because the time-constant ratio has no impact on the confidence region when only a precision error is applied (the 95 % confidence regions of output h_1-h_2 solution-pairs are exactly the same as in Figure 5).

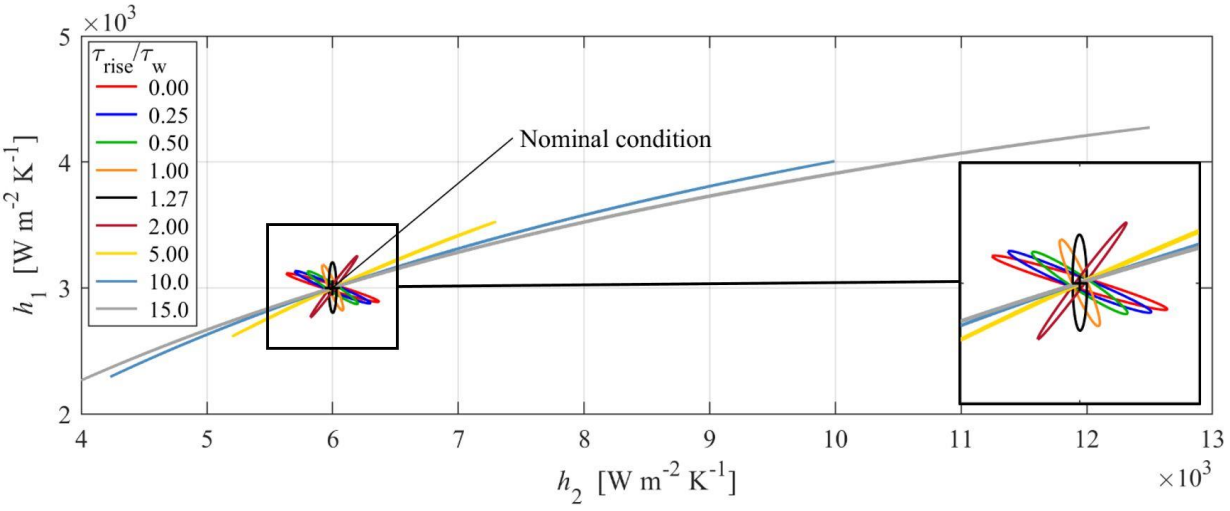


Figure 11: 95 % confidence regions for h_1-h_2 solution-pairs as a function of the time-constant ratio ($\tau_{\text{rise}}/\tau_{\text{w}}$) for bias errors $\beta = \pm 0.01$.

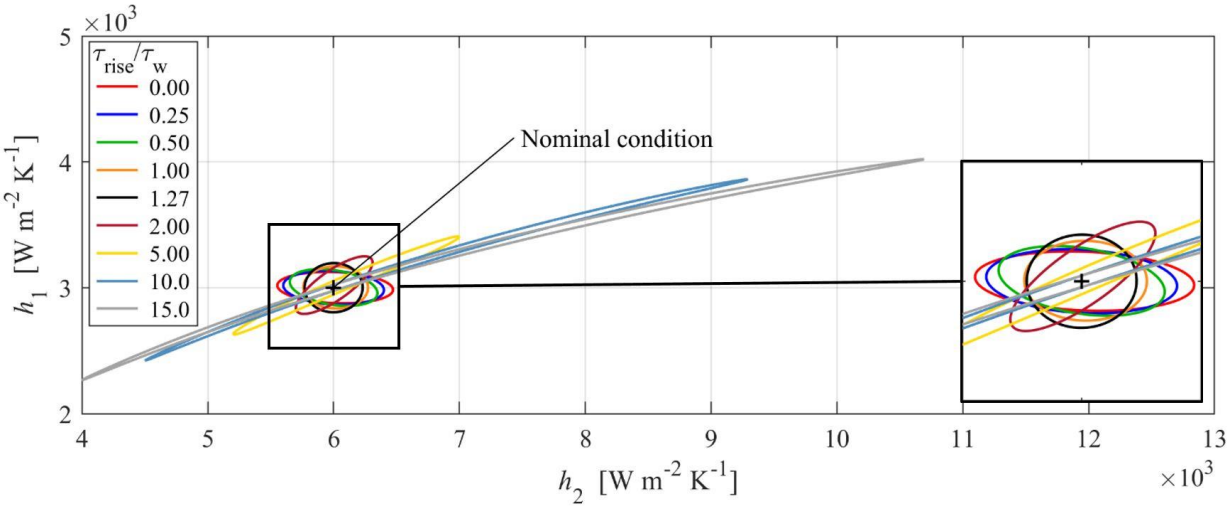


Figure 12: 95 % confidence regions for h_1-h_2 solution-pairs as a function of the time-constant ratio ($\tau_{\text{rise}}/\tau_{\text{w}}$) for bias and precision errors $\beta = \varepsilon = \pm 0.01$.

In both Figure 11 and Figure 12, we see that the confidence regions become significantly elongated with increasing time-constant ratio ($\tau_{\text{rise}}/\tau_{\text{w}}$) for $\tau_{\text{rise}}/\tau_{\text{w}} \geq 5$. Not only does the aspect ratio change, but—more importantly—the elongated 95 % confidence regions cover significantly larger ranges of h_1 and h_2. This effect arises because of the decreasing sensitivity with increasing time-constant ratio of $T_{\text{w1}}(t)$ to changes in h_1 and h_2. That is, fixed changes in $T_{\text{w1}}(t)$ caused by a bias shift from the *nominal value* require larger changes in h_1 and h_2 to satisfy the offset value of $T_{\text{w1}}(t)$ (with bias shift applied) as the time-constant ratio increases. That is, *the particular combination* h_1-h_2 is poorly constrained. Interestingly, however, the *relationship* between individual possible h_1-h_2 solution-pairs is reasonably well constrained for higher time-constant ratios (very high aspect ratio—i.e. long and thin—shape to the 95 % confidence regions): if we know one variable (h_1 or h_2) we can determine the other variable more accurately. We discuss this in the next section.

We also observe that the 95 % confidence region of h_1-h_2 solution-pairs rotates as the time-constant ratio changes (we see clockwise rotation as the time-constant ratio increases). This is particularly obvious in Figure 11 (bias errors only) but can also be seen in Figure 12 (bias and precision errors). Looking at Figure 11, rotation of the confidence region of h_1-h_2 solution-pairs shows changes in the relative sensitivity to h_1 and h_2 in matching best fit target external wall temperature responses arising from the superposition of the bias error distribution and the nominal external wall temperature response. Even for the results of Figure 11 the reason for the change in relative sensitivity is hard to explain, but might reasonably be assumed to be an artefact of the particular shape of the wall temperature rise, and therefore not of particular inherent interest. For the data of Figure 12, in which the effect is conflated with precision

error noise, we see same effect, but the 95 % confidence regions of h_1-h_2 solution-pairs have aspect ratios generally closer to unity (for lower values of $\tau_{\text{rise}}/\tau_{\text{w}}$), and therefore the effect is significantly less pronounced.

As examples of achieving best fits to the target external wall temperature responses corrupted with only a bias error for different time-constant ratios, consider Figure 13 which shows the normalised nominal external wall thermal responses (solid black lines), and the same external wall thermal responses with a positive bias error added (dashed black lines), for three time-constant ratios: $\tau_{\text{rise}}/\tau_{\text{w}}$ = 0, 1.27 and 2. The nominal (input) heat transfer coefficients for these simulations were $h_{1,\text{nom}}$ = 3000 W m^{-2} K^{-1}, $h_{2,\text{nom}}$ = 6000 W m^{-2} K^{-1}. For each of the three cases, we predict the nominal external wall temperature responses, $\phi_{\text{w1,nom}}(t)$, then add a bias error which we set equal to +0.06 (i.e. 6 % of the possible range of $\phi_{\text{w1,nom}}$). This large value (6 times larger than the value used for Figure 11) was somewhat arbitrarily selected to allow the trends to be clearly separated, providing better visualization of the fit. We refer to the thermal responses with bias error added as the *target responses*, $\phi_{\text{w1,trg}}(t)$. For each of the time-constant ratio, we calculate the best fit external wall temperature response, $\phi_{\text{w1,best fit}}(t)$, shown by the green solid lines in Figure 13 for any combination of values $h_{1,\text{best fit}}$ and $h_{2,\text{best fit}}$. Here we define the best fit to be the pair of values ($h_{1,\text{best fit}}$ and $h_{2,\text{best fit}}$) that minimizes the RMS temperature difference $\Delta T_{\text{w1,RMS}}$ (defined by Equation 9) between the two temperatures defined by $\phi_{\text{w1,best fit}}(t)$ and $\phi_{\text{w1,trg}}(t)$ over the time windows (t_{s}–t_{e}) shown in Figure 13. We find the optimum pair of values $h_{1,\text{best fit}}$ and $h_{2,\text{best fit}}$ for each of the three sample problems (with three time-constant ratios $\tau_{\text{rise}}/\tau_{\text{w}}$ = 0, 1.27 and 2) represented in Figure 13. We can see in Figure 13 that the best fit responses (green solid lines) are reasonably close the target responses (black dashed lines), which provides a visual demonstration of the best-fitting process. We note that the error (characterized by $\Delta T_{\text{w1,RMS}}$) is finite for all fits to offset trends of type $\phi_{\text{w1,nom}}(t)$ + bias. This is explained—even in the absence of precision error noise—by the fact that whilst an offset applied to the initial temperature of the external surface can occur in principle (surface still warm from a previous heated run for instance), a response with a bias offset ($\phi_{\text{w1,nom}}(t)$ + bias) is not a physical solution to the nominal temperature boundary conditions $T_{01}(t)$ and $T_{02}(t)$. This means that there is no possible h_1-h_2 pair that will lead to a perfect fit of the offset response.

In Table 5, we see that the best fit values $h_{1,\text{best fit}}$ and $h_{2,\text{best fit}}$ vary significantly with the time-constant ratio. The particular relationship (with time-constant ratio) is difficult to explain. Some insight is given by Figure 11, however, in which we see that both the overall extent of the solution confidence region (in h_1-h_2 space), and the shape (in particular the rotational orientation of the major axis of the quasi-ellipses) are strong functions of $\tau_{\text{rise}}/\tau_{\text{w}}$. The driving influences have been discussed, in particular the shift from primary dependence on h_1, through to significant dependence on both h_1 and h_2, and eventually primary dependence on the ratio h_1/h_2. Somewhat counterintuitive perhaps, lower sensitivity (here we define the word loosely) to a particular variable, implies that solution pairs (i.e. any h_1-h_2) very close to the best fit pair (i.e. $h_{1,\text{best fit}}$ and $h_{2,\text{best fit}}$) in terms of error minimization (i.e. $\Delta T_{\text{w1,RMS}}$ only slightly larger than the value for the best fit pair) can have with a large range in the particular variable.

Table 5 summarizes the nominal (input) values $h_{1,\text{nom}}$ and $h_{2,\text{nom}}$, and the best fit (output) values $h_{1,\text{best fit}}$ and $h_{2,\text{best fit}}$ for the data of Figure 13. The goodness of fit—in terms of $\Delta T_{\text{w1,RMS}}$—is also given.

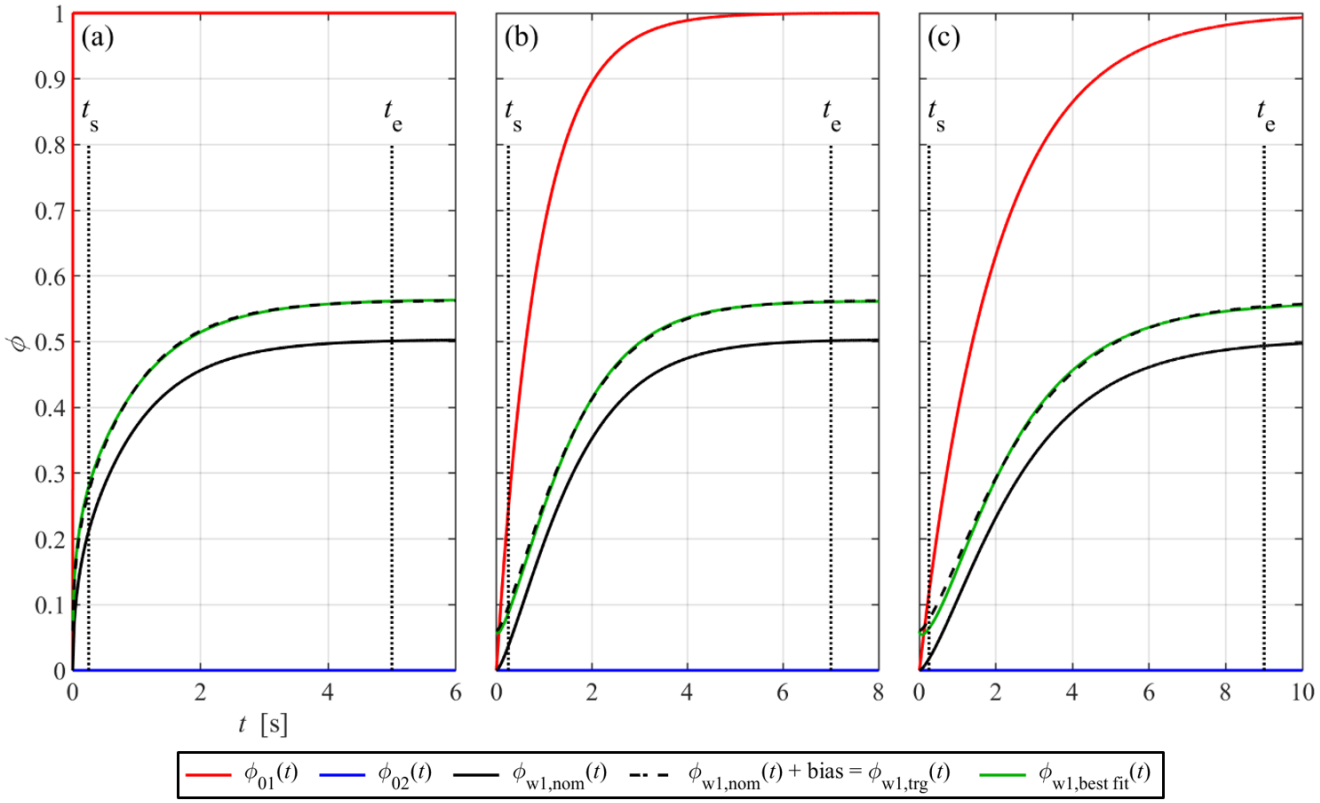


Figure 13: Normalised external wall thermal responses as a function of h_1 and h_2 for different time-constant ratios: (a) τ_{rise}/τ_w = 0; (b) τ_{rise}/τ_w = 1.27; (c) τ_{rise}/τ_w = 2.

We can see in Figure 13 that the best fit responses (green solid lines) are reasonably close the target responses (black dashed lines), which provides a visual demonstration of the best-fitting process. We note that the error (characterized by $\Delta T_{w1,RMS}$) is finite for all fits to offset trends of type $\phi_{w1,nom}(t)$ + bias. This is explained—even in the absence of precision error noise—by the fact that whilst an offset applied to the initial temperature of the external surface can occur in principle (surface still warm from a previous heated run for instance), a response with a bias offset ($\phi_{w1,nom}(t)$ + bias) is not a physical solution to the nominal temperature boundary conditions $T_{01}(t)$ and $T_{02}(t)$. This means that there is no possible h_1-h_2 pair that will lead to a perfect fit of the offset response.

In Table 5, we see that the best fit values $h_{1,best\ fit}$ and $h_{2,best\ fit}$ vary significantly with the time-constant ratio. The particular relationship (with time-constant ratio) is difficult to explain. Some insight is given by Figure 11, however, in which we see that both the overall extent of the solution confidence region (in h_1-h_2 space), and the shape (in particular the rotational orientation of the major axis of the quasi-ellipses) are strong functions of τ_{rise}/τ_w. The driving influences have been discussed, in particular the shift from primary dependence on h_1, through to significant dependence on both h_1 and h_2, and eventually primary dependence on the ratio h_1/h_2. Somewhat counterintuitive perhaps, lower sensitivity (here we define the word loosely) to a particular variable, implies that solution pairs (i.e. any h_1-h_2) very close to the best fit pair (i.e. $h_{1,best\ fit}$ and $h_{2,best\ fit}$) in terms of error minimization (i.e. $\Delta T_{w1,RMS}$ only slightly larger than the value for the best fit pair) can have with a large range in the particular variable.

Table 5: Best fit h_1 and h_2 for a fixed bias error for different time-constant ratios.

τ_{rise}/τ_w	0	1.27	2
$h_{1,nom}$, W m^{-2} K^{-1}	3000	3000	3000

$h_{2,\mathrm{nom}}$, W m^{-2} K^{-1}	6000	6000	6000
$h_{1,\mathrm{best\ fit}}$, W m^{-2} K^{-1}	3426	3800	4414
$h_{2,\mathrm{best\ fit}}$, W m^{-2} K^{-1}	4823	6003	8481
$\Delta T_{\mathrm{w1,RMS}}$, K	0.086	0.098	0.159

PRACTICAL APPLICATIONS

Consider an overall cooling effectiveness experiment in which the transient normalised temperature traces $\phi_{01}(t)$, $\phi_{02}(t)$ and $\phi_{\mathrm{w1}}(t)$ are as shown in Figure 14. In this example, the time-constant ratio ($\tau_{\mathrm{rise}}/\tau_{\mathrm{w}}$) is 5, and the bias and precision errors are of amplitude ±0.01. The following subsections provide practical examples in which underlying boundary conditions are extracted from transient temperature traces like those in Figure 14.

Example 1: determination of h_1 and h_2 when both parameters are unknown

If both h_1 and h_2 are unknown, we can obtain a 95 % confidence region of possible h_1-h_2 solution-pairs that satisfy the measurements $T_{01}(t)$, $T_{02}(t)$ and $T_{\mathrm{w1}}(t)$. This is shown as the solid grey line in Figure 15. The most likely h_1-h_2 solution-pair, and the size of the 95 % confidence region (in h_1-h_2 space) depend on both the bias and the precision errors in the measurements of $T_{01}(t)$, $T_{02}(t)$ and $T_{\mathrm{w1}}(t)$ and on the time-constant ratio.

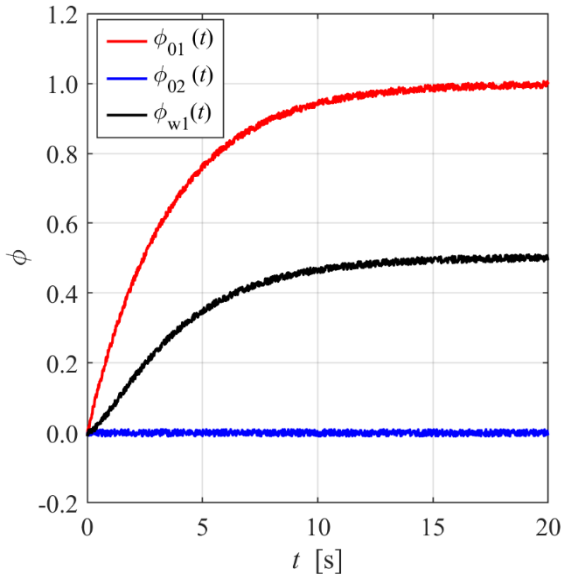


Figure 14: Normalised temperature traces with a bias and precision error $\beta = \varepsilon = \pm 0.01$ with time-constant ratio $\tau_{\mathrm{rise}}/\tau_{\mathrm{w}} = 5$.

The most likely output combination of h_1 and h_2 that satisfies the measurements $T_{01}(t)$, $T_{02}(t)$ and $T_{\mathrm{w1}}(t)$ is $h_{1,\mathrm{ml}} = 3006$ W m^{-2} K^{-1}, $h_{2,\mathrm{ml}} = 6026$ W m^{-2} K^{-1}. This is marked by "+" in Figure 15. The simulation input values (i.e. the underlying values in the numerical experiment) were $h_{1,\mathrm{nom}} = 3000$ W m^{-2} K^{-1}, $h_{2,\mathrm{nom}} = 6000$ W m^{-2} K^{-1}. As we have said previously, in a simulation with no measurement uncertainty, the underlying h_1-h_2 solution-pair would be exactly recovered. Interestingly, the impact of finite measurement uncertainty is not only a statistical distribution of possible h_1 and h_2 pairs (the 95 % confidence region in h_1-h_2 space) but also a shift (albeit very small) in the most likely value. That is, we are unable to exactly recover the most likely solution.

Examining the 95 % confidence region and the corresponding PDFs of h_1 (solid orange line in Figure 15) and h_2 (solid green line in Figure 15), we see that for this particular case, the range of h_2 (5200–7000 W m^{-2} K^{-1}) is more than two times the range of h_1 (2600–3400 W m^{-2} K^{-1}). As explained in the previous sections, for certain time-constant ratios ($\tau_{\mathrm{rise}}/\tau_{\mathrm{w}}$), the external wall thermal response, $T_{\mathrm{w1}}(t)$, is more sensitive to changes in h_1 than to changes in h_2. The high aspect ratio of the 95 % confidence region is explained by the fact that for high values of the ratio $\tau_{\mathrm{rise}}/\tau_{\mathrm{w}}$, the external wall temperature response can be considered to be quasi-steady-state (i.e. always close to the value it would assume if there were no further change in the external flow temperature). Thus, the external wall temperature is—essentially—only a function of the *ratio* h_1/h_2. A corollary of this is that for higher ratios $\tau_{\mathrm{rise}}/\tau_{\mathrm{w}}$, the *particular combination* h_1-h_2 is poorly constrained (significant absolute range of the 95 % confidence region) but the *relationship* between individual possible h_1-h_2 pairs is reasonably well constrained (narrow confidence region, approaching a single line of constant $T_{\mathrm{w1}}|_{t=\infty}$ in the limit of zero error).

Example 2: determination of h_2 when h_1 is known from a supplementary experiment and vice-versa

If h_1 or h_2 is known from a supplementary experiment, then it is possible to determine the other parameter by intersecting the measured parameter and its error band with the 95 % confidence region obtained from the overall cooling effectiveness experiment to more accurately determine the unknown parameter. For instance, h_1 could be measured as $h_1 = 3000$ W m^{-2} K^{-1} in an accurate experiment with an error band of ±2.5 % to 95 % confidence (2925–3075 W m^{-2} K^{-1}). In Figure 15 we show the 95 % confidence region of h_1-h_2 solution-pairs if both h_1 and h_2 are unknown (solid grey line) and the measured value of h_1 with its constrained PDF from the supplementary experiment (solid red line). By randomly sampling h_1-h_2 solution-pairs within the 95 % confidence region according to the weighting of the h_1 PDF, we create an output constrained PDF for h_2 (solid blue line) which defines the error band for h_2 constrained by information from the supplementary experiment in which h_1 was determined more precisely. For our particular example, we find that the most likely value of h_2 is 6003 W m^{-2} K^{-1} and its constrained 95 %

confidence interval is 5801–6205 W m^{-2} K^{-1}. The value of h_2 is therefore more accurately extracted than when both h_1 and h_2 are unknown, and the length of its 95 % confidence interval is reduced by 4.5 times compared to the confidence interval of h_2 when both h_1 and h_2 are unknown.

The same procedure could be repeated with a known h_2 to determine h_1 with more confidence. For instance, this approach would be of interest when trying to determine the external heat transfer (h_1) of a deteriorated gas turbine vane or blade due to service. If the internal heat transfer coefficient (h_2) is known from the original design since the internal cooling passages do not deteriorate with service, it would be possible to intersect the known h_2 with the 95 % confidence region of possible combinations of h_1 and h_2 obtained from the overall cooling effectiveness experiment performed with the deteriorated parts. This would enable the impact of in-service deterioration (oxidation, erosion and deposition) on h_1 to be determined with greater confidence.

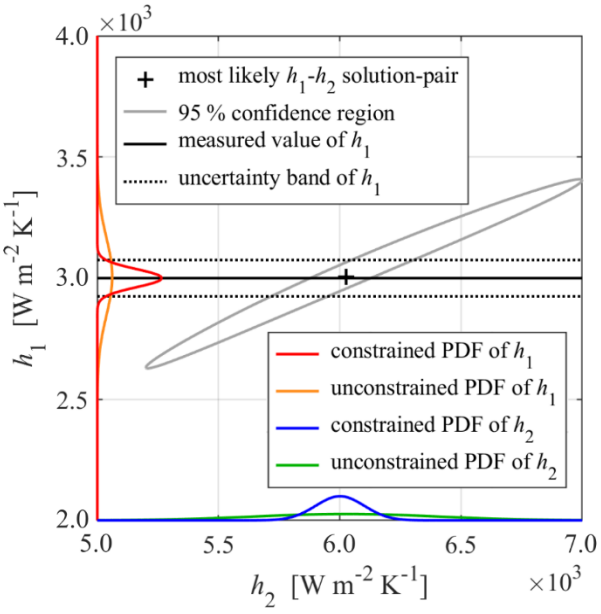


Figure 15: Intersection of the measured h_1 and its error band with the 95 % confidence region of h_1-h_2 solution-pairs.

Example 3: accuracy with which a design extrapolation can be implemented

If the measured nominal steady state ($t = \infty$) normalised external wall temperature (for example, the value $\phi_{\mathrm{w1,nom}}|_{t=\infty}$ = 0.5 in Figure 14) is found to be too high or too low, then a designer might wish to modify the external wall temperature to another value $\phi_{\mathrm{w1,extrap}}|_{t=\infty}$, which we refer here as the extrapolated value, by changing either the internal or external heat transfer coefficient, or both. To evaluate the accuracy with which the *extrapolation* can be performed we use information from both the transient region of the run (to best define the underlying values of h_1 and h_2), and from the steady state region of the run (assumed to be a true representation of the non-dimensional wall temperature) to predict the *extrapolation error* in the extrapolated value $\phi_{\mathrm{w1,extrap}}|_{t=\infty}$ (based on a measured value $\phi_{\mathrm{w1,nom}}|_{t=\infty}$). We evaluate the extrapolation error $\beta_{\mathrm{extrap}} = 2(\sigma_{\phi_{\mathrm{w1,extrap}}|_{t=\infty}} - \sigma_{\phi_{\mathrm{w1,nom}}|_{t=\infty}})$ as a function of the extrapolation length $\Delta\phi_{\mathrm{w1}}|_{t=\infty} = (\phi_{\mathrm{w1,extrap}}|_{t=\infty} - \phi_{\mathrm{w1,nom}}|_{t=\infty})$. Plots of the extrapolation uncertainty are presented for both a change in h_1 alone and a change in h_2 alone (the two choices potentially available to the designer). For simplicity, we do this in all cases for an initial value $\phi_{\mathrm{w1,nom}}|_{t=\infty}$ = 0.5.

We first show an example of the analysis involved in determining the extrapolation error. We consider the case of zero error in the measured temperatures signals ($T_{01}(t)$, $T_{02}(t)$ and $T_{\mathrm{w1}}(t)$), and also the case with bias and precision errors of amplitude ±0.01 in the measured temperature signals.

In the case of zero error in the measured temperature signals (underlying data of Figure 14, but without precision or bias error), best fitting of the predicted temperature response yields (as output) the nominal (i.e. input) h_1-h_2 solution-pair $h_{1,\mathrm{nom}}$ = 3000 W m^{-2} K^{-1} and $h_{2,\mathrm{nom}}$ = 6000 W m^{-2} K^{-1}. There is no error because the fitting is perfect. This nominal h_1-h_2 solution-pair is the *base case* (starting point of the extrapolation) for the case of no measurement error.

For the case of finite measurement uncertainty, we use information from both the *transient* and the *steady state* regions of the external wall temperature response (Figure 14) to best constrain the possible h_1-h_2 solution-pairs *for the purpose of performing the most accurate extrapolation*.

By analysing the transient region of the measured external wall temperature response (with errors), we can determine the 95 % confidence region of h_1-h_2 solution-pairs, which corresponds to the minimum area containing 95 % of the output h_1-h_2 solution-pairs from the Monte Carlo simulation (grey solid line in Figure 16; a repeat of result of Figure 15). As we have discussed, the extent of this region depends on the bias and the precision errors in the measurements of $T_{01}(t)$, $T_{02}(t)$ and $T_{\mathrm{w1}}(t)$, and on the time-constant ratio $\tau_{\mathrm{rise}}/\tau_{\mathrm{w}}$. This is the first constraint in our overall solution. By analysing the steady state value of the normalised external wall temperature $\phi_{\mathrm{w1,nom}}|_{t=\infty}$, we recall that this is satisfied by the contour line of $\phi_{\mathrm{w1,nom}}|_{t=\infty}$ in the h_1-h_2 space (solid black line in Figure 16) with a contour line band bounding $\phi_{\mathrm{w1,nom}}|_{t=\infty}$ (95 % confidence bands) represented by the dotted black lines in Figure 16. This is the second constraint in our overall solution. By taking the two constraints together, we can achieve the best constraint on the h_1-h_2 solution-pairs relevant to performing our extrapolation. Taking both pieces of information together, we define a region of h_1-h_2 solution-pairs delimited by the dark blue solid line in Figure 16. The most likely solution-pair (we refer to it as $h_{1,\mathrm{ml}}$-$h_{2,\mathrm{ml}}$) in the constrained distribution is $h_{1,\mathrm{ml}}$ = 3006 W m^{-2} K^{-1} and $h_{2,\mathrm{ml}}$ = 6026 W m^{-2} K^{-1}, and is marked by "+" in Figure 16. This most likely solution-pair is

the *base case* (starting point of the extrapolation) for the case with measurement error.

We now turn our attention to the problem of the extrapolation. In this particular example, we define the required extrapolation to be from $\phi_{\mathrm{w1,nom}}|_{t=\infty}$ = 0.5 to $\phi_{\mathrm{w1,extrap}}|_{t=\infty}$ = 0.6. The extrapolation could be achieved by varying h_1 alone or by varying h_2 alone (or, of course, combinations of both). As an example, in Figure 16, we illustrate the case of varying h_1 alone. In the case of zero error in the measured temperature signals, the extrapolation is achieved by changing h_1 by Δh_1 = 1449 W m^{-2} K^{-1} from $h_{1,\mathrm{nom}}$ = 3000 W m^{-2} K^{-1} to $h_{1,\mathrm{extrap}}$ = 4449 W m^{-2} K^{-1}. In combination with the original value of $h_{2,\mathrm{nom}}$, this delivers the required extrapolated value of wall temperature $\phi_{\mathrm{w1,extrap}}|_{t=\infty}$ = 0.6. We take this to be the *required change* to deliver the extrapolated value of external wall steady state temperature. With zero error in the input data the extrapolation is achieved exactly.

In the case of finite measurement errors, we start with the most likely h_1-h_2 solution-pairs extracted from the input data: that is $h_{1,\mathrm{ml}}$ = 3006 W m^{-2} K^{-1}, $h_{2,\mathrm{ml}}$ = 6026 W m^{-2} K^{-1}. Taking this as the starting solution pair, we determine that the required change in h_1 (to reach the extrapolated value of $\phi_{\mathrm{w1,extrap}}|_{t=\infty}$ = 0.6) is Δh_1 = 1443 W m^{-2} K^{-1} from $h_{1,\mathrm{ml}}$ = 3006 W m^{-2} K^{-1} to $h_{1,\mathrm{extrap}}$ = 4449 W m^{-2} K^{-1}. Making only the design change Δh_1, the shifted range of possible h_1-h_2 solution-pairs for the case of finite measurement errors is delimited by the light blue solid line in Figure 16 (c.f. the original dark blue solid line).

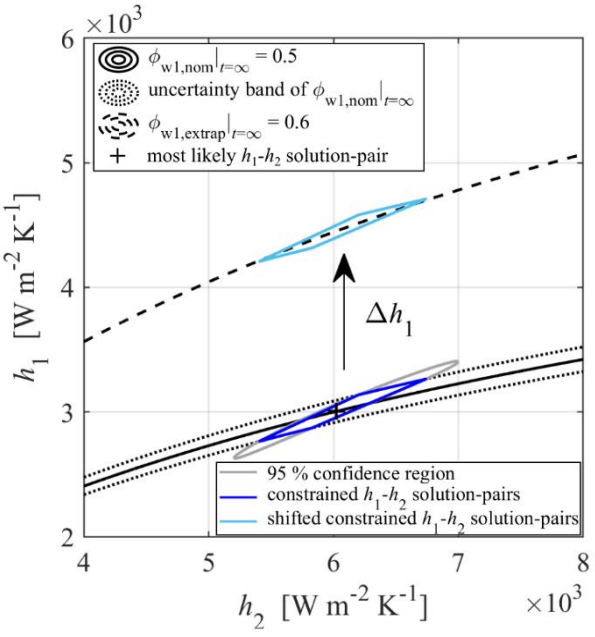


Figure 16: h_1-h_2 solution-pairs in the presence of measurement errors.

Figure 17 shows the PDFs of $\phi_{\mathrm{w1,nom}}|_{t=\infty}$ for zero and finite measurement errors, and the corresponding PDFs of $\phi_{\mathrm{w1,extrap}}|_{t=\infty}$ following the design change Δh_1. For zero error in the measured temperature signals, the PDF of $\phi_{\mathrm{w1,nom}}|_{t=\infty}$ is a delta function (black solid line in Figure 17). The corresponding PDF of $\phi_{\mathrm{w1,extrap}}|_{t=\infty}$ (black dashed line in Figure 17) is also a delta function. When there is no uncertainty in the measured temperature signals ($T_{01}(t)$, $T_{02}(t)$ and $T_{\mathrm{w1}}(t)$), there is no uncertainty in $\phi_{\mathrm{w1,nom}}|_{t=\infty}$ and no uncertainty in the extrapolated value $\phi_{\mathrm{w1,extrap}}|_{t=\infty}$. The error change due to the extrapolation is zero. In the case of finite measurement errors, the PDFs of $\phi_{\mathrm{w1,nom}}|_{t=\infty}$ (for the error range specific to this example) is shown by the dark blue solid line in Figure 17 and the corresponding PDFs of $\phi_{\mathrm{w1,extrap}}|_{t=\infty}$ is shown by the light blue solid line. Perhaps counterintuitively, we see that in this particular example the error in $\phi_{\mathrm{w1,extrap}}|_{t=\infty}$ is lower than the error in $\phi_{\mathrm{w1,nom}}|_{t=\infty}$. This is because the new ("shifted") h_1-h_2 solution-pairs lead to less spread in the output values $\phi_{\mathrm{w1,extrap}}|_{t=\infty}$ than the original ("non-shifted") h_1-h_2 solution-pairs do in the output values $\phi_{\mathrm{w1,nom}}|_{t=\infty}$. In general, the uncertainty in the extrapolated value ($\phi_{\mathrm{w1,extrap}}|_{t=\infty}$) can be larger or smaller than that in the input value ($\phi_{\mathrm{w1,nom}}|_{t=\infty}$), and depends on the extrapolation direction (positive or negative change $\Delta\phi_{\mathrm{w1}}|_{t=\infty}$), length (magnitude of $\Delta\phi_{\mathrm{w1}}|_{t=\infty}$), and design change path taken (change in h_1 and h_2). We now examine this in more detail.

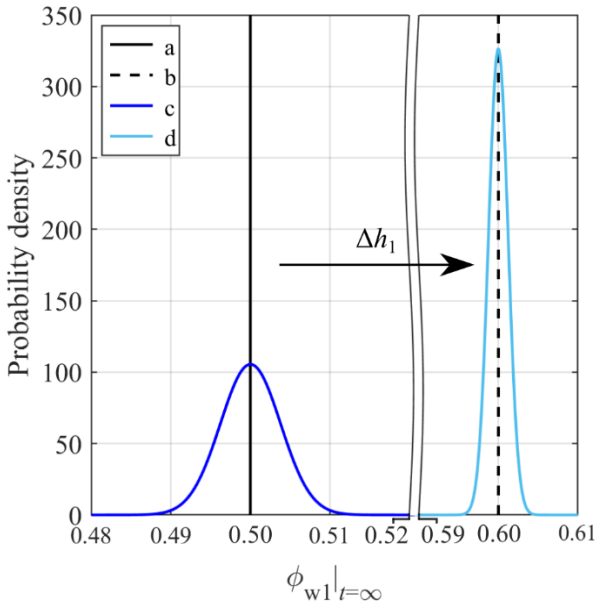


Figure 17: PDFs of: (a) $\phi_{\mathrm{w1,nom}}|_{t=\infty}$ with zero error; (b) $\phi_{\mathrm{w1,extrap}}|_{t=\infty}$ with zero error; (c) $\phi_{\mathrm{w1,nom}}|_{t=\infty}$ with

measurement errors; (d) $\phi_{\mathrm{w1,extrap}}\big|_{t=\infty}$ with measurement errors.

We now consider the *extrapolation error*, which we define as $\beta_{\mathrm{extrap}} = 2(\sigma_{\phi_{\mathrm{w1,extrap}}|_{t=\infty}} - \sigma_{\phi_{\mathrm{w1,nom}}|_{t=\infty}})$. Figure 18 shows the extrapolation error normalised by the extrapolated value $\beta_{\mathrm{extrap}}/\phi_{\mathrm{w1,extrap}}\big|_{t=\infty}$ (black solid line, left vertical axis) as a function of the extrapolation length $\Delta\phi_{\mathrm{w1}}|_{t=\infty}$ and the design change path (change in h_1, frame (a), or change in h_2, frame (b)) for the underlying data of Figure 14. The dotted line (right vertical axis) shows the corresponding change in the relative value of h_1 or h_2 with respect to their nominal values.

The extrapolation error is a complex function of the extrapolation length, $\Delta\phi_{\mathrm{w1}}|_{t=\infty}$, and depends on the design change path. Over most of the extrapolation range considered, $-0.2 \le \Delta\phi_{\mathrm{w1}}|_{t=\infty} \le 0.2$, the extrapolation error is positive: that is, the uncertainty in the extrapolated overall cooling effectiveness value is greater than the uncertainty in the measured overall cooling effectiveness. The maximum normalised extrapolation error over this range is approximately 6.0 %, or an additional effectiveness error of 0.03. Interestingly, in some regions of the plot there is a negative extrapolation error: that is, the confidence in the extrapolated value is greater than that in the measured value. This effect has been discussed.

In Figure 18 (b) we see vertical asymptote $\Delta h_2/h_{2,\mathrm{nom}} \to \infty$ at $\Delta\phi_{\mathrm{w1}}|_{t=\infty} = -0.15$. This corresponds to the limit of infinite internal surface heat transfer coefficient, or an inner wall temperature equal to the internal gas temperature. It is impossible to effect design changes beyond this limit, at which the maximum heat that pass into the internal cooling flow is limited only by the thermal resistance of the wall.

Similar figures to those of Figure 18 can be used to provide designers with information on how accurately a design extrapolation could likely be performed. Such charts are easily constructed for a particular transient overall cooling effectiveness experimental result, using the method presented.

CONCLUSIONS

The purpose of this paper was to present methods to extract the individual underlying boundary conditions from transient overall cooling effectiveness experimental data, and to describe the drivers—in terms, for example, of the precision and bias errors in the directly measured parameters—for the resulting uncertainty in these derived quantities. To explain aspects of this relatively complex problem, we considered the simplest possible system: a one-dimensional heat transfer problem with measured internal and external gas temperatures (with errors), and measured external wall temperature (with errors), and unknown internal and external heat transfer coefficients (the boundary conditions, which were the subject of the study). We showed the following:

i) The uncertainty in the individual underlying values of h_1 and h_2 grows quadratically with the amplitude of the precision and bias errors applied on the three measured temperature signals.

ii) When the time constant of the external flow temperature rise is small in comparison to the time constant of the wall ($\tau_{\mathrm{rise}}/\tau_{\mathrm{w}} \le 2.00$), possible h_1-h_2 solution-pairs are tightly constrained (small 95 % confidence region in h_1-h_2 space) when measurement errors are low (β, $\varepsilon \le 0.02$).

iii) When the time constant of the external flow temperature rise is larger in comparison to the time constant of the wall ($\tau_{\mathrm{rise}}/\tau_{\mathrm{w}} > 2.00$), possible h_1-h_2 solution-pairs are relatively poorly constrained even if the measurement errors are low (β, $\varepsilon \le 0.02$).

iv) Interestingly, in some cases (iii) where h_1-h_2 solution-pairs are relatively poorly constrained, the 95 % confidence region can be thin and elongated in h_1-h_2 space. Thus, although the uncertainty associated with picking a *particular* h_1-h_2 solution-pairs might be high, the relationship between h_1 and h_2 *within* a pair is relatively low.

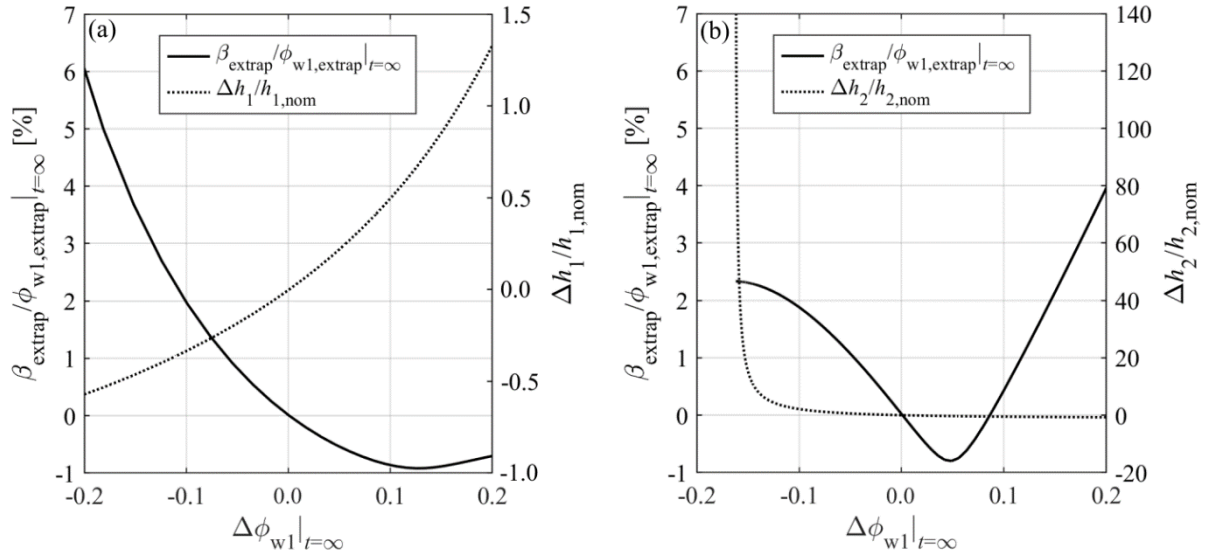


Figure 18: Extrapolation error as a function of extrapolation length for: (a) a change in h_1 alone; (b) a change in h_2 alone.

v) A consequence of (iv) is that if either h_1 or h_2 is known from supplementary experiment, the remaining parameter can be determined with higher accuracy than the situation in which both h_1 or h_2 are unknown and simultaneously extracted from a single experiment

vi) If a particular overall cooling effectiveness result has been achieved in an experiment, and a design extrapolation is required to either increase or decrease the overall cooling effectiveness to a new target value, then the accuracy with which the target can be achieved following the design change depends both on the extent of the extrapolation and whether the design change is made by varying h_1 or h_2. In general, the predicted uncertainty in the target value of overall cooling effectiveness is greater than that in the original experiment, but certain combinations of initial value and extrapolation range can lead to small reductions in uncertainty.

Increasing sophistication in overall cooling effectiveness experiments has allowed very detailed assessment of particular cooling system designs. We believe that using analysis of the sort described in this paper—with further developments—it may be possible to go some way to *decoupling* underlying boundary conditions from these experiments, providing deeper insights and understanding of complex coupled systems, making the overall cooling effectiveness technique even more powerful than it currently is. However, the presented method was developed for 1D problems and it would require significant development to extend it to multidimensional (2D and 3D) problems, which would involve solving for an internal and external field of heat transfer coefficient rather than two values. In addition, setting the lateral thermal boundary condition to the studied part (or even just to an area of interest) would be very difficult to achieve in a simple thermal model.

APPENDIX A: CHOICE OF INITIAL TEMPERATURE DISTRIBUTION OF WALL

In the process of best fitting the target external wall thermal response $T_{\text{w1,trg}}(t)$—normally the measured external wall response in an experiment—by minimizing the RMS value $\Delta T_{\text{w1,RMS}}$ (Equation 9) between a particular prediction $T_{\text{w1,prt}}(t)$ and the target external wall response $T_{\text{w1,trg}}(t)$, an initial temperature distribution (with depth) of the wall in the particular prediction ($T_{\text{w1,prt}}|_{t=0}$) has to be chosen. This choice must be made somewhat arbitrarily, but can be informed by thinking about the uncertainty of the underlying measurements. If we assume that in a typical overall cooling effectiveness experiment, the three temperature signals $T_{01}(t)$, $T_{02}(t)$ and $T_{\text{w1,trg}}(t)$ are measured with similar absolute uncertainty, then in the situation they are *all the same* (i.e. the typical example of isothermal starting conditions ahead of a step change in the external flow temperature), there would be no good reason for assuming that any one measurement is any more reliable than another, and therefore we might argue that an average value should be taken so as to use all the information in the system. On closer scrutiny, however, we see that there are many situations in which this is not the case, for example, a situation in which the overall cooling surface remains heated with respect to both the initial mainstream and initial coolant temperature, on account of—for example—residual heat from a previous run. Indeed, on the basis that the relaxation time of the wall is relatively short (order of several seconds) in comparison to the typical time between experiments (order of minutes, or longer) we see that an average temperature (average of $T_{01}|_{t=0}$, $T_{02}|_{t=0}$ and $T_{\text{w1,trg}}|_{t=0}$) becomes a poor choice for the initial temperature of the wall for the prediction, and

therefore the logical choice is to use $T_{\mathrm{w1,trg}}\big|_{t=0}$ alone: that is, we set $T_{\mathrm{w1,prt}}\big|_{t=0} = T_{\mathrm{w1,trg}}\big|_{t=0}$.

A second consideration is the choice of temperature distribution with depth within the wall. If the internal wall initial temperature were measured ($T_{\mathrm{w2,trg}}\big|_{t=0}$), then a linear initial temperature profile could be set between the internal and external surfaces, and this would be the best choice in an experiment in which the information were available. In most overall cooling effectiveness experiments the internal wall temperature is not measured, however, and in the absence of additional information this forces the assumption of a uniform (with depth) initial temperature distribution (result of relaxation).

To further justify this assumption, consider an example of achieving a best fit to a target external wall temperature response with both an initial temperature offset (a real pre-heating effect, for example) and bias error. Figure 19 shows the normalised nominal external wall thermal response with an arbitrary positive initial normalised temperature offset of +0.2 (solid black line), and the same nominal external wall thermal response with a positive bias error (+0.06) added (dashed black line). The nominal (input) heat transfer coefficients for the simulation were $h_{1,\mathrm{nom}}$ = 3000 W m^{-2} K^{-1} and $h_{2,\mathrm{nom}}$ = 6000 W m^{-2} K^{-1}, and the time-constant ratio $\tau_{\mathrm{rise}}/\tau_{\mathrm{w}}$ = 2. We then calculate the best fit external wall temperature response to the target external wall temperature with two different initial wall temperature assumptions: i) the initial wall temperature is set to the initial temperature of the flows, i.e. $\phi_{\mathrm{w1,best\ fit\ 1}}\big|_{t=0} = \phi_{01}|_{t=0} = \phi_{02}|_{t=0}$ (orange solid line in Figure 19); ii) the initial wall temperature is set to the initial target wall temperature $\phi_{\mathrm{w1,best\ fit\ 2}}\big|_{t=0} = \phi_{\mathrm{w1,target}}\big|_{t=0}$ (green solid line in Figure 19). For both initial conditions, we evaluate the best-fit $h_{1,\mathrm{best\ fit}}$-$h_{2,\mathrm{best\ fit}}$ pair (the values that minimize the RMS temperature difference $\Delta T_{\mathrm{w1,RMS}}$ (defined by Equation 9) between the $\phi_{\mathrm{w1,best\ fit}}(t)$ and $\phi_{\mathrm{w1,trg}}(t)$ over the time window $t_{\mathrm{s}} \leq t \leq t_{\mathrm{e}}$ (Figure 19).

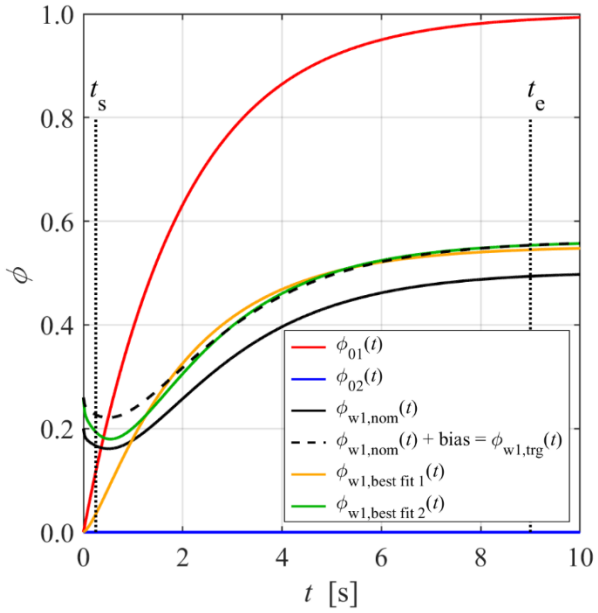


Figure 19: Best fit external wall thermal responses for different thermal initial conditions.

Table 6 lists the nominal (input) values of $h_{1,\mathrm{nom}}$ and $h_{2,\mathrm{nom}}$, and the best fit (output) values $h_{1,\mathrm{best\ fit}}$ and $h_{2,\mathrm{best\ fit}}$. Using the second assumption of initial boundary condition (the initial wall temperature is set to the initial target wall temperature) we see that: the error between input and output pairs is lower; and the goodness of the fit (in terms of $\Delta T_{\mathrm{w1,RMS}}$) is better. We can see the same result in (Figure 19). Setting the initial temperature of the wall to the initial temperature of the target external wall thermal response ($T_{\mathrm{w1,trg}}\big|_{t=0}$) is generally the method least likely to result in significant error.

Table 6: Best fit h_1 and h_2 for different thermal initial conditions.

Parameter	Initial condition 1	Initial condition 2
$h_{1,\mathrm{nom}}$, W m^{-2} K^{-1}	3000	3000
$h_{2,\mathrm{nom}}$, W m^{-2} K^{-1}	6000	6000
$h_{1,\mathrm{best\ fit}}$, W m^{-2} K^{-1}	7156	4603
$h_{2,\mathrm{best\ fit}}$, W m^{-2} K^{-1}	9873	9272
$\Delta T_{\mathrm{w1,RMS}}$, K	0.62	0.44

NOMENCLATURE

Abbreviations

HTC heat transfer coefficient
IR infrared
PDF probability density function
RMS root mean square

Roman variables

b	thickness, m
c	specific heat capacity, J kg^{-1} K^{-1}
h	heat transfer coefficient, W m^{-2} K^{-1}
k	thermal conductivity, W m^{-1} K^{-1}
t	time, s
T	temperature, K
y	position through the wall, m

Greek variables

α	thermal diffusivity, m^2 s^{-1}
β	bias error
δ	fraction
Δ	difference
ε	precision error
μ	mean
ϕ	normalised temperature
σ	standard deviation
ρ	density, kg m^{-3}
τ	time constant, s

Subscripts

e	end
extrap	extrapolated
j	wall node index
ml	most likely
nom	nominal
n	number of nodes in the wall
prt	particular
rise	temperature rise
s	start
trg	target
w	wall
0	total property
1	external side
2	internal side

Superscripts

p = time step index

REFERENCES

[1] Albert, J. and Bogard, D., 2013, "Measurements of Adiabatic Film and Overall Cooling Effectiveness on a Turbine Vane Pressure Side With a Trench," ASME Journal of Turbomachinery, 135(5):051007.

[2] Luque, S., and Povey, T., 2011, "A Novel Technique for Assessing Turbine Cooling System Performance," ASME Journal of Turbomachinery, 133(3): 031013.

[3] Luque, S., Batstone, J., Gillespie, D., Povey, T. and Romero, E., 2013, "Full Thermal Experimental Assessment of a Dendritic Turbine Vane Cooling Scheme," ASME Journal of Turbomachinery, 136(2): 021011.

[4] Luque, S., Jones, T. and Povey T., 2017, "Effects of Coolant Density, Specific Heat Capacity, and Biot Number on Turbine Vane Cooling Effectiveness," ASME Journal of Turbomachinery, 139(11):111005.

[5] Kirollos, B., Lubbock, R., Beard, P., Goenaga, F., Rawlinson, A., Janke, E. and Povey, T., 2017, "ECAT: An Engine Component AeroThermal Facility at the University of Oxford," Proceedings of the ASME Turbo Expo 2017, Charlotte, NC, USA, paper no. GT2017-64736.

[6] Kirollos, B. and Povey T., 2017, "Laboratory Infrared Thermal Assessment of Laser-Sintered High-Pressure Nozzle Guide Vanes to Derisk Engine Design Programs," ASME Journal of Turbomachinery, 139(4): 041009.

[7] Alizadeh, M., Izadi, A., and Fathi, A., "Sensitivity Analysis on Turbine Blade Temperature Distribution Using Conjugate Heat Transfer Simulation," ASME Journal of Turbomachinery, 136(1):011001.

[8] Chowdhury, N. H. K., Zirakzadeh, H., Han, J. C., 2017, "A Predictive Model for Preliminary Gas Turbine Blade Cooling Analysis," ASME Journal of Turbomachinery, 139(9):091010.

[9] Takahashi, T., Watanabe, K., and Sakai, T., 2005, "Conjugate Heat Transfer Analysis of a Rotor Blade With Rib-Roughened Internal Cooling Passages," Proceedings of ASME Turbo Expo 2005, Reno, NV, USA, paper no. GT2005-68227.

[10] Zecchi, S., Arcangeli, L., Facchini, B., and Coutandin, D., "Features of a Cooling System Simulation Tool Used in Industrial Preliminary Design Stage," Proceedings of ASME Turbo Expo 2004, Vienna, Austria, paper no. GT2004-53547.

[11] Bergman, T., Lavine, S., Incropera, F. and Dewitt, D., *Fundamentals of Heat and Mass Transfer*, 7th ed., John Wiley, New York, 2011.

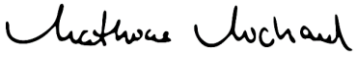
Statement of Authorship for joint/multi-authored papers for PGR thesis

To appear at the end of each thesis chapter submitted as an article/paper

The statement shall describe the candidate's and co-authors' independent research contributions in the thesis publications. For each publication there should exist a complete statement that is to be filled out and signed by the candidate and supervisor **(only required where there isn't already a statement of contribution within the paper itself).**

Title of Paper	Methods to Extract Underlying Boundary Conditions from Transient Metal Effectiveness Measurements
Publication Status	■ Published □ Accepted for Publication □Submitted for Publication □Unpublished and unsubmitted work written in a manuscript style
Publication Details	Michaud, M. and Povey, T., 2021, "Methods to Extract Underlying Boundary Conditions from Transient Metal Effectiveness Measurements," AIAA Journal of Thermophysics and Heat Transfer, 35(4), p. 657-668.

Student Confirmation

Student Name:	Mathias Michaud		
Contribution to the Paper	Mathias Michaud wrote all the modelling codes, post-processed the data, wrote the manuscript and contributed to the analysis. Thomas Povey provided the original research idea, contributed to the analysis and the writing of the manuscript.		
Signature 		Date	07/12/2021

Supervisor Confirmation

By signing the Statement of Authorship, you are certifying that the candidate made a substantial contribution to the publication, and that the description described above is accurate.

Supervisor name and title: Professor Thomas Povey		
Supervisor comments: I certify that the candidate made a substantial contribution to the publication, and that the description described above is accurate.		
Signature 	Date	22/01/2022

This completed form should be included in the thesis, at the end of the relevant chapter.

8. Conclusions

This thesis combines five academic publications focused on the development of high TRL turbine aerothermal research covering four topics: experimental research facilities; instrumentation; post-processing decoupling methods; and in-service deterioration. While a broad range of topics was covered, it is hoped that—as a whole—it will contribute to the advancement of high TRL turbine aerothermal research. High-level conclusions on each topic are now summarised. Proposals for future studies are also discussed.

8.1. Annular dump diffuser and deswirl system

This paper described the design and commissioning of a novel back-pressure control system combining an annular dump-diffuser and deswirl system with an integrated choke plate. A series of experiments validated the precise back-pressure control of the transonic cascade with this compact system while maintaining a good optical and probe access. It is hoped that this system will be considered as an option by facility designers for back-pressure control in a transonic environment.

Naturally, this new system will be used in the ECAT facility for future studies isolating Mach number, Reynolds number or mainstream-to-coolant temperature ratio effects (and maintaining all the other operating conditions constant). The new system will also be used for the validation of new designs of HP NGVs at different engine operating conditions (cruise, MTO, descent, etc.).

8.2. Infrared calibration instrumentation

This paper demonstrated with simple modelling how bias errors can be easily introduced in the calibration process due to the installation of the calibration thermocouple in the presence of through-wall heat flux and lateral flow temperature gradients. It is hoped that this paper will provide researcher a framework for quantifying such errors. A new calibration system was also

proposed and validated to significantly reduce those errors, and can be used in film cooling studies (adiabatic surface with significant lateral temperature variations) and in overall cooling effectiveness studies on internally- and even film-cooled conductive components.

8.3. Boundary condition decoupling method

This paper described a method to extract the individual underlying boundary conditions from transient overall cooling effectiveness experimental data. A detailed uncertainty analysis using synthetic experiments showed how the errors (precision and bias) in the directly measured quantities and the operating conditions would affect the uncertainty in the extracted quantities. With further development, methods of this type could allow an accurate decoupling of the underlying boundary conditions, providing deeper understanding in complex coupled systems (e.g. cooled turbine components).

Further developments of this work would include: performing an experimental validation of the decoupling method using an internally cooled flat plate; exploring how to reduce the uncertainty in the extracted boundary conditions by using two runs at different mainstream temperature rise time constants and intersecting their confidence regions; exploring the feasibility of including adiabatic film cooling effectiveness as a third extracted boundary condition. The latter point would lead to confidence volumes in three dimensions (three variables) rather than confidence regions in two dimensions (two variables) in the uncertainty analysis.

8.4. Aerothermal impact of in-service deterioration on turbines

These papers described the aerothermal measurements on 15 real-engine in-service-deteriorated HP NGVs with a broad variety of deterioration features. They address a gap in literature by providing the first detailed analysis of the *overall* impact of combined in-service deterioration features on the overall aerodynamic and thermal performance of HP NGVs. It is

hoped that the results from this paper will be a useful step towards whole-life engine performance modeling and assessment.

As measurements in this study were taken at a single engine operating point (near cruise condition), measurements could also be performed at other engine operating points (e.g. max-take-off). Further work would be to perform parametric studies isolating deterioration features to better decouple the deterioration effects. This could include artificially damaging (machining) the TE of real engine vanes to measure the aerodynamic loss contribution of TE damage. It could also include artificially roughening the external surface of real engine vanes to isolate the contribution of increase surface roughness on aerodynamic loss and overall cooling effectiveness.

9. References

[1] Cumpsty, N. , 2003, *Jet Propulsion - A simple guide to the aerodynamic and thermodynamic design and performance of jet engines*. Cambridge University Press, Cambridge, UK.

[2] Crook, G., and Horlor, M., 2005, *The Jet Engine*, 5th ed., Rolls-Royce Technical Publications, London, England, UK.

[3] Parker, J. A., Romero, E., and Povey, T., 2019, "A Modular Transonic Turbine Cascade for Cooled Rotor Metal Effectiveness Investigations." Proceedings of the ASME Turbo Expo 2019, Phoenix, Arizona, USA. Paper No. GT2019-91697.

[4] Kirollos, B., and Povey, T., 2017, "Laboratory Infrared Thermal Assessment of Laser-Sintered High-Pressure Nozzle Guide Vanes to Derisk Engine Design Programs." ASME Journal Turbomachinery 139(4): 041009.

[5] Calvert, H. F., Cochran, R. P., Dengler, R. P., Hickel, R. O., and Norris, J. W., 1970, "Turbine Cooling Research Facility." NASA Technical Report TM X-1927.

[6] Rådeklint, U. R., and Hjalmarsson, C. S., 1998, "A New Test Facility for Testing of Cooled Gasturbine Components." Proceedings of the ASME 1998 International Gas Turbine and Aeroengine Congress and Exhibition, Stockholm, Sweden. Paper no. 98-GT-557.

[7] Fujimoto, S., Okita, Y., and Nakamata, C., 2009, "Experimental Study on the Cooling Performance of a Turbine Nozzle With an Innovative Internal Cooling Structure." Proceedings of the ASME Turbo Expo 2009, Orlando, Florida, USA, paper no. GT2009-59597.

[8] Wiers, S. H. and Fransson, T. H., 1998, "A New Annular Sector Cascade Test Facility to Investigate Steady State Cooling Effects." Proceedings of the 14th Symposium on Measuring Techniques for Transonic and Supersonic Flow in Cascades and Turbomachines, Limerick, Ireland.

[9] Gladden, H. J., Yeh, F. C. and Fronek, D. L., 1985, "Heat Transfer Results and Operational Characteristics of the NASA Lewis Research Center Hot Section Cascade Test Facility." NASA technical report TM-86890.

[10] Povey, T., Sharpe, M., and Rawlinson, A., 2011, "Experimental Measurements of Gas Turbine Flow Capacity Using a Novel Transient Technique." ASME Journal of Turbomachinery, 133(1): 011005.

[11] Kirollos, B., Lubbock, R., Beard, P., Goenaga, F., Rawlinson, A., Janke, E., and Povey, T., 2017, "ECAT: An Engine Component Aerothermal Facility at the University of Oxford." Proceedings of the ASME Turbo Expo 2017, Charlotte, North Carolina, USA. Paper no. GT2017-64736.

[12] Hilditch, M. A., Fowler, A., Jones, T. V., Chana, K. S., Oldfield, M. L. G., Ainsworth, R. W., Hogg, S. I., Anderson, S. J., and Smith, G. C., 1994, “Installation of a Turbine Stage in the Pyestock Isentropic Light Piston Facility.” Proceedings of the ASME Turbo Expo 1994, The Hague, Netherlands. Paper no. 94-GT-277.

[13] Sieverding, C. H. and Arts, T., 1992, “The VKI Compression Tube Annular Cascade Facility CT3.” Proceedings of the ASME 1992 International Gas Turbine and Aeroengine Congress and Exposition, Cologne, Germany. Paper no. 92-GT-336.

[14] Rehder, H, Pahs, A, Bittner, M, and Kocian, F., 2017, “Next Generation Turbine Testing at DLR.” Proceedings of the ASME Turbo Expo 2017, Charlotte, North Carolina, USA. Paper no. GT2017-64409.

[15] Erhard, J., and Gehrer, A., 2000, “Design and Construction of a Transonic Test-Turbine Facility.” Proceedings of the ASME Turbo Expo, Munich, Germany. Paper no. 2000-GT-0480.

[16] Paniagua, G., Cuadrado, D., Saavedra, J., Andreoli, V., Meyer, T., Solano, J. P., Herrero, R., Meyer, S., and Lawrence, D., 2018, "Design of the Purdue Experimental Turbine Aerothermal Laboratory for Optical and Surface Aerothermal Measurements," ASME Journal of Engineering for Gas Turbines and Power, 141(1): 012601.

[17] Bernardini, C., Takakura, T., Perez, E., Cameron, J. D. and Morris, S. C., 2019, “Development of a 10 MW Facility for Gas Turbine Engine and Component Testing.” AIAA Propulsion and Energy Forum, Indianapolis, Indiana, USA, paper no. 2019-4001.

[18] Anthony, R. J. and Clark, J. P, 2013, “A Review of the AFRL Turbine Research Facility.” Proceedings of the ASME Turbo Expo 2013, San Antonio, Texas, USA. Paper No. GT2013-94741.

[19] Dunn, M. and Mathison, R., 2014, “History of Short-Duration Measurement Programs Related to Gas Turbine Heat Transfer, Aerodynamics, and Aeroperformance at Calspan and The Ohio State University.” ASME Journal of Turbomachinery, 136(4): 041004.

[20] Hodson, H. P., Dominy, R. G., 1993, “Annular and Rotating Cascades.”, AGARDograph 328, Chapter 3, AGARD-AG-328.

[21] Burdett, D., Hambidge, C., and Povey, T., 2020, “Analysis of ultra-low uncertainty gas turbine flow capacity measurement techniques,” Proceedings of the Institution of Mechanical Engineers, Part A: Journal of Power and Energy.

[22] Doorly, J. E. and Olfield, M. L. G., 1987, “The Theory of Advanced Multi-layer Thin Film Heat Transfer Gauges.” International Journal of Heat and Mass Transfer, 30(6), pp. 1159–1168.

[23] Anthony, R. J., Clark, J. P., Kennedy, S. W., Finnegan, J. M., Johnson, D., Hendershot, J. and Downs, J., 2011, “Flexible Non-Intrusive Heat Flux Instrumentation for the AFRL Research Turbine.” Proceedings of the ASME 2011 Turbo Expo, Vancouver, British Columbia, Canada. Paper No. GT2011-46853.

[24] Chamberlain, J. R., 1987, “Temperature Indicating Paint and Method of Preparing a Sample,” U.S. Patent No. 5008136 A.

[25] Glezer, B., 2003, “Selection of a Gas Turbine Cooling System,” in *Handbook of Turbomachinery*, 2nd edition.

[26] Ireland, P. T. and Jones, T. V., 2000, “Liquid Crystal Measurements of Heat Transfer and Surface Shear Stress.” Measurement Science and Technology, 11(7).

[27] Luque, S. and Povey, T., 2011, “A Novel Technique for Assessing Turbine Cooling System Performance.” ASME Journal of Turbomachinery, 133(3): 031013.

[28] Krumme, A., Tegeler, M. and Gattermann, S., 2019, “Design, Integration and Operation of a Rotating Combustor-Turbine-Interaction Test Rig Within the Scope of EC FP7 project FACTOR.” Proceedings of 13th European Conference on Turbomachinery Fluid Dynamics & Thermodynamics, Lausanne, Switzerland. Paper No. ETC2019-035

[29] CC BY-SA Olivier Cleynen.

[30] Kurz, R. and Brun, K, 2001, “Degradation in Gas Turbine Systems.” ASME Journal of Engineering for Gas Turbines and Power, 123(1): 70–77.

[31] Hamed, A., Tabakoff, W. and Wenglarz, R. V., 2006, “Erosion and Deposition in Turbomachinery.” AIAA Journal of Propulsion and Power, 22:2, 350-360.

[32] Tabakoff, W., Hamed, A., and Shanov, V., 1998, “Blade Deterioration in a Gas Turbine Engine.” International Journal of Rotating Machinery, 4.

[33] Swar, R., Hamed, A., Shin, D., Woggon, N., and Miller, R., 2012, “Deterioration of Thermal Barrier Coated Turbine Blades by Erosion.” International Journal of Rotating Machinery.

[34] Bogard, D. G., Schmidt, D. L., and Tabbita, M., 1998, “Characterization and Laboratory Simulation of Turbine Airfoil Surface Roughness and Associated Heat Transfer.” ASME Journal of Turbomachinery, 120(2): 337–342

[35] Dunn, M. G., 2012, “Operation of Gas Turbine Engines in an Environment Contaminated with Volcanic Ash.” ASME Journal of Turbomachinery, 134(5): 051001

[36] Kurz, R., Brun, K., and Wollie, M., 2009, “Degradation Effects on Industrial Gas Turbines.”ASME Journal of Engineering for Gas Turbines and Power, 131(6): 062401.

[37] Ozgurluk, Y., Doleker, K. M., Ahlatci, H. and Karaoglanli, A. C., 2018, “Investigation of Hot Corrosion Behavior of Thermal Barrier Coating (TBC) Systems With Rare Earth Contents.” Arabian Journal of Geosciences, 11:267.

[38] Bhushan, B., 2013, *Introduction to Tribology*. John Wiley & Sons, New York.

[39] Goodhand, M. N., Walton, K., Blunt, L., Lung, H. W., Miller, R. J., and Marsden, R., 2016, "The Limitations of Using Ra to Describe Surface Roughness." ASME Journal of Turbomachinery, 138(10):101003.

[40] Glasenapp, T., Puetz, F., Schulz, A., and Bauer, H., 2017, "Assessment of Real Turbine Blade Roughness Parameters for the Design of a Film Cooling Test Rig." Proceedings of the ASME Turbo Expo 2017, Charlotte, NC, USA. Paper no. GT2017-63088.

[41] Schlichting, H., 2003, *Boundary Layer Theory*, 8th ed., Springer-Verlag, Berlin.

[42] Bons, J. P., 2010, "A Review of Surface Roughness Effects in Gas Turbines." ASME Journal of Turbomachinery, 132(2): 021004.

[43] Sigal, A. and Danberg, J. E., 1990, "New Correlation of Roughness Density Effect on Turbulent Boundary Layer." AIAA Journal, 28(3), pp. 554-556.

[44] Bons, J. P., 2005, "A Critical Assessment of Reynolds Analogy for Turbine Flows." ASME Journal of Heat Transfer, 127(5): 472–485.

[45] van Rij , J. A., Belnap , B. J., and Ligrani, P. M., 2002, "Analysis and Experiments on Three-Dimensional, Irregular Surface Roughness." ASME Journal of Fluids Engineering, 124(3): 671–677.

[46] Waigh, D. R. and Kind, R. J., 1998, "Improved Aerodynamic Characterization of Regular Three-Dimensional Roughness." AIAA Journal, 36(6): 1117-1119.

[47] Bons, J. P. and McClain, S. T., 2004, "The Effect of Real Turbine Roughness With Pressure Gradient on Heat Transfer" ASME Journal of Turbomachinery, 126(3): 385–394.

[48] Erickson, E. L., Ames, F. E. and Bons, J. P., 2010, "Effects of a Realistically Rough Surface on Vane Aerodynamic Losses Including the Influence of Turbulence Condition and Reynolds Number." Proceedings of the ASME Turbo Expo 2010, Glasgow, UK. Paper no. GT2010-22173.

[49] Erickson, E. L., Ames, F. E., and Bons, J. P., 2012, "Effects of a Realistically Rough Surface on Vane Heat Transfer Including the Influence of Turbulence Condition and Reynolds Number." ASME Journal of Turbomachinery, 134(2): 021013.

[50] Abuaf, N., Bunker, R. S. and Lee, C. P., 1998, "Effects of Surface Roughness on Heat Transfer and Aerodynamic Performance of Turbine Airfoils." ASME Journal of Turbomachinery, 120(3): 522–529.

[51] Taylor, R. P., 1990, "Surface Roughness Measurements on Gas Turbine Blades." ASME Journal of Turbomachinery, 112(2): 175–180.

[52] Bons, J. P., Taylor, R. P., McClain, S. T. and Rivir, R. B., 2001, "The Many Faces of Turbine Surface Roughness." ASME Journal of Turbomachinery, 123(4): 739–748.

[53] Kellersmann, A., Weiler, S., Bode, C., Friedrichs, J., Städing, J. and Ramm, G., 2018, “Surface Roughness Impact on Low-Pressure Turbine Performance Due to Operational Deterioration.” ASME Journal of Engineering for Gas Turbines and Power, 140(6): 062601.

[54] Yun, Y. I., Park, I. Y. and Song, S. J., 2005, “Performance Degradation due to Blade Surface Roughness in a Single-stage Axial Turbine.” ASME Journal of Turbomachinery, 127(1): 137–143.

[55] Lorenz, M., Schulz, A., and Bauer, H. J., 2012, “Experimental Study of Surface Roughness Effects on a Turbine Airfoil in a Linear Cascade—Part II: Aerodynamic Losses.” ASME Journal of Turbomachinery, 134(4): 041007.

[56] Kind, R. J., Serjak, P. J., and Abbott, M. W. P., 1998, “Measurements and Prediction of the Effects of Surface Roughness on Profile Losses and Deviation in a Turbine Cascade.” ASME Journal of Turbomachinery, 120(1): 20–27.

[57] Matsuda, H., Otomo, F., Kawagishi, H., Inomata, A., Niizeki, Y., and Sasaki, T., 2006, “Influence of Surface Roughness on Turbine Nozzle Profile Loss and Secondary Loss.” Proceedings of ASME Turbo Expo 2006, Barcelona, Spain. Paper no. GT2006-90828.

[58] Hummel, F., Lötzerich, M., Cardamone, P. and Fottner, L., 2004, “Surface Roughness Effects on Turbine Blade Aerodynamics.” ASME Journal of Turbomachinery, 127(3): 453–461.

[59] Bammert, K., and Sandstede, H., 1976, “Influences of Manufacturing Tolerances and Surface Roughness of Blades on the Performance of Turbines.” ASME Journal of Engineering for Gas Turbines and Power, 98(1): 29–36.

[60] Vera, M., Zhang, X. F., Hodson, H., and Harvey, N., 2007, “Separation and Transition Control on an Aft-Loaded Ultra High-Lift LP Turbine Blade at Low Reynolds Numbers: High-Speed Validation.” ASME Journal of Turbomachinery, 129(2): 340–347.

[61] Boyle, R. J., and Senyitko, R. G., 2003, “Measurements and Predictions of Surface Roughness Effects on the Turbine Vane Aerodynamics.” Proceedings of the ASME Turbo Expo 2003, Atlanta, Georgia, USA. Paper no. GT2003-38580.

[62] Vazquez, R., Torre, D., Partida, F., Armananzas, L., and Antoranz, A., 2011, “Influence of Surface Roughness on the Profile and End-Wall Losses in Low Pressure Turbines.” Proceedings of the ASME Turbo Expo 2011, Vancouver, Canada, paper no. GT2011-46371.

[63] Turner, A. B., Tarada, F. H. A. and Bayley, F. J., 1985, "Effects of Surface Roughness on Heat Transfer to Gas Turbine Blades." AGARD-CP-390.

[64] Bunker, R. S., 1997, "Separate and Combined Effects of Surface Roughness and Turbulence Intensity on Vane Heat Transfer." Proceedings of the ASME 1997 International Gas Turbine and Aeroengine Congress and Exhibition, Orlando, Florida, USA. Paper no. 97-GT-135.

[65] Stripf, M., Schulz, A., and Wittig, S., 2005, "Surface Roughness Effects on External Heat Transfer of a HP Turbine Vane." ASME Journal of Turbomachinery, 127(1): p. 200–208.

[66] Lorenz, M., Schulz, A., and Bauer, H., 2012, "Experimental Study of Surface Roughness Effects on a Turbine Airfoil in a Linear Cascade— Part I: External Heat Transfer." ASME Journal of Turbomachinery, 134(4): 041006.

[67] Blair, M. F., 1994, "An Experimental Study Heat Transfer in a Large-Scale Turbine Rotor Passage." ASME Journal of Turbomachinery, 116(1): p. 1–13.

[68] Rutledge, J. L., Robertson, D., and Bogard, D. G., 2006, "Degradation of Film Cooling Performance on a Turbine Vane Suction Side due to Surface Roughness." ASME Journal of Turbomachinery, 128(3): p. 547–554.

[69] Abuaf, N., Bunker, R. S., and Lee, C. P., 1998, "Effects of Surface Roughness on Heat Transfer and Aerodynamic Performance of Turbine Airfoils." ASME Journal of Turbomachinery, 120(3): p. 522–529.

[70] Hoffs, A., Drost, U., and Bölcs, A., 1996, "Heat Transfer Measurements on a Turbine Airfoil at Various Reynolds Numbers and Turbulence Intensities Including Effects of Surface Roughness." Proceedings of the ASME 1996 International Gas Turbine and Aeroengine Congress and Exhibition, Birmingham, UK. Paper no. 96-GT-169.

[71] Boyle, R. J., and Senyitko, R. G. "Effects of Surface Roughness on Turbine Vane Heat Transfer." Proceedings of the ASME Turbo Expo 2005, Reno, Nevada, USA. Paper no. GT2005-69133.

[72] Bacci, T., Picchi, A., Lenzi, T., Facchini, B., and Innocenti, L., 2021, "Effect of Surface Roughness and Inlet Turbulence Intensity on a Turbine Nozzle Guide Vane External Heat Transfer: Experimental Investigation on a Literature Test Case." ASME Journal of Turbomachinery. 143(4): 041006.

[73] Erickson, E. L., Ames, F. E., and Bons, J. P., 2012, "Effects of a Realistically Rough Surface on Vane Heat Transfer Including the Influence of Turbulence Condition and Reynolds Number." ASME Journal of Turbomachinery, 134(2): 021013.

[74] Barlow, D. N., and Kim, Y. W., 1995, "Effect of Surface Roughness on Local Heat Transfer and Film Cooling Effectiveness." Proceedings of the ASME 1995 International Gas Turbine and Aeroengine Congress and Exposition, Houston, Texas, USA. Paper no. 95-GT-014.

[75] Lawson, S. A., and Thole, K. A., 2011, "Effects of Simulated Particle Deposition on Film Cooling." ASME Journal of Turbomachinery, 133(2): 021009.

[76] Goldstein, R. J., Eckert, E. R. G., Chiang, H. D., and Elovic, E., 1985, "Effect of Surface Roughness on Film Cooling Performance." ASME Journal Engineering of Gas Turbines and Power, 107(1): 111–116.

[77] Schmidt, D. L., and Bogard, D. G., 1996, "Effects of Free-Stream Turbulence and Surface Roughness on Film Cooling." Proceedings of the ASME 1996 International Gas Turbine and Aeroengine Congress and Exhibition, Birmingham, UK. Paper no. 96-GT-462.

[78] Schmidt, D. L., Sen, B., and Bogard, D. G., 1996, "Effects of Surface Roughness on Film Cooling." Proceedings of the ASME 1996 International Gas Turbine and Aeroengine Congress and Exhibition, Birmingham, UK. Paper no. 96-GT-299.

[79] Bogard, D. G., Snook, D., and Kohli, A., 2003, "Rough Surface Effects on Film Cooling of the Suction Side Surface of a Turbine Vane." Proceedings of the ASME 2003 International Mechanical Engineering Congress and Exposition, Washington, D. C., USA. Paper no. IMECE2003-42061.

[80] Rätzer-Scheibe, H.-J. and Schulz, U., 2007, "The Effects of Heat Treatment and Gas Atmosphere on the Thermal Conductivity of APS and EB-PVD PYSZ Thermal Barrier Coatings." Surface & Coatings Technology, 201(18): p. 7880–7888.

[81] Wellman, R. G., and Nicholls, J. R., 2007, "A Review of the Erosion of Thermal Barrier Coatings." Journal of Physics D: Applied Physics, 40(16): p. 293–305.

[82] Darolia, R., 2013, "Thermal Barrier Coatings Technology: Critical Review, Progress Update, Remaining Challenges and Prospects." International Materials Reviews, 58(6): p. 315–348.

[83] Sjolander, S., Isaacs, D., and Klein, W., 1993, "Aerodynamics of Turbine Blades With Trailing-Edge Damage: Measurements and Computations," XI International Symposium on Air Breathing Engines, Tokyo, Japan, paper no. ISABE 93-7130.

[84] Di Mare, L., Imregun, M., Smith, A., and Elliott, R., 2007, “A Numerical Study of High Pressure Turbine Forced Response in the Presence of Damaged Nozzle Guide Vanes.” The Aeronautical Journal, 111(1125), 751-757.

[85] Meyer, M, Parchem, R, and Davison, P., 2011, “Prediction of Turbine Rotor Blade Forcing due to In-Service Stator Vane Trailing Edge Damage.” Proceedings of the ASME 2011 Turbo Expo, Vancouver, Canada, paper no. GT2011-45204.

[86] Bouchard, D., Asghar, A., LaViolette, M., Allan, W. D. E., and Woodason, R., 2014, “Experimental Evaluation of Service-Exposed Nozzle Guide Vane Damage in a Rolls Royce A-250 Gas Turbine.” ASME Journal of Engineering for Gas Turbines and Power, 136(10): 102601.